

See discussions, stats, and author profiles for this publication at: <https://www.researchgate.net/publication/327671865>

Luminescent properties of Pb-based (PbX) colloidal quantum dots (CQDs) in vacuum, on silicon and integrated with a silicon-on-insulator (SOI) photonic integrated circuit (PIC)

Thesis · April 2016

DOI: 10.14288/1.0228629

CITATIONS

0

READS

6,329

1 author:



Charles A. Foell III

University of British Columbia

12 PUBLICATIONS 89 CITATIONS

SEE PROFILE

**Luminescent properties of Pb-based (PbX)
colloidal quantum dots (CQDs) in vacuum, on
silicon and integrated with a silicon-on-insulator
(SOI) photonic integrated circuit (PIC)**

by

Charles Alden Foell III

M.Sc. Physics, University of Vermont, 2006

B.Sc. Physics, University of Vermont, 2004

A THESIS SUBMITTED IN PARTIAL FULFILLMENT
OF THE REQUIREMENTS FOR THE DEGREE OF

Doctor of Philosophy

in

THE FACULTY OF GRADUATE AND POSTDOCTORAL
STUDIES
(Physics)

The University Of British Columbia
(Vancouver)

May 2016

© Charles Alden Foell III, 2016

Abstract

In the rapidly evolving field of experimental quantum information processing, one important sub-field pursues a potentially scalable implementation that transports quantum information encoded in photons throughout “photonic circuits” fabricated in a silicon wafer. A key component is an efficient on-demand source of these single photons, and this dissertation aimed to assess the feasibility of one proposed realization of such a source by integrating few PbSe colloidal quantum dots (CQDs, demonstrated single photon emitters in nanoparticle form) into the mode volume of an optical microcavity designed to efficiently direct quantum dot emission into a silicon photonic circuit. Although no direct evidence of *single* photon emission was observed, results prompted a number of follow-up experiments and considerable theoretical modeling to understand this quantum dot, photonic circuit system.

The methods of investigation included (1) temporally-, spectrally-, and spatially-resolved photoluminescence (PL) measurements of PbSe CQDs integrated into SOI PICs and relatable environments (solution, thick film, thin film), (2) temperature-dependent, air-exposure studies of PbSe CQD thick film PL, (3) development and application of kinetic and quantum mechanical cavity-coupled modeling that admit complete accounting of the photonic density of states, depolarization effects, and non-radiative decay, and (4) a photon coincidence test of single photon emission.

The main findings of this work are: (1) while capture of cavity-enhanced PbSe CQD emission into a silicon photonic circuit was demonstrated, the overall photon generate rate is inadequate for any useful implementation, (2) the measured coupling rate can be modeled and explained in terms of

system parameters extracted from auxiliary experimental results obtained with the PbSe CQDs in isolation, or on isolated microcavities, and (3) consistent results could only be obtained after nontrivial depolarization factors and non-radiative decay processes are properly accounted for. From this it is clear that the performance of PbSe CQDs in this configuration of a single photon source in silicon is currently limited by a long-lived trap state with a several microsecond lifetime, and large depolarization effects that inhibit emission. Although plausible future efforts may mitigate these effects substantially, performance may still be hindered by the intrinsic emission strength of PbSe CQDs.

Preface

Identification and large-scale design of the research program was primarily set by my research supervisor and our group principal investigator, Jeff F. Young. My role was primarily implementation and development of the experimental setups, measurements, modeling, and analysis used to implement the research program.

Three publications arising partially or entirely from the work within this dissertation are as follows:

- C. A. Foell, E. Schelew, H. Qiao, K. A. Abel, S. Hughes, F. C. J. M. van Veggel, and J. F. Young, Saturation behaviour of colloidal PbSe quantum dot exciton emission coupled into silicon photonic circuits, *Optics Express*, Vol. 20, Issue 10, pp. 10453-10469 (2012) [73]
- C. A. Foell, K. A. Abel, F. C. J. M. van Veggel, and J. F. Young, Kinetic analysis of the temperature dependence of PbSe colloidal quantum dot photoluminescence: Effects of synthesis process and oxygen exposure, *Phys. Rev. B* 89, 045139 (2014) [74]
- R. Quintero-Torres, C. A. Foell, J. Pichaandi, F. C. J. M. van Veggel and J. F. Young, Photoluminescence dynamics in solid formulations of colloidal PbSe quantum dots: Three-dimensional versus two-dimensional films, *Appl. Phys. Lett.* 101, 121904 (2012) [173]

The experimental results of Foell *et al.* (2012) [73] are presented in Chapter 2, and related modeling in Chapter 3. Much of the text of this publication is directly incorporated into this dissertation. My role in this

publication was all modeling, including FDTD and quantum mechanical. I also contributed to the majority of the manuscript preparation and review of it. The stand-alone cavity was fabricated, sample prepared, and measurements performed by Haijun Qiao. Photonic circuits in that publication, and used in this dissertation in Chapter 4 were designed and characterized by Simon Dickreuter, Jacob Slack, Jeff F. Young, and Ellen Schelew. The quantum mechanical model used in modeling was proposed by Stephen Hughes and Jeff Young. CQDs were synthesized by Keith Alexander Abel.

The experimental results of Foell *et al.* (2014) [74] are presented in Chapter 2 and related modeling in Chapter 3. Much of the text of this publication is also directly incorporated into this dissertation. My role in this publication was all sample preparation, measurements and modeling. I also contributed to the majority of the manuscript preparation and review of it. The kinetic model used was proposed by Jeff F. Young. CQDs were synthesized by Jothirmayanantham Pichaandi. The “dip-coating” apparatus and inert environment glove box were developed in large part by summer students Nancy Liu and Manveer Bains.

The experimental results of Quintero-Torres *et al.* (2012) [173] are presented in Chapter 2 and related FDTD dielectric modeling in Chapter 3. My role in this publication was all sample preparation and dielectric modeling. I also contributed to portions of the manuscript and review of it. Measurements were performed by Rafael Quintero-Torres and CQDs were synthesized by Jothirmayanantham Pichaandi.

Reproduction of content from these publications is with permission from the respective publishers.

Table of Contents

Abstract	ii
Preface	iv
Table of Contents	vi
List of Tables	x
List of Figures	xi
Acknowledgments	xxvii
1 Introduction	1
1.1 Dissertation overview	1
1.2 Quantum information processing (QIP)	5
1.2.1 QIP overview	6
1.2.2 Bits and qubits	6
1.2.3 Classical and quantum logic gates	8
1.2.4 Quantum teleportation: an example	11
1.2.5 Linear optical quantum information processing (LOQIP) .	12
1.3 LOQIP in the SOI platform	19
1.3.1 Overview	19
1.3.2 Linear optical components	20
1.3.3 Single photon detectors	27
1.3.4 Single photon sources	30

1.3.5	Hybrid approaches to SOI platform single photon sources	35
1.4	Lead-based (PbX) colloidal quantum dots (CQDs) for single photon sources in SOI LOQIP	36
1.4.1	Basic CQD photophysics	36
1.4.2	Band structure context, CdX CQD comparison	39
1.4.3	Non-radiative recombination, defect/surface states, and CQD formulation	42
1.4.4	Impact of dielectric environment on CQD emission: depolarization and radiative density of states	45
1.4.5	CQD emission on silicon and in SOI PICs	46
1.5	Dissertation aim restatement, methodology, and organization	47
2	Experiment (non-PIC)	49
2.1	Substrates and photonic component fabrication	49
2.1.1	SOI and silicon substrates	49
2.1.2	Photonic crystal cavities	50
2.2	PbX CQD formulations and integration methods	51
2.2.1	PbX CQD formulations	52
2.2.2	PbX CQD integration methods	53
2.3	PL measurements overview and optical setups	58
2.3.1	PL measurements overview	58
2.3.2	Head-on continuous wave (CW) laser excitation	59
2.3.3	Pulsed excitation in back-scatter geometry	60
2.4	Power saturation of cavity-coupled CQD PL	62
2.5	Time-resolved decay of CQDs in various formulations	65
2.6	Air exposure influence on CQD thick film temperature-dependent PL	68
3	Modeling	72
3.1	Overview of model	72
3.1.1	Exciton thermalization in the ground state manifold .	74
3.1.2	Depolarization, spontaneous emission rates	75

3.1.3	Intrinsic dipole moment	78
3.2	Power saturation of cavity-coupled CQD PL	79
3.2.1	Master equation model	80
3.2.2	Model dielectric environment	83
3.2.3	“Simple” model parameters	83
3.2.4	Spontaneous emission rate $\gamma_{XG} = \gamma_{XG,\epsilon(\mathbf{r})}$	84
3.2.5	Cavity-QD coupling g	85
3.2.6	Laser-QD coupling Ω	87
3.2.7	Fit parameter	88
3.2.8	Saturation modeling results	90
3.2.9	Saturation modeling conclusions	93
3.3	Modeling time-resolved decay of CQDs in various formulations	93
3.3.1	Dielectric model accounting of radiative decay	94
3.3.2	Radiative efficiency from time-resolved emission and dielectric modeling	95
3.3.3	Discussion	96
3.4	Air exposure dependence of exciton kinetics	97
3.4.1	Fit methods and extracted parameters	103
3.4.2	Results	105
3.4.3	Discussion	108
3.4.4	Conclusions	109
3.5	Modeling discussion	111
4	PbX CQDs in SOI PICs	114
4.1	Sample preparation (SOI PICs, CQD integration)	114
4.2	Measurement overview and optical setups	116
4.2.1	Optical setup	117
4.2.2	Microphotoluminescence	122
4.2.3	Photon coincidence	126
4.3	Discussion	134
4.3.1	Extrapolation of PIC-coupled photon rate	134
4.3.2	Estimated single CQD results	136
4.3.3	Comparisons and potential use as a single photon source	136

5 Conclusions	138
5.1 Conclusions, discussion and significance	139
5.2 Limitations, strengths, and future work	140
Bibliography	142
A Dip coating procedural details	171

List of Tables

Table 2.1 PbSe CQD thick film sample descriptions, for integrated PL traces plotted in Figure 2.10.	69
Table 3.1 PbSe CQD thick film sample descriptions, for integrated PL traces plotted in Figure 3.8. Samples from our lab, already presented in Section 2.6, are reproduced here for convenient comparison to samples from other labs. “Alkyl-” for studies mentioned here refer to alkylselenide [93]. . .	99

List of Figures

Figure 1.1 Bits and qubits. Bits take on one of two values, e.g. 1 or 0. Qubits may be represented by a complex linear superposition of two orthogonal basis vectors. In the Bloch sphere parametrization, a pure qubit state is represented by a vector of unit length and of angular direction (θ, ϕ) , such that unitary operations upon the qubit rotate the vector to some other other direction. Bit measurement is commonly deterministic, whereas qubit measurement is generally probabilistic.	7
Figure 1.2 Example classical logic circuit and logic gates NOT, AND, and XOR. Any algorithm may be encoded in a circuit constructed of suitable arrangement of a universal (functionally complete) set of logic gates, e.g. of the gate set consisting of the NOT gate and AND gate.	9
Figure 1.3 Example universal set of quantum gates consisting of three single qubit rotation gates and one two-qubit CNOT gate, with circuit symbols, depictions, and representations. Single qubit gates include rotations about each of the Bloch sphere axes, generated by the Pauli matrices X , Y , and Z . The two qubit CNOT gate flips the target qubit $ q_t\rangle$ if and only if the control qubit $ q_c\rangle$ is $ 1\rangle$. Any multi-qubit state may be constructed with these gates. . .	10

Figure 1.4	Quantum teleportation circuit. See Figure 1.3 for quantum gate definitions. Single lines are quantum channels and double lines are classical channels. A quantum state is transported from location A to location B using two classical information channels and one quantum channel.	11
Figure 1.5	(A): General dual rail optical qubit basis states consist of single photon absence/presence in one of two optical modes. (B) and (C): Free-space polarization encoded photonic qubits that exemplify dual rail qubits, and (D): mechanism to convert polarization encoded qubits to path encoded qubits.	14
Figure 1.6	Universal LOQIP quantum gates, constructed from (A) phase shifters, (B) beam splitters, and photon detectors, for path encoded optical qubits. Rotation angles θ and ϕ map directly onto the Bloch sphere. (C): CNOT gate success, i.e. $ \psi_{\text{target,out}}\rangle$ equaling $ \psi_{\text{control,in}} \oplus \psi_{\text{target,in}}\rangle$, coincides with photon detection in the output ancillary modes $ a_{\text{ancillary,out}}\rangle$ and $ b_{\text{ancillary,out}}\rangle$	15
Figure 1.7	Hong-Ou-Mandel (HOM) effect measurement setup, with “HOM dip” in photon detection event coincidences. A dip to zero coincidences (for zero path length difference from the beam splitter to each detector, controlled by a variable delay) is evidence of photon interference of the two photon sources and indication of the photon sources emitting photons indistinguishable from each other.	17
Figure 1.8	The SOI platform, for LOQIP. (A): Typical silicon-on-insulator (SOI) dimensions used for SOI-based photonic integrated circuits and (B) example etching steps. Additional functionality may be achieved by lithographic integration of metal contacts, ion doping, and deposition of other materials. (C): Example LOQIP circuit layout and depicted embedment in an SOI wafer.	21

- Figure 1.9 (A): Total internal reflection at silicon-air and silicon-oxide interfaces. (B) and (C): Ridge waveguide that utilizes total internal reflection to contain light within the waveguide. (C): Example electric field mode profile, showing non-zero field beyond the silicon. (D): Ridge waveguide beam splitter, labeled with a characteristic bending radius (typically around $10 \mu\text{m}$ for these materials) that limits the minimum size in accordance with the total internal reflection angles described in (A). Beam splitters admit R_y^α single qubit rotations and, along with single photon detectors, may be used to realize a CNOT gate. 22
- Figure 1.10 Example phase shifter, capable of producing single qubit rotations R_z^ϕ . A small current passing through a metallic strip, connected to the control electronic microcircuitry, may locally heat and change the index of refraction, thus the relative optical path length (note that the metallic strip is not necessarily in contact with the waveguide, but more likely embedded in a layer above or below it). 23
- Figure 1.11 Photonic band gap confinement mechanism used in SOI photonic circuits. (A): Slab hexagonal lattice photonic crystal. (B): Definitions of TE and TM propagating modes. (C): Example photonic band structure for slab photonic crystal similar to the one depicted in (A). 25

Figure 1.12 Photonic crystal structures. (A): Photonic crystal waveguide, consisting of a line defect in a slab photonic crystal, joined with a ridge waveguide. (B): Photonic crystal cavity, consisting of a point defect in a slab photonic crystal, accompanied by a sketch of the local photonic density of states (ρ DOS) as a function of embedded emitter frequency ω at the cavity center. Slab photonic crystals may consist of a regular pattern of air holes which, for the cases of photonic crystal waveguides and cavities, are omitted (i.e. not made) along a line or localized region during patterning of the remainder of the structure. 26

Figure 1.13 (A): Waveguides terminating in a diffraction grating, the latter for free-space/on-chip light conversion. (B): Partial band structure diagram for the photonic crystal with photonic crystal waveguide bands (green). Guided (slab-like) modes in red and blue. Modes within the light cone are not confined to the device silicon. A bound state such as a photonic crystal cavity (not shown in this diagram) would also lie within the TE band gap. The in-slab amplitude of propagating waveguide modes (below the light line) decays exponentially in the grating region (i.e. is non-propagating and above the light line) as the field is diffracted out of the device slab.

Figure 1.14 Example integrated detectors, in which photodetective material is placed atop waveguide within waveguide mode. (A): perspective view of detecting material atop waveguide, with connected electrical wires. (B): head-on view, overlayed with waveguide profile. Size of photodetective material in (A) and (B) is slightly exaggerated for drawing purposes. (C): Realized integrated, superconducting single photon detector from the Young lab [9]. 29

37

38

Figure 1.20 Comparison of band and state structures of PbSe and CdSe bulk crystals and quantum-confined nanocrystals. (A) and (B): Bulk band diagrams for PbSe and CdSe, respectively, adapted with permission from [236]. (C) and (D): (left) bulk and quantum confined (right) band edge energy levels, including electronic and spin degrees of freedom. Bulk energy levels do not include splitting due to crystal field or spin orbit coupling, but quantum confined levels do, along with splittings due to other interactions.

40

- Figure 2.1 (A): Schematic and scanning electron micrograph of an “L3” microcavity. (B): Fundamental in-gap cavity mode electric field intensity at the silicon-air interface, with etched holes outlined. Axes originate at the L3 slab centroid, and \hat{z} is perpendicular to \hat{x} and \hat{y} . Yellow scale bars are 500 nm in length. Figure adapted from [164].

Figure 2.2 Dip-coating for thin film formulations, in an inert-gas glove box. (A): The glove box and dipping setup used for monolayer, sub-monolayer, and generally dip-coating formulations. (B): Example scanning electron micrograph of a sub-monolayer of CQDs on a silicon surface using the setup in (A) and described in-text, published in [173].

Figure 2.3 Site-selective binding technique, as published in [164], used to integrated PbX CQDs to primarily within the main antinode of the the fundamental cavity mode of a standalone L3 photonic crystal cavity, for the sample studied in this chapter. Prior to the AFM site-selective surface oxidation depicted in (A), the silicon is coated with dodecyl molecules. In (B), application of a voltage from the AFM locally removes the dodecyl molecules and oxidizes the silicon surface. Immersion in a buffered oxide etch removes the oxidized silicon but leaves the dodecyl coated silicon intact. The sample is finally dipped in a suspension of CQDs (C), which adhere preferentially to the hydrogen-terminated silicon (relative to the dodecyl coated silicon). (D) and (E) are atomic force micrographs of the sample surface, with (E) corresponding to the region within the white rectangle in (D). (F): resulting microphotoluminescence (μ PL) collected directly from the cavity region. Yellow scale bar is 500 nm in (D) and 50 nm in (E). Unit conversion: 1 eV \leftrightarrow 1240 nm, 0.8625 eV \leftrightarrow 1500 nm.

Figure 2.4 Head-on continuous wave (CW) HeNe excitation setup used for power saturation measurements of PbX CQD emission coupled to a standalone L3 cavity and steady-state integrated PL of PbSe CQD thick films. Mirror pair $M_{T1,T2}$ diverts collected light down ($-\hat{x}$) and then in the direction of the Bruker FTIR; details are available in the insets of Figure 4.4F.	60
Figure 2.5 Back-scattering geometry with pulsed laser excitation setup used for time-resolved studies in [173] and presented in Section 2.5.	61
Figure 2.6 Comparison of power dependence of PbSe CQDs in thin formulations in different dielectric environments. (A): Example low and high excitation power PL spectra of CQDs on the surface of a SOI L3 optical microcavity, integrated by dip-coating, and labels indicating cavity-coupled and background contributions at a cavity mode wavelength. (B): Example low and high excitation power PL spectra of a thin film of PbSe CQDs on a bare silicon surface, also deposited by dip-coating, for the same excitation setup used for data in (A). (C): Power dependence comparison for cavity-coupled PL of (A) and monolayer PL of (B), for the same excitation conditions, showing how the power dependent PL of the monolayer is nearly linear but strongly saturated for the cavity-coupled PL. (D): Power dependence comparison for samples with Nd:YAG excitation and identical excitation/collection geometries, again exemplifying the difference in saturation powers. (E): Same as in (D), but the monolayer data scaled along the power axis by the excitation enhancement factor calculated in section 3.2 (a factor of 9) and scaled vertically to best match the cavity-coupled data fit. Note the good overlap, which can be interpreted with Chapter 3 modeling.	63

Figure 2.7	Experimental setup and resulting data modeled in this article. (A): Schematic of excitation/collection geometry: excitation (at 633 nm) and collection performed with a common 100X microscope objective. Red-filled circle indicates $1/e$ excitation spot intensity. Shaded square indicates span of grafted PbSe CQDs. (B): Example PL spectrum with cavity-coupled emission indicated, and cavity-coupled PL versus pump power.	64
Figure 2.8	Time-dependent PL at 300 K for PbSe CQDs dispersed in hexanes (black dots); drop-cast film (blue circles); and sub-monolayer (red squares). The inset shows the steady state PL spectra from drop-cast (top, blue), solution (middle, black), and sub-monolayer dispersions (bottom, red) of the same batch of CQDs. The monolayer was excited with 3000 times more average power than the drop-cast film.	66
Figure 2.9	Histograms of the shortest time constants, τ_1 (left, (A) and (C)), and the average time constants $\frac{A_1\tau_1+A_2\tau_2}{A_1+A_2}$ (right, (B) and (D)) components of the measured lifetimes extracted from two-exponential fits to decay curves taken from various locations on the drop-cast samples (bottom, (C) and (D)), and the dip-coated samples (top, (A) and (B)). The mean values are (A) 90 ns, (B) 135 ns, (C) 190 ns, (D) 200 ns. (E): Tabular summary of known and unknown radiative and non-radiative decay parameters, after measurements indicated in this section but before modeling of the photonic density of states performed in Chapter 3.	67

Figure 2.10 Integrated PL data sets (black squares), normalized to their maximum values, along with best-fit model yield curves (calculated below) in solid red and corresponding model PL contributions from each of two possible emissive states or clusters of emissive states in dotted and dashed lines, respectively. Modeling is described in Chapter 3. Table 2.1 contains descriptions of the samples. 70

Figure 3.1 Overview of general considerations for modeling PbX CQD emission in nanophotonic environments. (A): Excitonic states are numerous and the distribution of transition dipole moment magnitudes is varied across a number of computational studies. (B): Simplified excitonic state structure, for which rapid decay from higher-lying state(s) $|P\rangle$ to a ground state excitonic manifold is understood $|X\rangle$, but the decay from the ground state excitonic manifold $|X\rangle$ to the CQD ground state $|G\rangle$ is generally environment dependent. (C): Example depolarization effect on the electric field for a dielectric sphere, one environmental contribution to exciton decay dynamics. 73

Figure 3.3 Model dielectric environment $\epsilon(\mathbf{r}, \omega) = \epsilon_{L3}(\mathbf{r}, \omega) + \epsilon_{CQDs}(\mathbf{r}, \omega)$. Nanocrystal array $\epsilon_{CQDs}(\mathbf{r}, \omega)$ on left, centered on the L3 cavity surface. The computational volume for FDTD calculations (see text) is restricted to the 3 μm cube centered about the centroidal CQD. The intrinsic “test” dipole is located at the center of centroidal CQD, position \mathbf{r}_{CQD} . The device silicon slab is surrounded by vacuum above and below, with backing silicon 1.2 μm below.	84
Figure 3.4 Spontaneous emission rate of a point dipole source of frequency $\omega_{\text{cav}} + \delta\omega$, for positions along the \hat{z} -axis of the L3 cavity, <i>excluding</i> the cavity mode and CQD array, for electric dipole orientations along axes \hat{x} , \hat{y} , or \hat{z} (see text and orientation definitions in Figure 2.1). All values normalized to the free-space spontaneous emission rate $\gamma_{XG,0}$	86
Figure 3.5 Intensity profiles of HeNe excitation field, as modulated by the L3 cavity $\epsilon_{L3}(\mathbf{r})$. Gaussian laser field was injected along the \hat{z} axis towards increasingly negative z , indicated by black arrow. Air-silicon interfaces lined in black. (left) Profile several nanometers above the slab surface, the plane containing the PbSe CQDs. (right) Profile in the $x = 0$ plane.	89
Figure 3.6 Best (minimum χ^2) fits to cavity-enhanced photoluminescence for only three electronic levels (left), i.e. without a non-radiative state, and for four electronic levels (right), i.e. including a non-radiative “trap” state.	90

- Figure 3.7 Trap state lifetime $\tau_{\text{trap}} = \gamma_{YG}^{-1}$ required to fit the data. Parametrization of τ_{trap} is in terms of the “effective depolarization”, DPF , which is defined in-text (see Equation 3.24) and is equal to the laser field inside the CQD in the full model dielectric environment relative to the laser field inside the same CQD in vacuum. Variation of τ_{trap} with DPF is dominated by uncertainties in parameters specific to our dielectric environment (photonic crystal cavity, CQD array), whereas variation of τ_{trap} for a particular DPF is dominated by parameter uncertainty not specific to our dielectric environment (e.g. solvent permittivity from solvent-based CQD properties). Points are sampled from the model parameter space. 92
- Figure 3.8 Integrated PL data sets (black squares), normalized to their maximum values, along with best-fit model yield curves (calculated below) in solid red and corresponding model PL contributions from each of two possible emissive states or clusters of emissive states in dotted and dashed lines, respectively. Samples series *A* and *B* are from work published in references [43, 93], and sample series *C* and *D* were already described in Section 2.6 but reproduced here for convenient comparison. Table 3.1 contains descriptions of these samples. 98
- Figure 3.9 Modeled energy level arrangement. Levels *A* and *B* are in thermal quasi-equilibrium and populated by pumping of higher-lying levels at a rate g_{ex} . They respectively consist of N_A and N_B states of average radiative decay rates $\overline{\gamma_A}$ and $\overline{\gamma_B}$. The general non-radiative decay Γ , the nature of which is described in detail in-text, is not specific to level *A* or *B* for the purposes of this kinetic modeling, and is indicated by the dashed arrow. 101

Figure 3.10 Subscript j indexes the non-radiative decay pathways, e.g. as indexed in Equation 3.32. Bars represent the ranges of parameter values that, upon substitution into Equation 3.29, using Equation 3.27, generate or nearly generate the model curves in Figure 2.10. Rates are normalized as described in-text (leading up to Equation 3.32), and energies are in meV. Sample labeling is as in Figure 2.10 and Table 2.1. Parameter $\Delta\epsilon_{BA}$ is restricted from above to 80 meV for reasons described in-text. Rates sufficiently small to render their corresponding energies meaningless are omitted, along with those energies.	104
Figure 4.1 (A): Full photonic integrated circuit (PIC) designed and characterized in-lab [189] and used in this dissertation as a PIC in which PbSe CQDs were integrated and their luminescence was measured. (B): PIC transmission measurement schematic. (C): Transmission spectrum of the PIC, prior to CQD integration. (D): PL of PbSe CQDs in solution, prior to their integration into the PIC.	115
Figure 4.2 Optical setup used for characterizing PbX CQD emission in and near the photonic integrated circuits, including (a) steady-state, Nd:YAG excited microphotoluminescence (μ PL) spectroscopy, (b) spectrally-integrated, time-resolved μ PL emission using a 660 nm pulsed laser, and (c) photon coincidence (correlation) measurements.	118
Figure 4.3 Simple overlay of excitation and collection regions relative to the PIC components. Collection area and position was controlled with the far apertures $FA_{L,C,R}$. Position of the excitation spot was controlled by adjusting the position of the excitation lens assembly ELA and mirrors preceding it. The $1/e^2$ minimum power diameters were 20 μ m and 3.5 μ m for the Nd:YAG and 660 nm pulsed laser excitation sources, respectively.	119

Figure 4.4	Detailed illustrations of excitation and collection geometries, an elaboration upon the larger scale diagrams depicted in Figures 4.2 and 4.3.	120
Figure 4.5	Example steady-state μ PL for excitation with several mW of Nd:YAG laser focused onto the cavity region with a $1/e^2$ power waist of $20 \mu\text{m}$. (A): PL collected over the cavity region. (B): PL collected over the grating region. (C): Aperture (both near and far) spectrum collected over part of the grating region, with a transmission plot (red) of the PIC, measured prior to CQD integration. (D): Power-saturation of the circuit-coupled, cavity-enhanced CQD PL, collected from the grating using the apertures per (C).	123
Figure 4.6	Example spectra (200 FTIR scans, 1 nm resolution) and time-resolved decay (with superimposed single exponential decay fits) of PL collected, for excitation with the 660 nm Sepia pulsed laser source with $1/e^2$ power waist of $3.5 \mu\text{m}$, 10 MHz repetition rate (1 MHz for collection from the cavity region), and ≈ 0.05 mW average incident power. Background PL spectra with the Sepia laser excitation differ from background PL spectra with the 1064 nm Nd:YAG excitation, which is not unexpected given differences in excitation spot size, intensity, and wavelength. The single exponential $1/e$ decay times for PL collected from the gratings are 30 ns, but don't capture the faster decay at short time scales. Decay from the cavity region is characterized by a $1/e$ decay time of 60 ns.	124

Figure 4.7 (A): Idealized stream of regularly emitted on-demand photons (red) compared to a stream of photons exhibiting photon bunching. (B): Histogram of photons within a fixed time interval for a Poissonian source (striped yellow, purple) and an ideal stream of regularly emitted photons from an on-demand source. (C): Basic photon coincidence setup to test if a source emits only a single photon at a time. 126

Figure 4.8 (A) and (B): PL spectra collected from diffraction gratings connected to the same cavity, for the cavity excited with pulsed 660 nm Sepia light, as used for coincidence measurements described later in this chapter, and *before* any spectral filtering was performed. See Figure 4.9 for spectral filtering performed. Insets are the same spectra, plotted over a smaller wavelength range around the cavity wavelength, with Lorentzian fits and indicated ratio of peak PL to background PL at the cavity wavelength (after proper baseline subtraction). Spectra are noisier than those presented previously in this section due to a higher spectral resolution relative to a number of FTIR scans. Each cavity to background ratio for this sample is smaller than for the samples in previous sections, but this sample was the only, at the time of measurements, from which cavity coupled PL collected from both gratings dominated the total PL signal at the cavity wavelength. 128

Figure 4.9 Spectral filtering used for coincidence measurements. (A): The band pass free-space filter (FSF) from Edmunds blocks (with OD4) all but the wavelength range 1550 nm to 1600 nm. (B): The tunable narrow band pass fiber filter (FF) from Koshin Kogaku possesses an approximately Lorentzian lineshape with 1.2 nm FWHM and can be tuned to the cavity wavelength. (C): Schematic of the free-space to fiber coupler assembly and in-line fiber filter (FF), with pre- and post- filtering locations, as plotted in (D) through (F), circled. (D): Example measured spectrum (from Figure 4.8B) before spectral filtering. (E): Extrapolated PL after propagating the spectrum through the free space filter and into the fiber, using the measured pre-filter spectrum $S(\lambda)$ and free space filter transmission spectrum $T_{FSF}(\lambda)$, as well as the measured free-space to fiber coupling efficiency. (F): Extrapolated PL, after both the free space and fiber filters, using the filter transmission spectra $T_{FF}(\lambda; \lambda_0)$ and $T_{FSF}(\lambda)$, and exemplified for the tunable filter both tuned to the cavity wavelength and slightly detuned from it. 132

Figure 4.10 Example coincidence plots for total count rate (dark counts plus signal), dark counts only, and the difference of the two. No evidence of antibunching was found for detection and excitation settings considered. 134

Acknowledgments

For Chapter 3, I gratefully acknowledge the insight regarding band structure models in this system provided by Paweł Hawrylak and Oleksandr Voznyy. I also acknowledge the financial support of the Natural Sciences and Engineering Research Council, and the Canadian Institute for Advanced Research.

For Chapter 4, I acknowledge the funding support of the Natural Sciences and Engineering Research Council, the Canadian Institute for Advanced Research, CMC Microsystems, and the Natural Resources and Applied Sciences (NRAS) Research Team Program of the Government of British Columbia. I also acknowledge Jacob Slack and Simon Dickreuter for their contributions to the SOI devices, Lumerical Solutions, Inc. for their FDTD software and software support, and Westgrid [2] for computing time on their cluster.

I also acknowledge Haijun Qiao, Keith Abel, Ellen Schelew, Jothir Mayanantham Pichaandi, Jonathan Massey-Allard, Hamed Mirsadeghi, Hailong Ning, Mario Beaudoin, Georg Rieger, and Mohsen Akhlaghi for useful discussions about research pertaining to this topic. This dissertation is built upon the knowledge of many people before me and alongside me, and I am thankful for that.

Chapter 1

Introduction

1.1 Dissertation overview

This dissertation describes a combination of materials and process synthesis, optical spectroscopy, and numerical modeling results obtained while attempting to develop a non-classical, single photon light source in a silicon-based, planar photonic circuit platform. Such a source is one of the key elements required to potentially realize scalable quantum information processing based on photons. This chapter motivates the work, and provides essential background information regarding relevant materials, concepts, and prior state of knowledge.

A variety of natural and man-made sources of electromagnetic radiation (photons) with wavelengths in the range of a few hundred to a few thousand nanometers are familiar; starlight, burning embers, lightning, incandescent filaments, fluorescent tubes, light emitting diodes, lasers etc. The nature of these sources differs qualitatively and quantitatively, but all are considered “classical light sources” owing to the statistical distribution of photons they emit (e.g. variance in photon emission times). Illumination and display are the obvious applications for many of these classical light sources, but they are also indispensable for manufacturing (laser cutting), metrology (measuring the flatness of surfaces, laser radar (LIDAR)), information processing (optical storage disks, fiber-optic transmission links that drive the Internet), and

scientific exploration (e.g. formation of Bose-Einstein condensates).

The technical definition of “classical light”, as worked out by Glauber over half a century ago [78], is an electromagnetic state that can be described by a proper, positive probability density function $P(\alpha)$ over Poissonian superpositions of quantum mechanical photon number states known as coherent states $|\alpha\rangle$ (e.g. with density operator $\rho = \int d\alpha P(\alpha)|\alpha\rangle\langle\alpha|$). The distribution of states describing the emission from thermal sources is Gaussian, whereas it is typically Poissonian in the case of light emitted by lasers.

An ideal *on-demand single photon source* [36, 47, 64, 131, 184] emits a single, indistinguishable photon, upon triggering, into a specific optical mode, with unity efficiency, no temporal jitter, narrow bandwidth, at a high repetition rate (on order GHz). Such a stream of individual photons is non-classical in that its formal quantum mechanical state cannot be expressed in terms of a proper probabilistic distribution of coherent states.

Interest in developing high quality single photon sources has been largely driven by the rapid growth of quantum information science and technology. Quantum information research aims to understand and exploit the fundamental quantum mechanical properties of physical systems as they pertain to the acquisition and processing of information in ways that are impossible using classical tools. Three of the most compelling examples include “noise-free” measurement; the ability to overcome the fundamental statistical noise inherent in measurements based on classical probes of physical properties, quantum computation; quantum mechanically-based algorithms exist for factoring large numbers, or searching vast databases that could never be accomplished using classical information algorithms, and quantum communications; the pursuit of encoding, transmitting, and decoding quantum state information. In order to realize the predictions of quantum information science, it is necessary to develop the technology to *control* and *engineer* the quantum mechanical state of discrete physical entities. While the field is vast, a significant fraction of it is focused on demonstrating this control over photons. “Perfectly secure” quantum optical communication channels have already been demonstrated, and designs for an all-optical quantum computer have been available for over a decade [110].

Until recently, the best - but far from ideal - single photon sources consisted of bulk optical nonlinear crystals that, when pumped by relatively powerful laser beams, stochastically emit entangled photon pairs to realize “heralded” single photon sources, in which measurement of one photon guarantees the presence of another photon in the absence of losses. Powerful laser-pumped bulk optical crystals are unlikely to form the basis of a manufacturable quantum information technology. After approximately a decade of effort, single photon sources based on nanometer-scale photonic components have started to compete with these bulk optical sources in terms of raw performance, but interest in such sources derives as much from their potential high quality, as the potential they offer as a scalable, manufacturable quantum technology platform.

Interestingly, the past decade and a half has seen the parallel development of new platforms for processing *classical information* using classical laser light in “photonic circuits”, motivated by the need to make more manufacturable the increasingly complex interfaces between microelectronic computer chips, and the optical fiber network that interconnects them. Starting in the 1990’s, much effort has gone into the development of *photonic integrated circuits* (PICs) that consist of miniaturized photon sources, detectors, and passive optical components to guide and manipulate light, all embedded on a centimeter scale chip to overcome bulk component limitations. While commercial implementations of PICs exist in a variety of material platforms, the most desirable is arguably *silicon-on-insulator* (SOI), for which major benefits include mature electronic integrated circuitry, and widely available electronic and photonic integrated circuit foundries [111, 122].

All of the above strongly motivates the investigation of silicon-on-insulator based photonic circuit chips as a platform for realizing a manufacturable photon-based quantum information processor. The linear-optical quantum information processing (LOQIP) architecture alluded to above requires “only” high-quality single photon sources, single photon detectors, and linear optical components (such as beam splitters and phase shifters) [110, 114, 115]. High-quality, miniature linear optical components and single photon detectors have been demonstrated in the SOI material system; and

while further improvements in these components are still required, the main challenge at the moment is the realization of a high-quality single photon source that is compatible with the SOI platform that typically functions best at C-band telecommunication wavelengths around $1.55\text{ }\mu\text{m}$ [9, 198, 199].

The development of single photon sources compatible with SOI significantly lags that of state-of-the-art sources realized in III-V semiconductor PICs [36, 208]. These successful sources in III-V platforms are based on post-processing epitaxially-grown wafers in which high-quality single photon emitters composed of a relatively small direct band gap III-V semiconductor (e.g. InAs) “quantum dot” naturally grown in well-defined atomic planes of a distinct host III-V semiconductor (e.g. GaAs) [36] with a relatively large band gap. While silicon-germanium quantum dots can be epitaxially grown in a similar manner in chemical beam epitaxy (CBE) growth systems, their optical emission properties have yet to meet the standard attained by their III-V counterparts, at least in part due to the indirect band gap of silicon-germanium.

The realization of integrated, on-demand single photon sources in the SOI platform with performance comparable to those realized in III-V PICs therefore currently relies on a fundamentally different strategy. First, a high-quality single photon emitter near $1.55\mu\text{m}$ must be synthesized independently of the SOI wafer production, and then a process must be developed to controllably and judiciously position a single such emitter upon a photonic circuit fabricated in the SOI, so as to efficiently couple the single photon emission into a low-loss waveguide to allow photon transport to other places on the photonic chip. Importantly, the process for selectively locating the single photon emitter in the silicon photonic circuit using this hybrid approach must preserve the high optical quality of the emitter.

As explained below, some progress in this regard had been made both within the Young group and elsewhere prior to the research described in this thesis. The new experimental and modeling results obtained by the author and described in this dissertation demonstrated for the first time that exciton emission from incoherently-excited colloidal PbSe nanocrystals with diameters $\sim 5\text{ nm}$ can be coupled to single mode silicon waveguides in commercial

SOI wafers. However, the efficiency of this process is currently so low that it has not been possible to experimentally demonstrate single-photon emission behavior. The remainder of the dissertation describes research done to understand what physical phenomena are limiting the current coupling efficiency. This work serves to inform a final assessment as to the future prospects for using this approach to realize single photon sources in a silicon platform.

The remainder of this chapter is intended to (i) motivate the desire to develop tools required to manipulate the quantum state of photons for quantum information processing purposes (Section 1.2), (ii) explain the basic principles behind the approach adopted in this dissertation for hybridly integrating PbSe nanocrystals with planar photonic crystal microcavities and waveguides in silicon-on-insulator wafers, to act as a single photon source (Section 1.3), and (iii) provide background information regarding the electronic structure of PbSe nanocrystals and the electrodynamic principles upon which the photonic crystal microcavities are designed (Section 1.4). The presentation presumes the reader is knowledgeable in general graduate-level physics. Following this introductory material is a more concise statement of the dissertation aim, and organization (Section 1.5). Sections and subsections especially relevant to understanding the methodology include Single photon sources for LOQIP in the SOI platform 1.3.4, Hybrid approaches to SOI platform single photon sources 1.3.5, and Lead-Based (PbX) Colloidal Quantum Dots (CQDs) for Single Photon Sources in SOI LOQIP 1.4.

1.2 Quantum information processing (QIP)

This section reviews some basic elements of general quantum information processing (QIP), and the linear optical approach to QIP (LOQIP) in order to motivate the need to integrate single photon sources (and in particular on-demand single photon sources) in the silicon-on-insulator (SOI) platform.

1.2.1 QIP overview

Quantum technologies refer to those that fundamentally rely on controlling the quantum state of a physical system. The performance of certain classes of devices that do not make explicit use of quantum physics have already been surpassed by the performance of devices that do, e.g. SQUID-based magnetometers [98] or squeezed-state interferometers [5, 42]. Information processing technologies, such as numerical simulation, computation, and communication, have an enormous impact on society, and in the early to mid 1980's the idea of making explicit use of quantum physics to enhance information processing was put forth by Feynman and others [60, 71, 136].

Quantum information processing (QIP) involves initializing the state of a collection of quantum mechanical objects and then manipulating the quantum mechanical properties of those objects to communicate or extract information, or to solve computational problems. Benefits of existing and proposed QIP applications include increased communication security [22, 65], improved metrology precision [114], increased simulation speed of many-body quantum systems [4, 71, 129], and increased computational speed [60] for important and difficult mathematical problems (e.g. integer factoring [196], database searching [83], and expectation values [88]).

1.2.2 Bits and qubits

Information processing protocols generally encode information in a collection of bins. In the vast majority of digital *classical information processors* each bin contains one *bit*, of information, that can take on one of two distinct (Boolean) values (e.g. 1 and 0). In contrast, information in QIP is typically encoded into quantum mechanical entities denoted *qubits*, which are the quantum states of a two-dimensional Hilbert space, as depicted in Figure 1.1. Correspondingly, any *two level system* (TLS) maps onto a qubit. Qubits may be represented by a complex linear superposition of two orthogonal basis vectors. In the Bloch sphere parametrization, a pure qubit state is represented by a vector of unit length that can point in any angular direction (θ, ϕ) .

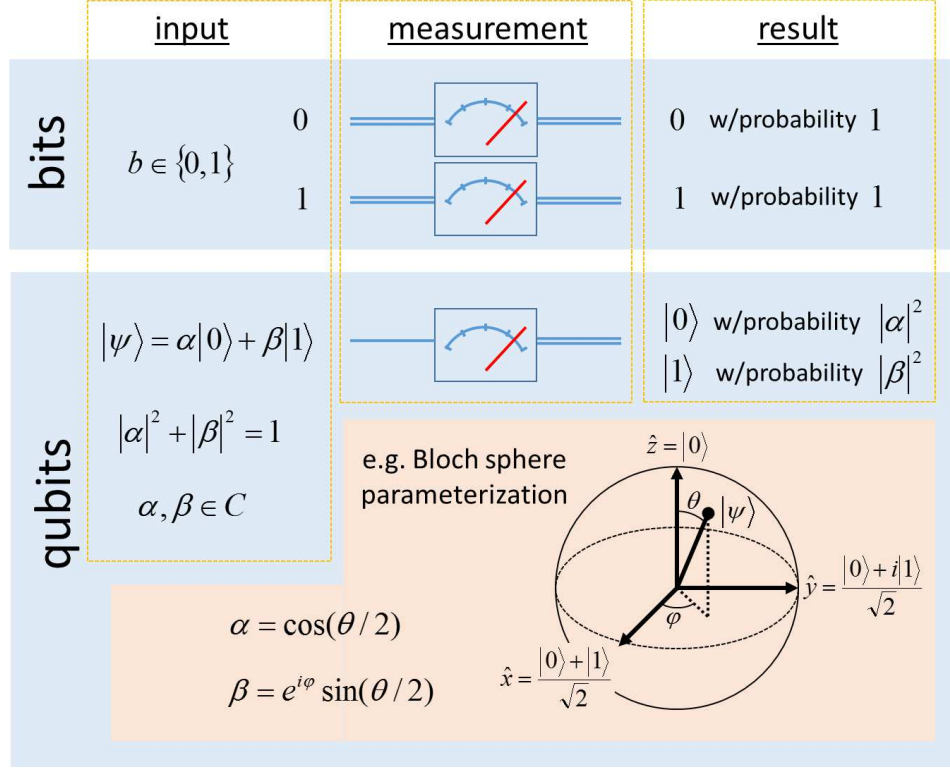


Figure 1.1: Bits and qubits. Bits take on one of two values, e.g. 1 or 0. Qubits may be represented by a complex linear superposition of two orthogonal basis vectors. In the Bloch sphere parametrization, a pure qubit state is represented by a vector of unit length and of angular direction (θ, ϕ) , such that unitary operations upon the qubit rotate the vector to some other other direction. Bit measurement is commonly deterministic, whereas qubit measurement is generally probabilistic.

The state of any N -bit system may be represented by a simple tensor product of bit values, e.g. expressed as a string of integers: $b_1 b_2 b_3 \dots b_N$. The simplest state for an N -qubit system, often the initial state for a QIP procedure, is similar, and consists of a tensor product of qubit states, i.e. $|q_1\rangle|q_2\rangle|q_3\rangle\dots|q_N\rangle$, where each state is some superposition of an eigenstate basis, $|q_n\rangle = a_n|0_n\rangle + b_n|1_n\rangle$. QIP functionality however requires *entanglement* of at least some qubits [19, 60], e.g. as found in the two-qubit entangled

state $|0_1\rangle|0_2\rangle + |1_1\rangle|1_2\rangle$, which cannot be factored into a simple tensor product $|q_1\rangle|q_2\rangle$ of the two individual qubits. A general form for the state of a N -qubit system may be written as the sum over all tensor products of qubit eigenstates:

$$|\Psi\rangle = \sum_{\{j_1, \dots, j_N\}_i \in \{b_1, \dots, b_N\}} \alpha_{\{j_1, \dots, j_N\}_i} |j_1\rangle|j_2\rangle\dots|j_N\rangle \quad (1.1)$$

where $\{b_1, \dots, b_N\}$ represents all length- N sequences of binary numbers b_n .

1.2.3 Classical and quantum logic gates

Universal *classical* information processing requires (a) bit value initialization, (b) bit value manipulation and comparison, and (c) resultant bit value readout. These components and operations may be arranged in a circuit, as exemplified in Figure 1.2. Bit state information is physically transported along classical channels (typically wires) and manipulation and comparison is done by application of bit logic gates that typically change the output bit state given a stable set of input bit states, when triggered by a clock pulse. The new output state typically becomes (one of) the stable input states for a downline gate that operates on it upon the arrival of the subsequent clock pulse. A set of logic gates which any algorithm may be built up from is deemed universal and may, for example, consist of NOT and AND gates, also shown in Figure 1.2.

Analogously, universal QIP requires (a) qubit state initialization, (b) qubit state manipulation and comparison, and (c) resultant qubit state(s) measurement. In the quantum circuit model of QIP, clock pulses still initiate gate operations on stable input qubit states, however the physical “flow” of state information can take a variety of forms, as elaborated on below. Quantum logic gates perform unitary operations upon quantum states. A universal set of quantum logic gates for information processing with N qubits must be capable of implementing an arbitrary unitary operator defined over the state space of all N qubits. A particularly simple-to-understand set of *universal* gates consists of a subset that can arbitrarily rotate each individual

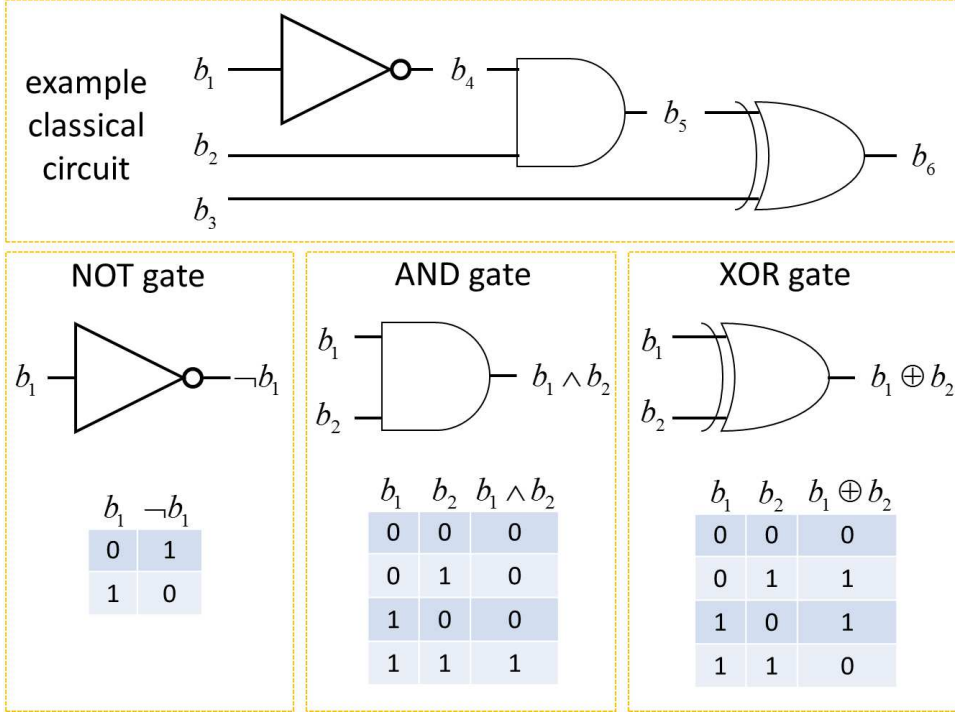


Figure 1.2: Example classical logic circuit and logic gates NOT, AND, and XOR. Any algorithm may be encoded in a circuit constructed of suitable arrangement of a universal (functionally complete) set of logic gates, e.g. of the gate set consisting of the NOT gate and AND gate.

qubit on its Bloch sphere, along with a collection of CNOT gates that can entangle any pair of qubit states, as exemplified in Figure 1.3.

It is important to note the difference between quantum and classical circuit diagrams. In classical circuit diagrams as in Figure 1.2, the lines typically represent physical wires, the voltage of which represents the bit state at the input or output of the gates. Cascaded gates are physically cascaded as shown, and the information effectively flows, or is processed from left to right by one gate “length” during each clock pulse. Hence the horizontal axis also corresponds in some sense to time.

Quantum circuit diagrams can represent quite distinct physical situa-

	<u>input state</u>	<u>circuit symbol</u>	<u>output state</u>	<u>operator depictions and representations</u>
Qubit rotations	$ q_1\rangle$	R_z^α	$ q_2\rangle = R_z^\alpha q_1\rangle$	$R_z^\alpha \equiv e^{-i\alpha Z/2} = \begin{pmatrix} e^{-i\alpha/2} & 0 \\ 0 & e^{+i\alpha/2} \end{pmatrix}$
	$ q_1\rangle$	R_y^α	$ q_2\rangle = R_y^\alpha q_1\rangle$	$R_y^\alpha \equiv e^{-i\alpha Y/2} = \begin{pmatrix} \cos(\alpha/2) & -\sin(\alpha/2) \\ \sin(\alpha/2) & \cos(\alpha/2) \end{pmatrix}$
	$ q_1\rangle$	R_x^α	$ q_2\rangle = R_x^\alpha q_1\rangle$	$R_x^\alpha \equiv e^{-i\alpha X/2} = \begin{pmatrix} \cos(\alpha/2) & -i\sin(\alpha/2) \\ -i\sin(\alpha/2) & \cos(\alpha/2) \end{pmatrix}$
CNOT	$ q_c\rangle$		$ q_c\rangle$	$ q_c\rangle \otimes q_c \oplus q_t\rangle = U_{CNOT} q_c\rangle \otimes q_t\rangle$
	$ q_t\rangle$		$ q_c \oplus q_t\rangle$	$U_{CNOT} = \begin{pmatrix} \langle 0_c 0_t & \begin{matrix} 1 & 0 & 0 & 0 \\ 0 & 1 & 0 & 0 \\ 0 & 0 & 0 & 1 \\ 0 & 0 & 1 & 0 \end{matrix} \\ \langle 0_c 1_t & \\ \langle 1_c 0_t & \\ \langle 1_c 1_t & \end{pmatrix}$

Figure 1.3: Example universal set of quantum gates consisting of three single qubit rotation gates and one two-qubit CNOT gate, with circuit symbols, depictions, and representations. Single qubit gates include rotations about each of the Bloch sphere axes, generated by the Pauli matrices X , Y , and Z . The two qubit CNOT gate flips the target qubit $|q_t\rangle$ if and only if the control qubit $|q_c\rangle$ is $|1\rangle$. Any multi-qubit state may be constructed with these gates.

tions, depending on the implementation. For instance, if the qubits are discrete two level systems, e.g. based on states of nuclear spin, electron spin or number, atomic spin, or Josephson junctions at two distinct physical locations, then the horizontal axis of the gate circuits in Figure 1.3 can really only be interpreted as time, as the input and output lines represent the same physical qubit [61, 121, 126, 149]. Such an implementation could be based entirely on these so called “stationary qubits”. As explained below, when individual photons are instead used to encode the qubit state, there is usually propagation involved, in which case they are referred to as “flying qubits”, and then the circuit diagrams can, at least in some cases, be interpreted more like classical circuit diagrams, with the input and output lines

to gates representing distinct optical channels (optical fiber, waveguides, or locations in free-space) [107].

Common challenges for both stationary and flying qubits include (a) preservation of qubit coherence during transport or gate operations, (b) achieving sufficient qubit interaction in multi-qubit gates, and (c) achieving adequate state preparation and measurement efficiencies. Scaling up to many-qubit systems is a major challenge that motivates implementations within which components may be fabricated scalably. We now provide a concrete example of a useful quantum information process, quantum teleportation, to help tie together these theoretical foundations and practical challenges, and thus to motivate the integrated photonic circuit approach.

1.2.4 Quantum teleportation: an example

Consider how a qubit state $|\psi_{in}\rangle$ initialized at location A, can be transferred to a second qubit at a remote location B, using four single gate operations and two CNOT gate operations, along with two classical measurements. This is an essential process used in, for example, quantum cryptographic applications.

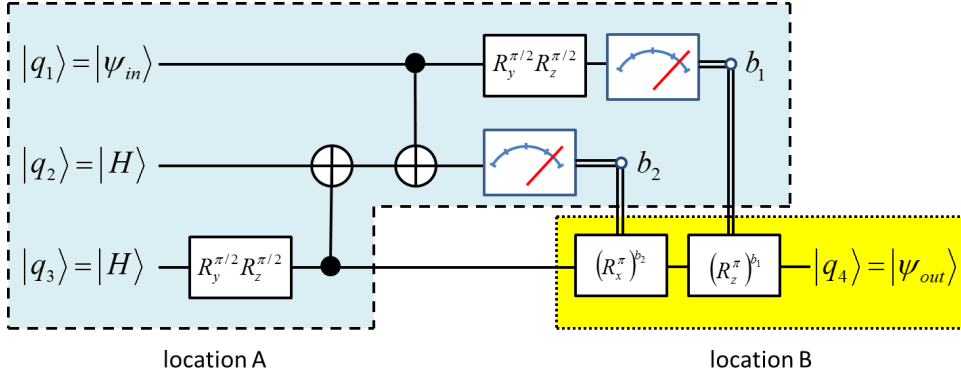


Figure 1.4: Quantum teleportation circuit. See Figure 1.3 for quantum gate definitions. Single lines are quantum channels and double lines are classical channels. A quantum state is transported from location A to location B using two classical information channels and one quantum channel.

Shown in Figure 1.4, the state $|\psi_1\rangle$ is first entangled with a maximally entangled Bell State (e.g. $(|1\rangle|1\rangle + |0\rangle|0\rangle)/\sqrt{2}$) and two measurements (projections) are made on the resulting entangled state and the Hadamard-transformed ($R_y^{\pi/2}R_z^{\pi/2}$, see Figure 1.3 for symbol definitions) initial state $|\psi_1\rangle$, all at location A. The maximally entangled Bell State is produced at location A using two identically prepared qubits $|\psi_2\rangle$ and $|\psi_3\rangle$, as inputs to a Hadamard/CNOT gate sequence. The results of the measurements are then transported classically, along with the Hadamard ($R_y^{\pi/2}R_z^{\pi/2}$) transform of $(|\psi_3\rangle)$ to location B, where a rotation of the received qubit is performed, conditional on the classical results of the measurements done at location A. Ideally this results in $|\psi_4\rangle = |\psi_1\rangle$; teleportation.

This teleportation scheme can in principle be realized using a variety of stationary implementations of the initial and final qubit states, but in order to operate between remote locations A and B, at least the rotated version of $|\psi_3\rangle$ must be encoded in a flying qubit, as only photons thus far have been proven capable of carrying quantum information over long (e.g. exceeding 100 m) distances. The entire system may be based on flying qubits, too.

1.2.5 Linear optical quantum information processing (LOQIP)

The teleportation application is one of many QIP functions that may benefit from the unique qualities of photonic-based qubits, e.g. exemplary long-distance qubit transport, or making use of scalable, photonic integrated circuits (PICs) [134, 155, 168, 212]. A persistent challenge however is that virtually all of these more general applications require a deterministic photonic entanglement gate, commonly a deterministic photonic CNOT gate, true realization of which has seen many theoretical proposals [147, 149], but not yet been experimentally realized. This is largely due to the requirement that single photons must be able to *nonlinearly* interact via some material medium, which in turn requires very strong light-matter coupling.

Although much experimental progress is being made in this direction [216], most of the experimental optical QIP community has focused instead on demonstrating *probabilistic CNOT gate* operation, which can be achieved

using only *linear* optical components [35, 40, 95, 110, 114, 115, 170]. This line of research followed a seminal paper by Knill, Laflamme, and Milburn scheme [110] which theoretically demonstrated that universal QIP can in principle be achieved using only single photon sources, single photon detectors, linear optical components (phase shifters such as waveplates, and beam splitters), and classical electronics.¹

The remainder of this subsection reviews the basics of LOQIP, with an emphasis on realization of an ideal on-demand single photon source, as per the dissertation aim.

Quantum gates

The single photon detectors, beam splitters, and waveplates called for in LOQIP are readily available in high quality in the visible portion of the spectrum, so most of the experimental work on LOQIP has been done with bulk optical components in the visible. The following briefly explains how the single qubit operations and probabilistic CNOT gate can be implemented using path-encoded qubits generated by single photon sources, together with beam splitters and single photon detectors.

In bulk optical setups, flying qubits have commonly been encoded into a basis set consisting of orthogonal polarization states of photons, e.g. “horizontal” and “vertical”, as depicted in Figure 1.5B, and a single polarization qubit may propagate along a single optical path. Qubit basis states need not only be polarization encoded, but may also correspond to absence/presence of photons within a pair of mutually exclusive optical paths, i.e. the dual rail path encoding, as depicted in Figure 1.5A. Transformation to a path encoding from a polarization encoding may be achieved with a polarization beam splitter, as shown in Figure 1.5D, and admits integration of optical components in ways not available to photons propagating along a single optical path. Further, path encoding is particularly useful for inte-

¹Linear optical QIP in computational contexts is often referred to as linear optical quantum computing (LOQC), and in this dissertation we use the term linear optical quantum information processing (LOQIP) to include LOQC and other QIP tasks executable using linear optical methods.

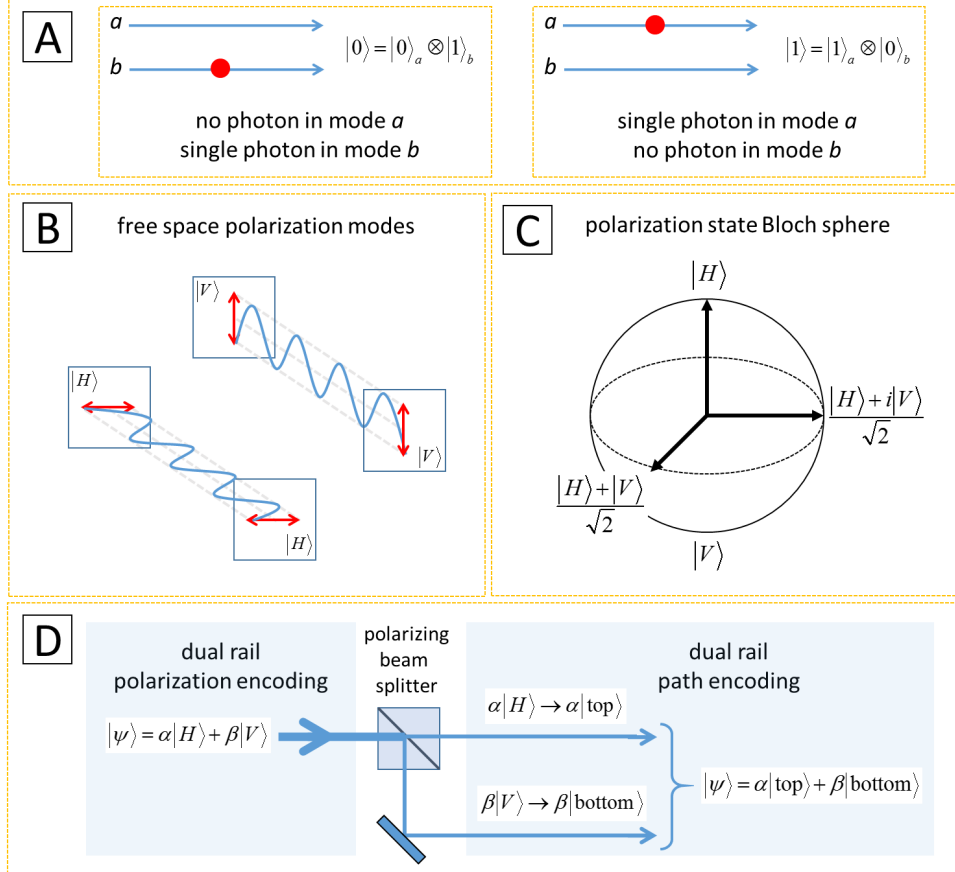


Figure 1.5: (A): General dual rail optical qubit basis states consist of single photon absence/presence in one of two optical modes. (B) and (C): Free-space polarization encoded photonic qubits that exemplify dual rail qubits, and (D): mechanism to convert polarization encoded qubits to path encoded qubits.

grated optical environments for which polarization control and manipulation is challenging.

The phase shifter and beam splitter components in Figure 1.6 illustrate how the two required single qubit rotation gates have been implemented in the case of the path encoding of the photonic qubits. The full $SU(2)$ symmetry group may be generated by beam splitters alone [39], and Figure 1.6 illustrates a configuration of beam splitters that transforms the input

path-encoded qubit proportional to R_y^α . The rotation angle relates to the classical electric field intensity reflectivity η by $\cos(\theta/2)^2 = \eta$. Phase shifters are proportional to R_z^α . These two operations are sufficient to generate all single qubit states ($R_x^\alpha = R_z^{\pi/2} R_y^{(-\alpha)} R_z^{(-\pi/2)}$ may be formed from them).

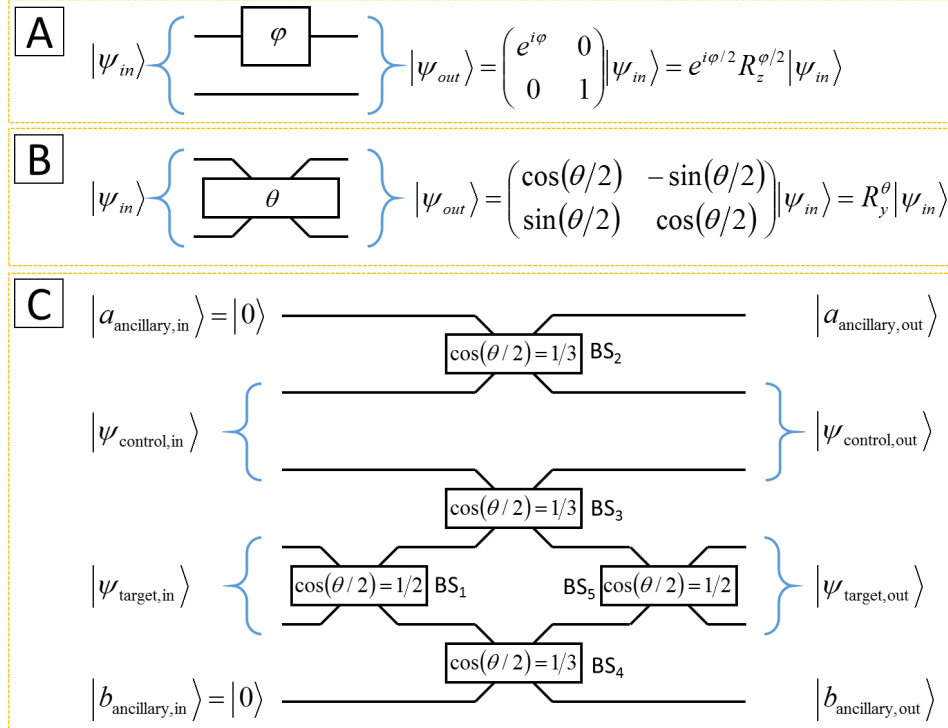


Figure 1.6: Universal LOQIP quantum gates, constructed from (A) phase shifters, (B) beam splitters, and photon detectors, for path encoded optical qubits. Rotation angles θ and ϕ map directly onto the Bloch sphere. (C): CNOT gate success, i.e. $|\psi_{\text{target,out}}\rangle$ equaling $|\psi_{\text{control,in}}\oplus\psi_{\text{target,in}}\rangle$, coincides with photon detection in the output ancillary modes $|a_{\text{ancillary,out}}\rangle$ and $|b_{\text{ancillary,out}}\rangle$.

The final gate in Figure 1.6 exemplifies how a probabilistic CNOT gate can be implemented using a collection of beam splitters and single photon state inputs [177]. Beam splitters are asymmetric and induce a sign change upon reflection off the top for the top two beam splitters (BS₂, BS₃) and

upon the bottom for the bottom four beam splitters (BS_1 , BS_3 , BS_4 , BS_5). Consider special case operations: first, where the upper path of the input control qubit is occupied by a photon (and the lower control path is not) the target qubit passes through a symmetric combination of beam splitters and exits as it enters ($|\Psi_{\text{target,in}}\rangle = |\Psi_{\text{target,out}}\rangle$) for the cases where an input target photon does not exit the target qubit transmits into either the lower control target path or lower ancillary path, and the input control photon exits via the top ancillary path 1/3 of the time. If instead the lower path of the control qubit is occupied by a photon, this photon interferes with the target state and it can be shown that the target qubit is flipped, i.e. a photon in the upper input target path exits the lower exit target path and vice versa, assuming the target photon does not exit to the lower ancillary path. Thus, the CNOT operation is performed in cases where control or target photons do not exit the target and control paths. In cases where a photon is measured in both a target exit path and control exit path, the gate is successful (behaves according to standard CNOT gate operation) and this happens 1/9 of the time.

The operation described above assumes that at some moment when the CNOT operation is assumed to take place, four distinct single photon states (here, dual rail encoded) are present at the input. The reliance on interference at the beam splitters within the CNOT gate requires precise timing of the input states and that the input photons are indistinguishable. A key experiment that quantifies the ability of the photon sources to interfere, and thus quantum photonic gates to be realized, is the Hong-Ou-Mandel (HOM) effect [92], which measures the extent to which emitted photons can destructively interfere upon recombination at a beam splitter.

A basic HOM setup is illustrated in Figure 1.7, wherein the coincidences of photons transmitted through the two beam splitter outputs are monitored as a function of relative optical path length between the beam splitter and the detectors. How low the detected coincidence rate can be - i.e. seen by a “dip” in the coincidence curve for zero path length difference - indicates how well photons from the two paths can interfere. Photons that are truly indistinguishable will destructively interfere perfectly at an ideal beam

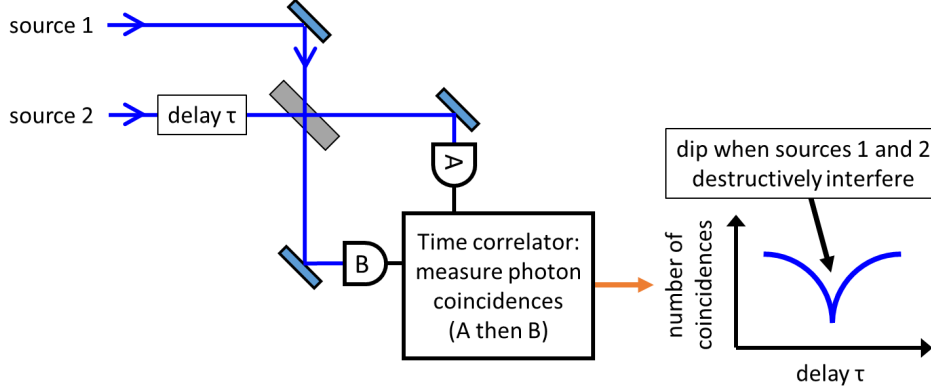


Figure 1.7: Hong-Ou-Mandel (HOM) effect measurement setup, with “HOM dip” in photon detection event coincidences. A dip to zero coincidences (for zero path length difference from the beam splitter to each detector, controlled by a variable delay) is evidence of photon interference of the two photon sources and indication of the photon sources emitting photons indistinguishable from each other.

splitter when simultaneously incident upon the beam splitter, such that the measured coincidence rate can dip to zero (e.g both photons have to exit the beam splitter together, with equal probability in either direction).

Adequate photon interference places demands on the single photon sources, now discussed.

Photon sources

Bulk optical QIP demonstrations have typically relied on either (i) strongly attenuated laser beams [64, 80], (ii) entangled photon pairs generated at frequencies ω_1 and ω_2 via parametric down-conversion of photons at frequency $\omega_3 = \omega_1 + \omega_2$ in nonlinear optical crystals possessing large second order non-linear coefficients $\chi^{(2)}$ [64, 80, 120, 148], or (iii) trapped ions, molecules, or atoms [50, 108, 119].

None of these sources are ideal. Trapped atom and ion sources typically require large, complicated setups that have not yet yielded competitive single photon sources given the relative ease of implementing laser or down con-

version sources. Nonetheless, they have remained an important source of very high quality, indistinguishable photons for which state-of-the-art quantum optical experiments have been performed for decades. For both lasers and parametric down-conversion sources, suppression of unwanted photon coincidences to levels low enough for QIP demonstrations comes at the expense of suppressing the desired photon generation rate. These low rates result in impractically long experimental integration times, especially when compounded with probabilistic gates (such as the CNOT gate above).

Entangled photon pair sources based on parametric down-conversion see widest use of these aforementioned source types, offering the highest single photon generation rates for adequately low accidental coincidences, the latter property enabled by gated operation in the heralded scheme in which arrival of one of the photons, say at ω_1 , is “heralded” by the detection of its partner at ω_2 . Although the source rate of these entangled photon pair sources has improved to the MHz range [36, 148, 169] and exceeds the rates of attenuated laser sources for equivalent accidental coincidence rates, the probabilistic nature of the photon arrival time from such sources severely limits the overall throughput of any quantum logic operation, such as the CNOT gate.

For example, successful operation of teleportation and CNOT gates with heralded sources requires waiting for the output of multiple identical photon sources to coincide temporally at the CNOT gate or teleportation circuit inputs, which degrades both the latency and throughput of QIP algorithm implementations [36, 64], and practically prohibits - via long experimental integration times - algorithm implementation for even a handful of independent photon input states. For example, state-of-the art LOQIP experiments using heralded sources report 4-mode photonic state generation at a rate of 20 Hz for a photon coincidence rate of each heralded source equal to 160 KHz [139].

Thus, despite the current popularity of heralded photon sources, scaling up QIP algorithms to significantly more qubits - as is needed for many proposed QIP benefits - requires overcoming the indeterministic timing of their photon output by replacing them with on-demand photon sources in

which photon output is fixed relative to trigger pulses; in particular, an ideal on-demand single photon source will emit exactly one photon a certain amount of time (no jitter) for each and every trigger pulse applied, and do so with high emission rate. A variety of systems have been actively pursued to produce high-quality, truly on-demand single photon sources, including semiconductor quantum dots embedded in a variety of micro cavities or nano-pillar dielectric environments, and crystal defects (e.g. NV centers in diamond) that are efficiently coupled into optical fibers. Indistinguishability as high as 60% for independent on-demand photon sources has been observed [163], suggesting promise for high quality beyond already established high emission rates in the GHz range.

Availability of single photon source quality is one major factor considered in implementation of a LOQIP experiment, but not the only one. We now review LOQIP in the silicon-on-insulator (SOI) platform, for which single photon source development is the major challenge but the platform is pursued for otherwise providing major LOQIP benefits.

1.3 LOQIP in the SOI platform

This section describes many of the components and processes involved in realizing LOQIP in the silicon-on-insulator (SOI) platform, and as such provides important context and background information specific to the aims of this dissertation.

1.3.1 Overview

One of the most significant drivers for photonic-based QIP is its potential scalability (e.g. to incorporate multiple teleportation channels on a single transceiver chip). The beam splitters and phase shifters and single photon detectors required for LOQIP, as reviewed above, can all be miniaturized and integrated in planar lightwave circuits fabricated using well-established lithographic patterning and chemical etching techniques. Host waveguide materials include silicon on insulator (SOI) [24], silica-on-silicon [40, 167], III-V semiconductors (e.g. gallium-based) [70, 218], diamond [8, 82, 89],

lithium niobate [15, 99, 202], silicon nitride [225], and silicon carbide [28, 38].

The silicon-on-insulator (SOI) platform is pursued in this dissertation, because mature circuits that integrate both passive photonic and electronic circuitry [109, 204, 208, 237] have already been commercialized in this platform after considerable industrial development. This investment in classical integrated photonic circuitry is being leveraged to demonstrate scalable QIP-grade operations [27, 59, 87, 198] operating in the C-band (around 1.55 μm wavelengths), which takes advantage of the massive telecommunications infrastructure [104, 117, 232] in place worldwide. The following describes the principles and techniques used in this thesis towards integrating an on-demand single photon source in the SOI platform, starting with an overview of SOI-based photonic circuitry.

1.3.2 Linear optical components

Platform and circuit overview

Optical modes in the SOI platform suitable for scalable transport, manipulation, and interaction of photons, may be constructed through a CMOS-compatible lithographic process, and reside primarily within a few-hundred nm silicon device layer, depicted in Figure 1.8A. Due to strong total internal reflection at the silicon-air, and silicon-oxide interfaces (i.e. only light propagating almost normal to the interface can escape the thin silicon layer), light coupled into the top silicon “device layer” is robustly confined to propagate long distances within the plane of the wafer; this confinement mechanism is depicted in Figure 1.9A. The light can be further routed and manipulated by defining patterns that are etched into, typically completely through, the silicon device layer. The method for patterning these in-plane waveguides and waveguide devices is illustrated in Figure 1.8B. An example LOQIP PIC layout, as would be fabricated on a SOI wafer, is depicted in Figure 1.8C.

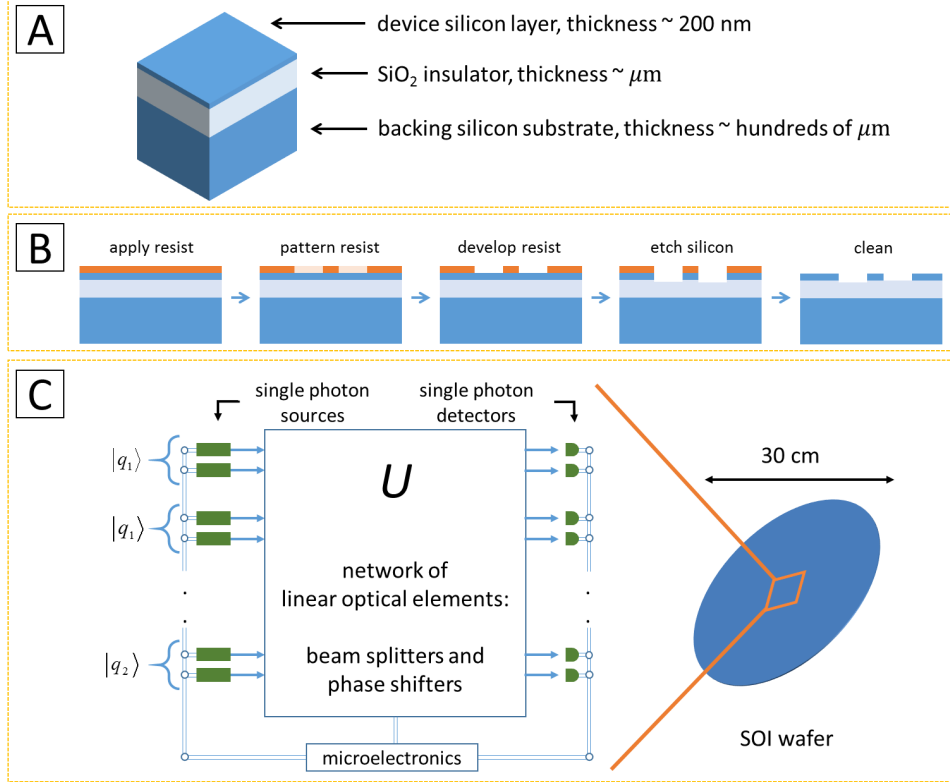


Figure 1.8: The SOI platform, for LOQIP. (A): Typical silicon-on-insulator (SOI) dimensions used for SOI-based photonic integrated circuits and (B) example etching steps. Additional functionality may be achieved by lithographic integration of metal contacts, ion doping, and deposition of other materials. (C): Example LOQIP circuit layout and depicted embedment in an SOI wafer.

Integrated waveguides, beam splitters, and phase shifters

Waveguides, e.g. ridge waveguides depicted in Figure 1.9B through D, fulfill the role of quantum channels. As is the case for guidance of light in the device slab, light is confined to within a ridge waveguide by internal reflection. Figure 1.9B depicts a silicon ridge waveguide superimposed a silicon-oxide layer and surrounded by air (or vacuum), and Figure 1.9C exemplifies a cross section with mode profile, for ridge waveguides small enough to support just

the fundamental waveguide mode (i.e. single antinode near the center of the waveguide), of dimensions in the vicinity of 500 nm in height and width. A pair of parallel waveguides constitutes a dual rail qubit.

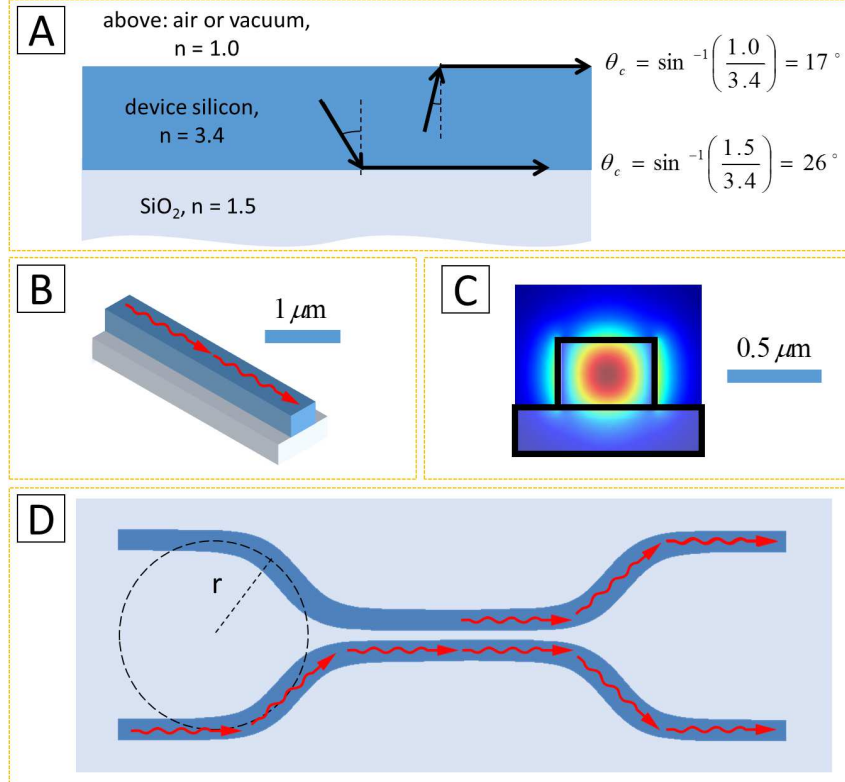


Figure 1.9: (A): Total internal reflection at silicon-air and silicon-oxide interfaces. (B) and (C): Ridge waveguide that utilizes total internal reflection to contain light within the waveguide. (C): Example electric field mode profile, showing non-zero field beyond the silicon. (D): Ridge waveguide beam splitter, labeled with a characteristic bending radius (typically around $10\ \mu\text{m}$ for these materials) that limits the minimum size in accordance with the total internal reflection angles described in (A). Beam splitters admit R_y^α single qubit rotations and, along with single photon detectors, may be used to realize a CNOT gate.

The evanescent portion of the field profile extending beyond the higher

index core of the waveguide admits waveguide-waveguide coupling, exemplary of frustrated internal reflection. This coupling constitutes the underlying mechanism of beam splitters, illustrated in Figure 1.9D. Because the photon amplitude distribution over the two waveguides may be altered by photon transfer between the waveguides, a beam splitter effectively rotates a dual rail photonic qubit with the Bloch rotation angle θ tied to waveguide-waveguide distance, abutting length, and shape.

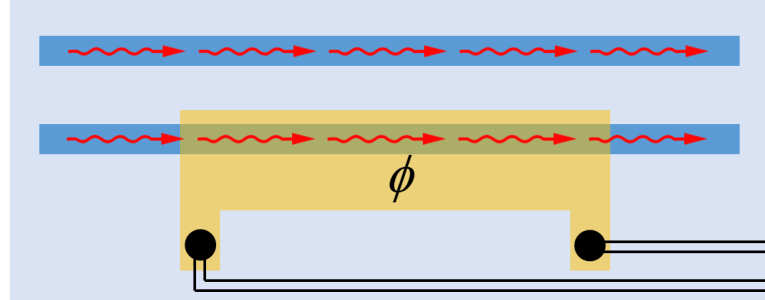


Figure 1.10: Example phase shifter, capable of producing single qubit rotations R_z^ϕ . A small current passing through a metallic strip, connected to the control electronic microcircuitry, may locally heat and change the index of refraction, thus the relative optical path length (note that the metallic strip is not necessarily in contact with the waveguide, but more likely embedded in a layer above or below it).

Beyond quantum channels and beam splitters, a phase shifter for a dual rail qubit may be realized when one ridge waveguide out of a pair possesses a different optical path length - e.g. via index of refraction - than the other waveguide. One low loss way to do this is thermally [87], e.g. by application of an electrical current, as shown schematically in Figure 1.10. The difference in optical path length for photons traveling along different paths in the phase shifter results in differing amounts of accumulated phase, without changing the relative amplitude of the photon in either path, effectively rotating a qubit state about an eigenstate axis by some angle ϕ . Beam splitters and phase shifters have both been realized, often in tandem, in the SOI platform [26, 27, 198, 199]. These linear optical components may be combined with

single photon detectors to realize conditional qubit gates, e.g. the LOQIP CNOT gate in Figure 1.6C.

Photonic band gaps: tighter confinement and improved functionality

Although total internal reflection in this high index contrast environment enables on-chip optical components much smaller than bulk counterparts, a second photon confinement mechanism, based on “photonic band gap” materials, allows for even further miniaturization, and importantly enables key functionalities not feasible using only ridge waveguides. As elaborated on below, efficient generation and detection of single photons in silicon photonic circuits depends on their effective interaction strength with electrons in quantum emitters or superconducting wires that are placed in proximity to the silicon device layer where the photons propagate. This effective interaction strength can be enhanced by engineering the dielectric environment so that the photons are tightly localized in the vicinity of the emitter/absorber, and localized for many optical cycles. Photonic crystals offer the best means of achieving these objectives.

In 1987, Yablonovich and John independently described a means of artificially creating a band of frequencies within which there are no propagating solutions to the Maxwell equations [100, 228]. Even in non-absorbing material, if a 3-dimensional (3D) periodic texture with appropriate symmetry is imposed with sufficiently high refractive index contrast, it is possible to prevent photon propagation within a continuous range of frequencies, in any direction, with any polarization, analogous to the periodic electronic potential in an electronic crystal giving rise to electronic band gaps. The resulting “photonic band gap” is centered at a wavelength on the order of the pitch of the texture (taking account of the average refractive index of the medium).

Figure 1.11A through C, illustrates how a 2-dimensional (2D) photonic band gap material can be realized in the SOI slab waveguide geometry to effect a *quasi* photonic band gap for slab modes propagating in the device silicon layer. The dielectric contrast is sufficiently high (~ 3.4 to 1) when etching holes through the silicon layer, to create relatively large ($\sim 10\%$

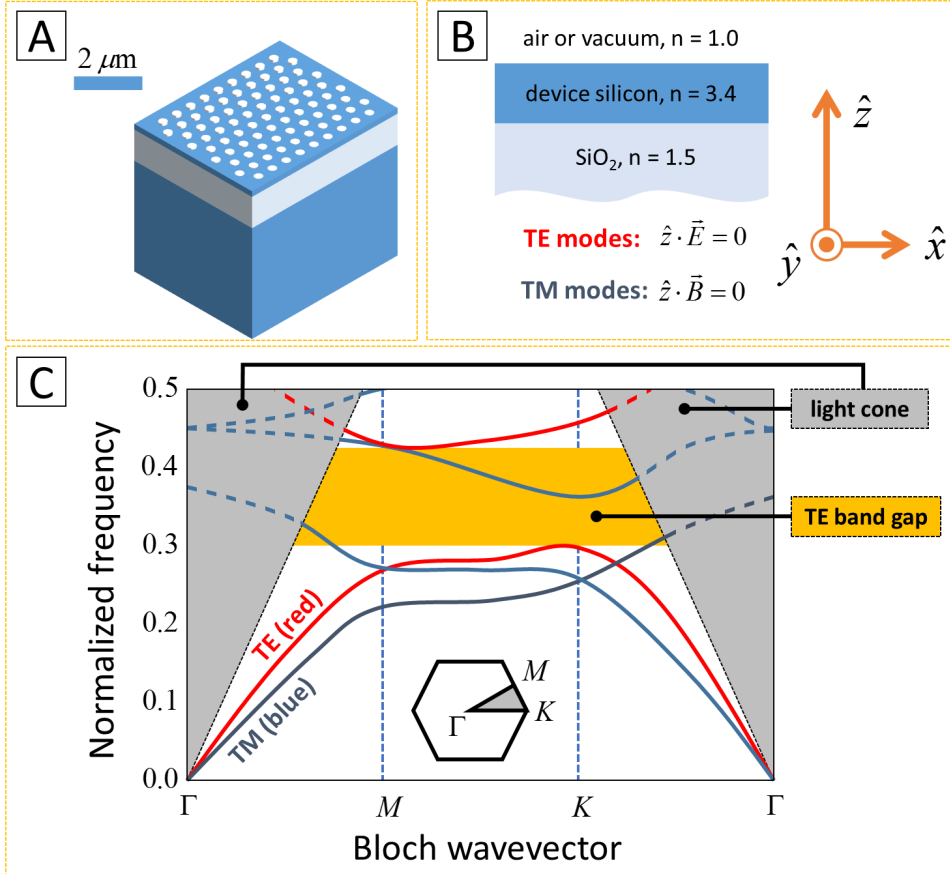


Figure 1.11: Photonic band gap confinement mechanism used in SOI photonic circuits. (A): Slab hexagonal lattice photonic crystal. (B): Definitions of TE and TM propagating modes. (C): Example photonic band structure for slab photonic crystal similar to the one depicted in (A).

to 15% of the center frequency) ranges of frequency where 2D waveguide modes of TE polarization cannot propagate. Although technically there is no complete photonic band gap in this frequency range, because TM (see TM and TE definitions in Figure 1.11B) polarized slab modes and near-normally incident waves that aren't localized to the silicon device layer can still propagate in it at these frequencies, by limiting operation to the TE

polarization, these 2D photonic crystals are very effective at reflecting slab modes propagating in *any* in-plane direction.

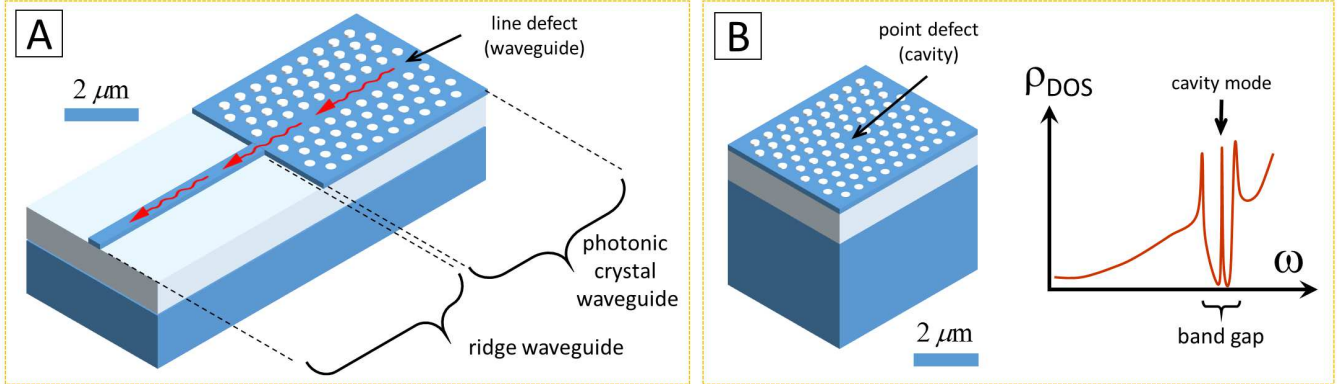


Figure 1.12: Photonic crystal structures. (A): Photonic crystal waveguide, consisting of a line defect in a slab photonic crystal, joined with a ridge waveguide. (B): Photonic crystal cavity, consisting of a point defect in a slab photonic crystal, accompanied by a sketch of the local photonic density of states (ρ_{DOS}) as a function of embedded emitter frequency ω at the cavity center. Slab photonic crystals may consist of a regular pattern of air holes which, for the cases of photonic crystal waveguides and cavities, are omitted (i.e. not made) along a line or localized region during patterning of the remainder of the structure.

Thus instead of using TIR to guide light in 1-dimensional (1D) ridge waveguides, it is possible to use photonic crystal (PhC) regions to confine light to propagate in a 1D channel, as depicted in Figure 1.12A. Right angle bends in such waveguides can be designed to be almost lossless, yielding an effective bending radius of less than 1 μm . The photonic crystal defect feature can in turn be used to localize light in 3D to volumes of a fraction of a cubic vacuum wavelength by simply leaving out one or more holes in the photonic crystal, as shown in Figure 1.12B. These 3D photonic crystal microcavities can have quality factors (roughly how many optical cycles trapped light remains in the cavity) easily in the range of 10^5 [159, 203]. This offers a means of dramatically increasing the effective interaction strength

of light and electronic media that might be placed in the microcavity.

As shown in Figure 1.11C, there is a range of the folded-zone band structure diagram where the continuum of radiation modes overlaps with the confined mode dispersion (i.e. above the light cone in the surrounding medium (air or SiO₂). The bound modes associated with the 1D waveguides and 3D microcavities discussed above are all formed from states lying below the light cone, which do not couple out of the plane. However in applications requiring long-distance transport of photons, e.g. through free space or in optical fibers over meter to kilometer distances much larger than the SOI chip, photons from in a ridge or photonic crystal waveguide need to be directed off-chip. This can be accomplished by utilizing modes near the center of the Brillouin zone that do intrinsically couple to radiation modes (they diffract out of the device layer as they propagate).

An example configuration enabling this is depicted in Figure 1.13, in which a photonic crystal waveguide couples to a ridge waveguide, then a parabolic tapered waveguide terminating in a diffraction grating. Photonic crystal pitch, hole size, ridge waveguide width, and grating coupler pitch are all quantities that must be engineered in unison for efficient transmission of light; see, for example, work from our lab in references [17, 188, 189]. A lens may collect light from the grating (as will be seen in Chapter 4) or an optical fiber may be bonded to or near it.

Single photon detectors and single photon sources for LOQIP in SOI PICs are now reviewed, exemplifying the important role of photonic band gap confinement in these contexts.

1.3.3 Single photon detectors

Ideal single photon detectors possess unity efficiency (one detection pulse out per one input photon), zero dark counts (no spurious detection pulses), and zero recovery time (ready for photon detection immediately after detecting a photon) [84]. As silicon is non-absorbing in the C-band, other types of materials need to be integrated on the chips to realize efficient photon detection. Germanium (Ge), or a silicon-germanium compound (Si_xGe_{1-x})

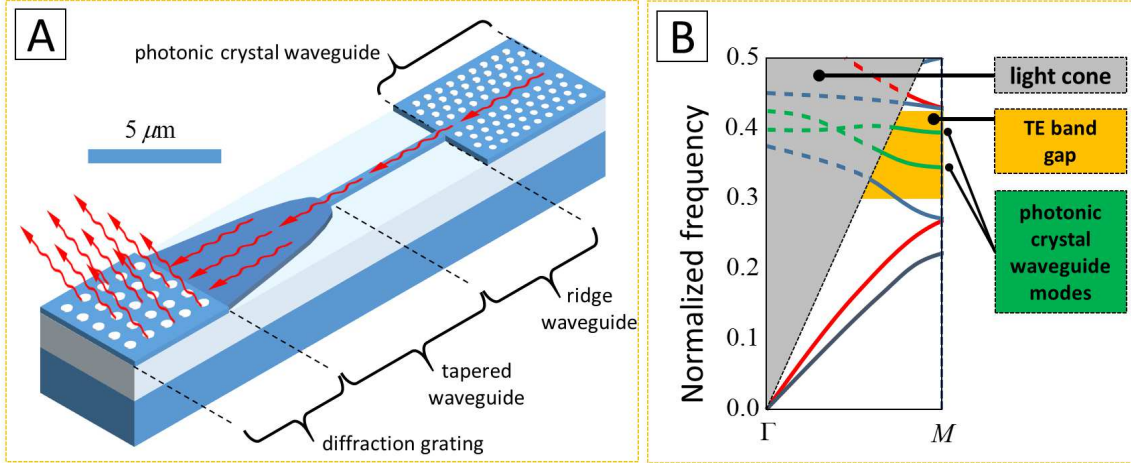


Figure 1.13: (A): Waveguides terminating in a diffraction grating, the latter for free-space/on-chip light conversion. (B): Partial band structure diagram for the photonic crystal with photonic crystal waveguide bands (green). Guided (slab-like) modes in red and blue. Modes within the light cone are not confined to the device silicon. A bound state such as a photonic crystal cavity (not shown in this diagram) would also lie within the TE band gap. The in-slab amplitude of propagating waveguide modes (below the light line) decays exponentially in the grating region (i.e. is non-propagating and above the light line) as the field is diffracted out of the device slab.

can be epitaxially incorporated in the device silicon layer, and are compatible with CMOS foundries. While conventional photodiodes for classical telecommunications have been successfully developed using this material, attempts to fabricate high quality avalanche photodiodes capable of single-photon detection have been plagued by excess noise.

Arguably the most successful stand-alone infrared single photon detectors are based on superconducting nanowires, exemplified in Figure 1.14. Recently the Young lab has successfully integrated a short NbTiN nanowire on 1-dimensional photonic crystal microcavity etched in an otherwise silicon ridge waveguide and demonstrated near unity quantum efficiency for converting a single waveguide-bound incident photon into an electronic “click”

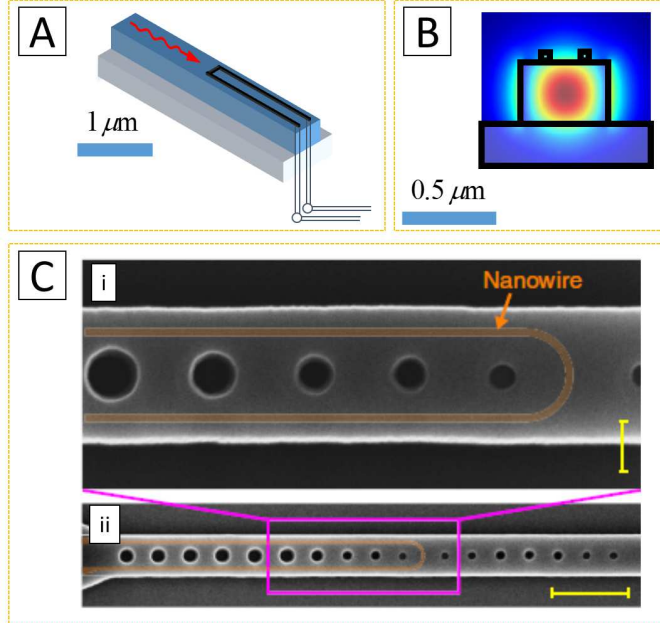


Figure 1.14: Example integrated detectors, in which photodetective material is placed atop waveguide within waveguide mode. (A): perspective view of detecting material atop waveguide, with connected electrical wires. (B): head-on view, overlayed with waveguide profile. Size of photodetective material in (A) and (B) is slightly exaggerated for drawing purposes. (C): Realized integrated, superconducting single photon detector from the Young lab [9].

triggered by the resistance change across the superconducting wire when the energy absorbed from the photon causes it to go normal. The device was made ultra-compact, as illustrated in [9], by routing the 8 nm by 35 nm area superconducting nanowire through the center of a 1D photonic crystal-defined microcavity, shown in Figure 1.14C. This compactness admitted the small microcavity mode volume required for enhanced interaction between a microcavity photon and the detecting nanowire, in turn admitting high photon detection probability. The back PhC mirror is essentially 100% reflecting, and the front PhC mirror's reflectivity is designed to exactly match the absorption rate of a cavity photon by the nanowire, which maximizes

the absorption rate of waveguide-bound photons. The near unity quantum efficiency and sub Hz intrinsic dark count rate of these detectors when operated at 2 K means that high fidelity quantum optical experiments can already be carried out with them [9, 146, 165, 205].

1.3.4 Single photon sources

This subsection describes the key concepts that underpin the approach and methodologies used in this dissertation to develop an on-demand single photon source in the SOI platform. The main topics include the microcavity and waveguide photonic elements, the colloidal PbSe quantum dot emitters, with an emphasis on how they optically couple.

Basic approach

Since both high-quality linear optical components and single photon detectors have been demonstrated in the SOI platform, the outstanding impediment to SOI LOQIP is the lack of good on-demand single photon sources [72, 144, 208]. The essential elements of an ideal on-demand, fully integrated source are (i) a bright, efficient quantum emitter that emits one and only one photon from a well-defined transition every time it is externally excited, as in Figure 1.15A, and (ii) a dielectric environment surrounding the quantum emitter that ensures the photon from the emitter is eventually routed into a specific silicon ridge waveguide channel with unity efficiency, as in Figure 1.15B. The relevant quantum emitter characteristics are discussed in detail below in Section 1.4.

The following subsection concentrates on the dielectric environment required to efficiently couple the excited quantum emitter transition to a quasi-normal mode of the silicon circuit wherein all power is transported away from the quantum emitter through a single mode silicon ridge waveguide.

Dielectric environment geometries

Consider what might happen if a quantum emitter at frequency ω_0 is located on top of an isolated silicon ridge waveguide, as shown schematically in

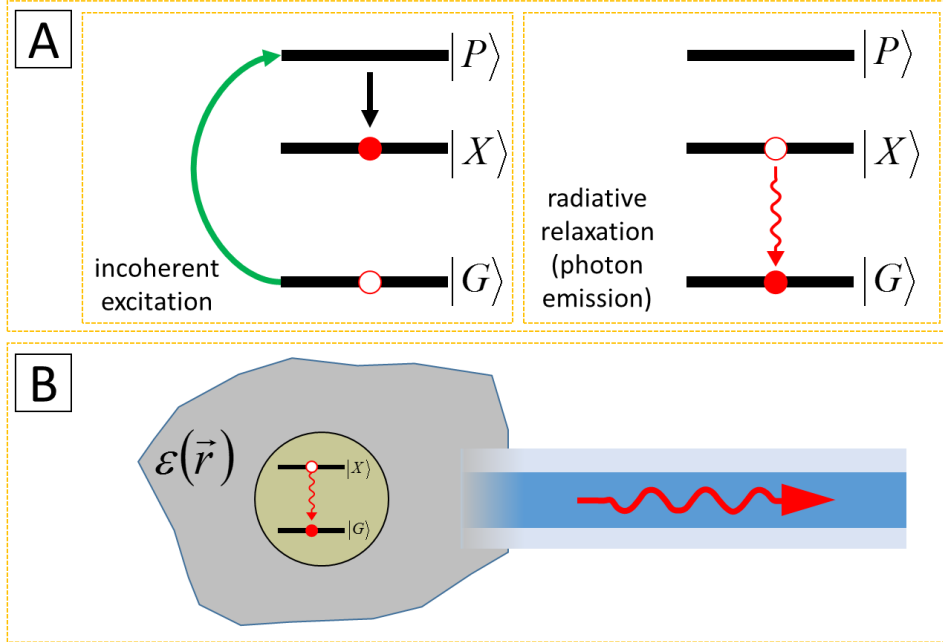


Figure 1.15: (A): Single photon emission from an incoherently pumped (via state $|P\rangle$) two level system ($|G\rangle, |X\rangle$). (B): Integrated single photon source geometry, consisting of a radiative two level system embedded in a dielectric environment that efficiently channels photon emission into a ridge waveguide.

Figure 1.16A.

The excited state can in general decay into any electromagnetic mode that has non-zero field amplitude and a polarization not perpendicular to the transition dipole matrix element $\vec{\mu}$ of the emitter, at the location of the emitter. The total radiative decay rate is simply related via Fermi's Golden Rule, i.e. proportional to the amplitude of the transition dipole moment $|\vec{\mu}|$ and linear in the local density of photonic states ρ : $R \propto |\vec{\mu}|^2 \rho$. There is always a continuum of radiation modes (intuitively thought of as plane waves traveling in various directions at ω_0 , slightly renormalized in the vicinity of the waveguide due to scattering) and, depending on the waveguide geometry, there can also be a continuum of 1D guided modes, traveling in the forward and backward directions, evanescently penetrating the surrounding cladding

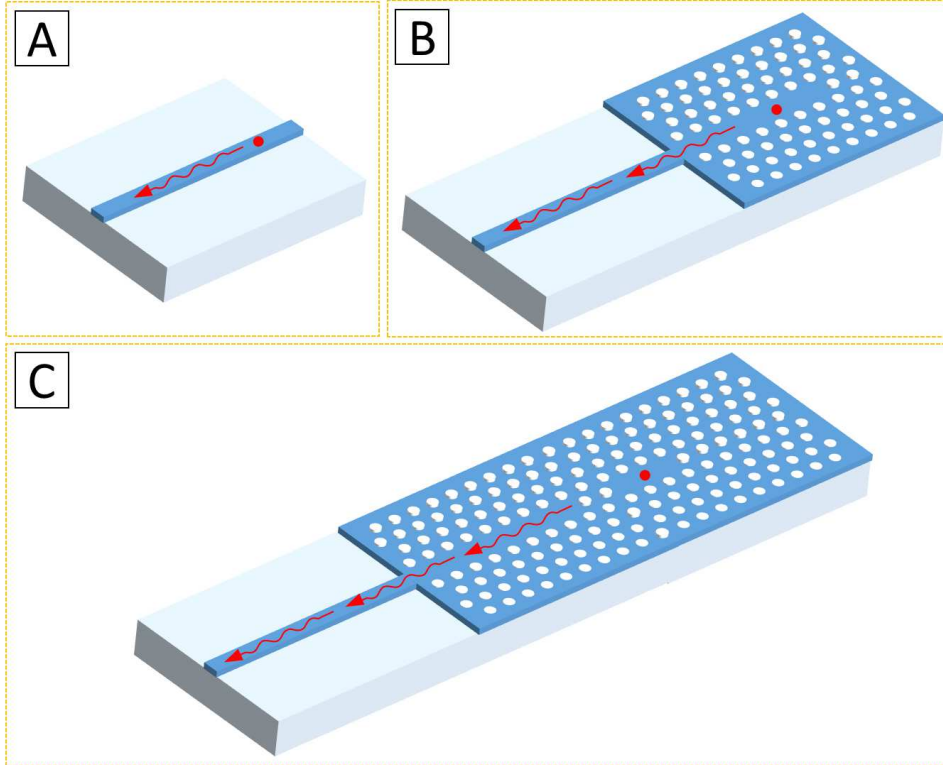


Figure 1.16: Integrated emitter geometries for realization of a single photon source. (A): Emitter directly atop a ridge waveguide. (B): Emitter atop a photonic crystal waveguide. (C): Emitter in a waveguide-coupled photonic crystal cavity. Geometry (C) offers the best into-circuit emitter collection efficiency of these three geometries owing to the largest collection efficiency by the cavity, followed by availability of highly efficient transfer of cavity photons to the ridge waveguide through the photonic crystal waveguide.

regions. It is relatively easy to design the waveguides in SOI to support only one TE and one TM polarized continuum waveguide mode in the C-band, for a waveguide of dimensions around 200 nm tall by 500 nm wide. If the receiving LOQIP circuit were situated to the right of the emitter, ideally the excited state of the coupled emitter would decay directly into the rightward TE polarized 1D bound mode with an overwhelmingly larger probability

than any of the other modes. Sometimes the ratio of coupling strength into the desired mode, versus all other modes, is denoted by β .

It is perhaps not surprising that the β calculated for the simple geometry shown in Figure 1.16A is much less than unity. However, by replacing the ridge waveguide by a PC waveguide, terminated at one end, as shown in Figure 1.16B, it is theoretically possible to achieve quite large β factors for coupling into a TE polarized PC waveguide channel [124, 135]. The explanation for this is most easily cast in terms of the various contributions to the total local density of states (LDOS) for photon modes at the location of the emitter, which is directly proportional to the imaginary part of the photon Green's function characteristic of the dielectric environment (i.e. characterizing the impulse electromagnetic response). While there will always be some non-zero contribution from 3D radiation modes (except inside a perfect 3D photonic crystal's band gap), if properly engineered, the combination of the 2D photonic crystal and the waveguide channel can concentrate a significant fraction of the free-space radiation modes into the waveguided mode at frequencies near the cutoff of the 1D channel. This is illustrated in the band structure diagram of Figure 1.13B, where owing to the flatness of the dispersion near the Brillouin zone boundary, the LDOS associated with the near-band edge 1D bound modes can be dramatically enhanced compared to the contribution from residual radiation modes. Theoretical and experimental results in GaAs, using embedded epitaxially-grown InAs quantum dots as quantum emitters, show that this approach can yield β values in excess of 0.85 [124, 135].

Another way to engineer the LDOS is shown schematically in Figure 1.16C, where the emitter is now located at the antinode of a 3D microcavity formed by introducing a localized defect (e.g. three missing holes) into a uniform PC. The LDOS can be made very large at the cavity mode resonant frequency, almost ensuring that the excited state emits into the cavity mode [23, 67, 157, 183]. If the cavity mode can in turn be efficiently coupled to a single mode silicon ridge waveguide with a β_{wg} close to unity (with the same intent of efficient transfer of a photonic crystal cavity photon to a photonic crystal waveguide [68, 69, 105, 132, 152, 193, 217]), then the overall system

will constitute a good single photon source [17, 68, 130, 189, 192, 230, 231]. The latter system where the emitter is coupled to a cavity, and the cavity is coupled to single mode silicon ridge waveguides, is the approach taken in this thesis work.

Single photon emitters

III-V semiconductor photonic circuit platforms can have similar dielectric profiles as SOI (refractive index of GaAs or InP and alloys are roughly the same as silicon in the C-band), and in many regards there have been more proof-of-principle demonstrations of useful LOQIP functionality in the III-V system than in SOI to date. The main drawback is the relative cost and lack of substantial industrial infrastructure for large-scale integration of both photonic and microelectronic circuits in the III-V platform. The huge advantage of the III-V platform is that high-quality quantum emitters can be relatively easily grown directly in the middle of the device waveguide layer via the Stranksy-Strazanov strained layer epitaxy technique, resulting in isolated, nanometer scale 3D islands of relatively low electronic band gap material like InAs, surrounded by higher electronic band gap material like GaAs, wherein the interface between the two is essentially free of electronic defects. The direct band gap nature of the III-V alloys, together with this near ideal interface between the 3D island and the surrounding cladding layer, means that the quantum yield of the excitonic transition associated with these quantum dots can be very high at cryogenic temperatures, and the associated dipole transition moment is large. By far the best performing on-demand single photon sources to date (coupled to optical fibers, not as yet to integrated circuits) are based on these III-V epitaxial quantum emitters [23, 101, 178, 183, 192, 219], orders of magnitude faster than the commonly implemented heralded single photon sources [53, 59, 96, 190].

Although it is possible to epitaxially grow $\text{Si}_x\text{Ge}_{1-x}$ quantum dots in silicon, the dimensions are typically much larger than the III-V islands, and due to the indirect band gap, the dipole transition moments of the associated excitons are relatively weak [127, 128, 224, 226, 227, 233, 234]. Coupling of

single SiGe QDs to high quality photonic crystal cavities has been recently reported [233], although the radiative efficiency is still very low compared to III-V QDs on III-V substrates. The large size of the islands also makes it relatively difficult to isolate a single transition.

1.3.5 Hybrid approaches to SOI platform single photon sources

While it is possible to wafer bond III-V substrates containing epitaxial quantum dots to SOI, there has been limited success efficiently coupling them to waveguide modes in the silicon. There have also been reports of epitaxially growing III-V materials directly on silicon substrates. The quality of planar III-V material grown in this way is poor, but growth of nanowires from nanoscale seeds can produce relatively high-quality material. Although this route has considerable potential, there are a number of challenges that have to be overcome in order to site-selectively locate the III-V emitter in a way that allows efficient coupling to the thin device layer of the SOI.

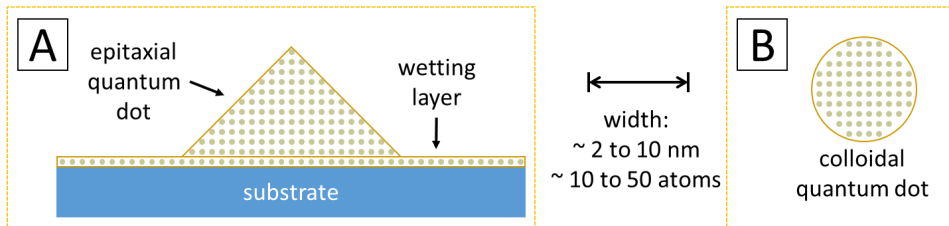


Figure 1.17: Illustrations of semiconductor quantum dots (QDs), (A) epitaxial and (B) colloidal/nanocrystal. QDs are nanometer-scaled semiconductor crystals that quantum confine the otherwise bulk excitonic spectrum, resulting in synthetic two level systems and demonstrated single photon emission.

An alternative approach, and the one adopted in this thesis work is to develop ways to incorporate colloidal quantum dot (CQD) emitters (see Figure 1.17B) in SOI-based photonic circuits [31, 73, 164]. These CQDs, described in more detail below, are synthesized in solution [145], and some are demonstrated single photon emitters in the C-band [55]. This disserta-

tion addresses various aspects associated with attempts to incorporate PbX, where X represents either Se or S, CQDs as the single photon emitters in SOI-circuit-based single photon sources. Relevant background information on PbX CQDs is presented in the following section.

1.4 Lead-based (PbX) colloidal quantum dots (CQDs) for single photon sources in SOI LOQIP

This section contains crucial background information about PbX CQD photophysics required for interpreting the results of this dissertation work. A brief overview of basic CQD photophysics is presented, followed by a more detailed picture of the electronic structure, particularly as it relates to their integration into SOI photonic environments.

1.4.1 Basic CQD photophysics

Generally, quantum dots are synthetic structures in which a quantum quasi particle is confined in three dimensions owing to a 3D local minimum in the potential energy. Prevalent are colloidal semiconductor quantum dots (CQDs), in which bulk crystalline Wannier excitons, illustrated in Figure 1.18A, are confined to nanocrystals smaller than the excitonic Bohr radius, as in Figure 1.18B. As is well understood, quantum confinement may tend a near continuum of states - e.g. bulk Wannier exciton states - towards a discrete spectrum, as depicted in Figure 1.18C. The extent of confinement is related to the size of the object, and to the strength of the confining potential, with the latter determined by the bulk material host, and the former being controlled during colloidal synthesis [145].

The absorption edge and photoluminescent emission energy are typically dominated by a ground state excitonic state manifold (more details below), so by controlling the size of the CQD, their optical properties can be varied over a wide range of energies, limited by the confining potential. The relatively large confining potential and the ability to control the size on the single nanometer scale has led to extensive use of CQDs as biomarkers

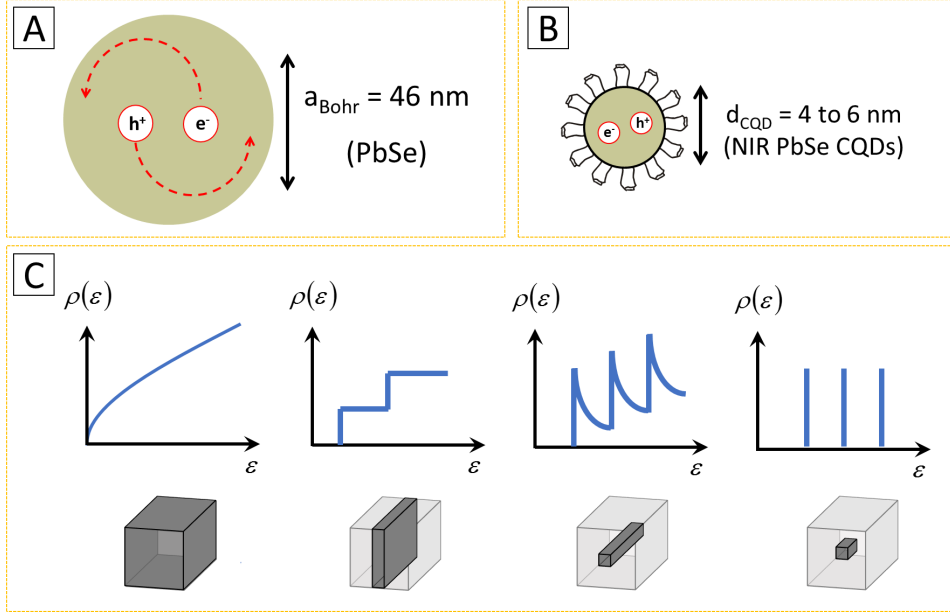


Figure 1.18: Confinement of excitons in CQDs, exemplified for PbSe semiconductor. (A): Wannier exciton in bulk PbSe. (B): Colloidal PbSe quantum dot, capped with organic ligands. CQDs generally possess multiple crystallographic facets, not drawn here. Ligands for CQDs measured in this dissertation are oleic acid, a fatty acid roughly 2 nm long (end to end, including a typical molecular bend) composed primarily of a hydrocarbon chain, which has an orientation with respect to the CQD dependent upon the orientation of crystallographic facet to which it is attached. (C): General effect of quantum confinement on the electronic density of states $\rho(\epsilon)$.

[140], in emulsions (also known as CQD solids or thick films) as solar cells [153, 154], in fiber and waveguides as gain media [14, 44], as photodetectors [51, 171], and as emitters for consumer displays and lighting [41, 195]. Most relevant to this thesis, if the quantum confinement and confining potential are substantial compared to the operating temperature, the decay from a singly-occupied ground state manifold of exciton states can be used as the basis of a single photon source.

Figure 1.19A shows a typical absorption and emission spectrum of a so-

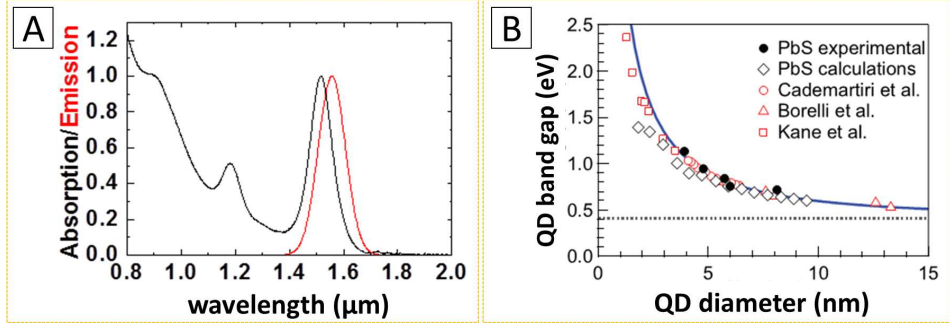


Figure 1.19: Example photophysical properties of PbX CQDs with C-band exciton emission. (A): Example absorption and emission spectra of PbSe CQDs in a colloidal suspension. (B): Collection of theoretical and experimental values of first absorption peak energy versus CQD size for PbS CQD, reprinted with permission from [142] (Copyright 2009 American Chemical Society). Unit conversion: 1 eV \leftrightarrow 1240 nm, 1550 nm \leftrightarrow 0.8 eV.

lution of hexanes containing a concentration of PbSe CQDs with a nominal diameter of 5 nm. The single peak in absorption, and the lowest peak in emission are usually attributed to the exciton transitions with significant oscillator strength within the ground state manifold. The second peak in the absorption spectrum (around 1.2 μm), is usually attributed to transitions associated with a second quantized manifold of excitons made up primarily of conduction band states from the second quantized manifold, and valence band states from the same combination of the first and second quantized manifolds of valence band states, with recent comparisons of ab initio, anisotropic $k \cdot p$ band modeling, and comparison to 2-photon absorption spectra suggesting dominance from the second quantized manifold of valence band states for PbSe CQDs emitting in the C-band [75, 150]. The relatively large separation in energy from the ground state manifold (much larger than $k_B T$ even at room temperature) is characteristic of CQDs, with their relatively large confining potential compared to III-V epitaxial QDs: sharp excitonic emission peaks are only observed at cryogenic temperatures

in most III-V epitaxial QD samples.

The threshold absorption peak energy follows an inverse relationship with CQD size as reliably documented for a variety of semiconductor compositions, and exemplified for PbS CQDs in Figure 1.19E. Numerically, lead sulfide (PbS) and lead selenide (PbSe) CQDs of diameters around 4-6 nm exhibit emission and first absorption peaks in the C-band of around 0.8 eV (compared to bulk band gaps of 0.3 eV for PbSe and 0.4 for PbS [52]), the target emission energy range for SOI photonics (0.8 eV = 1.55 μ m [48, 63, 220, 221]).

These basic absorption and emission characteristics are sufficient to understand why and how CQDs are deployed in many sensing applications, and to qualitatively understand why CQDs are candidate single-photon emitters compatible with silicon. A more in-depth consideration of the CQD electronic properties, as provided below, is required to appreciate the more subtle processes that turn out to impact in particular the PbSe exciton emission rate when placed in vacuum, on a silicon surface.

1.4.2 Band structure context, CdX CQD comparison

This subsection describes how discrete excitonic states can be thought of as a superposition of the continuum bulk crystalline electronic states. Correspondence between the two sets of states has been best understood in CdX CQDs (where X may be Se, S, Te), for which the vast majority of the extensive applications of CQDs referred to above have been based. This is largely because the bulk band gap of the corresponding binary semiconductors is in the range of 1.5 to 2.4 eV, so that CQDs with sizes in the range of a few nm can have emission/absorption energies tunable through the visible part of the spectrum (\sim 1.6 to 3.1 eV). All of the applications have driven a continuous improvement in Cd-based CQD radiative efficiency, price, and ease of synthesis on the one hand, and a corresponding amount of scientific study aimed at quantitatively understanding the optical properties of excitons in these materials. In this subsection, we compare PbX CQDs frequently to CdX CQDs to emphasize where PbX CQD understanding is lacking.

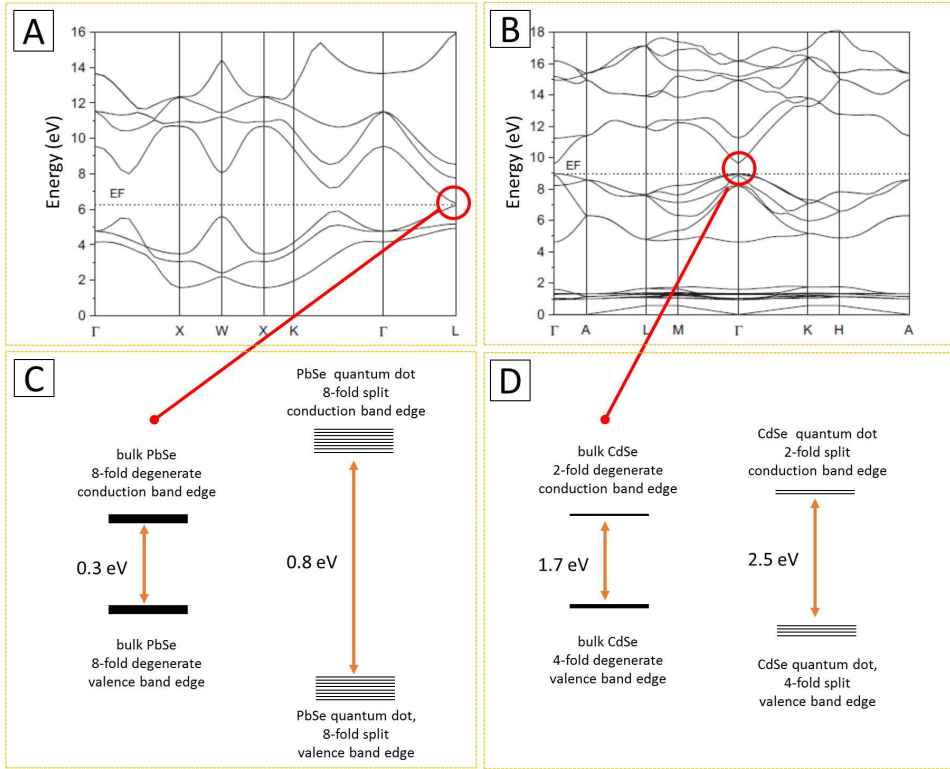


Figure 1.20: Comparison of band and state structures of PbSe and CdSe bulk crystals and quantum-confined nanocrystals. (A) and (B): Bulk band diagrams for PbSe and CdSe, respectively, adapted with permission from [236]. (C) and (D): (left) bulk and quantum confined (right) band edge energy levels, including electronic and spin degrees of freedom. Bulk energy levels do not include splitting due to crystal field or spin orbit coupling, but quantum confined levels do, along with splittings due to other interactions.

Compare the bulk band structures of CdSe (wurtzite crystal) and PbSe (rock salt crystal), shown in Figure 1.20A and B. Both are direct band gap semiconductors but the band edge states occur at different locations in the Brillouin zone. At the zone center, CdSe conduction band edge states are two-fold degenerate in spin and the valence band edge states are four-fold degenerate (two spin, two electronic), for a total number of 8 excitonic states, while for PbSe there is both a twofold spin degeneracy, and a fourfold valley degeneracy associated with the 4 equivalent valleys at the L point of the Brillouin zone for each of the conduction and valence edges, resulting in a total of 64 possible excitonic states. These degeneracies are broken in faceted CQDs when quantum confinement shifts the bulk states up (conduction) and down (valence) in energy. When exchange terms are also included, then depending on the faceting, the lowest lying conduction and valence band states qualitatively shift with respect to their bulk counterparts as shown schematically in Figure 1.20C and D.

The spectral width of the absorption and emission peaks is thus constituted by a combination of (i) the distribution of CQD sizes in the solution under study (inhomogeneous broadening) (ii) the distribution of ground state manifold states with significant oscillator strengths, and (iii) the pure dephasing (homogeneous broadening) [172] of each of those radiative states. Inhomogeneous line widths for size distributions with several percent of the mean diameter are typically on the order of tens of meV over a wide range of CQD compositions, and so these typically dominate solution spectra.

The spread of ground state manifold states with significant oscillator strengths is thought to be 25 meV (i.e. the crystal field) in CdS and CdSe, but as discussed in Chapter 3 below, there is no real agreement for this distribution in PbSe or PbS CQDs. Similarly, homogeneous line widths have been fairly convincingly measured in some CdX CQDs, but there is little consistency in the relatively few attempts to determine this parameter in PbX materials. The band edge transitions of single CdX CQDs exhibit homogeneous line widths as low as 100 μ eV, typical of most epitaxial III-V QDs but not as good as the best-observed, nearly radiative lifetime-limited line widths of QDs observed at low temperatures (around 1 μ eV). Estimates

of the homogeneous line width in PbX CQDs vary from tens of meV [172] to as low as 5 meV [137]. Measurements of homogeneous line widths are often difficult to interpret, especially when there is a large degeneracy of states in the underlying bulk material, so it is probably true that there has been no reliable measurement of the homogeneous line width in PbSe or PbS CQDs: it is probably more likely that some combination of the distribution of ground state manifold states with significant oscillator strength, and their homogeneous line widths, are on the order of a few meV.

When illuminated by high energy photons well above the renormalized band gap energy, electrons from a variety of occupied valence band states can be promoted to empty conduction band states shifted by the incident photon energy. The relatively high energy electron and hole states so excited relax rapidly down into the ground state manifold via phonon emission within typically a few picoseconds. Each of these single exciton states in the ground state manifold will have a certain oscillator strength (dipole transition moment). Depending upon the sample temperature, the exciton will occupy some range of states with some Boltzmann-like probability, and the net probability for its decay will be a statistically weighted average of the decay rates from each of the available states. In the absence of non-radiative decay processes, the net radiative decay rate at any given temperature will be the statistically weighted radiative decay rate determined by the distribution of oscillator strengths within the ground state manifold.

1.4.3 Non-radiative recombination, defect/surface states, and CQD formulation

Excitons in the ground state manifolds discussed in the previous section can decay, or recombine, either radiatively, via the emission of a photon (the desired decay mechanism), or non-radiatively via phonon emission and intermediate “defect states” (parasitic mechanisms). Non-radiative recombination processes turn out to play a critical role in interpreting our various experimental data. It is challenging to accurately calculate and experimentally confirm the energy and oscillator strength distribution of the “intrinsic” ground state manifold of excitonic states, let alone the “defect states”. This

is true even in the relatively well understood CdSe CQDs, and it is significantly more challenging for PbSe CQDs. The relatively good extent of agreement between theory and experiment for CdSe CQDs is exemplified in reference [200], in which experimental observation of the number of optically active transitions, their magnetic field dependence, and nanocrystal anisotropy dependence corroborated long-developed theory of this ground state excitonic manifold. This agreement between the predicted behavior of “intrinsic” exciton states, and the observed behavior in CdX CQDs is consistent with the relatively weak non-radiative decay in these highly-evolved CQDs. In stark contrast, non-radiative recombination processes are found to dominate the exciton decay in PbX CQDs integrated into an SOI environment and quantifying this behavior formed a major part of this dissertation.

An important contribution to non-radiative processes are *surface states* that bear significantly on CQD emission [10, 16, 21, 97], which is well-established for Cd-based CQDs emissive at visible wavelengths, and believed to carry over in some way to PbX CQDs. These surface states lie energetically within the band gap and admit additional exciton recombination pathways, including “trap states” that may suppress CQD emission intermittently (e.g. “blinking”). Whether entirely non-radiative or resulting in emission of lower energy photons, surface states are deleterious to single photon source applications that call for a high efficiency, narrow band emitter. Alleviation of sensitivity arising from these surface states is largely achieved by passivating the CQDs with organic ligands such as oleic acid, or with a shell of relatively high band gap inorganics [10, 56, 106]. For PbX CQDs, the role of surface states has been inconsistent, ranging from early arguments that they should have little or no bearing on emission [11, 63, 220] to having substantial nanocrystal size and shape dependencies [46, 81].

Estimates of in-solution radiative efficiency range from several tens of percent to 85% at room temperature [63, 194, 220], with upper estimates comparable to high quality epitaxial QDs and CdX CQDs. The CQD formulation, in this case referring to in solution vs in thick film (as commonly studied) or in thin film (as closer to a device setting) may affect ligand availability and thus bear on non-radiative recombination. A lack of lig-

and availability CQDs integrated sparsely into an SOI PIC is suspected to strongly degrade radiative efficiency relative to CQDs in solution, and this possible contribution is clarified in the studies in this dissertation.

A better known aspect of CQD non-radiative recombination is that (with few exceptions [43, 93]) integrated photoluminescence at lower temperatures is larger than at room temperature, indicating *thermal activation* of these non-radiative pathways [7, 172]. Studying the temperature dependent PL can thus provide an understanding of non-radiative recombination beyond studies only at one temperature. For example, work in our group prior to the dissertation work reported here focused on quantitatively explaining the temperature dependent emission spectra from relatively thick films of PbSe CQDs on silicon substrates [172].

When trying to understand and improve on these properties, one of the biggest challenges has been in reproducing consistent results, within a research group, from batch to batch, and across research groups. After several years of effort, the PbX synthesis group who collaborated on this dissertation work were able to provide quite reproducible batches of PbSe CQDs, which motivated an attempt to comprehensively study their optical properties with an emphasis on performance out of solution. Thick film PL (including temperature dependent spectra) provided the most reproducible out-of-solution data, and it was somewhat reassuring that to the extent possible with published data, these samples appeared to behave similarly to at least a subset of those reported by other groups [103, 180, 213].

Despite excellent agreement between modeling and measurements in our thick film studies, results reported by another group [43, 93] exhibited markedly different behavior of thick film temperature-dependent PL and that work highlighted the large impact of air exposure on their results. Although earlier work from our lab characterized air effects at room temperature [207], it did not consider air dependent kinetics. To unify the disparate thick film behavior, with the particular intent to understand the possible influence of air exposure on our specific CQDs, this dissertation includes temperature-dependent thick film PL studies of CQDs from the same source (our collaborators, the van Veggel group at the University of

Victoria) and varied extents of air exposure, along with development and application of a general and useful PL kinetics framework in order to understand temperature-dependent non-radiative recombination. As a note of clarification, studies (e.g. [207]) support oxygen being the dominant influence of air exposure on PbSe CQDs, and correspondingly air and oxygen are often used interchangeably in such literature.

1.4.4 Impact of dielectric environment on CQD emission: depolarization and radiative density of states

The non-radiative recombination, absolute and relative to radiative recombination, is tied not just to intrinsic photophysics, but also to the dielectric environment. For example, the radiative lifetimes of excitons in both CdX (of order 10 ns) and PbX (of order 1 μ s) CQDs are relatively long, in comparison to their III-V epitaxially-grown counterparts (often 100 ps to 1 ns range), attributable in part due to the strong depolarization field that reduces the amplitude of vacuum fluctuations inside the high dielectric constant CQDs, which are typically surrounded by solvent or vacuum, as opposed to being buried within a high-dielectric bulk III-V host. Slow exciton recombination directly impedes photon emission rate and thus single photon source performance. This depolarization effect also influences the ability to excite CQDs.

Beyond depolarization at the CQD-environment interface, determined by the host dielectric environment, the dielectric environments also bears significantly on the photonic modes available for the CQD to radiate into, which in turn affects radiative recombination rates relative to non-radiative recombination, and thus the radiative efficiency. The choice of cavity plus waveguide geometry in 1.3.4 represents one aspect of optimizing the dielectric environment for improved photon collection efficiency and guidance into a PIC. Proper accounting of the influence of depolarization and the photonic density of states is essential in understanding CQD emission in SOI PICs, and a major portion of this dissertation is dedicated to doing so (specifically Chapter 3).

1.4.5 CQD emission on silicon and in SOI PICs

As indicated above, researchers have made considerable progress in understanding and improving the optical properties of CdX CQDs in particular, and to a lesser degree CQDs based on PbX materials. Much of this progress has been achieved in solvent environments where the CQDs are synthesized, and where their organic passivation layers can thrive. To be useful as quantum emitters in SOI circuits, the PbX CQDs must function out of solution, on or near a silicon surface, in vacuum, or encapsulated with some protective solid film. Accounting for the influence of environment on CQD emission is a major part of the understanding developed in this dissertation, constituting the majority of the experiment and modeling in Chapters 2 and 3, respectively. With many of the key photophysical processes of PbX CQDs reviewed earlier in this section, consider now PbX CQD photophysics specifically in SOI PICs and related environments.

Prior to PbX CQD integration into SOI photonic circuit components, CQD emission enhancement by a microcavity (Cd-based CQDs at visible wavelengths) in 2003 [166] and PbS CQD emission enhancement by photonic crystal microcavities (at 900 nanometers for AlGaAs-host cavities) in 2005 [76] were demonstrated. Proposed realization of a C-band single photon source via integration of PbX CQDs in SOI-host photonic crystal cavities in 2005 [30] was followed by C-band PbX CQD emission enhancement by SOI photonic components primarily photonic crystal cavities) [31, 33, 34, 62, 90, 133, 138, 164, 175, 176, 223, 229].

A particular concern raised in these studies [175, 223] was potentially low radiative efficiency of sub- to few-layer PbX CQDs on substrates, reported to be as low as around 1% [125, 185, 206], much less than reported in solution. A low radiative efficiency, when combined with already slow emission lifetimes and low detection efficiencies in the near infrared (NIR), also increases the challenge to measure CQD emission, impeding studies of their properties out of solution [175, 223]. A proposed mechanism for low radiative efficiency on substrates was poor passivation due to ligand unavailability, and subsequent trapping of exciton population in non-radiative

surface states [185, 206], supported in part by sub-linear power scaling of CQD emission [175].

Prior work in Young’s group [164] advanced previous research by others [125, 133, 175, 223] on improving understanding of PbX on-substrate radiative efficiency and emission rates into SOI photonic circuits. Noted in these earlier works was the lack of a consistent relationship between measured CQD PL cavity enhancement (as quantified by the Purcell factor) and the cavity quality factor [133], a relationship already understood for single epitaxial QDs in III-V photonic systems [67, 179, 191, 215]. The lack of consistency could be attributed to most works indiscriminately coating the silicon cavities with an ensemble of CQDs, causing indeterminacy in the CQD-cavity coupling. The work from our lab in Reference [164] established site-selectively binding of PbSe nanocrystals to within the main antinode of an SOI photonic crystal microcavity which solved this problem, but at the time that work was published, the data was not fully analyzed. A major portion of this dissertation involved modeling the power saturation of this cavity-coupled emission in an effort to overcome assumptions holding back interpretation of other studies, including proper accounting of the dielectric environment and allowing for sufficiently general non-radiative recombination as a free parameter.

1.5 Dissertation aim restatement, methodology, and organization

The aim of this thesis work was to assess the feasibility of using PbSe CQDs as the source of single photons that could be efficiently coupled into single mode silicon waveguides in conventional SOI photonic circuits operating near $1.55 \mu\text{m}$ wavelengths. The author carried out a number of novel experiments that involved CQD sample preparation and their integration with previously fabricated SOI photonic circuits, and quantitative optical emission measurements at temperatures ranging from 4 K to 300 K. A considerable fraction of the research involved developing models and solving them numerically in order to quantitatively interpret various measurements

that in one way or another elucidated the radiative and non-radiative decay rates of ground-state-manifold excitons in PbSe CQDs in various dielectric environments.

Chapter 2 explains the experimental methodologies used for sample preparation and all of the optical experiments done with the PbSe CQDs either in solution, or in thin or thick film formulations on silicon surfaces, or site-selectively attached to isolated photonic crystal microcavities (specifically excluding all of the photonic circuit coupling work, which is described in Chapter 4). With the exception of the temperature-dependent photoluminescent yield data obtained as a function of air exposure, all of the experimental optical data in Chapter 2 was gathered by other members of the Young group; it is presented because all of the modeling of that data, done entirely by the author, as described in Chapter 3, is based on this data. Chapter 4 is self-contained, and describes all of the experimental and modeling work done by the author, characterizing the coupling of PbSe exciton emission into single mode silicon waveguides. Chapter 4 also draws on results from Chapter 3, for interpreting the photonic circuit data. Chapter 5 summarizes the knowledge gained from this body of work by first summarizing the key factors that limited the circuit-based performance obtained in this research, and then speculating on the feasibility for improving on these results through future efforts.

Chapter 2

Experiment (non-PIC)

This chapter describes the experimental setups and methodologies used to obtain PbSe photoluminescence spectra directly from the photo-excited region of various textured and untextured substrates. Corresponding modeling is contained in Chapter 3. Studies of the PbSe CQD PL coupled into single mode silicon waveguide circuits is dealt with in Chapter 4.

2.1 Substrates and photonic component fabrication

2.1.1 SOI and silicon substrates

Much of the work in this thesis involved taking PbSe CQDs out of their native solvent environment and placing them on either bare silicon, or on the device layer of patterned or unpatterned SOI. The band gap of silicon, corresponding to its linear absorption edge, is at 1.1 eV (≈ 1100 nm free space wavelength) at room temperature. In the high resistivity samples used for photonic applications, the residual absorption associated with band tail states and phonon absorption bands at longer wavelengths result in a broad local minimum in absorption that spectrally includes the important 1.55 micrometer wavelength near-infrared (NIR) absorption minimum of long-haul silica fiber.

At those wavelengths, silicon has a high index of refraction of ≈ 3.4 which allows for tight confinement of light. This high refractive index is exploited to form low-loss planar waveguides in silicon-on-insulator (SOI) wafers that consist of a thin, typically ≈ 200 nm high quality, high-resistivity silicon device layer atop an electrically insulating, low-index of refraction silicon dioxide layer on the order of 1 μm thick, all of which is supported on a thicker (upwards of 1 mm) silicon backing wafer. In some instances, the silicon dioxide layer underneath the photonic crystal is etched away by immersing the sample in aqueous HF for 10 to 20 minutes, thereby increasing the refractive index contrast further.

SOI wafers with a silicon device layer thickness of 198^{+4}_{-4} nm, oxide layer thickness of 1193^{+10}_{-10} nm from Galian Photonics were used for e-beam lithographic fabrication of the standalone photonic crystal cavity used in this chapter, where super- and sub-scripts denote uncertainty deviations from in-line numerical value. Bare and SOI silicon surfaces were cleaned before integration of PbSe CQDs, as described in the section below.

2.1.2 Photonic crystal cavities

As discussed in Chapter 1, integrated single-photon source schemes based on luminescent CQDs as emitters often invoke a microcavity to efficiently collect the CQD excitonic emission, in a microcavity mode at a rate that exceeds the emission rate into other electromagnetic modes. The enhancement of the radiative decay rate of the exciton into any given cavity mode, relative to the free space decay rate, is quantified by that mode's *Purcell factor* F . The Purcell factor of any mode is proportional to its *quality factor* Q (as used generally for resonances) divided by its *mode volume* V , the latter quantifying how tightly the mode is distributed spatially. In formulae:

$$F = \frac{3}{4\pi^2} \left(\frac{\lambda}{n} \right)^3 \frac{Q}{V} \quad (2.1)$$

$$V = \int d\mathbf{r} \frac{\epsilon(\mathbf{r}) |\mathbf{E}_{\text{cav}}(\mathbf{r})|^2}{\epsilon(\mathbf{r}_0) |\mathbf{E}_{\text{cav}}(\mathbf{r}_0)|^2} \quad (2.2)$$

where \mathbf{r}_0 is the location at which $\epsilon(\mathbf{r}) |\mathbf{E}_{\text{cav}}(\mathbf{r})|$ is maximum, where the cavity mode field is $\mathbf{E}_{\text{cav}}(\mathbf{r})$ and the cavity structure is defined by the dielectric function $\epsilon(\mathbf{r})$.

Large Purcell factors are crucial for efficient photon collection and many cavity designs have been explored to achieve this. A cavity design for which large quality factor and small mode volumes, and thus potentially efficient photon collection, has been realized in the SOI platform is the “L3” configuration, shown in Figure 2.1, along with an intensity profile of its fundamental in-gap cavity mode. Such cavities can be coupled efficiently to photonic crystal waveguides that are impedance matched to low-loss, sub- μm scale silicon channel waveguides [17]. Other in-gap (localized) modes are also supported by L3 cavities, but the fundamental mode typically exhibits the highest quality and Purcell factors.

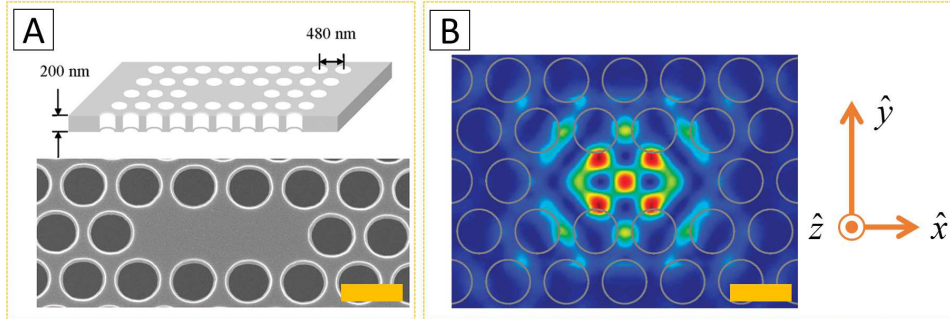


Figure 2.1: (A): Schematic and scanning electron micrograph of an “L3” microcavity. (B): Fundamental in-gap cavity mode electric field intensity at the silicon-air interface, with etched holes outlined. Axes originate at the L3 slab centroid, and \hat{z} is perpendicular to \hat{x} and \hat{y} . Yellow scale bars are 500 nm in length. Figure adapted from [164].

2.2 PbX CQD formulations and integration methods

This section describes CQD formulations (solvent, thin film, thick film) and methods of integrating PbX CQDs onto and near silicon substrates as used

in this dissertation.

2.2.1 PbX CQD formulations

Solvent: Colloidal quantum dots are synthesized, stable, most commonly measured, and exhibit their highest observed quantum efficiency with reliably measured radiative lifetime, in solution. Each other formulation (described below) either derives from or utilizes the solution formulation. Thus, in-solution measurements represent a useful reference for all other CQD experiments. For our experiments, CQDs are synthesized according to [207] by collaborators at the University of Victoria. To avoid inter-CQD effects, solution measurements are performed for CQD concentrations below which the spectral profile is unchanged if the concentration is further reduced, typically well below ≈ 5 mg/mL CQD weight by volume in solution.

The photostability of these PbX CQDs was thoroughly characterized before the work in this dissertation, results of which are largely contained in reference [207]. Exposure to air and light tended to shift and degrade in-solution PbX CQD PL spectra over days to months time scales, which can be prevented by storing PbX CQDs in sealed vials filled with Argon (to prevent air from entering the vial) in the dark (e.g. wrapped in aluminum foil and stored in a dark cabinet), and also be helped by refined synthesis methods. These early photostability studies included effects of air exposure on the room temperature integrated photoluminescence of PbSe thick films, noting long-term photostability under vacuum, degradation when exposed to air, and recovery once placed back under vacuum. These studies informed the integration methods described below.

Thin film: Many device settings, particularly single photon sources, call for few (ideally one) CQD in the vicinity of a substrate in vacuum or atmosphere, not in solution. This formulation falls within what will be referred to herein as the “thin film” formulation. The composition of such films is typically inhomogeneous across the surface, consisting of regions containing isolated CQDs, close-packed monolayers of CQDs, with the possible inclusion of two or three layer thick islands. The exact morphology depends

critically on the thin film formation process, as discussed below.

Thick film: A relatively simple means of obtaining homogeneous formulations of CQDs out of solution is by means of drop-casting dense solutions of CQDs on substrates. Depending on the method of depositing the solution (spin-coating or from a pipette), these “thick films” are typically tens of μm thick. There are many studies of CQD emission from thick film emulsions reported in the literature. The Young group had previously published detailed results of the temperature dependence of the luminescence lineshape from thick film PbSe emulsions [172]. In this and the following chapters, the temperature dependence of the photoluminescence yield is studied, with particular attention paid to the impact of air exposure.

2.2.2 PbX CQD integration methods

Use of inert gas environments and vacuums: In between experiments, CQDs are stored in glass vials that are sealed with parafilm under Nitrogen or Argon gas flow, and wrapped in light-blocking aluminum film, to help prevent air and/or light mediated changes to the CQD emission and absorption properties. Vials of CQDs in solution were checked regularly (over time scale of months) to make sure solvent had not evaporated, and in the exceptional situations when solvent did evaporate, addition of solvent (to the original solvent level) followed by re-sealing under inert gas flow was performed. Some other formulation steps, e.g. when drop-casting or dip-coating, were performed either under low nitrogen gas flow, or in a glove box filled with nitrogen gas (described further below). After CQD integration onto a substrate, samples are placed under vacuum to preserve the CQDs and allow for low-temperature measurements (also described further below). If held under vacuum, the optical properties of these films remained almost unchanged for at least several months.

Solvent transfers: CQDs are received from our collaborators in a suspension in toluene, an organic solvent for which photophysical properties of PbX CQDs were found to be largely preserved when stored long-term in the dark [6] (tetrachloroethylene (TCE) also works well for long-term storage).

Suspension of CQDs in other solvents, notably hexanes, were found better for CQD integration processes, so a solvent transfer from toluene to hexanes was performed prior to immersion of a silicon or SOI sample in a CQD solution. Solvent transfer therefore involves evaporation of solvent under dry nitrogen gas flow for upwards of a few hours, followed by reconstitution with the target solvent. In a variety of experiments, it was useful to quantify the CQD concentration, and this may conveniently be done during the solvent transfer process as follows: (a) Before solvent transfer, weigh the destination vial. (b) Fill the destination vial with the toluene (or TCE)-dispersed CQDs, then evaporate under dry nitrogen flow for upwards of several hours. (c) Weigh the destination vial plus dried CQDs, and subtract from this the weight of the empty destination vial. The resulting weight is of the CQDs plus ligands, and reconstitution with a known volume of solvent permits knowledge of the mass of CQDs (plus ligands) per volume of solvent.

Drop-casting: After as-received CQDs are transferred to a solution of hexanes, much of the hexanes solvent is evaporated under Nitrogen gas flow, until the concentration of CQD mass per volume is on the order of ≈ 50 mg/mL, a process that typically takes several hours. During evaporation, a silicon or silicon on insulator wafer portion is removed of organic residues by RCA-1 and RCA-2 cleaning procedures (see, for example, [102]). The cleaned wafer portion is mounted in a cryostat and nitrogen gas is pumped through the cryostat, such that a slight positive pressure of nitrogen gas inside the cryostat is maintained. The dense suspension of CQDs is then pipetted onto wafer surface (temporarily lifting the cryostat window for each deposition), resulting in approximately a few square mm of coverage and sub-mm thickness. The influence of air on CQDs emission and absorption requires we study these properties for CQDs under vacuum, so the sample is placed under vacuum after the CQD solid is drop-casted. A Janis Inc. ST-500 cryostat was the sole cryostat used in the work in this dissertation. The sample chamber was pumped down to 10^{-4} millibar with a turbo pump capable of reaching low 10^{-6} millibar vacuums, then pumped for another 30 minutes. Shortly prior to measurements, the cryostat chamber would be re-pumped until the vacuum reached the 10^{-6} millibar range, typically ~ 10

to 15 minutes.

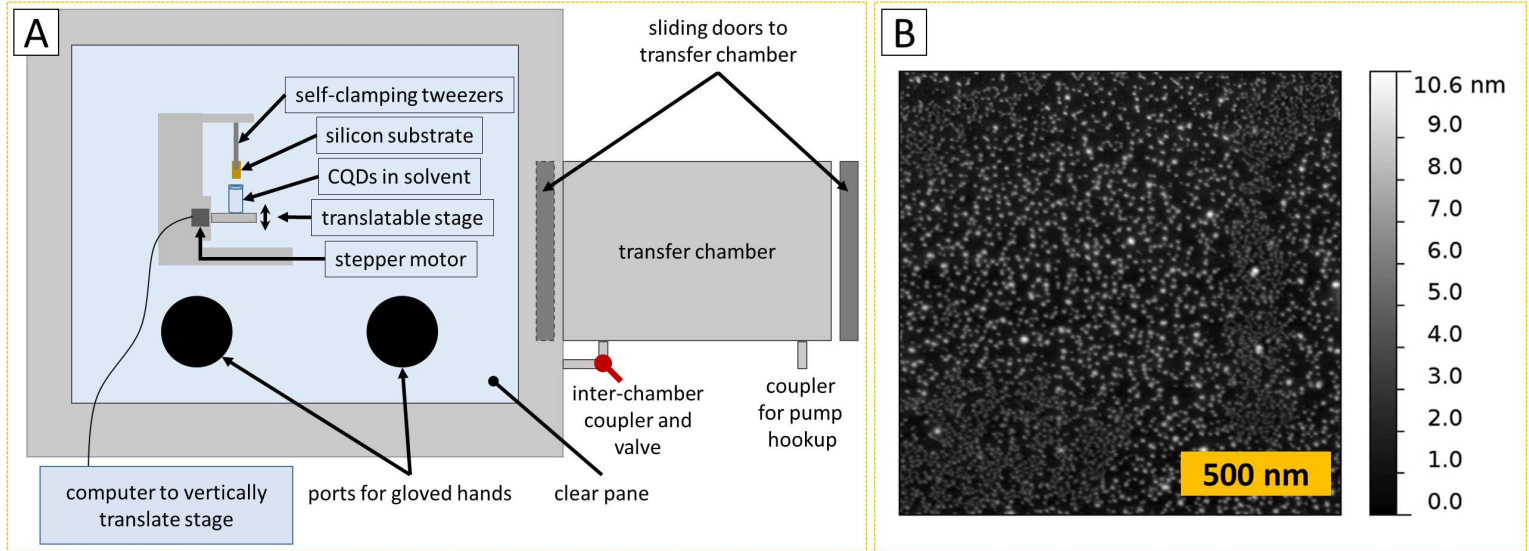


Figure 2.2: Dip-coating for thin film formulations, in an inert-gas glove box. (A): The glove box and dipping setup used for monolayer, sub-monolayer, and generally dip-coating formulations. (B): Example scanning electron micrograph of a sub-monolayer of CQDs on a silicon surface using the setup in (A) and described in-text, published in [173].

Dip-coating: Samples for which a monolayer or submonolayer thickness of CQDs on a silicon surface are prepared as follows, with additional details found in Appendix A. For reference, the procedure is often called “dip-coating” and is depicted, with example results, in Figure 2.2. Firstly, silicon or silicon-on-insulator substrates are cleaned of organic residues by RCA-1 and RCA-2 cleaning. Following this cleaning, the silicon surface is prepared to improve adhesion of the CQDs to it. As also described in [164], the oleate (ligand)-capped PbSe CQDs used in our laboratory adhere preferentially (by a few orders of magnitude) to hydrogen-terminated silicon relative to oxidized silicon (a ~ 1 nm layer on the silicon surface), the latter forming rapidly and commonly upon exposure of a silicon surface to air. Hydrogen-terminated silicon is achieved by thoroughly cleaning a silicon surface of

organic residues (in our case, with RCA-1 and RCA-2 procedures), followed by gentle hand-held agitation of the silicon sample in 2% aqueous HF for 10 to 20 minutes. The aqueous HF treatment etches away any exposed oxidized silicon and produces the hydrogen-terminated surface. Oleate-capped PbSe CQDs also adhere relatively poorly to dodecyl-coated silicon [164], as used in AFM-assisted site-selective binding (described below).

CQDs are dispersed in hexanes to a concentration of \approx 5 mg/mL CQD weight by volume in solution (see solvent transfer information above for how this concentration is measured). The CQD solution, sample, and cryostat are then placed in an inert nitrogen gas glove box. In the nitrogen environment, the sample substrate is mounted on tweezers with its plane vertical. Directly below the sample is a mechanically controlled stage upon which an open vial of the solution is placed. The stage can move up or down at a specified speed by LabView control of an attached stepper motor. Group member Stephanie Flynn studied the effect of dipping speeds monolayer spectra, and found insensitivity to the speed at which the sample substrate is introduced into the CQD solution, but high sensitivity to the speed at which the substrate is removed from solution. For PbSe CQDs similar to those used in this dissertation, withdrawal speeds of 0.8 mm/s to 1.0 mm/s provided larger and more consistent spectra than 1.2 mm/s, and a speed of 0.8 mm/s was used for samples in this dissertation. Upon removal of the sample from solution, the sample is placed in the cryostat and subsequently under vacuum, as done for drop-cast samples.

AFM-assisted site-selective binding: This procedure is published in reference [164], and used for integration of the CQDs into the standalone cavity used in power saturation measurements in this chapter. Figure 2.3 summarizes these steps. Preferential binding of PbSe CQDs via hydrogen-termination of the silicon surface is also utilized in this integration method by locally oxidizing areas of desired CQD binding with application of a voltage between a positioned conducting AFM tip and subsequently immersing the sample in aqueous HF. All other areas, i.e. in which CQDs are not desired, are chemically coated with dodecyl, a molecule that (a) is destroyed during local oxidation by the application of the AFM voltage, (b) protects the

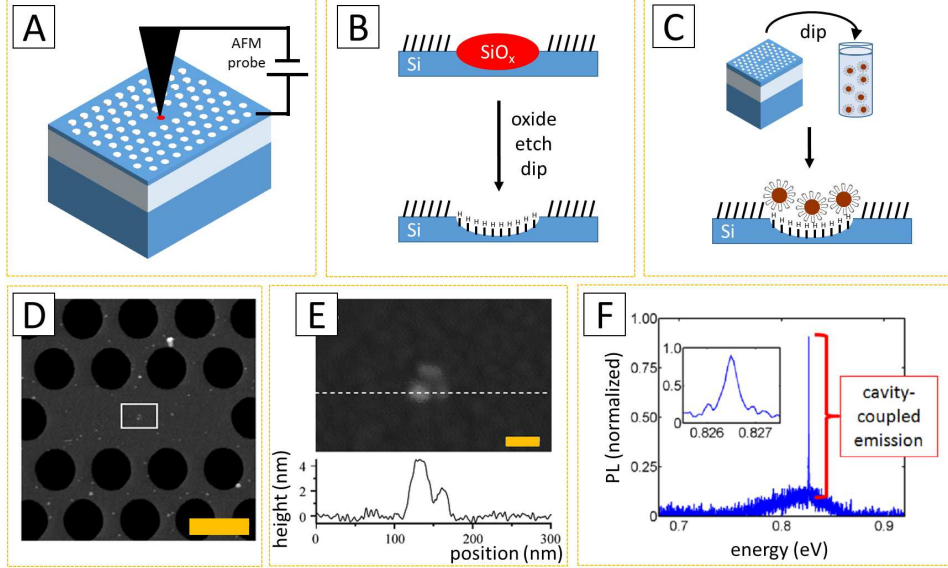


Figure 2.3: Site-selective binding technique, as published in [164], used to integrated PbX CQDs to primarily within the main antinode of the fundamental cavity mode of a standalone L3 photonic crystal cavity, for the sample studied in this chapter. Prior to the AFM site-selective surface oxidation depicted in (A), the silicon is coated with dodecyl molecules. In (B), application of a voltage from the AFM locally removes the dodecyl molecules and oxidizes the silicon surface. Immersion in a buffered oxide etch removes the oxidized silicon but leaves the dodecyl coated silicon intact. The sample is finally dipped in a suspension of CQDs (C), which adhere preferentially to the hydrogen-terminated silicon (relative to the dodecyl coated silicon). (D) and (E) are atomic force micrographs of the sample surface, with (E) corresponding to the region within the white rectangle in (D). (F): resulting microphotoluminescence (μ PL) collected directly from the cavity region. Yellow scale bar is 500 nm in (D) and 50 nm in (E). Unit conversion: $1 \text{ eV} \leftrightarrow 1240 \text{ nm}$, $0.8625 \text{ eV} \leftrightarrow 1500 \text{ nm}$.

non-oxidized silicon surface from hydrogen termination when the sample is immersed in aqueous HF, and (c) preferentially (relative to hydrogen terminated silicon) rejects adhesion of oleate-capped PbSe CQDs. A typical

site oxidized by the AFM tip was roughly circular and ~ 50 nm in diameter, with CQD areal density of $\sim 3 \times 10^3$ nanocrystals per square μm (within each site), compared to ~ 10 nanocrystals per square μm on portions of the sample protected with the dodecyl layer [164].

2.3 PL measurements overview and optical setups

This section describes the experimental setups and alignment procedures used for the three non-circuit-based PbX luminescence measurements, and the three following sections describe the results of these measurements. The setup for two of these measurements - temperature and air exposure dependence of steady-state PbSe CQD thick film PL (Section 2.6), and power-dependence of cavity-coupled PbSe CQD PL (Section 2.4) - are nearly identical and presented in Subsection 2.3.2. The setup for the third measurement - time-resolved PbSe CQD emission in various formulations (Section 2.5) - contains similar elements and is summarized in Subsection 2.3.3.

2.3.1 PL measurements overview

The three sets of PL measurements contained in this section are as follows. The first set of measurements, performed by Haijun Qiao formerly of our group, is the power dependence of cavity-coupled PbSe CQD PL, for PbSe CQDs site-selectively integrated into the main antinode of an “L3” photonic crystal cavity. This power dependence, found to saturate at low excitation powers for which in-solution, sub-monolayer, and thick film PL are either linear or only slightly sub-linear, can provide insight into PbSe exciton dynamics when combined with the modeling efforts in Chapter 3. The second study involved systematic, time-resolved photoluminescence decay measurements of PbSe CQDs in solution, thick films, and sub-monolayer films, for the same PbSe CQDs used elsewhere in this dissertation, the results of which were later combined with dielectric modeling in Chapter 3 to improve understanding of the environmental dependence of non-radiative decay. The third set of measurements studied the impact of air exposure on the temper-

ature dependence of PbSe CQD thick films, which extends the air exposure dependence studies of [207] that were only performed at room temperature, and can be compared to the thorough temperature-dependent thick film studies of [172]. These studies provide new insight into the non-radiative decay kinetics.

2.3.2 Head-on continuous wave (CW) laser excitation

Both the μ PL of CQDs in silicon microcavities and thick CQD film PL were measured using the setup shown in Figure 2.4. Components not shown are temperature controller equipment and cryogen used to adjust the temperature of the thick CQD films. The white light source was not used in the thick film measurements, but was used in the μ PL measurements to image the sample for translation to the appropriate location. In both experiments the sample is prepared as described in the previous section, and is located in the cryostat.

A continuous wave Helium-Neon (HeNe) laser is collimated, passed through a neutral density filter wheel, diverted by a visible wavelength beam splitter that's transparent around $1.55\ \mu\text{m}$ wavelengths, and focused onto the sample surface using a 100X long working distance microscope objective to a $1/e^2$ power spot diameter of $2.0\ \mu\text{m}$. The same objective collects PL and diverts it to a Bruker Fourier transform infrared (FTIR) spectrometer, utilizing a liquid nitrogen cooled Germanium (Ge) detector. In μ PL experiments the spot is focused onto the cavity center, using the scattered HeNe light as an indicator of the spot position. In the thick CQD film measurements, the excitation spot position is adjusted to optimize integrated signal into the detector.

In thick CQD film experiments, the excitation intensity was adjusted such that both the integrated PL was proportional to the excitation intensity and the PL spectrum profile was unchanged, on the order of tens of μW . In μ PL/microcavity power saturation measurements, the PL was clearly brought out of this linear regime up to sub-linear, saturated regime (starting around several μW and measured up through $70\ \mu\text{W}$).

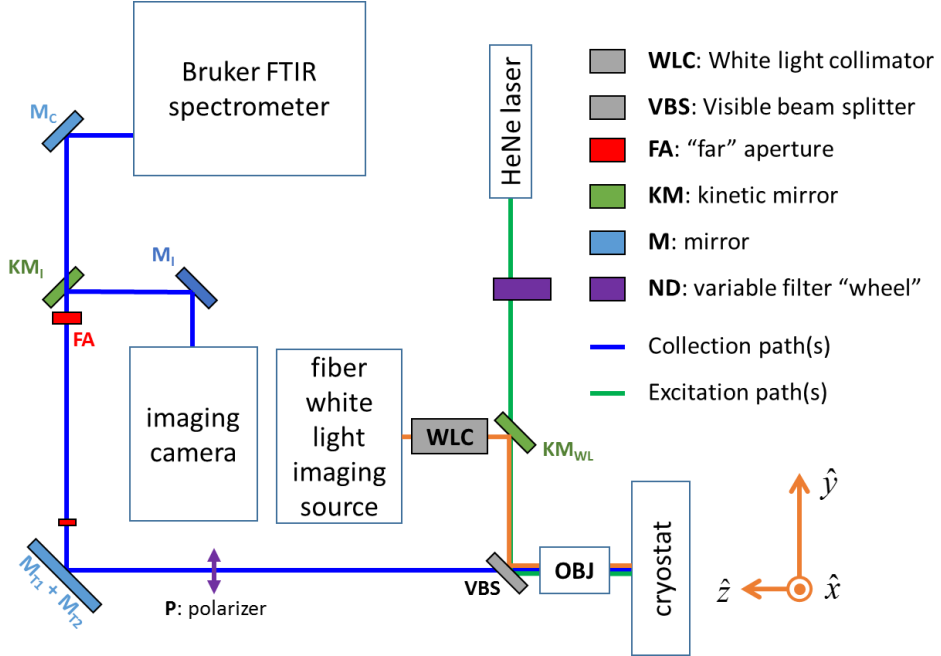


Figure 2.4: Head-on continuous wave (CW) HeNe excitation setup used for power saturation measurements of PbX CQD emission coupled to a standalone L3 cavity and steady-state integrated PL of PbSe CQD thick films. Mirror pair M_{T1,T2} diverts collected light down ($-\hat{x}$) and then in the direction of the Bruker FTIR; details are available in the insets of Figure 4.4F.

2.3.3 Pulsed excitation in back-scatter geometry

Excitation and collection equipment was similar for time-resolved PL measurements as it was for continuous wave (CW) PL measurements, but the CW laser was replaced by a 660 nm pulsed Sepia II diode laser with repetition rate of 1 MHz and pulse duration of 500 ps, and the additional functionality of gated single photon detection with a model ID210 photon counter from ID Quantique (detection range 900 nm to 1700 nm), plus PicoHarp 300 time correlator, were added, as seen in Figure 2.5. Results were corroborated with a pulsed Ti:Sapphire laser with a 1.2 ps pulse duration and emission wavelength of 800 nm. The oscillator used for laser pulses was used to gate photon detection in the photon counter, and used for sync

pulses for the time correlator. Toggling between gated photon counting and PL spectral measurements was done by addition of a kinetic mirror. PL diverted by the kinetic mirror was focused into a multimode fiber by a lens, a fiber that carried the PL to the single photon counter.

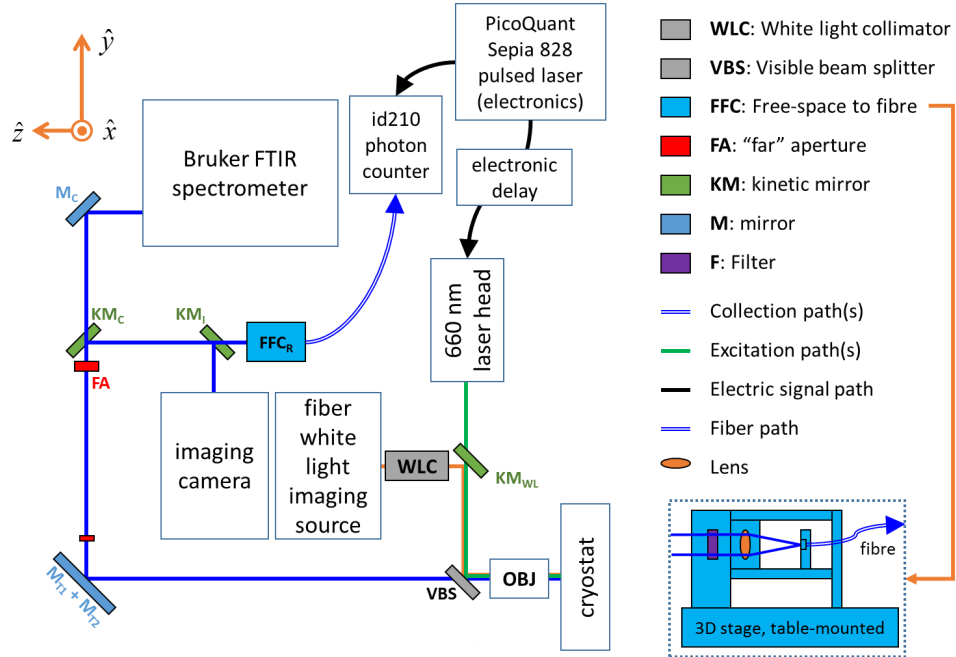


Figure 2.5: Back-scattering geometry with pulsed laser excitation setup used for time-resolved studies in [173] and presented in Section 2.5.

Pulse duration was ≈ 500 ps and the repetition rate and average power were kept low enough for spectra and time-resolved PL curve shapes to be insensitive to both repetition rate and excitation power. The corresponding average peak laser intensities were less than 300, 300, and 3000 Watts per square centimeter for solution, drop-cast, and dip-coated samples, respectively, and the corresponding repetition rate was 1 MHz. The excitation spot was $\approx 3 \mu\text{m}$ in diameter. Spectra were also obtained with the Bruker FTIR. CQD formulations on substrates were measured while in the cryostat, whereas the CQDs in solution were measured while in a vial.

2.4 Power saturation of cavity-coupled CQD PL

Power saturation measurements of CQD PL can provide insight into their excitonic population dynamics, particularly when the excitation field at the CQD location is known. For example, PL from a CQD with no non-radiative decay will only saturate when the excitation rate is comparable to the radiative relaxation rate, but saturation can occur at much lower powers for CQDs with a long-lived, non-radiative “trap state”. The emission rate in the power saturated regime is directly related to the maximum rate at which the CQD may emit photons. Both non-radiative recombination and maximum radiative emission rate are key figures of merit for single photon sources.

Our aim here is to understand the saturation behavior of cavity-coupled PbSe CQD emission into a SOI PIC, as it would affect the performance of an integrated single photon source. This power saturation behavior is presented in Chapter 4, and in this section and Chapter 3, the saturation behavior of a PbSe CQD emission coupled to a standalone SOI microcavity is presented and analyzed. The motivation to study the standalone cavity system is that it is significantly less complicated (relative to the full PIC) to account for the full dielectric environment in simulations, and there is no compelling reason to believe the core cause of power cavity-coupled PL in the two systems (full PIC vs standalone cavity) is different.

The motivation to study power saturation of cavity-coupled CQD PL is driven further by intriguing differences in the power dependence of cavity-coupled PbSe CQD emission relative to PbSe CQDs in a thin film formulation on bare silicon or SOI, wherein all factors (including dip-coating integration of CQDs and excitation with a HeNe laser) aside from the photonic environment are identical. What is observed, as exemplified in Figure 2.6, is that under these conditions the cavity-coupled PbSe CQD PL saturates faster than the uncoupled PL, and over the same power range the thin film CQD PL is unsaturated. Further, for thick film and solution CQD formulations, emission is linear over the same power range. En route to understanding the saturation of cavity-coupled PbSe CQD PL, may we self-consistently explain the saturation power differences?

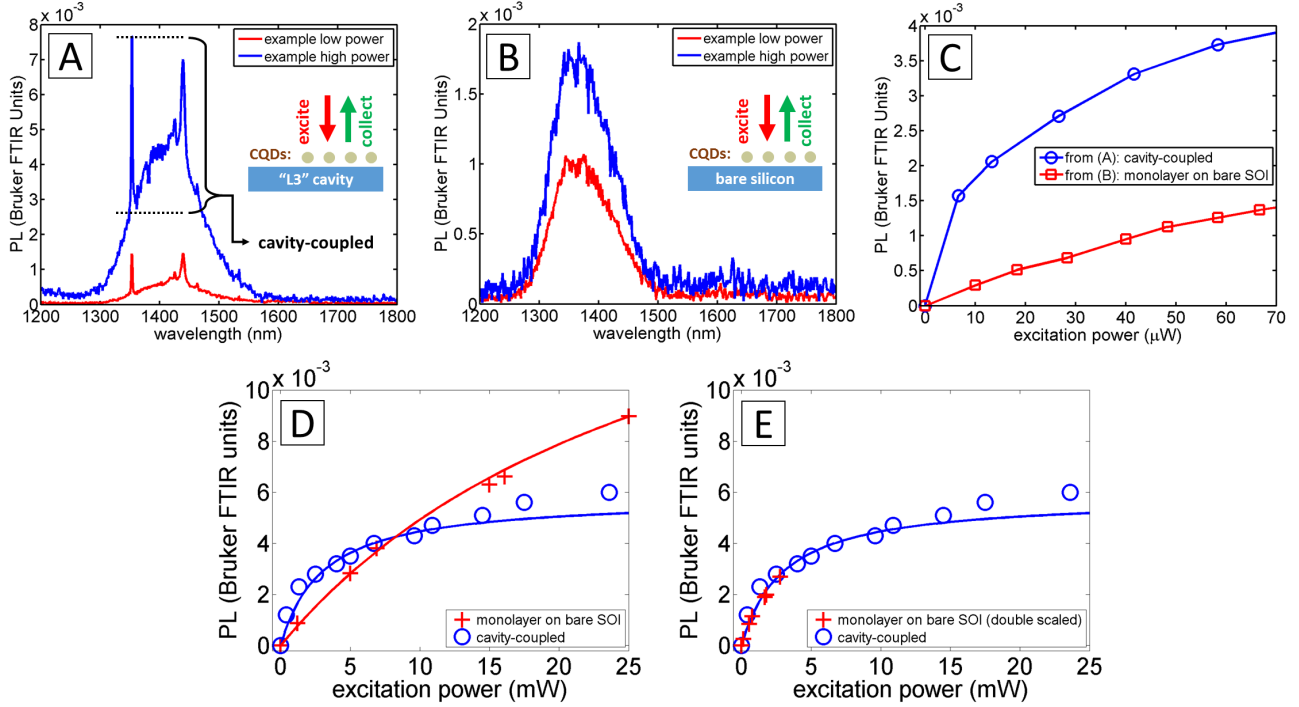


Figure 2.6: Comparison of power dependence of PbSe CQDs in thin formulations in different dielectric environments. (A): Example low and high excitation power PL spectra of CQDs on the surface of a SOI L3 optical microcavity, integrated by dip-coating, and labels indicating cavity-coupled and background contributions at a cavity mode wavelength. (B): Example low and high excitation power PL spectra of a thin film of PbSe CQDs on a bare silicon surface, also deposited by dip-coating, for the same excitation setup used for data in (A). (C): Power dependence comparison for cavity-coupled PL of (A) and monolayer PL of (B), for the same excitation conditions, showing how the power dependent PL of the monolayer is nearly linear but strongly saturated for the cavity-coupled PL. (D): Power dependence comparison for samples with Nd:YAG excitation and identical excitation/collection geometries, again exemplifying the difference in saturation powers. (E): Same as in (D), but the monolayer data scaled along the power axis by the excitation enhancement factor calculated in section 3.2 (a factor of 9) and scaled vertically to best match the cavity-coupled data fit. Note the good overlap, which can be interpreted with Chapter 3 modeling.

To improve understanding of the CQD PL power dependence, it is useful to reduce variation of as many system variables as possible. In order to do this, instead of indiscriminate integration of CQDs by dip-coating (as done in Figure 2.6), which results in an indeterminate coupling strength of CQDs to the cavity mode, we may site-selectively graft CQDs, using the AFM-assisted binding technique (Figure 2.3, reference [164]) to within just the main antinode of the L3 fundamental cavity mode, indicated by the 200 nm square patch in Figure 2.7A. Site-selective grafting of the CQDs to only the 200 nm square patch also reduces variation of the excitation laser field over the CQD region, relative to indiscriminate integration of CQDs.

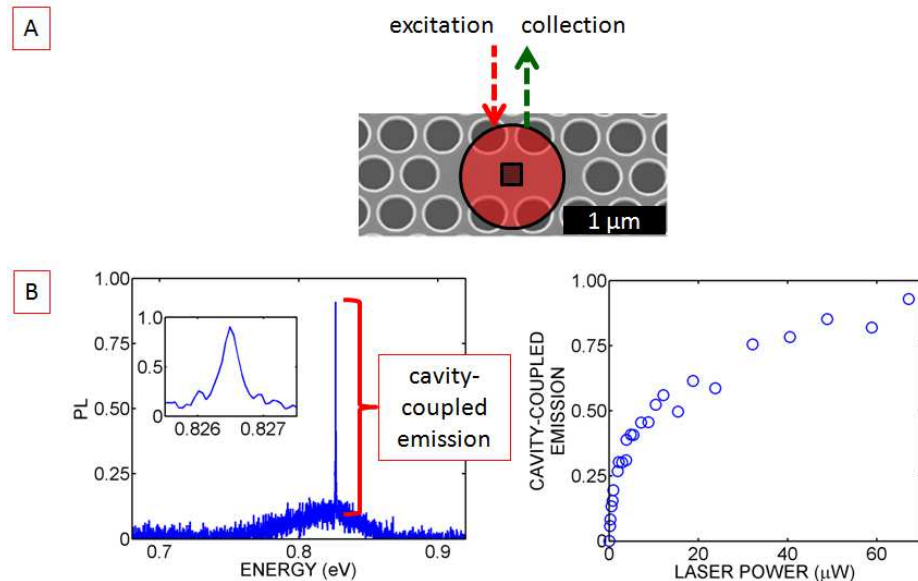


Figure 2.7: Experimental setup and resulting data modeled in this article. (A): Schematic of excitation/collection geometry: excitation (at 633 nm) and collection performed with a common 100X microscope objective. Red-filled circle indicates $1/e$ excitation spot intensity. Shaded square indicates span of grafted PbSe CQDs. (B): Example PL spectrum with cavity-coupled emission indicated, and cavity-coupled PL versus pump power.

Sample fabrication, AFM-assisted binding of the CQDs, and measure-

ments of the power-dependent PL of this sample was performed by Haijun Qiao, and the modeling thereof by the author of this dissertation in Section 3.2 of Chapter 3. Power dependent studies of silicon cavity-coupled PbX CQD PL have been performed before (e.g. [33, 175], but modeling is crucial for understanding the behavior, as it involves balance of several key factors, such as depolarization at the CQD surface, non-trivial photonic density of states available to the CQD, and an unknown contribution of non-radiative decay, the last of these not considered a free parameter in any modeling prior to the work in this dissertation.

The center of the stand-alone cavities was excited at normal incidence with continuous wave 633 nm HeNe laser light polarized in the \hat{y} -direction, using a 100X microscope objective that also collected light scattered normal to the sample surface. The $1/e^2$ intensity diameter was $2.0\ \mu\text{m}$ on the cavity surface, and the excitation power was varied by attenuation with various neutral density filters. Measurements were performed with the sample in vacuum, in the Janis ST-500 cryostat. An example spectrum, along with a plot of the power-dependent cavity-coupled PL that is modeled in detail in the following chapter, are shown in Figure 2.7B.

2.5 Time-resolved decay of CQDs in various formulations

In modeling the power saturation (measurements described in the previous section), information about non-radiative recombination was treated as a free parameter and extracted by consideration of the balance between excitation and relaxation as required to reproduce the observed saturation power. Alternatively, information about the non-radiative recombination may be obtained by combining the total PL decay time with knowledge of the radiative decay rate alone. This section describes measurements of the total PL decay times for CQDs in various formulations, which are combined with model simulation results of the corresponding radiative decay rates to determine relative radiative and non-radiative contributions for thin and thick film formulations.

Samples in each of solution, thin film and thick film formulations were prepared by the author of this dissertation, and the time-resolved decay curves were measured by Rafael Quintero-Torres (as published in [173]). The experimental setup consisted of the head-on pulsed laser excitation setup described in Subsection 2.3.3, and the resultant curves (normalized at zero time delay) are shown in Figure 2.8. Insets show corresponding spectra, normalized and vertically offset.

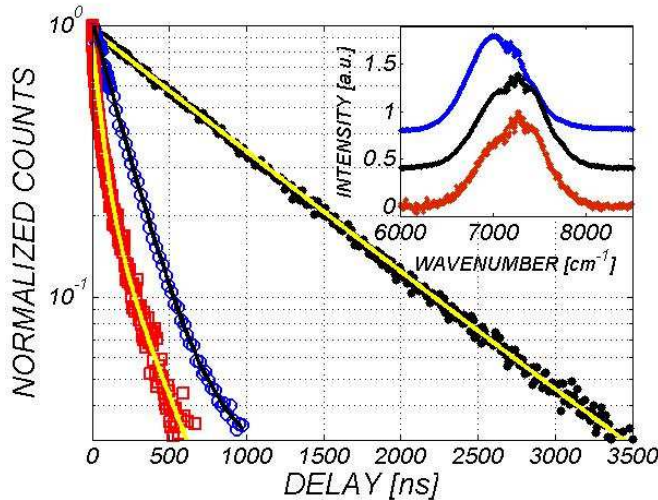


Figure 2.8: Time-dependent PL at 300 K for PbSe CQDs dispersed in hexanes (black dots); drop-cast film (blue circles); and sub-monolayer (red squares). The inset shows the steady state PL spectra from drop-cast (top, blue), solution (middle, black), and sub-monolayer dispersions (bottom, red) of the same batch of CQDs. The monolayer was excited with 3000 times more average power than the drop-cast film.

The steady-state, drop-casted integrated PL was 3000 times larger than sub-monolayer PL, and the solution PL in between those two. The red shift of the peak PL wavelength for the drop-casted film, relative to the solution and sub-monolayer spectra, arises from exciton diffusion from higher energy CQDs to lower energy CQDs; no such exciton diffusion exists for the latter two. Thorough measurements and modeling of exciton diffusion, mediated

by Förster energy transfer, of the drop-casted films were studied in our laboratory separately from the work contained in this dissertation [174].

While the decay of CQDs in solution can be well-described by a single decay constant, it is clear more than one decay constant is required to adequately fit the decay for thin and thick film formulations. Thus, for those latter two formulations, two decay constants (one short, one long) were extracted for each curve by fitting the time-resolved intensity to the $I(t) = A_1 \exp(-t/\tau_1) + A_2 \exp(-t/\tau_2)$. These fit curves are plotted with the raw data in Figure 2.8.

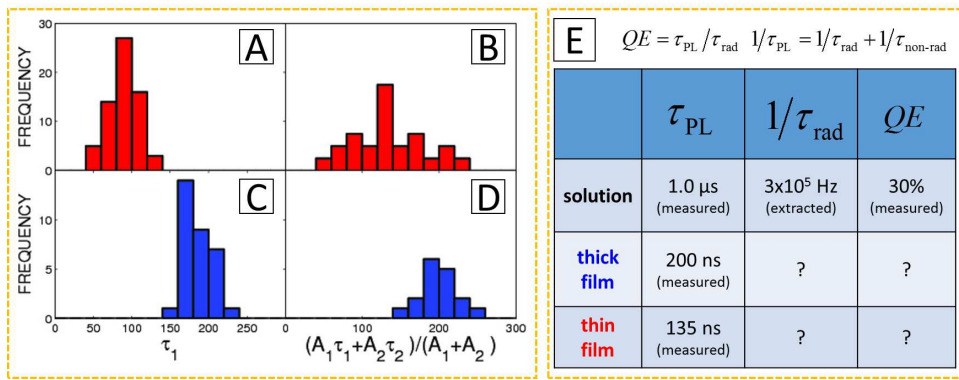


Figure 2.9: Histograms of the shortest time constants, τ_1 (left, (A) and (C)), and the average time constants $\frac{A_1\tau_1+A_2\tau_2}{A_1+A_2}$ (right, (B) and (D)) components of the measured lifetimes extracted from two-exponential fits to decay curves taken from various locations on the drop-cast samples (bottom, (C) and (D)), and the dip-coated samples (top, (A) and (B)). The mean values are (A) 90 ns, (B) 135 ns, (C) 190 ns, (D) 200 ns. (E): Tabular summary of known and unknown radiative and non-radiative decay parameters, after measurements indicated in this section but before modeling of the photonic density of states performed in Chapter 3.

Histograms of the shortest time constant extracted for each of the thin and thick films, τ_1 , are presented on the left hand side ((A) and (C)) Figure 2.9. A weighted average of the two extracted time constants (better representative of the overall PL decay time than either of the two time con-

stants extracted) for these formulations is presented on the right hand side (subfigures (B) and (D)). Clearly the thin film formulation decays fastest, and solution formulation slowest. The ~ 135 ns decay time of the thin film formulation is similar to some previous values reported for thin films (e.g. [32]).

The absolute quantum efficiency (QE) of the CQDs in solution formulation was reported by our collaborators to be 30%. With this absolute quantum efficiency and the measured total PL decay time, the radiative contribution to the total decay time was extracted and found to be $1/\tau_{\text{rad}} = 3 \times 10^5$ Hz. How much non-radiative recombination and radiative recombination each contribute to the total decay time for thin and thick films is determined by modeling, as described in the following chapter, the change in rate of radiative recombination going from solution formulation to the thin and thick film formulations.

2.6 Air exposure influence on CQD thick film temperature-dependent PL

Early photostability studies in reference [207] showed the integrated PL of PbSe CQDs thick films at room temperature can recover from air exposure, once returned to a vacuum environment. The temperature-dependence of PbSe CQD thick film PL in reference [172] from our group provided a convincing quantitative understanding of exciton diffusion and kinetics in this formulation, and consistent with the literature, namely a monotonic, Arrhenius-like decay of the integrated PL with increasing temperature from 5 K to 295 K, described by a single non-radiative pathway with activation energy of ~ 20 meV.

Not addressed by those studies, but a natural extension of them, is the air exposure dependence of the temperature-dependent PbSe CQD thick film PL, which could provide further insight into exciton dynamics. For example, if air exposure at lower temperatures is also recoverable, and what non-radiative pathways (if any) are introduced by exposure to air. The aim to pursue this understanding was further motivated by the work in refer-

Key	Description (air exposure extent and originating publication)
C_1	No air exposure as drop-cast, some during CQD synthesis, <i>Qiao et al.</i> [172]
C_2	No air exposure as drop-cast, some during CQD synthesis, <i>Qiao et al.</i> [172] Distinct drop-cast from C_1 .
D_1	No air exposure as drop-cast, some during CQD synthesis. Same CQD drop-cast sample as traces D_2 and D_3 .
D_2	30 minutes exposure as drop-cast, some during CQD synthesis, measured after 2 hours in vacuum
D_3	2 hours exposure as drop-cast, some during CQD synthesis, measured after 48 hours in vacuum

Table 2.1: PbSe CQD thick film sample descriptions, for integrated PL traces plotted in Figure 2.10.

ence [43, 93], in which air exposure dependence was carefully controlled at both CQD synthesis and post-formulation stages of temperature-dependent PbSe CQD thick film PL. In those studies the thick film PL took on behavior markedly different than previous studies, i.e. exhibiting non-monotonic temperature dependence.

Temperature control was achieved by cooling the cryostat cold finger to liquid helium temperatures then locally heating the cold finger using a feedback-enabled temperature controller. Finite time to achieve temperature stability of the cold finger and sample (as indicated by stability of measured temperature and observed PL spectrum) restricted temperature ramping to ~ 1 K per minute, or ~ 300 minutes (5 hours). These results were consistent with using this 1 K per minute ramp at low temperatures, where temperature dependence of the PL is greatest, combined with a slightly faster (several K per minute) ramp at higher temperatures. Cooling down directly to liquid helium temperatures could be performed much faster, on the order of 10 minutes. Prior to starting each measurement, the sample was pumped down for at least 30 minutes with an aforementioned turbo pump, to the 10^{-6} millibar range.

Table 2.1 summarizes the temperature-dependent, integrated PL for samples from our group (e.g. as partially published in [172] and from the new temperature-dependent integrated PL curves for different air exposures,

measured for this dissertation. Thick films were formulated as described in Section 2.2. Figure 2.10 contains plots of this data. The markedly different integrated PL behavior reported in [43] and [93] are presented in the corresponding modeling and discussion sections in Chapter 3.

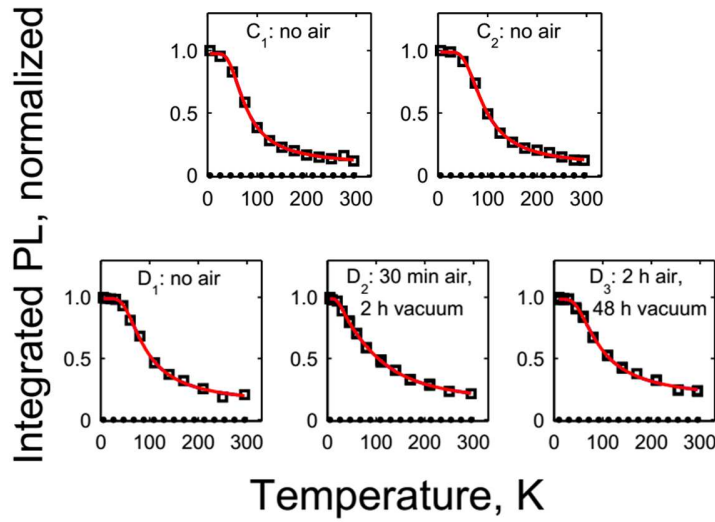


Figure 2.10: Integrated PL data sets (black squares), normalized to their maximum values, along with best-fit model yield curves (calculated below) in solid red and corresponding model PL contributions from each of two possible emissive states or clusters of emissive states in dotted and dashed lines, respectively. Modeling is described in Chapter 3. Table 2.1 contains descriptions of the samples.

Air exposure effect measurements presented in traces D_1 through D_3 were collected as follows: after measuring trace D_1 , the sample was exposed to air for a duration of 2 hours, in the dark. After this time, the sample chamber was pumped down again with the turbo pump for about 30 minutes, followed by quick cooling down to liquid helium temperatures and subsequent measurement of trace D_2 . After measurement of trace D_2 , the sample was exposed to air, in the dark, for 48 hours. After those 48 hours, the sample chamber was again put under vacuum, the sample cooled, and

then trace D_3 was measured. Section 3.4 contains the results of applying a physically-based kinetic model that captures the essential behavior of integrated PL data from all samples listed in Table 2.1 and the samples from references [43] and [93].

Chapter 3

Modeling

Experimental results of Chapter 2 are modeled in this chapter, in the same order as presented there.

3.1 Overview of model

Several key issues pervade modeling the emission of photoexcited PbSe CQDs: (a) upon excitation, a PbX CQD will quickly (on the order of picoseconds) relax to the lowest energy excitonic state, (b) this lowest energy excitonic state is really a manifold of multiple (many for PbX) electron-hole states with various associated transition dipole moments, (c) as supported by previous modeling of temperature dependent luminescence spectra from PbSe, the excitons in the ground state manifold are assumed to thermalize within their relatively long lifetimes, and (d) evidence points to significant non-radiative exciton recombination for CQDs in some environments, particularly out of solution. A sketch of these basic PbX CQD model elements is shown in Figure 3.1.

The aim of self-consistently modeling the data of Chapter 2 across CQD formulations and synthesis methods is to elucidate the exciton dynamics and radiative coupling in diverse environments. This chapter describes a kinetic model used to quantitatively determine radiative and non-radiative decay rates of primarily PbSe excitons in various CQD formulations. To

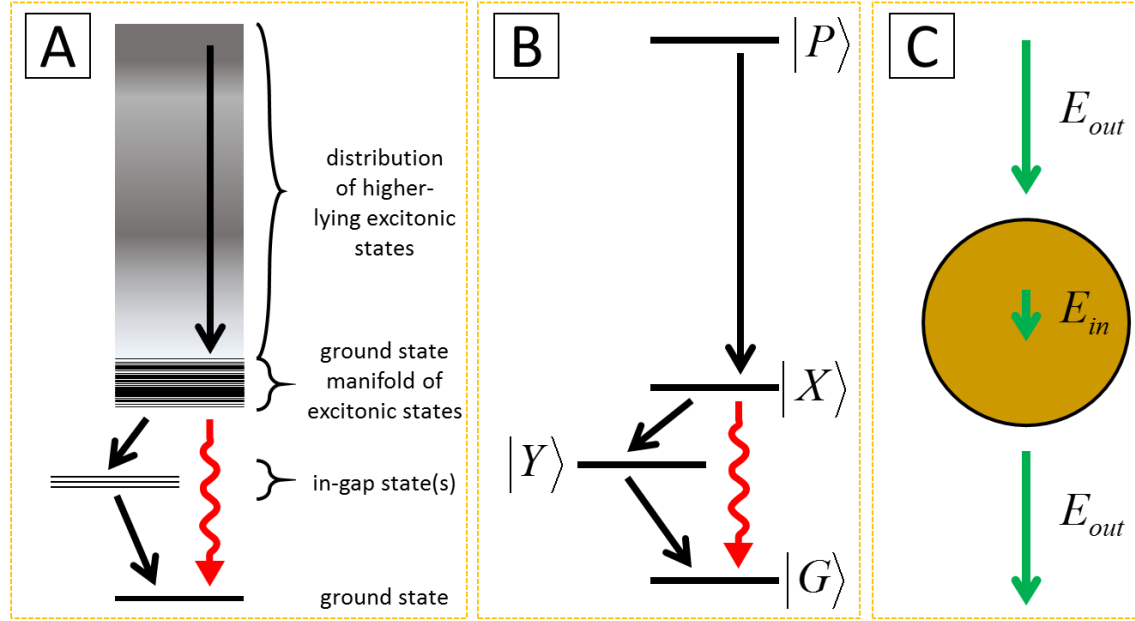


Figure 3.1: Overview of general considerations for modeling PbX CQD emission in nanophotonic environments. (A): Excitonic states are numerous and the distribution of transition dipole moment magnitudes is varied across a number of computational studies. (B): Simplified excitonic state structure, for which rapid decay from higher-lying state(s) $|P\rangle$ to a ground state excitonic manifold is understood $|X\rangle$, but the decay from the ground state excitonic manifold $|X\rangle$ to the CQD ground state $|G\rangle$ is generally environment dependent. (C): Example depolarization effect on the electric field for a dielectric sphere, one environmental contribution to exciton decay dynamics.

augment this kinetic modeling, it was necessary to also develop a method for taking into account the significant effects of depolarization, or local fields, on the radiative coupling of the excitons in these high-dielectric host materials embedded in relatively low dielectric solvents or vacuum.

The order of modeling efforts in this chapter are chronological, reflecting the fact that the successful first modeling of the cavity-coupled PL saturation underscored the importance of better understanding the non-radiative

pathways in PbSe CQD emission. This actually motivated the additional experimental and modeling work described in Chapters 2 and 3.

3.1.1 Exciton thermalization in the ground state manifold

Independent models [43, 93, 172] have been developed to quantify various aspects of the published PbSe CQD exciton kinetics. However, we are unaware of any account of a systematic attempt to fit the entirety of this disparate PbSe nanocrystal temperature-dependent integrated PL data from 5K to 300K using a single, physically-based model. Our model is as follows.

Various band structure calculations suggest that the 64-fold degenerate excitonic ground state of bulk PbSe is spread into a manifold of excitonic states in small (3 to 5 nm diameter) CQDs, with total electron and hole wavefunctions having predominantly S (spherical) symmetry [12]. Intervalley coupling splits the states over an energy range of tens of meV, while electron-hole exchange splitting further lifts the degeneracies by a smaller amount, on order of a few meV [12]. Of these 64 states, only a few have significant oscillator strength. Assuming that the excitons thermalize to a Fermi-Dirac distribution [181] within the ground state exciton manifold at all temperatures, the steady-state, spectrally integrated PL emission rate can be expressed as:

$$g_r = \int_{\epsilon_{min}}^{\epsilon_{max}} \frac{\gamma_r(\epsilon)f(\epsilon)}{e^{(\epsilon-\mu)/k_B T} + 1} d\epsilon, \quad (3.1)$$

where $f(\epsilon)$ is a sum of 64 delta functions defining the energies of the exciton states within the ground state exciton manifold, spanned by ϵ_{min} and ϵ_{max} , $\gamma_r(\epsilon)$ is the radiative decay rate distribution of the states within the manifold, and the remaining part of the integrand is the Fermi-Dirac occupation factor. Assuming weak (linear), non-resonant optical excitation into the high-lying quasi-continuum of the CQD absorption spectrum, and rapid decay to the ground state manifold at a rate g_{ex} , the steady-state

quasi-chemical potential μ of the excitons is determined by solving:

$$g_{ex} = \int_{\epsilon_{min}}^{\epsilon_{max}} \frac{[\gamma_r(\epsilon) + \Gamma_{nr}(\epsilon, T)] f(\epsilon)}{e^{(\epsilon - \mu)/k_B T} + 1} d\epsilon \quad (3.2)$$

for μ at each T , assuming the other parameters are fixed. Here $\Gamma_{nr}(\epsilon, T)$ is the distribution of non-radiative recombination rates for different exciton states in the ground state manifold, which can be temperature dependent.

3.1.2 Depolarization, spontaneous emission rates

Depolarization effects typically do not play an important role in III-V based quantum electrodynamic modeling of InAs QDs as there is negligible dielectric contrast between the InAs QDs and the surrounding host material. However, depolarization effects *must* be included in similar modeling of PbSe CQDs, as absorption and emission properties are typically measured in dilute solutions or in vacuum, on the surface of bulk silicon or a silicon photonic crystal in our experiments, where the dielectric contrast of the CQD and surrounding environment is large.

When a dipole is surrounded by a thin shell of high dielectric PbSe, the Maxwell equations dictate that the dipole field scatters from the interface between the PbSe and the solvent, which significantly modifies the field at the location of the dipole, and thus the radiated power. For very small spheres much less than the wavelength, the reduction of the field at the dipole location is essentially given by the “static” result for the depolarization of the field internal \mathbf{E}_{in} to a small sphere compared to the external field $\mathbf{E}_{in} = 3\mathbf{E}_{ext}/|2 + \epsilon_{PbSe}/\epsilon_{solvent}|$. Note that the dielectric constants that enter this Lorentz depolarization factor expression are evaluated at the frequency of the oscillating dipole.

For the values $\epsilon_{PbSe} = 23.0$ and $\epsilon_{solvent} = 2.1$ evaluated at the wavelength of $1.55 \mu\text{m}$, the depolarization factor is 0.23, and quantities quadratic in the local electric field - such as radiated power, to be discussed more below - can be reduced to a factor of $0.23^2 = 0.05$, exemplifying depolarization influence of two orders of magnitude. The practical relevance and impor-

tance of including depolarization effects [20, 45, 186] when quantitatively comparing various CQD optical properties has been nicely demonstrated in (1) relating PbSe CQD threshold absorption coefficients and oscillator strengths to radiative decay rates, in an analysis by Moreels *et al.* [142], and (2) in modeling short-wavelength, continuum PbSe CQDs absorption characteristics, particularly accounting for absorption coefficient differences of PbSe and PbSe/CdSe core/shell CQDs in terms of dielectric depolarization effects alone, in an analysis by De Geyter *et al.* [77]. The Lorentz local field factor was also found adequate in local-field modeling of emission lifetimes of CdSe/ZnS CQDs on various dielectric substrates [235].

The approach we take to account for depolarization effects on the radiative decay rates in our target dielectric environments (e.g. thick film, thin film, L3 cavity with thin film) is based on the fact that the ratio of radiative spontaneous emission rates ($\gamma_{XG,0}$ and $\gamma_{XG,\epsilon(\mathbf{r})}$) of a point-like two level system in two distinct dielectric environments is equal to the ratio of powers radiated ($P_{\text{rad},0}$ and $P_{\text{rad},\epsilon(\mathbf{r})}$) by a classical point dipole driven at the resonant frequency of the two level system in those two distinct dielectric environments (e.g. see references [20, 45, 151, 186, 201] for related derivations and discussions):

$$\frac{\gamma_{XG,\epsilon(\mathbf{r})}}{\gamma_{XG,0}} = \frac{P_{\text{rad},\epsilon(\mathbf{r})}}{P_{\text{rad},0}} \quad (3.3)$$

where the background dielectric environment is described by the (real) permittivity $\epsilon(\mathbf{r})$. In cases where the dipole emitter orientation is not fixed, three separate calculations are performed for dipole sources of orientation \hat{x} , \hat{y} , or \hat{z} , and then averaged appropriately. A major benefit of this approach is that it can be used to relate firm results from simple dielectric environments (e.g. single CQD in uniform solvent) to complicated environments - i.e. a CQD in a photonic crystal cavity - for which less data and no closed-form theoretical results exist. This radiated power approach was used in conjunction with finite difference time domain software from Lumerical Solutions Inc., chosen because it can produce accurate field distributions (as verified by numerous benchmarks), for both simple CQD environments and

richer nanophotonic environments (e.g. photonic crystal cavities).

To validate the use of the FDTD field solver to determine the power radiated by point dipoles in nanoscale dielectric environments, consider two scenarios: (a) the power radiated by a classical dipole at the center of a 5 nm diameter sphere of PbSe of a dielectric constant of ϵ_{PbSe} , embedded in a background solvent with dielectric constant $\epsilon_{\text{solvent}}$, and (b) the power radiated by the same dipole in a uniform solvent without the PbSe casing. The power radiated by a source of driving current density \mathbf{j} is $P = -\int d\mathbf{r} \mathbf{j}(\mathbf{r})^* \cdot \mathbf{E}(\mathbf{r})$, where $\mathbf{E}(\mathbf{r})$ is the total electric field. For a point dipole source at location \mathbf{r}_d , of moment \mathbf{p} , and driving at frequency ω (i.e. current density $\mathbf{j}(\mathbf{r}) = -i\omega\mathbf{p}\delta(\mathbf{r} - \mathbf{r}_d)$), the power radiated by the dipole is:

$$\langle P \rangle = \frac{\omega}{2} \text{Im}[\mathbf{p}^* \cdot \mathbf{E}(\mathbf{r}_d)] \quad (3.4)$$

and for the dipole in a uniform dielectric $\epsilon_{\text{solvent}}$, the result is:

$$\langle P \rangle = \frac{\omega^4 |\mathbf{p}|^2}{3\pi\epsilon_{\text{solvent}}c^3} \quad (3.5)$$

Applying the Lorentz field factor result to Equation 3.3, the power radiated from the dipole within the 5 nm PbSe dielectric sphere is:

$$\langle P \rangle = \frac{\omega^4 |\mathbf{p}|^2}{3\pi\epsilon_{\text{solvent}}c^3} \left| \frac{3}{2 + \epsilon_{\text{PbSe}}/\epsilon_{\text{solvent}}} \right|^2 \quad (3.6)$$

In FDTD simulations, the dipole source is defined as a “soft source”, meaning the electric field at the location of the source is a superposition of a driving, fixed electric field and a contribution from electric fields arising from interaction of the driving field with the dielectric environment (i.e. the total electric field). The driving electric field consisted of a finite pulse of Gaussian time envelope and known explicit time dependence. A “conformal” mesh, handled by the FDTD solver, was chosen for the majority of the simulation volume, with a finer mesh (fractions of a nm) override in the vicinity of the dielectric sphere (tested down to 4 nm diameter).

Absolute accuracy of better than 5% and convergence with simulation

settings to within 5% were achieved for both (1) the radiated power equation and (2) Lorentz factor closed-form example equations above (note that the local electric field needed to be averaged over several grid points). Convergence of the radiated power and local electric field each to a single value (within the 5% state FDTD solver accuracy) with incrementation of the following simulation parameters was achieved for both test and model dielectric environments: (a) computational simulation volume, (b) mesh step/discretization, and (c) location of power monitors. Values of these simulation parameters found adequate to achieve the converged powers and electric fields were (a) a $3 \mu\text{m}$ cube centered upon the test dipole, (b) 0.25 nm in the vicinity of the test dipole, and (c) along the surfaces of a one μm cube centered around the test dipole.

This approach was then used in the more complex dielectric environments encountered in the different experimental conditions described in Chapter 2, as summarized below.

3.1.3 Intrinsic dipole moment

The fact the emission rate modification of both a quantum transition dipole moment (between two states $|G\rangle$ and $|X\rangle$ separated by energy $\hbar\omega$) and a classical dipole emitter radiating at frequency ω may be accounted for with the same classical electromagnetic computation, for arbitrary dielectric environments, motivated our definition and extraction of an “intrinsic,” free-space dipole transition moment for the emissive exciton transition, $|\boldsymbol{\mu}_{XG,0}|$, independent of the variety of environments considered in this dissertation. In taking this approach, we firstly calculated the intrinsic dipole using the well-established in-solution emission data and basic application of the radiated power method and (as justified above) Lorentz field factor. We then considered this intrinsic dipole to be located within model dielectric environments (e.g. thick film, thin film, etc.), and the FDTD simulations were used to evaluate the electric field at the dipole, which included all depolarization factors with computational exactitude.

The intrinsic, free-space dipole moment $|\boldsymbol{\mu}_{XG,0}|$ of the $|X\rangle \leftrightarrow |G\rangle$ tran-

sition was extracted with reference to the reliably-measured and modeled spontaneous emission rates of a dilute solution of ~ 5 nm diameter PbX CQDs in solvent. In this environment, the radiative lifetime was taken to be $\gamma_{XG,CQD+sol}^{-1} = 3^{+1}_{-1} \mu\text{s}$, consistent with many photoluminescence lifetime and quantum efficiency reports of approximately 1 to 2 μs and several to many tens of percent, respectively. Relating this to $|\boldsymbol{\mu}_{XG,0}|$ was achieved by firstly relating $|\boldsymbol{\mu}_{XG,0}|$ to the free-space spontaneous emission rate $\gamma_{XG,0}$ via Fermi's Golden Rule, then relating $\gamma_{XG,CQD+sol}$ to $\gamma_{XG,0}$ with aid of the Lorentz field factor. In this approach, we obtained:

$$\gamma_{XG,CQD+sol} = \sqrt{\epsilon_{\text{sol}}} \left| \frac{3}{2 + \epsilon_{\text{CQD,nr}}(\omega_{XG})/\epsilon_{\text{sol}}} \right|^2 \gamma_{XG,0} \quad (3.7)$$

$$= \sqrt{\epsilon_{\text{sol}}} \left| \frac{3}{2 + \epsilon_{\text{CQD,nr}}(\omega_{XG})/\epsilon_{\text{sol}}} \right|^2 \frac{\omega_{XG}^3 |\boldsymbol{\mu}_{XG,0}|^2}{3\pi\epsilon_0\hbar c^3} \quad (3.8)$$

where $\epsilon_{\text{CQD,nr}}(\omega_{XG}) = (25.0^{+2.5}_{-2.5}) + (1^{+1}_{-1})i$ is the *non-resonant* CQD permittivity at ω_{XG} (i.e. excludes contribution from the $|X\rangle \leftrightarrow |G\rangle$ transition), which is based on calculations in [143], and $\epsilon_{\text{sol}} = 2.1^{+0.2}_{-0.2}$ is typical for a range of solvents in which PbSe CQDs are commonly dispersed.

The resulting values are $|\boldsymbol{\mu}_{XG,0}| = 7^{+3}_{-2}$ Debye and $\gamma_{XG,0} = 5^{+6}_{-2} \times 10^6$ Hz. The corresponding in-bulk PbSe spontaneous emission rate, for $n_{\text{bulk}} \approx 5$ and $\epsilon_{\text{CQD,nr}}(\omega_{XG})$ comparable to bulk PbSe permittivity at ω_{XG} [209], is $\gamma_{XG,\text{bulk}} \approx n_{\text{bulk}} \gamma_{XG,0} = 2^{+3}_{-1} \times 10^7$ Hz, which is 10 to 200 times slower than the typically 0.5 to 2 GHz spontaneous emission rates of epitaxial InAs QDs in bulk semiconductor hosts [54, 116, 161]. The “intrinsic” dipole transition moments of the PbSe excitons are therefore on order 3 to 7 times smaller than those of typical InAs QD excitons [29, 66, 197, 222].

3.2 Power saturation of cavity-coupled CQD PL

This section describes the full model used to analyze the saturation behavior of the PL from PbSe CQDs located at the antinode of an L3 photonic crystal microcavity, as described in Section 2.4. It includes a thorough treatment of the electromagnetic environment (including excitation source scattering,

local radiative density of states at PbSe CQD locations, and depolarization factors), and exciton dynamics within the CQD.

When comparing to related experiments using epitaxial InAs quantum dots in III-V host microcavities (e.g. [67, 68]), it is important to note (i) that, as discussed above, depolarization issues are not a factor in the III-V case, and (ii) the electronic/exciton dynamics at cryogenic temperatures in the III-Vs are much richer. In particular, for the epitaxial QD system, quantitative explanations of experimentally-measured emission spectra as a function of cavity-exciton detuning, and excitation power, require explicit treatment of acoustic phonon-scattering, rather than treating it phenomenologically, and do not require consideration of non-radiative recombination processes (e.g., see references [37, 91, 94, 123, 160, 182, 214, 231]). In contrast, room temperature experiments reported here involve solid-state formulations of colloidal PbSe CQDs with dephasing rates of tens of meV [85, 172], in excess of the cavity detuning, and quantum yields much less than unity [7, 63, 172, 207]. We find it necessary to explicitly include non-radiative decay processes to explain the saturation behavior, and a phenomenological treatment of phonon interactions is sufficient.

3.2.1 Master equation model

A simplified Hilbert space shown schematically in Figure 3.2 was used to model the observed saturation behavior. A single exciton state, $|X\rangle$, represents the low-energy, “brightest” component of the ground state manifold of excitonic states that is split by many factors in PbSe CQDs. This is the state responsible for exciting the cavity mode. Inclusion of more than 2 cavity mode Fock states did not change the calculated cavity photon population. A single higher-lying state, $|P\rangle$, resonantly absorbs energy from the HeNe excitation source and rapidly transfers it to the $|X\rangle$ state. In order to fit the observed saturation behavior, and to be consistent with the small quantum yield of exciton emission from monolayers of PbSe CQDs on silicon surfaces, a non-radiative decay channel via state $|Y\rangle$ was also included.

The model system Hamiltonian consists of the bare Hamiltonian, H_0 ,

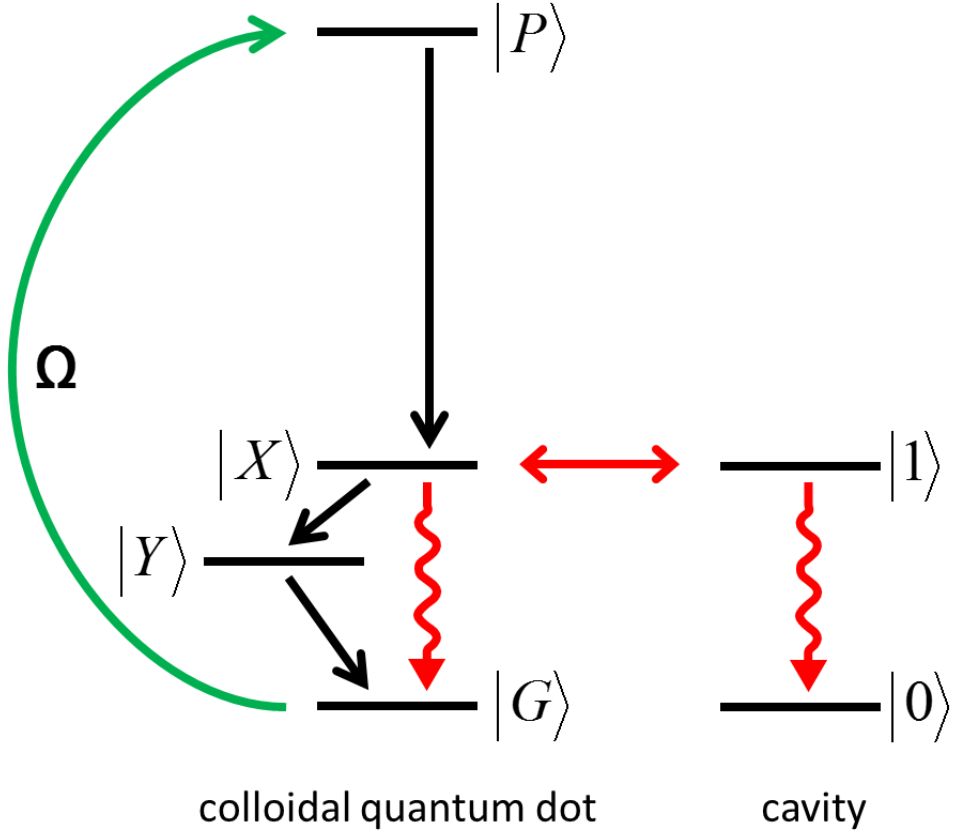


Figure 3.2: Minimal Hilbert space necessary to accommodate observed saturation behavior: four states (including trap state) for the CQD subspace and two for the cavity subspace. Significant decay paths indicated by solid blue arrows, of which squiggly lines are radiative and the remainder non-radiative. Laser field of Rabi coupling frequency Ω “pumps” the $|P\rangle$ state. The cavity is “fed” by coupling to the $|X\rangle \leftrightarrow |G\rangle$ transition with electric-dipole coupling strength g .

electric dipole coupling of the excitonic transition to the cavity field, H_{cav} , and a continuous wave laser field resonantly coupled to the higher energy electronic transition, H_{pump} :

$$H_0 = \sum_{\ell} \hbar\omega_{\ell} |\ell\rangle\langle\ell| + \hbar\omega_{\text{cav}} a^{\dagger}a \quad (3.9)$$

$$H_{\text{pump}} = \hbar\Omega (|P\rangle\langle G| + |G\rangle\langle P|) \cos(\omega_{\text{pump}}t) \quad (3.10)$$

$$H_{\text{cav}} = \hbar g (|X\rangle\langle G| + |G\rangle\langle X|) (a^{\dagger} + a) \quad (3.11)$$

$$H_S = H_0 + H_{\text{pump}} + H_{\text{cav}} \quad (3.12)$$

where ℓ indexes the CQD subspace, $\hbar\omega_{\ell}$ are CQD state energies, and a^{\dagger} is the creation operator in the cavity subspace. Products with subspace unit operators are implicit.

We calculated the steady state density matrix ρ with the Lindblad-form master equation, which allows explicit inclusion of the population decay (γ_{jk}) and pure dephasing (γ'_j) rates:

$$\begin{aligned} \frac{d\rho}{dt} = & \frac{i}{\hbar} [\rho, H_S] + \sum_{jk} \left[D_{jk} \rho D_{jk}^{\dagger} - \frac{1}{2} \left(D_{jk}^{\dagger} D_{jk} \rho + \rho D_{jk}^{\dagger} D_{jk} \right) \right] \\ & + \gamma_{\text{cav}} \left[a \rho a^{\dagger} - \frac{1}{2} \left(a^{\dagger} a \rho + \rho a^{\dagger} a \right) \right], \end{aligned} \quad (3.13)$$

$$D_{jk} = \sqrt{\gamma_{jk}} |k\rangle\langle j| \text{ quantum dot population decay, } |j\rangle \rightarrow |k\rangle \quad (3.14)$$

$$D_{jj} = \sqrt{\gamma'_j} |j\rangle\langle j| \text{ quantum dot pure dephasing} \quad (3.15)$$

To solve for the steady-state behavior, we first transformed these equations to a picture with no explicit time dependence in the rotating wave approximations for $\omega_{\text{cav}} \approx \omega_X - \omega_G = \omega_{XG}$ and $\omega_{\text{pump}} \approx \omega_P - \omega_G$. The collection of steady state density matrix element equations $d\rho/dt = 0$ was then cast into superoperator form, $\mathcal{L}\rho^v = 0$, in which the steady state density matrix elements are components of the eigenvector of the zero eigenvalue of the superoperator \mathcal{L} , and calculated via the inverse power method. From the steady state density matrix we calculated the cavity population $\langle a^{\dagger}a \rangle$,

which is proportional to the observed cavity intensity emission.

3.2.2 Model dielectric environment

The model dielectric environment of the CQDs in the saturation experiment is shown in Figure 3.3. The total permittivity, $\epsilon(\mathbf{r},\omega) = \epsilon_{L3}(\mathbf{r},\omega) + \epsilon_{CQDs}(\mathbf{r},\omega)$, consists of the silicon-host L3 photonic crystal cavity $\epsilon_{L3}(\mathbf{r},\omega)$ (with backing silicon) and a close-packed hexagonal array of 45 CQDs on the cavity surface $\epsilon_{CQDs}(\mathbf{r},\omega)$ with pitch varied from 6 nm to 8 nm. The CQD arrangement is based on electron microscope images of CQDs on silicon surfaces that exhibit short-range hexagonal order, packed with a pitch within the range adopted in our model. The intrinsic dipole was then considered to be located at the center of the centroidal CQD, at position \mathbf{r}_{CQD} . The L3 cavity slab has a thickness of 198^{+4}_{-4} nm, pitch of 420^{+4}_{-4} nm, air hole radius of 122^{+10}_{-10} nm, and the two holes on the \hat{x} -axis are shifted away from the cavity centroid by 10^{+4}_{-4} nm. The distance between the L3 cavity slab and backing silicon is 1193^{+10}_{-10} nm.

3.2.3 “Simple” model parameters

Before calculation of the intrinsic dipole moment and other depolarization-sensitive quantities, let us establish the many “simple” model parameters that are known already and are unaffected by depolarization specific to our dielectric environment.

The cavity mode frequency ω_{cav} was taken directly from the PL spectra, and for data fitting we set the exciton transition energy $\hbar\omega_{XG} = \hbar(\omega_X - \omega_G) = \hbar\omega_{cav}$. The pumped transition energy $\hbar(\omega_P - \omega_G)$ was set to the HeNe excitation photon energy, $\hbar\omega_{pump} = hc/633.0\text{nm}$, where h is Planck’s constant and c is speed of light in vacuum.

The measured cavity Q of 3×10^3 , along with ω_{cav} , sets $\gamma_{cav} = 7 \times 10^{10} \text{ Hz}$. CQD inclusion had negligible effect on the decay rate. The population decay time γ_{PX}^{-1} from $|P\rangle$ to $|X\rangle$ was taken to be 5 picoseconds, based on a variety of measured and calculated values [13, 18, 25, 86, 156]. Other significant decay parameters are described in the “fit parameter” subsection, below.

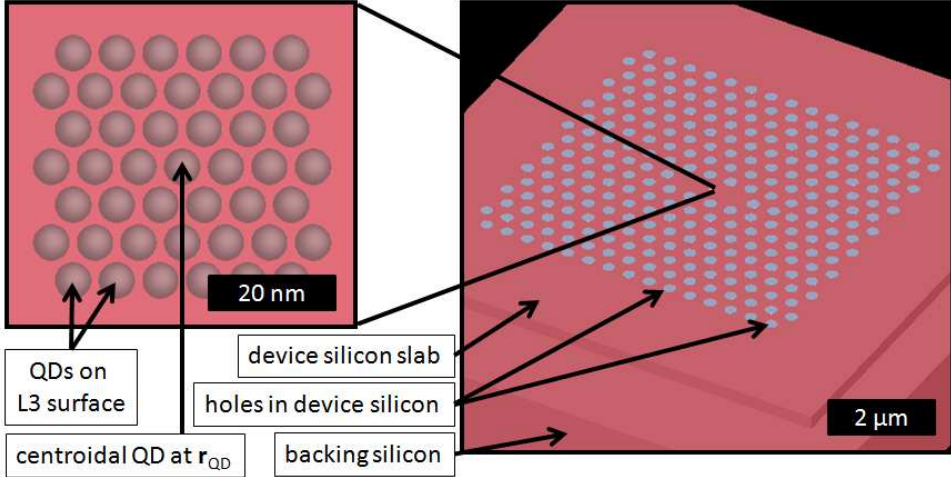


Figure 3.3: Model dielectric environment $\epsilon(\mathbf{r}, \omega) = \epsilon_{L3}(\mathbf{r}, \omega) + \epsilon_{CQDs}(\mathbf{r}, \omega)$. Nanocrystal array $\epsilon_{CQDs}(\mathbf{r}, \omega)$ on left, centered on the L3 cavity surface. The computational volume for FDTD calculations (see text) is restricted to the $3\text{ }\mu\text{m}$ cube centered about the centroidal CQD. The intrinsic “test” dipole is located at the center of centroidal CQD, position \mathbf{r}_{CQD} . The device silicon slab is surrounded by vacuum above and below, with backing silicon $1.2\text{ }\mu\text{m}$ below.

A pure dephasing rate of $\gamma'_X = 4.8 \times 10^{13}\text{ Hz}$ was taken from an analysis of PbSe thick film PL spectra [172]. The $|Y\rangle$ state pure dephasing was taken to be $\gamma'_Y = \gamma'_X$, but the exact value is neither known or consequential for our analysis. The ground state pure dephasing γ'_G was assumed negligible. For completeness (see “Laser-QD coupling Ω ” subsection), a value of $\gamma'_P = 10^{14}\text{ Hz}$ was used in the simulations reported here, although our modeling results are independent of γ'_P for a large range of γ'_P , owing to its large value.

3.2.4 Spontaneous emission rate $\gamma_{XG} = \gamma_{XG, \epsilon(\mathbf{r})}$

The spontaneous emission rate of an exciton associated with a CQD located within a hexagonally-packed array of CQDs on the L3 cavity surface (our $\epsilon(\mathbf{r})$ environment), into all electromagnetic modes except the cavity mode, $\gamma_{XG, \epsilon(\mathbf{r})}$, was calculated with the methods outlined in the previous section.

In doing so, we also (1) averaged $\gamma_{XG,\epsilon(\mathbf{r})}$ over all three dipole orientations, and (2) excluded the cavity mode contribution to $\gamma_{XG,\epsilon(\mathbf{r})}$, which is already accounted for in g , by considering only the power radiated at several cavity mode line widths above the cavity mode frequency (i.e. at $\omega_{\text{cav}} + \delta\omega$). The result is essentially independent of $\delta\omega$, and equals

$$\gamma_{XG} = \gamma_{XG,\epsilon(\mathbf{r})} \quad (3.16)$$

$$= \frac{\langle P_{\text{rad},\epsilon(\mathbf{r})}(\omega_{\text{cav}} + \delta\omega) \rangle_{\text{orientation}}}{P_{\text{rad},0}(\omega_{\text{cav}} + \delta\omega)} \gamma_{XG,0} \quad (3.17)$$

$$= 4^{+5}_{-2} \times 10^5 \text{ Hz} \quad (3.18)$$

Thus the spontaneous emission rate of excitons in this complex dielectric environment *coincidentally* turns out to be very similar to isolated CQDs in solution ($\gamma_{XG,\text{CQD+sol}}$). A decomposition of influences on the spontaneous emission rate is as follows: taking the CQDs out of solution and into air increases the dielectric contrast, resulting in a smaller spontaneous emission rate by a factor of 4 to 7 (depending on the originating solvent). In contrast, despite the presence of the photonic band gap, the L3 cavity - even excluding the cavity mode - increases an otherwise free-space spontaneous emission rate by a factor of ~ 4 , when averaged over three orthogonal dipole orientations. The spontaneous emission rate enhancement due to the L3 slab, excluding the cavity mode and CQD array, is presented in more detail in Figure 3.4. Such behavior at the surface of a uniform, hexagonal, silicon-host photonic crystal has been previously reported [112].

3.2.5 Cavity-QD coupling g

Given the intrinsic dipole transition moment, calculation of the cavity-QD coupling $g = \mu_{XG,0} \cdot \mathbf{E}_{\text{cav}}^{\text{vac}}(\mathbf{r}_{\text{CQD}})/\hbar$ was reduced to calculation of the cavity mode vacuum electric field at the CQD position, $\mathbf{E}_{\text{cav}}^{\text{vac}}(\mathbf{r}_{\text{CQD}})$. This too was calculated using FDTD Solutions, here by exciting the cavity mode in the full $\epsilon(\mathbf{r})$ dielectric environment, letting all electric fields except the cavity

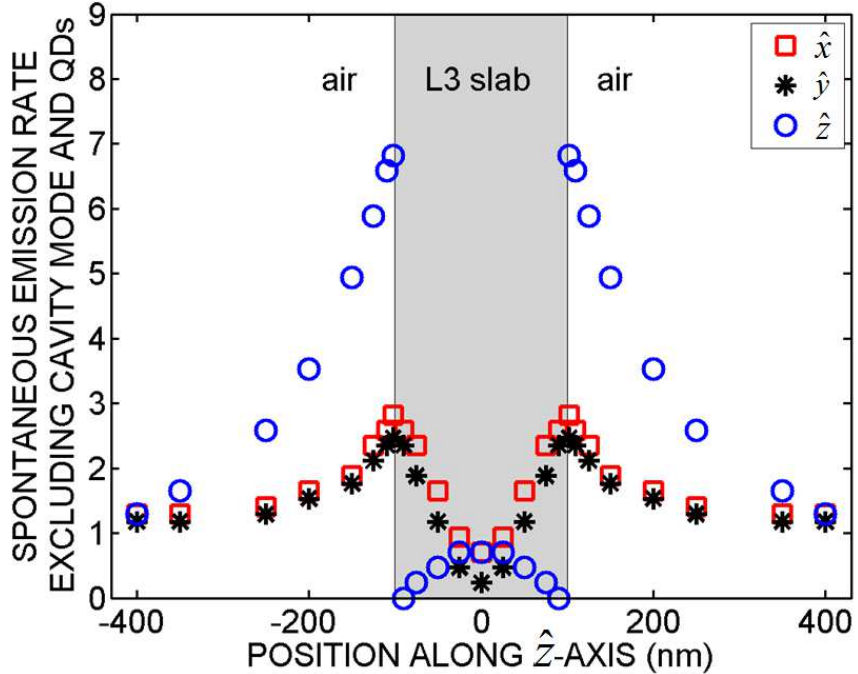


Figure 3.4: Spontaneous emission rate of a point dipole source of frequency $\omega_{\text{cav}} + \delta\omega$, for positions along the \hat{z} -axis of the L3 cavity, *excluding* the cavity mode and CQD array, for electric dipole orientations along axes \hat{x} , \hat{y} , or \hat{z} (see text and orientation definitions in Figure 2.1). All values normalized to the free-space spontaneous emission rate $\gamma_{XG,0}$.

mode field $\mathbf{E}_{\text{cav}}(\mathbf{r})$ decay entirely, then evaluating:

$$|\mathbf{E}_{\text{cav}}^{\text{vac}}(\mathbf{r}_{\text{CQD}})| = \sqrt{\frac{\hbar\omega_{\text{cav}}}{2\epsilon_0 \int d\mathbf{r} \epsilon(\mathbf{r}) \left(\frac{|\mathbf{E}_{\text{cav}}(\mathbf{r})|}{|\mathbf{E}_{\text{cav}}(\mathbf{r}_{\text{CQD}})|} \right)^2}} = 3_{-1}^{+1} \times 10^4 \text{ V/m}, \quad (3.19)$$

This expression is simply an application of the amplitude of the electric field operator for a photon, $E = (\hbar\omega/2\epsilon V)^{1/2}$. Integration was over the entire computational volume, and the value is consistent with the value from a corrected formula for non-Hermitian modes [118]. CQD inclusion has an

insignificant effect on the cavity mode volume. The cavity-CQD coupling strength is $g = 6_{-2}^{+4} \times 10^9$ Hz. The scattering rate into the cavity mode is $R_{\text{cav}} = g^2/\gamma'_X = 8_{-4}^{+13} \times 10^5$ Hz.

3.2.6 Laser-QD coupling Ω

Direct calculation of $\Omega = \boldsymbol{\mu}_{GP,0} \cdot \mathbf{E}_{\text{pump},\epsilon(\mathbf{r})}(\mathbf{r}_{\text{CQD}})/\hbar$ is impossible, as we know of no way to directly determine the laser-pumped dipole transition moment $\boldsymbol{\mu}_{GP,0}$ from experimental data. However, the saturation behavior of interest depends not on Ω alone, but instead on the absorption rate R of the CQD, related to Ω and the electric field intensity inside the CQD by

$$R \approx \frac{\Omega^2}{\gamma'_P} = \frac{|\boldsymbol{\mu}_{GP,0}|^2}{\hbar^2 \gamma'_P} |\mathbf{E}_{\text{pump}}(\mathbf{r}_{\text{CQD}})|^2 \quad (3.20)$$

Thus, as can be seen through this closed-form expression and as confirmed for our simulations, neither a specific value of Ω or γ'_P was necessary for simulating the saturation behavior. Instead, knowledge of the absorption rate R , particularly for a calculable laser field amplitude at the intrinsic dipole location, is adequate.

The in-solution absorption rate per CQD per incident electric field intensity at our pump wavelength of 633 nm was obtained from Moreels *et al.* [141] by way of their reported absorbance at 400 nm, $A_{400\text{nm}} = 1.246 \text{ cm}^{-1}$, of a known concentration $C_{\text{Q-PbSe}} = 0.32 \mu\text{M}$ of PbSe CQDs, and an absorption spectrum showing that the absorbance at 633 nm relative to the absorbance at 400 nm is $A_{633\text{nm}}/A_{400\text{nm}} \approx 0.2$. In terms of the laser field amplitude inside the CQD, $|\mathbf{E}_{\text{pump}}(\mathbf{r}_{\text{CQD}})|$, this absorption rate per CQD is

$$R = \frac{\frac{A_{400\text{nm}}}{C_{\text{Q-PbSe}}} \frac{A_{633\text{nm}}}{A_{400\text{nm}}}}{\hbar \omega_{\text{pump}}} \frac{\sqrt{\epsilon_{\text{sol}}}}{2\eta_0} \left| \frac{2 + \epsilon_{\text{CQD}}(\omega_{\text{pump}})/\epsilon_{\text{sol}}}{3} \right|^2 |\mathbf{E}_{\text{pump}}(\mathbf{r}_{\text{CQD}})|^2 \quad (3.21)$$

where η_0 is the electromagnetic wave impedance in free space (equal to in-air value within our uncertainties), and $\epsilon_{\text{CQD}}(\omega_{\text{pump}}) = (1+i)(25.0_{-2.5}^{+2.5})$ is the CQD permittivity evaluated at the pump HeNe wavelength.

To finalize application of these equations to our system, we needed to

relate the laser field amplitude inside the CQD for our full $\epsilon(\mathbf{r})$ dielectric environment, $|\mathbf{E}_{\text{pump},\epsilon(\mathbf{r})}(\mathbf{r}_{\text{CQD}})|$, to the measured power, P_0 , of our HeNe excitation source. This was accomplished by (1) FDTD simulations from which we extracted $|\mathbf{E}_{\text{pump},\epsilon(\mathbf{r})}(\mathbf{r}_{\text{CQD}})|/|\mathbf{E}_{\text{pump},0}|$, where $|\mathbf{E}_{\text{pump},0}|$ is the incident laser field amplitude, and (2) relating $|\mathbf{E}_{\text{pump},0}|$ to P_0 via the Gaussian beam profile and our measured minimum $1/e^2$ beam radius $W_0 = 1.0 \mu\text{m}$, $|\mathbf{E}_{\text{pump},0}|^2/2\eta_0 = 2P_0/\pi W_0^2$. Combining, we obtained:

$$\Omega = \sqrt{\gamma'_P R} \quad (3.22)$$

$$= \sqrt{\frac{2\sqrt{\epsilon_{\text{sol}}} \frac{A_{400\text{nm}}}{C_{\text{Q-PbSe}}} \frac{A_{633\text{nm}}}{A_{400\text{nm}}} \gamma'_P P_0}{\hbar\omega_{\text{pump}}\pi W_0^2}} \left| \frac{2 + \epsilon_{\text{CQD}}(\omega_{\text{pump}})/\epsilon_{\text{sol}}}{3} \right| \frac{|\mathbf{E}_{\text{pump},\epsilon(\mathbf{r})}(\mathbf{r}_{\text{CQD}})|}{|\mathbf{E}_{\text{pump},0}|}$$

$$= 3^{+1}_{-1} \times 10^5 \sqrt{\gamma'_P P_0} \quad (3.23)$$

for P_0 in Watts and γ'_P and Ω in Hz. The complex dielectric environment results in a highly structured HeNe scattered wave distribution, seen in Figure 3.5, necessitating computation. Within the estimated environment uncertainties, this wave distribution and the laser coupling Ω is insensitive to the photonic crystal air hole radius and the distance between the L3 slab and the backing silicon. Environment parameters bearing directly and significantly on the laser coupling g include the L3 slab thickness, photonic crystal pitch, and CQD array pitch, which account for approximately $\approx \pm 20\%$, $\approx \pm 5\%$, and $\approx \pm 15\%$ uncertainties in Ω , respectively.

3.2.7 Fit parameter

In previous subsections, we established the pump rate and rates for the two radiative decay paths, i.e. $|X\rangle \rightarrow |G\rangle$ and through the cavity. Of all the model parameters, the two not addressed in previous subsections are both associated with the *non-radiative* decay path, i.e. γ_{XY} and γ_{YG} . Neither of these are known for our particular CQDs beyond the modeling efforts here. However, the limit of $\gamma_{XY} \gg \gamma_{XG} + R_{\text{cav}}$ enables a unique determination of the non-radiative decay time $\tau_{\text{non-rad}} = \gamma_{YG}^{-1} + \gamma_{XY}^{-1}$ for a particular dielectric environment, and we chose this to be our sole fit parameter to characterize

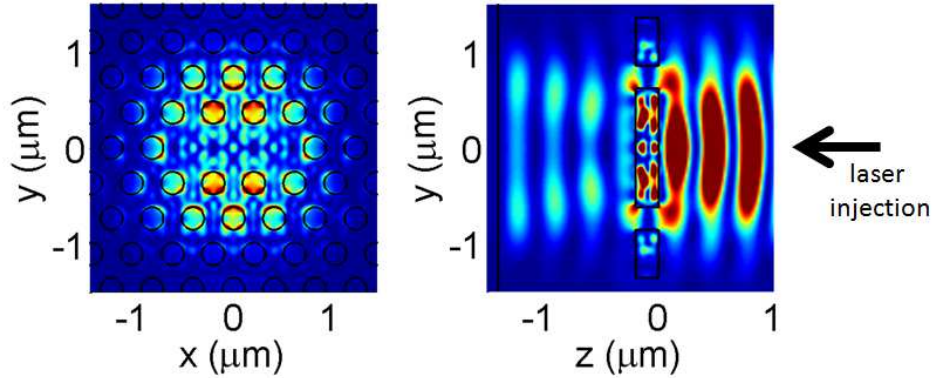


Figure 3.5: Intensity profiles of HeNe excitation field, as modulated by the L3 cavity $\epsilon_{L3}(\mathbf{r})$. Gaussian laser field was injected along the \hat{z} axis towards increasingly negative z , indicated by black arrow. Air-silicon interfaces lined in black. (left) Profile several nanometers above the slab surface, the plane containing the PbSe CQDs. (right) Profile in the $x = 0$ plane.

the non-radiative decay path (results next section). Drawing from $\gamma_{XG} = 4^{+5}_{-2} \times 10^5$ Hz and $R_{\text{cav}} = 8^{+13}_{-4} \times 10^5$ Hz as presented in previous subsections, the limit in which we extract $\tau_{\text{non-rad}}$ equates to $\gamma_{XY} \gg 1.2^{+1.8}_{-0.6} \times 10^6$ Hz.

This enabling limit is motivated by (1) measurements indicating low quantum yields of exciton emission from monolayers of PbSe CQDs on unpatterned SOI wafers, and (2) FDTD simulations indicating $R_{\text{cav}} + \gamma_{XG}$ calculated for our textured dielectric environment is not significantly larger than the spontaneous emission rate of CQDs in a monolayer on unpatterned SOI. These measurements consist of (1) published [172] thick-film integrated PL versus temperature in which the room-temperature PL is observed to be a factor of 10 lower than the low-temperature PL, thus establishing a maximum 10% quantum efficiency at room temperature, and (2) the PL lifetime measurements and modeling of non-radiative relaxation in monolayers of PbSe CQDs on unpatterned SOI wafers presented in this dissertation, shown to be several times faster than in thick films.

3.2.8 Saturation modeling results

Attempts to exclude the non-radiative decay path were unsuccessful in accommodating the observed cavity-coupled saturation behavior, as seen in Figure 3.6, in which the best (minimum χ^2) 3-state fits are inadequate. The best 3-state fits are presented for the smallest and largest saturation powers consistent with the model parameters. The smallest 3-state fit saturation power is still 5 times larger than the observed saturation power. The fourth state $|Y\rangle$ can, however, accommodate the lower observed saturation power if it possesses a sufficiently long lifetime, i.e. if it serves as a non-radiative “population-trapping” state, as seen in Figure 3.6, for which the 4-state fit is adequate. Consequently, minimally four CQD states are necessary to model our system.

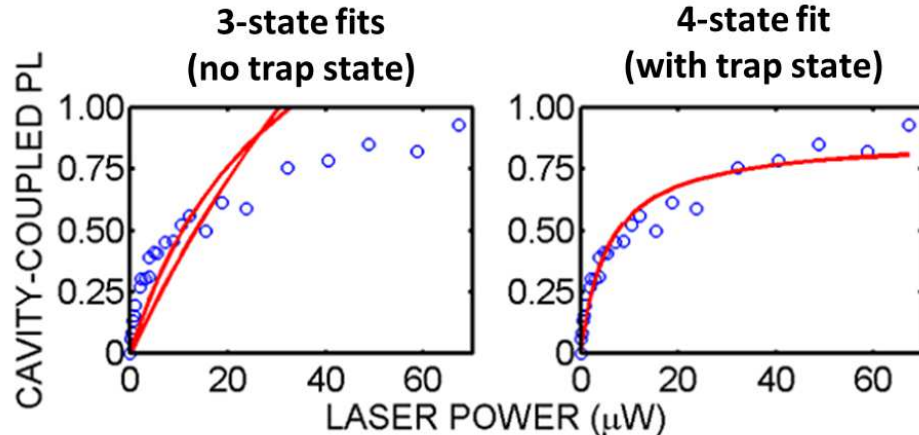


Figure 3.6: Best (minimum χ^2) fits to cavity-enhanced photoluminescence for only three electronic levels (left), i.e. without a non-radiative state, and for four electronic levels (right), i.e. including a non-radiative “trap” state.

Over our model parameter space, including all estimated uncertainties, we find the $\tau_{\text{non-rad}}$ values required for a 4-state fit are $\tau_{\text{non-rad}} \approx 3^{+3}_{-2} \mu\text{s}$. Further, because $\tau_{\text{non-rad}} = \gamma_{YG}^{-1} + \gamma_{XY}^{-1}$ and $\gamma_{XY} \gg 1.2^{+1.8}_{-0.6} \times 10^6 \text{ Hz}$, as established in the previous section, our fit parameter approximately coincides

with the trap state lifetime, $\tau_{\text{trap}} \equiv \gamma_{YG}^{-1}$. Thus the trap state lifetime consistent with our model parameters is $\tau_{\text{trap}} \approx 3^{+3}_{-2} \mu\text{s}$.

The span of τ_{trap} is dominated physically by (1) uncertainty in the CQD packing density, (2) uncertainty in the L3 slab thickness, and (3) stated uncertainty in the solvent permittivities. The first two of these three have a direct and significant bearing on the pump field inside the CQD, so for the purpose of graphically representing the influence of these factors on the trap state lifetime, it is convenient to define a plot parameter directly related to the pump field inside the CQD. We defined an effective depolarization parameter, DPF , that is equal to the pump field inside the CQD (for our full dielectric environment), normalized to the pump field in the CQD for an otherwise isolated CQD in free space, for a fixed pump power:

$$DPF = \frac{|\mathbf{E}_{\text{pump},\epsilon(\mathbf{r})}(\mathbf{r}_{\text{CQD}})|}{|\mathbf{E}_{\text{pump,QD}}(\mathbf{r}_{\text{CQD}})|} = \frac{|\mathbf{E}_{\text{pump},\epsilon(\mathbf{r})}(\mathbf{r}_{\text{CQD}})|}{|\mathbf{E}_{\text{pump},0}|} \left| \frac{3}{2 + \epsilon_{\text{CQD}}(\omega_{\text{pump}})} \right|^{-1} \quad (3.24)$$

Figure 3.7 contains the plot of τ_{trap} versus DPF . Variation of τ_{trap} with DPF is primarily due to uncertainty specific to our dielectric environment, e.g. relating to the photonic crystal cavity or CQD array, whereas variation of τ_{trap} for a fixed value of DPF is attributable primarily to the assumed uncertainty in the solvent permittivity that entered into our model through the estimated absorption rate R , and radiative lifetime $\gamma_{XG,\text{CQD+sol}}^{-1} = 3^{+1}_{-1} \mu\text{s}$, of the CQDs in solution.

The fact that the effective depolarization parameter is near unity reflects the fact that, despite the multitude of significant depolarization mechanisms (e.g. CQD array, SOI platform, L3 cavity), the laser field inside the CQD is comparable to the laser field inside the same CQD isolated in vacuum for the same pump intensity. *This is a coincidence of this particular dielectric environment*, and the contributing factors can be decomposed as follows: the SOI platform alone results in a decrease of the pump field in the CQD by a factor of ≈ 5 (relative to a free-space pump field), the L3 cavity texture increases the pump field by a factor of ≈ 3 (relative to a bare SOI substrate), and the surrounding CQD array increases the pump field inside the CQD by another factor of ≈ 1.4 ; compounding these results in a value of ≈ 0.8 for

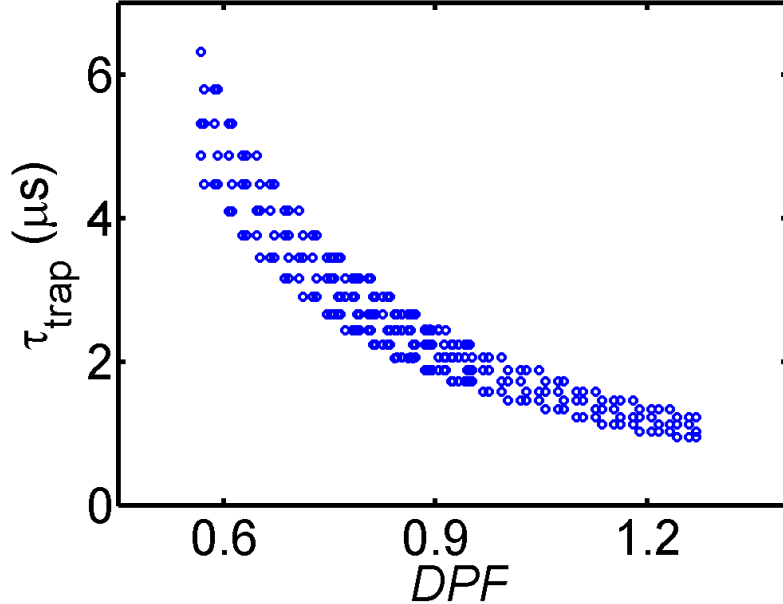


Figure 3.7: Trap state lifetime $\tau_{\text{trap}} = \gamma_{Y_G}^{-1}$ required to fit the data. Parametrization of τ_{trap} is in terms of the “effective depolarization”, DPF , which is defined in-text (see Equation 3.24) and is equal to the laser field inside the CQD in the full model dielectric environment relative to the laser field inside the same CQD in vacuum. Variation of τ_{trap} with DPF is dominated by uncertainties in parameters specific to our dielectric environment (photonic crystal cavity, CQD array), whereas variation of τ_{trap} for a particular DPF is dominated by parameter uncertainty not specific to our dielectric environment (e.g. solvent permittivity from solvent-based CQD properties). Points are sampled from the model parameter space.

the central set of parameters. Note that non-inclusion of any of these factors would result in a pump field amplitude outside our estimated uncertainties.

These modeling results are consistent with the power dependence data presented in Figure 2.6E, in which it was found that suitable excitation power scaling resulted in identically shaped saturation behavior of the

cavity-coupled and bare SOI PL. Although not presented in this dissertation, other in-lab data suggests this scaling holds for HeNe excitation too. This highlights the accuracy and necessity of including scattering effects at both the excitation and emission wavelengths in order to quantitatively describe the PbSe behavior in diverse dielectric environments.

3.2.9 Saturation modeling conclusions

Extensive quantitative modeling of the cavity-coupled emission saturation highlights the importance of dealing with large depolarization factors, or local field corrections, in this system, as compared to the more commonly studied InAs epitaxial CQD systems. The conclusion drawn from the modeling is that non-radiative trap states retain excited excitons, and prevent them from returning to the ground state with a time constant on the order of $\sim 3 \mu\text{s}$. This occurs when the rate γ_{XY} at which excitons decay to this non-radiative state far exceeds their *total radiative* decay rate to both the cavity and radiation modes, i.e. $\gamma_{XY} \gg 1 \times 10^6 \text{ Hz}$. These conclusions are consistent with low quantum yields observed for exciton emission from PbSe CQDs on silicon surfaces, in vacuum.

3.3 Modeling time-resolved decay of CQDs in various formulations

The time-resolved results presented in Section 2.5 clearly indicate exciton decay is faster for sub-monolayers than for drop-casts, and faster for drop-casts than for in-solution. However, without modeling of the influence of the dielectric environment on the radiative lifetime, or relatively challenging absolute quantum efficiency measurements, it is not clear from these results alone whether the large differences in exciton decay rates is due to changes in radiative rates, non-radiative rates, or some combination thereof. In this section, we use the depolarization modeling methods described earlier in this chapter to calculate the influence of each CQD formulation on the radiative decay rate of embedded (“intrinsic”) dipole emitters, then combine them with the time-resolved results to make inferences about both non-radiative

and radiative decay in each formulation.

Direct measurements of the relative radiative τ_{rad} and non-radiative $\tau_{\text{non-rad}}$ contributions to the total PL decay time τ_{PL} , related by $1/\tau_{\text{PL}} = 1/\tau_{\text{rad}} + 1/\tau_{\text{non-rad}}$, are challenging to measure in film formulations, but are available for the CQDs used in this dissertation when dispersed in solvent. This total decay time in solution, $\tau_{\text{PL}} = 1.0 \mu\text{s}$, is similar to solution-based decay times reported by others. Direct measurements of the quantum yield from similarly prepared PbSe quantum dots using an integrating sphere, and our own measurements with an integrating sphere, suggest the quantum yield in solution is $30^{+5}_{-5}\%$. The measured net lifetime and this quantum yield therefore suggest that the radiative lifetime in solution is $\tau_{\text{rad}} = 3.3^{+0.3}_{-0.3} \mu\text{s}$, and the corresponding non-radiative recombination time is $\tau_{\text{non-rad}} = 1.4^{+0.2}_{-0.2} \mu\text{s}$.

3.3.1 Dielectric model accounting of radiative decay

The radiative decay time of CQDs in a densely packed, three-dimensional (3D) array should be considerably different than that of isolated CQDs in a low-index solvent, due to depolarization effects associated with the large ($Re(\epsilon) \approx 23$) dielectric constant of the CQD. CQDs in solvent and in thin films on silicon (and SOI) were modeled as described in the previous section (sans photonic crystal). The drop-cast film was modeled in FDTD simulations by a sub-micron cube of hexagonally close-packed (7 nm pitch) spherical nanoparticles of 5 nm diameter in an oleic acid interstitial of refractive index $n_{\text{oa}} \approx 1.45$, with the remainder of the film modeled by a homogeneous medium of permittivity equal the average permittivity of the nanoparticle/interstitial region, all adjacent to a silicon substrate. The power radiated by test dipoles located at the center of various CQDs in the close-packed array is approximately three times that for isolated CQD in hexanes, when averaged equally over three orientations, one perpendicular to the substrate and two parallel to the substrate.

The same numerical estimate (test dipole, radiated power, three orientation average) for the radiative decay rate of a test dipole located (a) on

an isolated silicon surface or (b) in a 2D close-packed arrays of CQDs on a silicon surface suggests that for these on-silicon environments, the radiative decay rate is only increased over the solvent value by at most $\approx 50\%$. The 2D close-packed array led to an at most $\approx 20\%$ increase on the radiative decay rate of any particular CQD in the array relative to the bare silicon substrate. For comparison, radiative decay rates of an isolated CQD on any of bare silicon, bare SOI, or at the center of the L3 cavity surface (away from the cavity resonance, as discussed in the previous section) were all similar. Similarly, the decay rates of a CQD in a close-packed array on any of these three substrates were all similar.

3.3.2 Radiative efficiency from time-resolved emission and dielectric modeling

From these simulation results, we deduce that the quantum yield $QY = (1/\tau_{PL})/(1/\tau_{rad} + 1/\tau_{non-rad})$ in the drop-cast sample is $\approx 20\%$, with a corresponding non-radiative decay time of ≈ 250 ns. This follows from the relationship between the total PL decay time measured $\tau_{PL} = 190$ to 200 ns as presented in Figure 2.9, and the contributions from radiative and non-radiative decay described earlier in this section, for which the FDTD results indicated the radiative decay rate contribution increased by a factor of ≈ 3 compared to in-solution. The non-radiative decay rate is thus ≈ 6 times larger than in-solution.

We also conclude that the PL from the dip-coated samples, characterized by the both the measured time constants of ≈ 90 ns and ≈ 135 ns presented in Figure 2.9, is completely dominated by non-radiative decay processes. The average quantum yield for the dip-coated samples is thus $\approx 4\%$ to 10% . The non-radiative decay rate is thus a factor of ≈ 1.2 to 2.8 larger for CQDs isolated on a silicon surface relative to in a thick film (or ≈ 7 to 16 relative to solution).

To develop an appreciation for these quantities, note that this dip-coated quantum yield, when compared with the $\approx 20\%$ estimated quantum yields in the thick 3D film, is consistent with the ≈ 3000 times reduction in overall signal strength from the two sample types: the number of CQDs excited by

the 658 nm laser in the random close-packed (fill fraction $\approx 63\%$) emulsive film is estimated to be about 500 times larger than for the 2D film (estimated to have $\approx 7\%$ average coverage), assuming an absorption depth in the thick film at 658 nm of ≈ 250 nm. The remaining difference in signal strength is then, within uncertainty, the ratio of quantum yields.

Additional notes include (a) we find that solvent rinsing of the dip-coated samples using hexanes or TCE, before placing them in the cryostat, dramatically reduces the quantum yield of the sub-monolayer samples, and (b) the non-radiative decay time for CQDs in the thin film formulation, using the $1.4^{+0.2}_{-0.2} \mu\text{s}$ value in solution and ≈ 7 to 16 increase in non-radiative decay, is ≈ 80 to 200 ns.

Also, recall the simplifying assumption made in Subsection 3.2.7 in regard to the non-radiative decay time calculation in the saturation modeling, namely that the decay rate from the exciton state to the trap state, described by the rate γ_{XY} , was much faster than the total radiative decay rate, $\gamma_{XG} + R_{cav} = 4^{+5}_{-2} \times 10^5 \text{ Hz} + 8^{+13}_{-4} \times 10^5 \text{ Hz} = 1.2^{+1.8}_{-0.6} \times 10^6 \text{ Hz}$. This assertion is directly supported by the results in this section, in which - by combining time-resolved PL data and FDTD modeling of a thin-film CQD formulation - we see that the non-radiative decay rate of $1/(80 \text{ to } 200 \text{ ns}) = 5$ to 13 MHz is at least several times faster, and as high as 20 times faster, than the $1.2^{+1.8}_{-0.6}$ MHz total radiative decay rate of CQDs in the L3 cavity studied in the saturation modeling.

3.3.3 Discussion

From these results we deduce that the non-radiative decay rate of the CQD in the close-packed 3D emulsive films is increased by a factor of ≈ 6 compared to in-solution and further by a factor of ≈ 1.2 to 2.8 when the CQDs are more isolated, on a silicon surface. We attribute this increase in non-radiative decay rate to a degradation in surface passivation when there are no mobile ligands available to mend defects. An alternative interpretation would attribute the degradation to increased oxidation of the solid state dispersions. While this is a possible contributing factor, we note that for

both solid formulations, samples are stable for months when held in vacuum environments of $< 10^{-3}$ Torr. If oxidation is a factor, it would have to occur, for the thick films, during the brief (< 20 min) casting under nitrogen flow or, for the thin films, during the likewise brief (< 3 min) presence in the glove box of low but potentially non-negligible air content. However, as we do not observe significant changes in PL yields for various sample durations in the glove box, we suspect that ligand damage is the main source of the increased non-radiative decay rate in the 2D films. This is also consistent with the deleterious effects of solvent rinsing the sub-monolayer samples. Various methods for better protecting the excitons may help to reduce the degradation in quantum yield on silicon surfaces.

3.4 Air exposure dependence of exciton kinetics

The most prominent example of PbX CQD chemical sensitivity is exposure to air, believed to be dominated by the influence of oxygen in the air [207]. Prior to the work in this dissertation, it was known that emission of PbX CQDs in solution, in ambient (air) conditions, will diminish and blueshift, with the blueshift and x-ray diffraction results consistent with oxidation of the CQD surfaces [43, 57, 93, 207, 210, 211]. Enormous efforts have been put forth to decrease deleterious sensitivity of CQDs to air exposure, including use of alternative ligands, inorganic shells, post-formulation treatments, and synthesis modifications [16, 43, 46, 57, 58, 93, 113, 162, 187, 210].

Understanding the effect of air at a microscopic level has been confounded by a wide variety of results. One report in 2007 found that steady-state integrated photoluminescence at room temperature, for CQD emulsions (also referred to as quantum dot solids, or drop-cast films) in vacuum, recovers from temporary exposure to air [207]. Studies from 2011 [43] and 2012 [93] revealed markedly different photoluminescence than seen in the prior decade on PbX CQDs, for PbX CQDs synthesized in the absence of air, as opposed to synthesis in air. This behavior included (a) clear evidence of two emission peaks, one thermally activated around 100 K to 200 K, as opposed to the single or nearly single peak observed in nearly all other stud-

ies, and (b) insensitivity to air exposure when an alkyl-based (alkylselenide; not the typical oleic acid) ligand was used. In these studies, air exposure of the common oleic-capped CQDs tended the temperature-dependent PL qualitatively towards more commonly obtained results, but found effects of air exposure on these samples to be irreversible, as opposed to the previously reported reversibility of air exposure of oleic-capped PbX CQDs at room temperature [207].

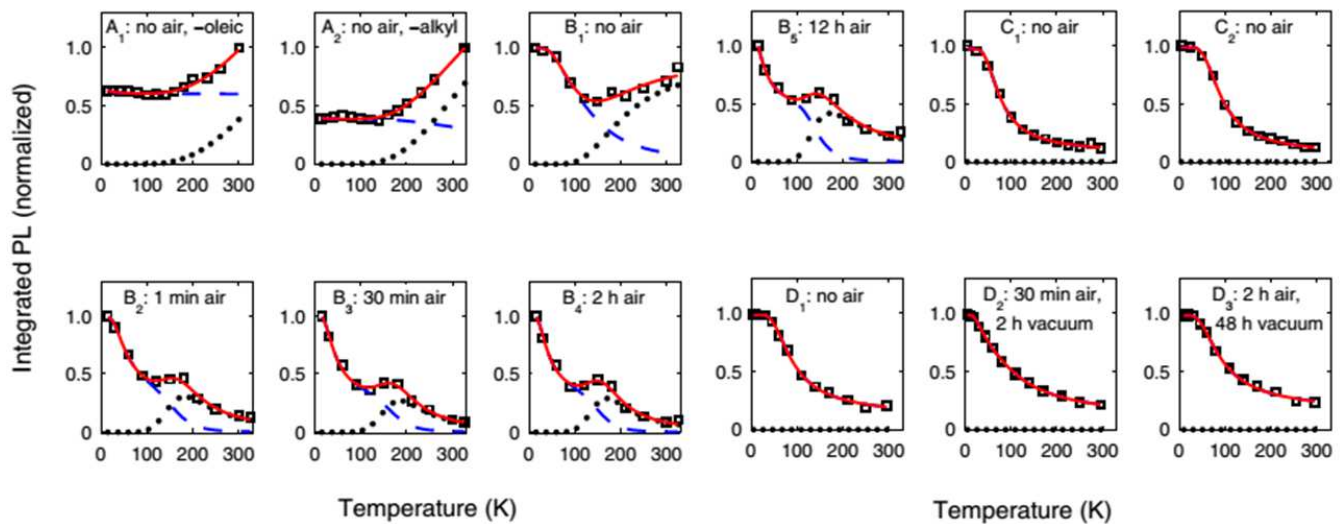


Figure 3.8: Integrated PL data sets (black squares), normalized to their maximum values, along with best-fit model yield curves (calculated below) in solid red and corresponding model PL contributions from each of two possible emissive states or clusters of emissive states in dotted and dashed lines, respectively. Samples series *A* and *B* are from work published in references [43, 93], and sample series *C* and *D* were already described in Section 2.6 but reproduced here for convenient comparison. Table 3.1 contains descriptions of these samples.

These results prompted us to carry out further temperature dependent studies of CQD PL from thick films as a function of air exposure, as reported in Chapter 2. This data was presented in Section 2.6 and is reproduced along with the data from [43] and [93] in Figure 3.8 and described in Table 3.1

for convenient comparison. This section compares our measurements of temperature dependent integrated PL strength under various air-exposure conditions with those reported by Chappell *et al.* and Hughes *et al.* The kinetic model used to analyze all of this combined data is then described, and the results of that analysis are used to infer similarities and differences between the two formulations of nominally very similar PbSe CQDs.

Key	Description (air exposure extent and originating publication)
A_1	No air exposure during CQD synthesis or as drop-cast, oleic- ligands, <i>Hughes et al.</i> [93]
A_2	No air exposure during CQD synthesis or as drop-cast, alkyl- ligands, <i>Hughes et al.</i> [93] Distinct drop-cast from A_1 .
B_1	No air exposure during CQD synthesis or as drop-cast, <i>Chappell et al.</i> [43] Same CQD drop-cast sample as traces B_2 through B_5 .
B_2	1 minute of air exposure as drop-cast, none during CQD synthesis, <i>Chappell et al.</i> [43]
B_3	30 minutes of air as drop-cast, none during CQD synthesis, <i>Chappell et al.</i> [43]
B_4	2 hours of air exposure as drop-cast, none during CQD synthesis, <i>Chappell et al.</i> [43]
B_5	12 hours of exposure as drop-cast, none during CQD synthesis, <i>Chappell et al.</i> [43]
B_5	12 hours of exposure as drop-cast, none during QD synthesis, <i>Chappell et al.</i> [43]
C_1	No air exposure as drop-cast, some during CQD synthesis, <i>Qiao et al.</i> [172]
C_2	No air exposure as drop-cast, some during CQD synthesis, <i>Qiao et al.</i> [172] Distinct drop-cast from C_1 .
D_1	No air exposure as drop-cast, some during CQD synthesis. Same CQD drop-cast sample as traces D_2 and D_3 .
D_2	30 minutes exposure as drop-cast, some during CQD synthesis, measured after 2 hours in vacuum
D_3	2 hours exposure as drop-cast, some during CQD synthesis, measured after 48 hours in vacuum

Table 3.1: PbSe CQD thick film sample descriptions, for integrated PL traces plotted in Figure 3.8. Samples from our lab, already presented in Section 2.6, are reproduced here for convenient comparison to samples from other labs. “Alkyl-” for studies mentioned here refer to alkylselenide [93].

The integrated CQD PL reported in Chappell *et al.* and Hughes *et al.*, corresponding to series A and B in Figure 3.8 and described in Table 3.1, is marked by either strong non-monotonicity and/or explicit increases with increasing temperature. This is in spite of nominally similar CQD syntheses for samples A_1 and B_1 through B_5 and no air exposure for samples A_1 ,

A_2 , and B_1 . Non-monotonic PL yield persists even after their samples are exposed to a controlled air environment from minutes to hours. This behavior is attributed to PL contributions from two distinct radiative states at different energies in these CQD samples, consistent with spectral line shape analysis, at least in dilute glass-encased samples, that reveals two peaks separated by several tens of meV, over a range of temperatures.

In order to limit the free parameters in the kinetic model presented earlier in this chapter, but be general enough to accommodate all kinetics we've mentioned, we make two assumptions: (i) there are at most two states, or more generally two clusters of closely spaced states, that have significant oscillator strengths, and (ii) the *net* non-radiative decay rate from the entire manifold can be fit using a temperature-dependent function that does not include any level-specific parameters.

These assumptions are schematically summarized in the energy level diagram of Figure 3.9. Non-radiative decay in our model is generally from the collective manifold of excitonic states instead of pathways specific to states within the manifold. Assumption (i) is chosen to be consistent with to-date observations of thick film PbSe PL, but can be relaxed if future works reveal otherwise. Assumption (ii) does not preclude a more state-specific interpretation of whatever temperature dependent function is fit to the non-radiative decay rate.

With reference to Figure 3.9, and to Equation 3.1 the two clusters of emissive states, A and B , have radiative decay rates $\{\gamma_A\}$ and $\{\gamma_B\}$ respectively, and the average or centroid energy of the B state cluster $\overline{\epsilon_B}$ lies $\Delta\epsilon_{BA}$ above the average or centroid energy $\overline{\epsilon_A}$ of the A state. The radiative emission rate is thus approximated as:

$$g_r = \frac{N_A \overline{\gamma_A}}{e^{(\overline{\epsilon_A} - \mu)/k_B T} + 1} + \frac{N_B \overline{\gamma_B}}{e^{(\overline{\epsilon_B} - \mu)/k_B T} + 1} \quad (3.25)$$

$$= \frac{N_A \overline{\gamma_A} + N_B \overline{\gamma_B}}{n_A \overline{\gamma_A} + n_B \overline{\gamma_B}}, \quad (3.26)$$

where the overline denotes the net or average value of the corresponding quantity associated with the A or B cluster of emissive states.

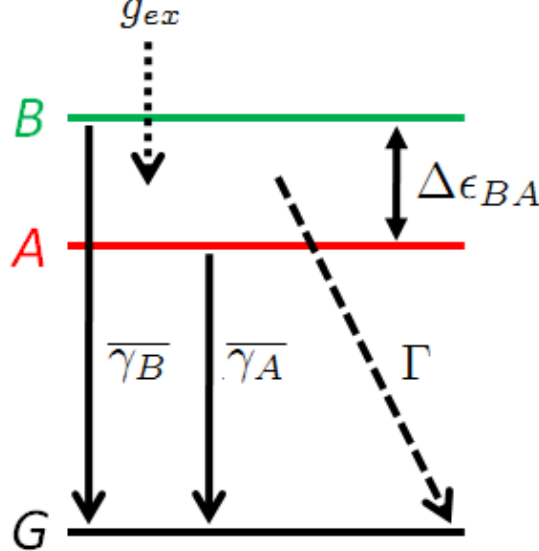


Figure 3.9: Modeled energy level arrangement. Levels A and B are in thermal quasi-equilibrium and populated by pumping of higher-lying levels at a rate g_{ex} . They respectively consist of N_A and N_B states of average radiative decay rates $\bar{\gamma}_A$ and $\bar{\gamma}_B$. The general non-radiative decay Γ , the nature of which is described in detail in-text, is not specific to level A or B for the purposes of this kinetic modeling, and is indicated by the dashed arrow.

The non-radiative contribution in Equation 3.2, denoted by g_{nr} , is

$$g_{nr} = \int_{\epsilon_{min}}^{\epsilon_{max}} \frac{\Gamma_{nr}(\epsilon, T)f(\epsilon)}{e^{(\epsilon-\mu)/k_B T} + 1} d\epsilon. \quad (3.27)$$

Thus the net PL yield, Y_{PL} , which is also proportional to the observed PL, is of the form:

$$Y_{PL} = g_r/g_{ex} \quad (3.28)$$

$$= \frac{1 + \frac{N_B \bar{\gamma}_B}{N_A \bar{\gamma}_A} e^{-\Delta \epsilon_{BA}/k_B T}}{1 + \frac{N_B \bar{\gamma}_B}{N_A \bar{\gamma}_A} e^{-\Delta \epsilon_{BA}/k_B T} + \frac{g_{nr}}{N_A \bar{\gamma}_A e^{-(\epsilon_A - \mu)/k_B T}}}, \quad (3.29)$$

where we have taken the Maxwell-Boltzmann limit of the Fermi-Dirac distri-

bution function. The model was solved more generally, but the experimental excitation conditions and model results are all consistent with this Maxwell-Boltzmann limit.

Using Equation 3.27 in the Maxwell-Boltzmann limit, the last term in the denominator of Equation 3.29 can be re-expressed as a normalized net non-radiative decay rate,

$$g'_{nr} = \frac{g_{nr}}{N_A \bar{\gamma}_A e^{-(\bar{\epsilon}_A - \mu)/k_B T}} \quad (3.30)$$

$$= \frac{1}{N_A \bar{\gamma}_A} \int_{\epsilon_{min}}^{\epsilon_{max}} \Gamma_{nr}(\epsilon, T) f(\epsilon) e^{-(\epsilon - \bar{\epsilon}_A)/k_B T} d\epsilon. \quad (3.31)$$

Excellent fits of the functional form ηY_{PL} , for temperature-independent constant η , to all data sets were found for g'_{nr} set equal to the sum of N Arrhenius terms, i.e.:

$$g'_{nr} = \sum_{j=1}^N \Gamma'_j e^{-\Delta E_j / k_B T}, \quad (3.32)$$

for N , ΔE_j , and Γ'_j dependent upon sample type, but in all cases only 1 or 2 non-radiative pathways are needed.

By modeling the manifold's net non-radiative decay using Equation 3.32, the only influential state energy for the purposes of our fitting methodology is that of the B state cluster, relative to that of the A state cluster, i.e. $\Delta\epsilon_{BA}$; energies $\bar{\epsilon}_A$ and ϵ_{min} become irrelevant. Individual terms in Equation 3.32 have no specific association with the exciton states in the manifold: any one term could in principle represent some combination of a thermal occupancy factor for a particular state (bright or dark) and an associated non-radiative decay rate, with the implication that there are three clusters of states through which most of the non-radiative recombination occurs. However, there are no such attributions implied by this more general functional fit.

3.4.1 Fit methods and extracted parameters

Extracted parameter values are plotted in Figure 3.10. In those plots, a vertical bar for a particular parameter and particular sample represents the range of that parameter value for which there exists a complimentary set of parameters such that the model fit satisfies $\chi^2 - \min(\chi^2) \leq 4$, where $\chi^2 = \Sigma(\text{observed} - \text{model})^2/\sigma^2$, “observed” is the observed PL, “model” is the model PL in the Maxwell-Boltzmann limit (ηY_{PL} for Y_{PL} of Equation 3.29), $\sigma = 0.02 \max(I_{PL})$, and $\min(\chi^2)$ is evaluated at the global best fit, obtained according to the procedures described below. The number of non-radiative pathways used to fit to any particular curve was chosen such that $\min(\chi^2)$, normalized to the number of data points for that curve, was less than 3. This threshold was found to admit best fits that captured qualitative behavior of all the sample curves, especially relating to the effects of air exposure.

The sole constraint imposed upon the parameters is an upper limit of 80 meV for $\Delta\epsilon_{BA}$, based on the spectral range over which the PL was integrated, and allowing for possible differences in the Stokes shifts associated with the two radiative levels in sample series *A* and *B*. Otherwise, the parameter search domains correspond to the plotting ranges in Figure 3.10.

The first segment of our best fit algorithm involves (1) sampling a set of parameters logarithmically from the parameter search domain, (2) applying the Levenberg-Marquardt algorithm with this set of parameters as an initial condition to determine the local best-fit parameters, (3) repeating (1) and (2) a total of 10^3 times, and (4) associating the best fit of these local best fits with the global best fit. This global best fit was corroborated via application of local minimization to a parameter search domain grid (the latter contrasted with random sampling of the parameter search domain). The logarithm of the likelihood function was found to be quadratic in most parameters near the best fit points.

Red lines in Figure 2.10 are the model curves corresponding to the best fit parameters found by this procedure. Dotted and dashed lines are plots of the individual model *A* state and *B* state contributions from each state for the same best-fit parameters.

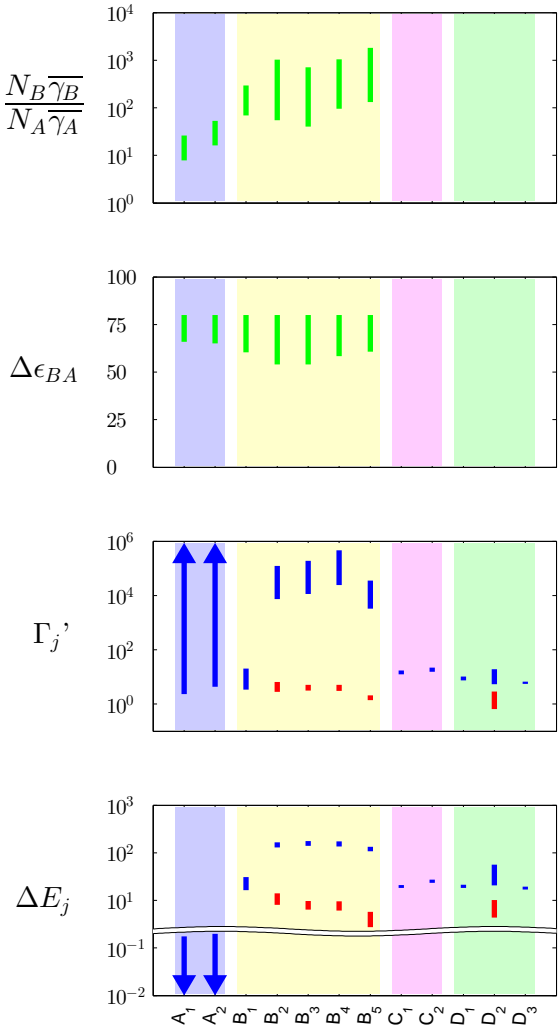


Figure 3.10: Subscript j indexes the non-radiative decay pathways, e.g. as indexed in Equation 3.32. Bars represent the ranges of parameter values that, upon substitution into Equation 3.29, using Equation 3.27, generate or nearly generate the model curves in Figure 2.10. Rates are normalized as described in-text (leading up to Equation 3.32), and energies are in meV. Sample labeling is as in Figure 2.10 and Table 2.1. Parameter $\Delta\epsilon_{BA}$ is restricted from above to 80 meV for reasons described in-text. Rates sufficiently small to render their corresponding energies meaningless are omitted, along with those energies.

The second segment of our fit routine - generation of the vertical parameter bars in Figure 3.10 - consisted of (5) dividing up each parameter search domain into a set of many narrow subdomains, (6) restricting, parameter by parameter of a particular sample, that parameter value to one of those narrow subdomains, (7) sampling a complimentary set of parameters logarithmically from the large parameter search domain, (8) applying the Levenberg-Marquardt algorithm to determine a local best fit, (9) repeating (7) and (8) at total of 10^2 times, (10) identifying the best fit of those local best fits, (11) checking to see if $\chi^2 - \min(\chi^2) \leq 4$ is satisfied for the best of those local best fits, and (12) repeating steps (6) through (12) for every other narrow subdomain. The vertical bars in Figure 3.10 are lines that extend from the minimum to maximum parameter values with which some $\chi^2 - \min(\chi^2) \leq 4$ exists, as found in steps (5) through (12).

Figure 2.10 indicates that good quality fits to the data are obtained using the Maxwell-Boltzmann limit of the model. This limit should apply only when $g_{ex}/N_A\bar{\gamma}_A \ll 1$, in which case the results are independent of g_{ex} . We estimated g_{ex} for both our data sets and those of Chappell *et al.* using measured laser powers and spot sizes, along with absorption coefficients from the literature [141]. The spontaneous emission rate of the lower emissive state was estimated from lifetime measurements of our drop cast films and dielectric modeling we previously employed [73]. For both our samples and those of Chappell *et al.*, we estimate $g_{ex}/N_A\bar{\gamma}_A \ll 10^{-1}$. Furthermore, if g_{ex} is increased to the point where the Maxwell-Boltzmann approximation breaks down, it becomes very difficult to fit any data set (impossible in the strongly degenerate limit).

3.4.2 Results

With reference to the parameter summary in Figure 3.10, the most significant difference between the various samples is that high-quality fits required $N_B\bar{\gamma}_B/N_A\bar{\gamma}_A \gg 1$ for all Chappell *et al.* and Hughes *et al.* samples, and $N_B\bar{\gamma}_B/N_A\bar{\gamma}_A \ll 1$ for all of our samples. This is consistent, in the former case, with the prominent mid-temperature increase in PL and double-peaked

mid-temperature spectra, and in the latter case, with our observation of only a single emission peak within the few-meV resolution of previously reported spectra [172]. Also, although a trend in $N_B\overline{\gamma_B}/N_A\overline{\gamma_A}$ with air exposure is admissible, any such trend does not follow necessarily from our kinetic analysis, and it is further clear that increasing air exposure does not trend $N_B\overline{\gamma_B}/N_A\overline{\gamma_A}$ in their samples towards the value for our samples.

Fits require the A - B energy separation for series A and B samples to be $\Delta\epsilon_{BA} \approx 55$ meV to 80 meV. It should be noted that the $\Delta\epsilon_{BA}$ value obtained from fits to the no-exposure data agrees reasonably well with the separation of the emission lines in the solution spectra, but not in the drop cast samples. This is to be expected since thermalization of the exciton populations is known [172] to have a strong influence on the temperature dependent Stokes shift of the peak PL emission energy, while there should be minimal effects of thermalization on the spectra obtained in a dilute solution, where the Förster interaction strength is negligible.

For all samples that were not intentionally exposed to air, the integrated PL can be fit assuming only a single non-radiative pathway. The associated parameters of this non-radiative pathway (an activation energy around a few tens of meV and normalized prefactor on the order of several to a few tens) are quite similar for the unexposed sample from Chappell *et al.* (B_1) and our unexposed samples (C series and D series excluding D_2). Non-radiative decay in series A samples is consistent with a single non-radiative pathway with a considerably lower activation energy. Without information regarding the absolute quantum yield in the case of series A samples, it is not possible from the fitting procedure to separate small differences in assumed activation energy and the corresponding prefactor for this single non-radiative decay process (hence the unbounded arrows for series A samples). Introduction of a second sub-10 meV non-radiative pathway increases fit quality for the Chappell *et al.* unexposed sample (B_1), but the difference in fit quality is small. The slight increase in integrated PL at low temperatures in the A_2 sample is not captured with our model, but a third, relatively dark level, just slightly below the A level in energy, could be introduced to capture this behavior.

Samples intentionally exposed to air (B_2 through B_5 and D_2) absolutely require the inclusion of two non-radiative pathways for adequate fits. One of these new pathways has a low (sub-10 meV) activation energy, with a corresponding prefactor in the range of 1 to 10, indicated by the red bars in Figure 3.10. In our air exposed sample (D_2), the parameters associated with the second non-radiative pathway are not dramatically different than before air exposure, whereas in the case of samples B_2 through B_5 , the second pathway has a very high activation energy (> 100 meV), and high normalized prefactor (100's of thousands). There is no indication of the need for a high energy pathway in any of the unexposed, or our air exposed samples. We note that while the low-energy non-radiative pathway is common amongst all air exposed samples, Chappell *et al.* report irreversibility of this air exposure effect for their samples, in stark contrast to the reversibility of the impact of our air exposure (see sample D_3 compared to D_1 and D_2). Finally, we note that inclusion of a third non-radiative pathway with an activation energy several tens of meV increases the quality of fit for the B_2 through B_5 samples, but again, the improvement is minor.

Regarding phonon-mediation of non-radiative decay, Chappell *et al.* and Hughes *et al.* assumed a N_{ph} -phonon absorption functional form for their low-energy, non-radiative pathway, [43, 93] and they reported fits suggested $N_{ph} = 4^{+2}_{-2}$. In cases where present, if we replace the several to ten meV non-radiative Arrhenius pathway ($\Gamma' e^{-\Delta E/k_B T}$) with a one-phonon emission functional form $\Gamma'_{ph} (1 - \exp(-E_{ph}/k_B T))^{-1}$, similar quality fits to those shown in Figure 2.10 can be obtained for a phonon energy of ≈ 5 to 10 meV. From this analysis, there is no preference for the single phonon versus low-activation energy Arrhenius process, but it is nevertheless unambiguous that a non-radiative decay channel with a low (< 10 meV) activation energy is required to fit all of their and our air-exposed samples. The lack of preference between these two functional forms can be attributed to substantial parameter covariance.

3.4.3 Discussion

The behavior of the lower energy *A* state for samples from series *B* is very similar to that of the only radiative state that manifests itself in our samples (series *C* and *D*). With no intentional air exposure, the integrated PL from the *A* transition in sample *B*₁ is almost identical to that observed in all series *C* and *D* samples save for the one exposed to air (*D*₂). In the case of all air-exposed samples from series *B* and *D*, the change in behavior of the *A* state contribution is very similar to the change in behavior of our single emissive state in sample *D*₂, up to temperatures above approximately 125 K, beyond which point the *A* state contribution in air-exposed *B* series samples decays more rapidly than in sample *D*₂. It would appear that air introduces a new, low-activation energy non-radiative decay path for state *A*, and our single emissive state, that causes more rapid (than in the absence of air exposure) falloff of the emission as temperature is increased from approximately 5 K. The difference in behavior at higher temperatures for the *A* state contribution from samples in series *B*, is apparently due to an additional, high activation energy non-radiative pathway that air exposure causes in those samples. It seems plausible that this high activation energy non-radiative channel is somehow tied to the *B* state that is apparent in all series *A* and *B* samples, but absent in our series *C* and *D* samples.

One explanation for the absence of radiative and non-radiative evidence of the *B* state in our samples is that the next highest lying state with significant oscillator strength in our samples has a $\Delta\epsilon_{BA}$ much larger than ≈ 80 meV. An alternate explanation for the lack of radiative evidence of the *B* state in our samples, is the possible impact of nanoparticle shape/symmetry on the oscillator strengths [79] of the states within the ground state exciton manifold. Positing explanations for these conjectures raises the issue of the nature of both the *A* and *B* states; are either or both “intrinsic” excitonic states constructed from the one electron and one hole single particle states typically calculated for these CQDs, or are either or both associated with defects, either bulk-like or surface-like? Based on most published band structure calculations for these systems, it is hard to identify an “intrinsic state

that could be associated with the *A* state in this analysis, since almost all of these calculations conclude that the ground states of the intrinsic manifold are “dark”, with the first “bright” states located on the order of 10 meV to 20 meV above the intrinsic ground state. Since, with the exception of the Hughes *et al.* sample *A*₂, and possibly other Hughes *et al.* samples similar to the *A* series, there is no experimental evidence of increasing PL emission from temperatures of 5 K, the *A* state must be close to the energetically lowest available excitonic state in the CQDs, whatever its nature. In the case of the Hughes *et al.* sample *A*₂, the weak rise in integrated PL at low temperature does suggest that the *A* state in those samples lies slightly above the ground state, but not by the amount suggested by most published band structure calculations. Thus, to the extent that current band structure calculations accurately capture the intrinsic properties of these CQDs, this suggests the *A* state in series *B* samples, and the only emissive state in our CQDs, is a defect state with non-negligible oscillator strength, or that some detail of the nanoparticle structure influences the theoretical oscillator strengths in such a way that low-energy exchange-split states have large oscillator strengths. If the impact of symmetry is sufficient to impact the low energy *A* state, it may not be so surprising that the higher energy *B* state’s oscillator strength could be quite sensitive to sample synthesis details.

Further experiments, and theoretical calculations that include defects and particles of various symmetries are required to explain the nature of the optically active states in PbSe CQDs, and the reversibility of the influence of air in some samples, and its irreversible nature in other samples.

3.4.4 Conclusions

A kinetic model that allows for luminescent emission from up to two bright clusters of states, and non-radiative decay from *any* of the excitonic states in the lowest manifold of PbSe CQD thin-films can accurately reproduce a diverse range of measured temperature-dependent integrated PL emission data from 5 to 300 K. A thorough statistical analysis of the best-fit parameters (at most 6, and in some cases as few as 2), including their covariance,

reveals the commonalities and differences in the optical emission properties of nominally similar PbSe CQD samples grown in different laboratories, including their response to oxygen and air exposure.

One set of samples (labeled *C* and *D*) effectively emit from only a single cluster of bright states that have energies at or very close to the lowest of the accessible excitonic states. In the absence of intentional air exposure, the non-radiative decay from these samples is well described by a single Arrhenius process with an activation energy on order of 20 meV. The other sets of samples (labeled *A* and *B*) exhibit significant emission from primarily two clusters of states separated by \approx 75 meV, with the lower energy state very close to the bottom of the manifold of accessible states. In the absence of intentional air exposure, samples *A* and *B* either exhibit the same \sim 20 meV activated non-radiative decay behavior of samples *C* and *D*, or a non-radiative decay with negligible activation energy, depending on the organic capping layer.

Air exposure of samples *B*, *C* and *D* changes their behavior in a way that can be described by introducing a second, distinct Arrhenius-like non-radiative decay channel with a relatively low activation energy. The biggest difference between samples *B* and samples *C* and *D* in this regard, is that the effects of air exposure on samples *B* is irreversible, while it is reversible for samples *C* and *D*.

This analysis and sample comparison suggests that the lower energy transition in samples *A* and *B* shares many attributes of the single emissive state in samples *C* and *D*. The fact that the energy of this bright state is very close to the bottom of the ground manifold of accessible exciton states is difficult to reconcile with existing calculations of the oscillator strength distribution within the “intrinsic” ground state manifold of PbSe CQDs. This, together with the apparently fickle nature of the higher energy emissive state evident in one set of samples but absent in the other, suggests that either (i) the low energy emissive state is associated with defects, and/or (ii) that current calculations of band structure and oscillator strengths fail to capture important details, perhaps associated with morphological details that have yet to be experimentally determined.

3.5 Modeling discussion

As exemplified by the studies in Chapters 2 and 3, there are numerous and significant challenges towards development of an integrated, NIR single photon source based on PbX colloidal quantum dots. The efficiency of such a source may suffer from low internal quantum efficiency when improperly passivated, particularly in combination with air exposure. Additionally, the radiative emission rate may be lowered by large depolarization effects.

The work in these chapters however provides a solid, self-consistent picture that addresses each of these influences, improving prospects to develop and interpret experiments much closer to a realized single photon source environment, i.e. studies of PbX CQDs integrated into photonic integrated circuits, the subject of the following Chapter 4. In this section, we summarize the picture of PbX CQD emission developed in this chapter and the previous, as a basis for interpretation of Chapter 4 results. Further, the value of this picture towards development of a single photon source is bolstered by the fact that the CQD synthesis method was held constant over all experiments in this dissertation, eliminating common inconsistent behavior arising from synthesis variations from group to group.

Consider firstly radiative efficiency estimates for thick films: the room temperature integrated PL and low-temperature integrated PL ratio ($\text{PL}(300\text{K})/\text{PL}(4\text{K}) = 0.1 \text{ to } 0.3$ in Figure 2.10 of Section 2.6) supports a radiative efficiency of 10% to 30% at room temperature. This is consistent with the independent time-resolved plus FDTD modeling results that indicated a radiative efficiency of around 20% at room temperature (Section 3.3).

FDTD modeling, combined with PL decay measurements, resulted in a radiative efficiency of 4% to 10% for PbSe CQD thin films on silicon. The modeling resulted in similar radiative decay rates for CQDs in the main antinode of an L3 cavity, calculated for the power saturation spectroscopy of cavity-coupled PL. Although no absolute radiative efficiency was determined in the power saturation study, the need for a significant non-radiative pathway (i.e. need for the four state model, including the trap state) to ac-

commodate the strong saturation was established and is consistent with low-on chip radiative efficiency of PbSe CQD thin films. The trap-state lifetime was obtained from the saturation modeling by presuming that decay from the excitonic state to the trap state is much faster than radiative decay. The time-resolved study of PbSe CQDs in a thin film, when combined with FDTD modeling, provided quantitative support of this assertion.

Modeling PbSe CQD emission involved accounting for numerous depolarization factors, yet with the time-resolved data provided self-consistent understanding of emission dependence on pump intensity: (a) the lack of saturation for CQDs on bare SOI or silicon, relative to the CQD PL coupled to a L3 cavity, is due to an enhancement of the excitation field arising from the L3 cavity texture. (b) the lack of saturation for thick films, relative to CQDs in the L3 cavity, is not tied to local field differences, but can be understood by studies from our lab external to this dissertation contents, i.e. by exciton diffusion [172, 174].

The saturation behavior is arguably the biggest problem for SPS applications. In principle, if the enhanced coupling of the CQD exciton to the cavity mode was sufficiently large, this problem could be mitigated to some extent, however from the simulations, the net rate of coupling to the cavity mode versus other radiative decay routes when the CQD is at the antinode on top of the L3 cavity was only 2 times. If the PbSe were in fact embedded within the silicon at the true antinode position, the better mode overlap (increased by a factor of ~ 9), along with reduced coupling to other radiative states (decreased by a factor of ~ 7 from Figure 3.4), and reduced depolarization effect (improved by a factor of ~ 10 , square of Lorentz field factor in solution vs in silicon), would all combine to increase this factor to ~ 1000 . Note that recent absorption measurements of PbX CQD deposited monolayer by monolayer on silicon waveguides [158] would offer useful data to further test our depolarization models.

The influence of air on CQD emission was studied in thick film formulations, and experimental conditions required to minimize its effect were developed (e.g. adequately rejecting air exposure influence by performing specific experimental steps in inert gas environments) and can be readily

adhered to in future studies. Air exposure introduces a low-energy (< 10 meV), non-radiative pathway beyond the most common (~ 20 meV) non-radiative pathway, and recovery from air exposure in thick film formulations is possible. A picture of ligand immobility, in thin film formulations, being the dominant culprit for non-radiative decay is supported. Through these three sets of measurements, which form the basis of Chapters 2 and 3, non-statistical photophysics of the ground state exciton of PbSe CQDs is self-consistently understood, paving the way for solid interpretation of PbSe CQDs in SOI PICs, the subject of the next chapter, as a next step towards evaluating this approach to realization of an SOI-integrated single photon source.

Chapter 4

PbX CQDs in SOI PICs

This chapter describes the study of CQDs integrated into a full silicon photonic circuit, starting with a description of the experimental setup, followed by characterization of the setup, experimental results, and finally modeling of the results.

4.1 Sample preparation (SOI PICs, CQD integration)

While microcavities are excellent for collecting emission from luminescent CQDs, an integrated quantum optical system requires us to carry that collected photon efficiently to other places on the photonic chip. The cavity is thus coupled to a low-loss single-mode ridge waveguide. SOI PICs with the circuit layouts employed in this dissertation were characterized in [189]. They are shown in Figure 4.1 and consist of an L3 cavity symmetrically coupled to two photonic crystal waveguides. The photonic crystal waveguides are in-turn coupled to channel waveguides, and for the sake of easy and efficient free-space collection of cavity-waveguide-coupled photoluminescence, each channel waveguide is coupled to a large multi-mode tapered waveguide, terminated with a diffraction grating-coupler.

The inclusion of two sets of waveguides plus gratings symmetrically coupled to the same cavity facilitated measurement of transmission spectra of

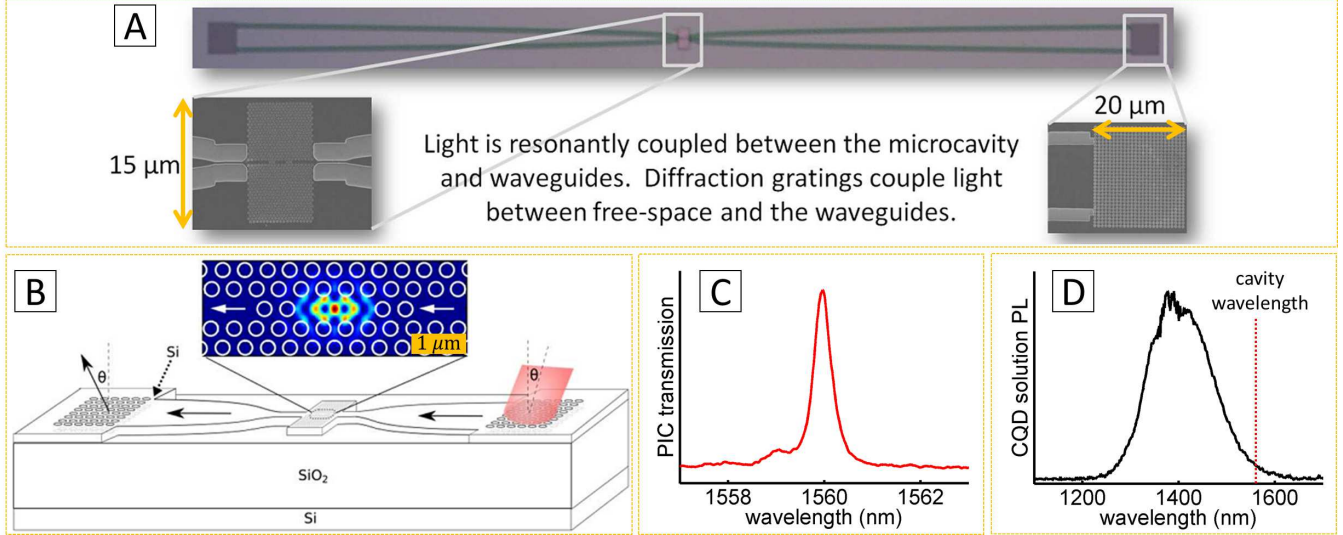


Figure 4.1: (A): Full photonic integrated circuit (PIC) designed and characterized in-lab [189] and used in this dissertation as a PIC in which PbSe CQDs were integrated and their luminescence was measured. (B): PIC transmission measurement schematic. (C): Transmission spectrum of the PIC, prior to CQD integration. (D): PL of PbSe CQDs in solution, prior to their integration into the PIC.

the PIC, and it also facilitated photon correlation measurements directly, without the need for an external beam splitter. This circuit design is an optimized version of an earlier realization in which our group measured efficient cavity-waveguide coupling in the absence of CQDs [17]. Fabrication was through ePIXfab [3] and IMEC [1].

As-received SOI photonic chips were spin-coated with 2 μm of AZ P4110 photoresist to ensure the cavity-wavelength emission would emanate from the grating coupler at a convenient collection angle θ . Photoresist over the photonic crystals (including photonic crystal cavities and waveguides) was removed by exposure to ultraviolet light and subsequent chemical development (using AZ P4110 specific developer, with deionized water at ratio of 1:4), while leaving resist over the tapered waveguides and grating couplers. Photonic crystals (again including photonic crystal cavities and waveguides)

and channel waveguides were undercut by dipping the sample in a buffered oxide etch solution for 20 minutes. The etch was arrested by rinsing the sample in deionized water, and then dried under nitrogen flow and stored in ambient conditions in a dark cabinet.

The PIC transmission spectrum, measured approximately 1 month prior to integration of the PbSe CQDs and about 1 year after the initial HF undercutting (removal of oxide underneath the PhC region), is shown in Figure 4.1C. The in-solution PL spectrum of the PbSe CQDs that were then integrated into the PIC is shown in Figure 4.1D. Integration of these PbSe CQDs was performed as follows: the sample was dipped for 10 seconds in a 0.5 mg/mL hexanes solution of PbSe CQDs and subsequently put under vacuum in accordance with the dip coating procedure outlined in Chapter 2 and detailed in Appendix A.

4.2 Measurement overview and optical setups

Three sets of measurements were performed on the luminescence of the PbSe CQDs integrated into the PIC: (a) steady-state microphotoluminescence (μ PL) spectroscopy using continuous wave (CW) Nd:YAG 1064 nm laser excitation applied at various locations across the sample surface, and monitoring the PL emission from various other locations, using different collection geometries. The main points of this work were to verify the saturation behavior observed from the stand-alone cavities, and to optimize the collection of waveguide-coupled exciton emission while minimizing the contribution from background luminescence. (b) time-resolved μ PL characterization, and corresponding μ PL spectra, using 660 nm pulsed excitation. This work helped to further refine the spectral filtering strategy required for photon correlation measurements, and it also provided lifetime data that could be compared to the thin film studies on uniform substrates as reported in Chapters 2 and 3. (c) photon correlation measurements of the circuit-coupled PL, using the same 660 nm pulsed excitation.

In pursuit of understanding the PIC-coupled, cavity-enhanced CQD PL, a persistent challenge was isolation of this signal from the relatively broad

emission from CQDs not located directly at the cavity antinode. This isolation was pursued in two ways: (a) spectral filtering, i.e. rejection of collected CQD μ PL not at the cavity wavelength, and (b) improvement of cavity-enhanced contrast, i.e. reducing non-cavity-coupled μ PL at the cavity wavelength relative to the cavity-coupled PL. Improvement of cavity-coupled PL contrast relative to non-cavity-coupled PL was achieved using two sets of apertures: (a) one in the far field to select light emitted only within a well-defined solid angle from the sample, in accordance with the angle at which cavity-coupled is diffracted from the PIC diffraction gratings, and (b) a separate set of apertures in an image plane to preferentially collect only the PL emitted from a specific location on the sample surface (typically just near the edge of one of the output grating couplers).

4.2.1 Optical setup

The general setup used for all luminescence measurements performed on the SOI PIC samples is shown in Figure 4.2. The excitation source, following the excitations paths drawn in green, was one of (a) a variable output power Nd:YAG 1064 laser and (b) the 660 nm pulsed Sepia laser used in Section 2.5. The Nd:YAG source was used instead of the HeNe source of Chapter 2 because excitation intensities required to achieve cavity-coupled power saturation could be achieved with it, but not with the HeNe source, given the PIC excitation geometry constraints (in particular the longer working distance and correspondingly larger spot size). Collected light was ultimately detected by one of (a) the Bruker FTIR or (b) the ID210 single photon detectors, each of which were also described in Chapter 2. The collection paths (blue lines) consisted of a 15X reflecting microscope objective (OBJ), sometimes preceded by an aperture plate (AP), passage through a \hat{y} -oriented linear polarizer (P), deflection towards the detectors by use of a mirror pair $M_{T1,T2}$, passage through a far aperture (one of $F_{AL,C,R}$), diversion to either the Bruker FTIR by a combination of mirrors, or to the free-space to fiber couplers ($FFC_{L,R}$), and in the latter case passage through a free-space filter (F), focusing lens, and in-line narrow band spectral filter ($FF_{L,R}$). Many of

the mirrors after the far apertures were kinetically mounted (KM), meaning they could be placed in and out of the optical setup with ease to change the collection paths. Details of the optical setup are as follows.

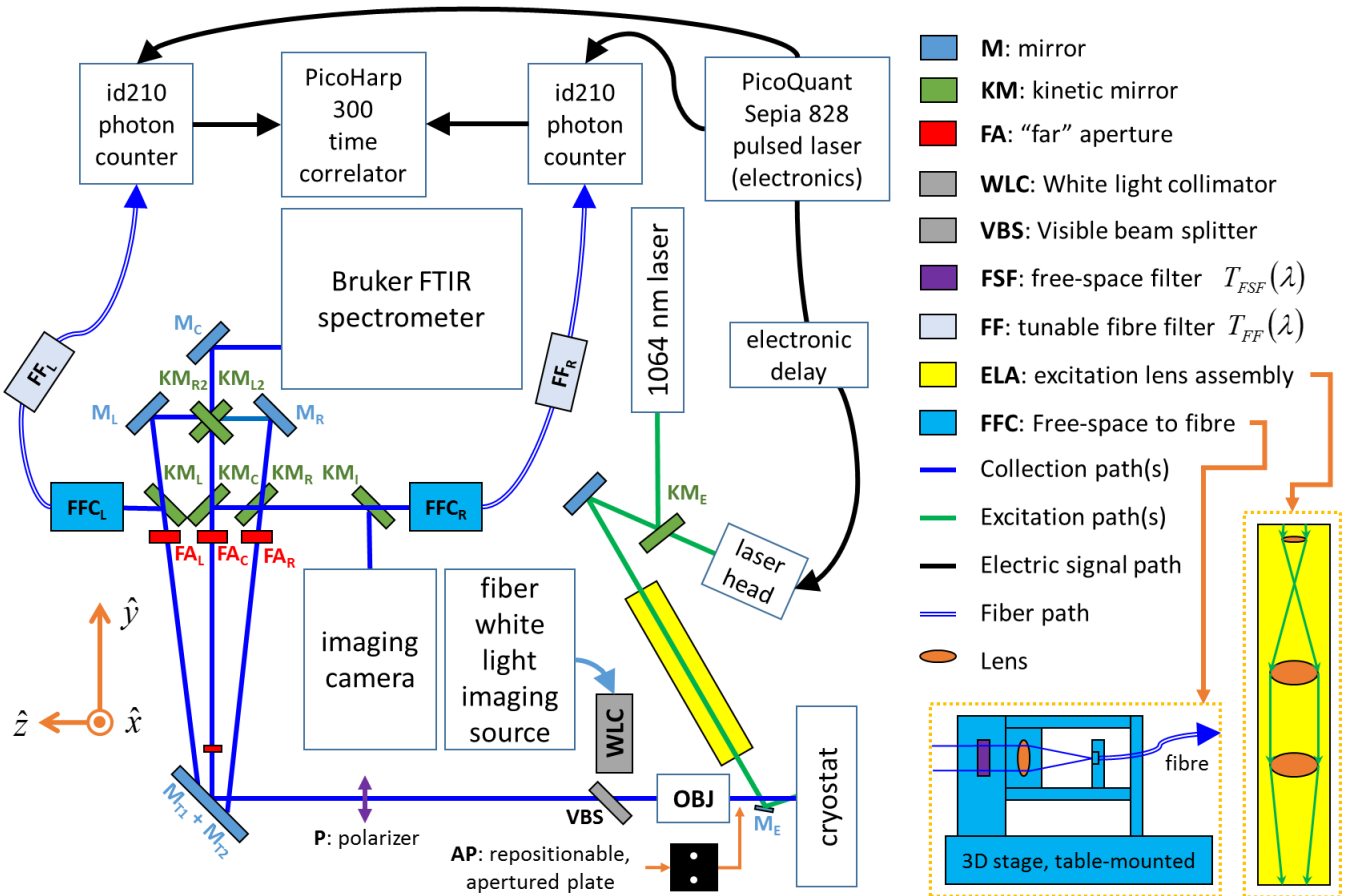


Figure 4.2: Optical setup used for characterizing PbX CQD emission in and near the photonic integrated circuits, including (a) steady-state, Nd:YAG excited microphotoluminescence (μ PL) spectroscopy, (b) spectrally-integrated, time-resolved μ PL emission using a 660 nm pulsed laser, and (c) photon coincidence (correlation) measurements.

Figure 4.3 contains a simple overlay of exemplary excitation and collection areas relative to the PIC components. Measurement of the position

and extent of the excitation and collection areas was done in part with the aid of a white light imaging system, which allows simultaneous broad-band, scattered white light imaging of the sample surface and scattered excitation light, thus a knowledge of both the collection and excitation area relative to the sample at any desired time. White light was directed towards the sample surface via a visible wavelength 50/50 beam splitter (VBS) located behind the 15X reflecting objective (OBJ) used for imaging and light collection from the sample (note that the beam splitter transmits all incident C-band light). Control of the collection area and position was done by adjusting the position and aperture diameter d_{iris} of the far apertures $\text{FA}_{\text{L,C,R}}$. The central far aperture FA_C was aligned early on to coincide with the optical axes of the collecting objective and Bruker FTIR spectrometer. Details of the far aperture system are contained in Figure 4.4D through F.

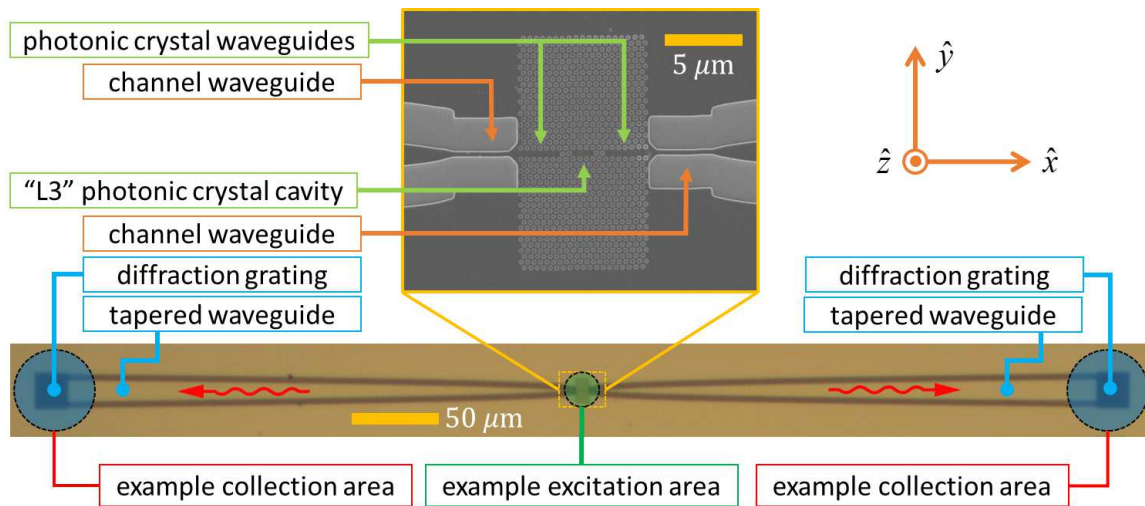


Figure 4.3: Simple overlay of excitation and collection regions relative to the PIC components. Collection area and position was controlled with the far apertures $\text{FA}_{\text{L,C,R}}$. Position of the excitation spot was controlled by adjusting the position of the excitation lens assembly ELA and mirrors preceding it. The $1/e^2$ minimum power diameters were $20 \mu\text{m}$ and $3.5 \mu\text{m}$ for the Nd:YAG and 660 nm pulsed laser excitation sources, respectively.

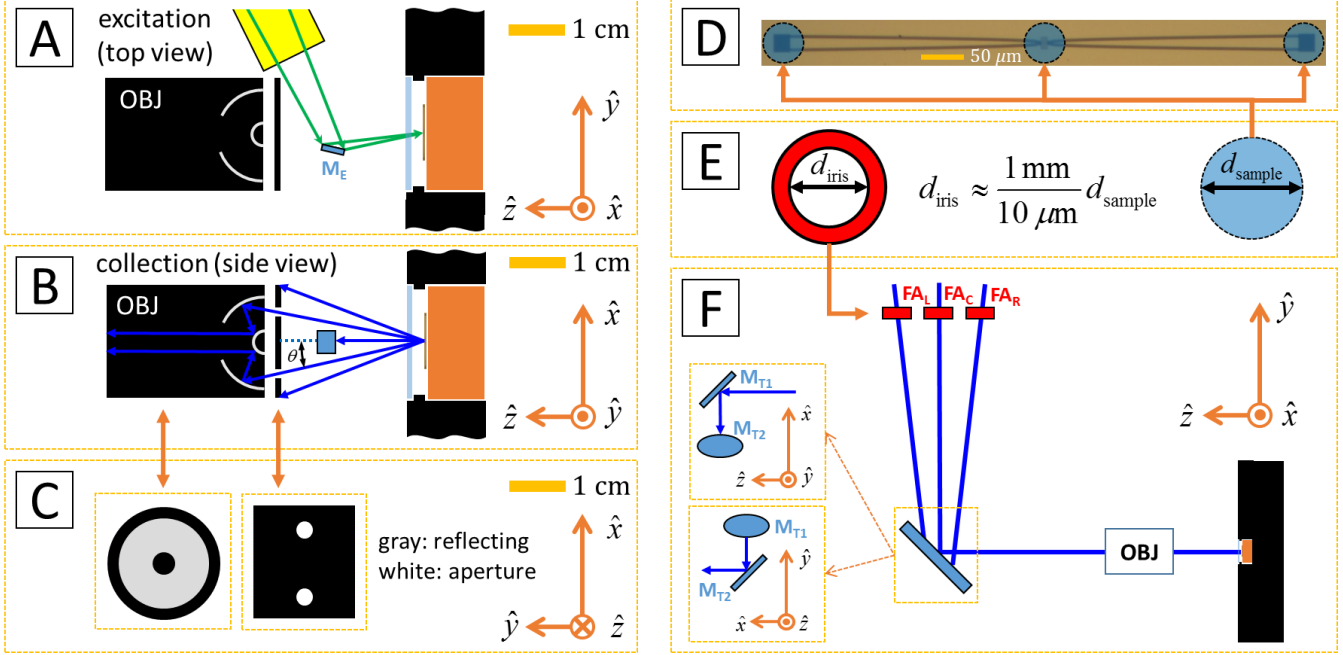


Figure 4.4: Detailed illustrations of excitation and collection geometries, an elaboration upon the larger scale diagrams depicted in Figures 4.2 and 4.3.

Excitation light was expanded, collimated, then focused using aspherical lenses to obtain the smallest excitation spot size possible given space and reasonable budget constraints, shown broadly in the lower right corner of Figure 4.2. For the Nd:YAG laser, the $1/e^2$ power waist was $20 \mu\text{m}$ and for the Sepia 660 nm pulsed source it was $3.5 \mu\text{m}$. The spatial constraint was set in part by the focal length (2.8 cm) of the reflecting objective used for collecting luminescence and white-light imaging the sample surface. Just enough space was available for a several-mm wide, square mirror in between the objective and cryostat window to divert excitation light onto the sample surface. The mirror was located to pass as much luminescence as possible from the chip to the collection objective while minimizing the spot size of the focused excitation laser on the sample surface. A major benefit of using the reflecting objective is that its focusing properties are largely wavelength

independent from VIS through NIR, meaning a good white light image of a specific PIC location obtained with the objective corresponds to near- or in-focus collection of NIR PL emitted from that location (which was verified for PbX CQD luminescence from various locations on the PIC). Refer to Figures 4.4A through C for detailed diagrams of the region near the collection objective, sample, and excitation turning mirror, as well as the apertured plate, now discussed.

A large number of similar circuits were available from the IMEC chip, each with slightly different cavity resonant frequency and grating coupling properties, as characterized in our lab [189]. For the present experiments devices were chosen so that photons at the cavity wavelength would be diffracted out of the grating couplers (when coated with photoresist), at angles within the 5 degree to 20 degree collection (relative to the optical axis) of the reflecting objective, such that all cavity light coupled to the waveguides and diffracted from the gratings could be collected. For the samples studied in this dissertation, $\sim 90\%$ of a given wavelength incident on the grating coupler (e.g. at the cavity emission wavelength), emanated within a 5 degree spread, $\Delta\theta$, of the nominal out-coupled direction θ . For the various samples studied, θ varied from 14 to 17 degrees. Generally, spurious CQD PL emission from the sample was across a much larger spread in solid angle, which permitted increasing the ratio of cavity-coupled PL diffracted from the gratings, relative to all other PL, by collecting light only from the small solid angle at which cavity-coupled PL diffracted. This was achieved by placing a re-positionable aperture plate (AP) between the collecting objective and the sample, about 1 mm away from the objective, as shown in Figure 4.4B.

Free space to fiber coupler assemblies ($FFC_{L,R}$), used in the photon coincidence measurements and detailed in Figure 4.8, consisted of precision 3-dimensional translation stages upon which a spectral filter (F), single focusing lens, and fiber tip were secured, and the position of the lens relative to the fiber tip could be finely adjusted in all three directions and done so independently of the position of the assembly relative to the far apertures. The $50\ \mu m$ core diameter, $125\ \mu m$ cladding diameter multimode fibers were

chosen to be compatible with coupling both to the ID210 detectors, and the Koskin Kogaku narrow band (1.2 nm FWHM) tunable, fiber band pass filters. The overall peak transmission efficiency from just before the free space to fiber coupler to the final output of the fiber (which attaches to the fiber input connector of the ID210 detector), as measured using laser light at the cavity wavelength and scattered off the sample surface, was 30%, at the peak transmission of the in-line filter.

4.2.2 Microphotoluminescence

Consider the steady-state μ PL spectra collected directly from cavity (e.g. a similar geometry to that described in the isolated cavity results in Chapters 2 and 3) compared to that collected from the grating couplers, for Nd:YAG (1064 nm) excitation shown in Figures 4.5A through C.

The narrow resonance near 1564 nm in each corresponds to the cavity-enhanced CQD PL, which excites only TE-polarized ($\hat{z} \cdot \mathbf{E} = 0$) channel waveguide modes that in turn couple out of the grating couplers with \hat{y} -polarization. Unpolarized PL collected directly from the cavity, not shown (instead, all spectra in Figure 4.5 are for \hat{y} polarization), is similar to the standalone cavity μ PL of Chapter 2, i.e. a broad PL background similar to the CQD solution PL, with cavity mode enhancements superimposed.

Isolation of the cavity-out-coupled signal of interest was improved by use of the apertured plate (AP) placed between the sample and collecting objective, and far apertures (FA_{L,C,R}). Figure 4.5 illustrates the utility of near and far apertures in greatly improving the ratio of on-cavity-wavelength PL to off-cavity wavelength PL. No spectral filtering was performed for any of the spectra shown in Figure 4.5.

The PIC-coupled, cavity-enhanced CQD PL also exhibits strong power saturation, plotted in Figure 4.5D. It is useful to compare the excitation source and saturation power to the standalone cavity power saturation of Chapter 2: in Chapter 2, the $1/e^2$ beam power waist was 2.0 μm , saturation power was several μW , and the absorption coefficient of CQDs at the HeNe wavelength used was 2/cm. Here, the saturation was observed for a beam

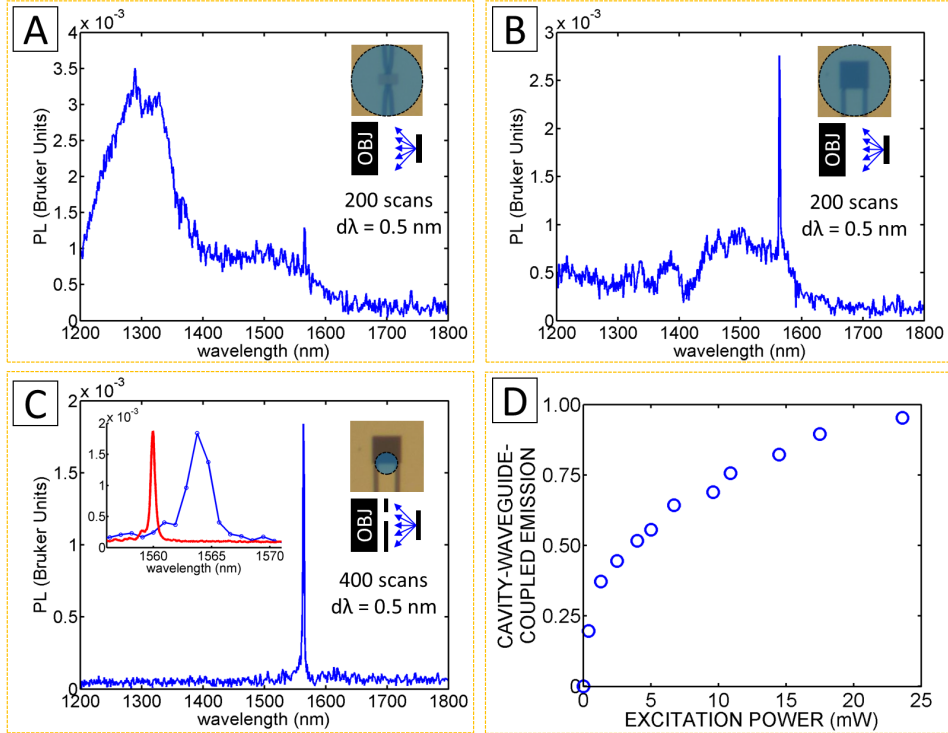


Figure 4.5: Example steady-state μ PL for excitation with several mW of Nd:YAG laser focused onto the cavity region with a $1/e^2$ power waist of $20 \mu\text{m}$. (A): PL collected over the cavity region. (B): PL collected over the grating region. (C): Apertured (both near and far) spectrum collected over part of the grating region, with a transmission plot (red) of the PIC, measured prior to CQD integration. (D): Power-saturation of the circuit-coupled, cavity-enhanced CQD PL, collected from the grating using the apertures per (C).

waist of $20 \mu\text{m}$, saturation power on the order of a mW, and the CQD absorption coefficient at 1064 nm excitation is $5/\text{cm}$, thus the differences in beam waist and absorption coefficient compensate for the $\sim 10^3$ difference in saturation powers between the two scenarios.

Figure 4.6 contains both time-averaged PL spectra and time-resolved, spectrally averaged decay plots obtained using the pulsed Sepia II 660 nm

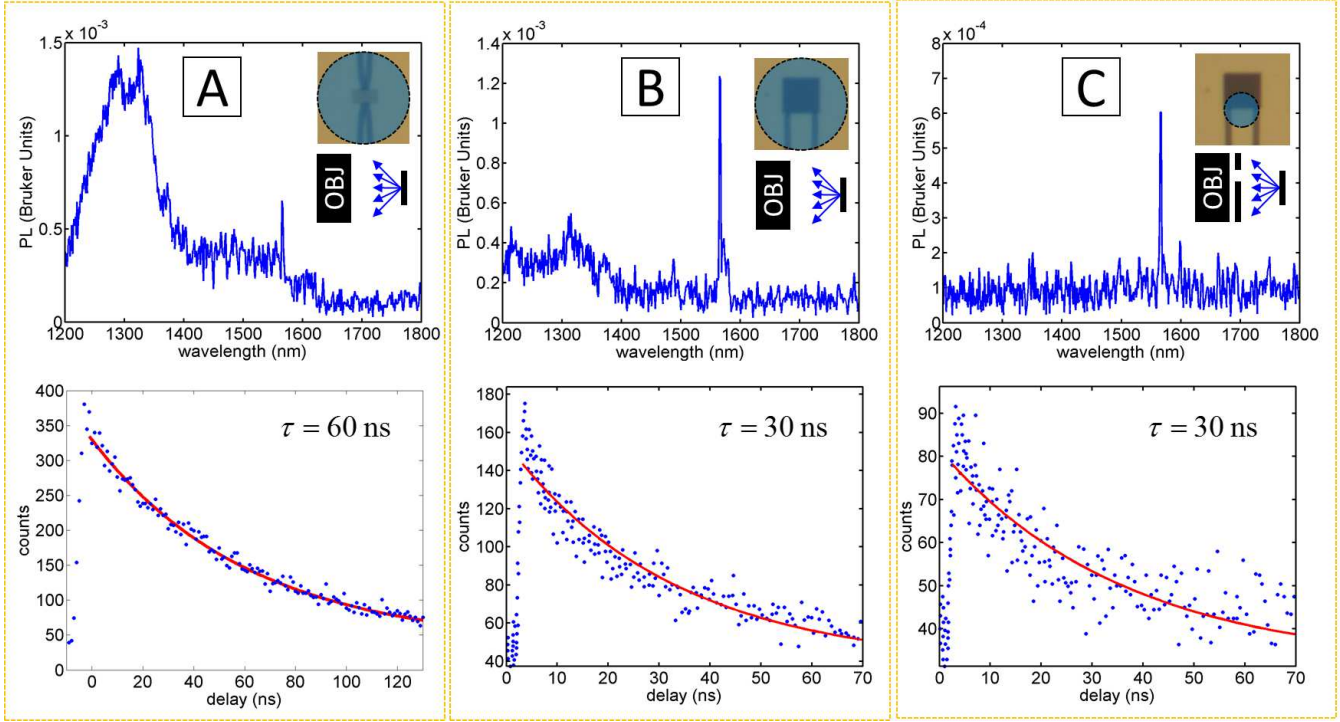


Figure 4.6: Example spectra (200 FTIR scans, 1 nm resolution) and time-resolved decay (with superimposed single exponential decay fits) of PL collected, for excitation with the 660 nm Sepia pulsed laser source with $1/e^2$ power waist of $3.5 \mu\text{m}$, 10 MHz repetition rate (1 MHz for collection from the cavity region), and ≈ 0.05 mW average incident power. Background PL spectra with the Sepia laser excitation differ from background PL spectra with the 1064 nm Nd:YAG excitation, which is not unexpected given differences in excitation spot size, intensity, and wavelength. The single exponential $1/e$ decay times for PL collected from the gratings are 30 ns, but don't capture the faster decay at short time scales. Decay from the cavity region is characterized by a $1/e$ decay time of 60 ns.

laser. The excitation source had a $1/e^2$ power waist of $3.5 \mu\text{m}$, 10 MHz repetition rate (1 MHz for collection over cavity region), and ≈ 0.05 mW incident power. Gated detection was performed with 5.00 ns gate width, 10% internal detector quantum efficiency (best available for gated operation),

and 100 ns dead time. The gate width is an effective width defined in the ID210 manual, not a strict rectangular apodization, so the temporal resolution appears better than the quoted 5 ns gate width. The time delay was controlled by sending the sync out of the Sepia power unit to a HP function generator controlled by a Matlab script that incremented the delay every 2 seconds. This script was started manually at the same time a script was run on the ID210, in which the ID210 integrated counts for 2 seconds, stored the result, then repeated. The width of the rising edge in the time-resolved PL curves is equal to this 2 to 3 ns value. No spectral filtering (free space or in-line) was performed for the results in Figure 4.6. Spectra obtained with the pulsed Sepia excitation are similar to those observed with Nd:YAG excitation, with some differences in the background spectral shape, which was not unexpected given the differences in excitation wavelengths.

The PL decay times of \approx 30 ns for PL collected from the grating region are significantly lower than observed for the thin or thick films of CQDs on bare silicon or SOI substrates. Since the microcavity PL only contributes a small portion to the total PL in these PL curves, the signal contributing to this decay is dominated by non-cavity coupled background PL and the short lifetime must be representative of another lifetime shortening process. Collection of PL from the cavity region, exhibiting a decay time of 60 ns, slightly less than the short decay time of 90 ns obtained for CQDs in a thin film formulation in Section 2.5. These results are discussed further at the end of this chapter.

Attempts to narrow down the dominant locations of the μ PL were made, including excitation upon areas other than the cavity region and collection from small areas other than centered on the cavity or grating. No PL was detectable when collecting and exciting over a coincident location on or near the gratings or tapered waveguides, and instead the background PL was coming from somewhere around the cavity region but possibly as far away as from stray CQDs on the PhC waveguides or single mode ridge waveguides. This is not unexpected since, even with the small excitation beam waist, excitation light is easily scattered off the highly textured PhC structures.

4.2.3 Photon coincidence

Basic principle

Photon coincidence measurements are the de facto method for determining whether a photon source emits only one photon at a time. The experimental setup for such measurements, illustrated in Figure 4.7, typically consists of a Hanbury, Brown and Twiss (HBT) configuration in which emission from the source of interest is sent to a beam splitter, the two outputs of which are sent to two single photon detectors, the outputs of which are then sent to a time correlator that keeps track of photon coincidence events.

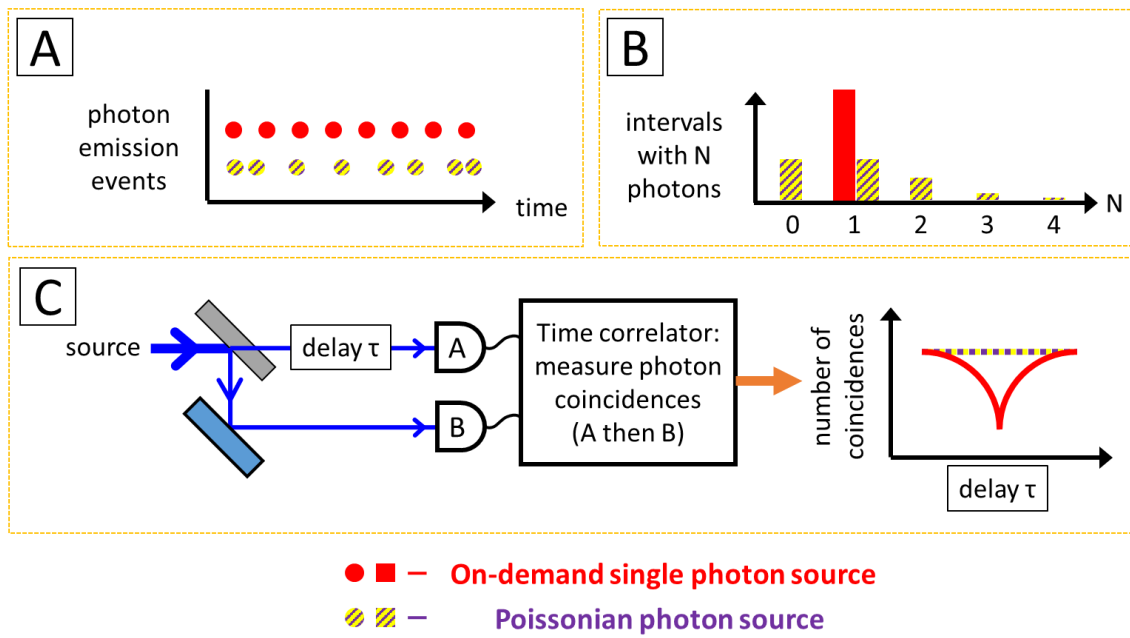


Figure 4.7: (A): Idealized stream of regularly emitted on-demand photons (red) compared to a stream of photons exhibiting photon bunching. (B): Histogram of photons within a fixed time interval for a Poissonian source (striped yellow, purple) and an ideal stream of regularly emitted photons from an on-demand source. (C): Basic photon coincidence setup to test if a source emits only a single photon at a time.

Coincidences in the HBT setup correspond to the number of times an event is measured on one counter then another within the same time bin, as a function of time delay between photon arrivals. Because an ideal single photon source does not emit more than one photon at a time, for zero path length difference between the source and the two detectors the coincidence rate theoretically drops to zero. The dip arising is a form of *antibunching*, corresponding to less “bunching” (more photons than average observed in a time interval) seen in Poissonian or thermal processes. Testing for this dip, or evidence of antibunching, is a key test of a single photon source.

Ideal versions of our PIC samples would send cavity-collected emission equally to each of the diffraction gratings, as a 50/50 beam splitter in a HBT setup. Thus by imaging the emission from the two grating couplers to two distinct single photon counters, the HBT experiment can be done without an external beam splitter. Ideally, the PIC would emit light from both gratings that only arrived at the grating coupler via the cavity and waveguide. The spectra from the grating regions would then consist of only a narrow peak at the cavity wavelength, and the signals could be sent directly to two single photon counters. In lieu of these idealized spectra, a good candidate PIC would exhibit large ratios of cavity-coupled PL to background PL at the cavity wavelength for PL collected from either grating. The PIC that best fit these criteria exhibited grating-collected spectra plotted in Figure 4.8. The ratio of PL at the cavity wavelength relative to slightly detuned from the cavity wavelength was 5 for collection from either grating, as indicated in the insets (raw spectral shown, but proper spectral background subtraction was required for this calculation).

Since there was significant background signal over a broad spectral range even using the two sets of apertures, spectral filters were added. Tunable narrow band pass (1.2 nm FWHM, Lorentzian lineshape $T_{FF}(\lambda; \lambda_0)$) fiber filters (FF in Figure 4.2) from Koshin Kogaku were used to preferentially pass the cavity-wavelength emission (of FWHM 1 nm). However, because background PL was significant outside the designed operating wavelength range of the fiber filters, additional spectral filtering was required. Free space band pass filters (FSF in Figure 4.2) of 50 nm bandwidth centered at 1575

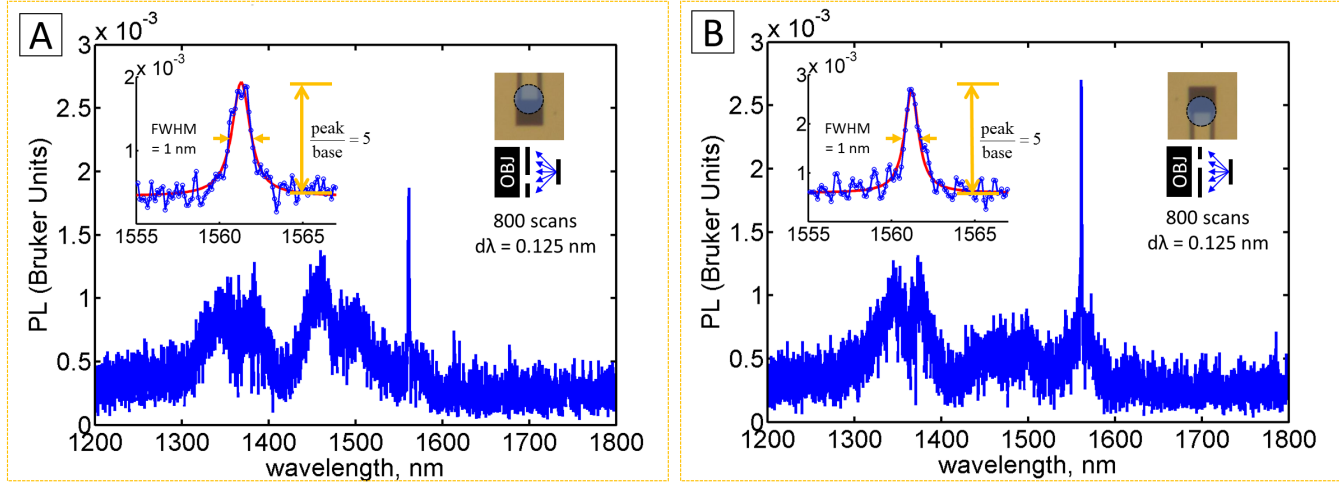


Figure 4.8: (A) and (B): PL spectra collected from diffraction gratings connected to the same cavity, for the cavity excited with pulsed 660 nm Sepia light, as used for coincidence measurements described later in this chapter, and *before* any spectral filtering was performed. See Figure 4.9 for spectral filtering performed. Insets are the same spectra, plotted over a smaller wavelength range around the cavity wavelength, with Lorentzian fits and indicated ratio of peak PL to background PL at the cavity wavelength (after proper baseline subtraction). Spectra are noisier than those presented previously in this section due to a higher spectral resolution relative to a number of FTIR scans. Each cavity to background ratio for this sample is smaller than for the samples in previous sections, but this sample was the only, at the time of measurements, from which cavity coupled PL collected from both gratings dominated the total PL signal at the cavity wavelength.

nm and OD4 (optical density 4) blocking outside the bandpass region from Edmunds were added to the free space to fiber assemblies (FFA) to achieve this additional spectral filtering. To optimize the ratio of cavity-coupled PL sent to the ID210 detectors, a robust alignment procedure, described in the subsection below along with spectral filtering results was required.

Optical alignment and results

Several alignment methods were attempted to optimize this ratio of cavity-coupled PL to background PL on the ID210 detectors. The most successful method, in terms of (a) the best ID210 on-cavity-wavelength PL detection rates, and (b) maximal ratios of on-cavity-wavelength PL to off-cavity-wavelength PL measured on the ID210, is as follows:

1. Prior to the steps below, ensure the fiber filter cartridges are tuned to the cavity wavelength by (a) performing a Bruker FTIR spectrum that resolves the cavity-coupled light, (b) diverting attenuated laser light towards the Bruker FTIR to make sure the laser output spectrum peak coincides with the cavity wavelength peak, (c) divert the tunable laser light towards the fiber tip in the free-space located in the free-space to fiber, and ensure only laser light is entering the fiber, and (d) tune the fiber filter cartridge to optimize ID210 count rate.
2. Perform an optimization using Bruker FTIR spectra. Positions of the apertures F_{AL} and F_{AR} were adjusted such that the peak solid angular density (e.g. power propagated per solid angle) cavity-coupled light passed through the center of each aperture. The excitation optics were then verified as positioned to optimize this cavity coupled PL collected from the gratings, without any adjustment to the collection optics, for Sepia pulsed laser excitation with 80 MHz rep rate. The far aperture diameter was chosen to be as large as possible without degrading the cavity-coupled to background PL ratio (at the cavity wavelength) by more than 10%.
3. Close down the far apertures very tightly, set the tunable laser output

to the cavity wavelength, send the laser light into the excitation lens assembly (Sepia pulsed laser off, excitation optics not moved relative to step (1), and scatter this laser light off the sample surface. Then, put the already designed/optimized apertured plate (AP) in position, to ensure the scattered laser light collected is collected at the same angle the cavity-coupled PL emanates from the grating (i.e. to mimic the cavity PL as best as possible).

4. Begin optimization of alignment on ID210 count rates (in free running detection mode). With no focusing lens of the free space to fiber assemblies (FFA) in place, iteratively adjust the angle of the KM_R and KM_L mirrors and position of the fiber tip such that (a) the peak solid angular density (e.g. power propagated per solid angle) is centered on the fiber tip, as indicated by the count rate on the ID210 detector, and (b) insertion of focusing lens does not displace the peak solid angular density off of the center of the fiber tip. This step ensures cavity-wavelength laser light, collected from the sample at the same angle as cavity-wavelength light emanating from the diffraction grating, is collected along a single collection path that is aligned with the fiber axis near the fiber entrance. Ideally this is done with cavity-wavelength PL collected from the diffraction grating, but the signal is not strong enough to practically align the system (if at all, given the finite mechanical drift).
5. The focusing lens was then translated along the collection path, relative to the fiber tip, to maximize ID210 count rate. It was then verified that the focusing lens is still along the collection path established in step (3) by verifying that small displacements of each of the optical elements perpendicular to the collection path established in (3) decreases the ID210 count rate. It was then verified that, for larger far aperture diameters, each of the optical elements are optimally (regarding ID210 count rates) positioned (i.e. that small displacements of any of these elements degrades ID210 count rates).

6. Now, turn the laser light off and Sepia pulsed laser back on (still at 80 MHz). Set the far aperture diameter to value established earlier. Set the ID210 to gated mode, using the sync out of the Sepia system. The internal delay of the ID210 was adjusted to identify the delay at which the peak ID210 rate relative to minimum ID210 rate is largest (corresponding to the leading excitation pulse edge), and the other ID210 settings (gate width, dead time) were adjusted to maximize the PL rate on the ID210 detector. The internal delay was adjusted again to make sure PL detection rate is optimal.
7. After optimizing the ID210 parameters in step (5), adjust the position of the free-to-fiber focusing lens position, along the collection path, to optimize the ID210 PL detection rate, then iterate (5) and (6) again to make sure ID210 detection settings and the collection path settings are jointly optimized for peak PL detection rate on the ID210.

After alignment, the on-cavity wavelength, off-cavity wavelength ratio was tested by tuning the fiber filter through the cavity PL wavelength. The ratio obtained was 3 for collection from either grating under conditions where the spectra from the gratings were as in Figure 4.8. This value is less than the value of 5 observed in the FTIR spectra in Figures 4.8, and is explained (and limited) by the finite band pass spectral width of the fiber filters, as illustrated in Figure 4.9, in which the observed grating-collected spectra $S(\lambda)$ from Figures 4.8A and B are multiplied by the filter transmission spectra $T_{FF}(\lambda; \lambda_0)$ and $T_{FSF}(\lambda)$. Symbolically:

$$\frac{\int d\lambda S(\lambda)T_{FSF}(\lambda)T_{FF}(\lambda; \lambda_{cav})}{\int d\lambda S(\lambda)T_{FSF}(\lambda)T_{FF}(\lambda; \lambda_{cav} + \delta\lambda)} \approx 3 \quad (4.1)$$

The $1/e$ lifetimes of PL measured for the fiber filter tuned to the cavity wavelength and slightly detuned from it were measured by monitoring the photon detection rates while adjusting the internal photon detector delays. When the fiber filter was slightly detuned from the cavity wavelength, the

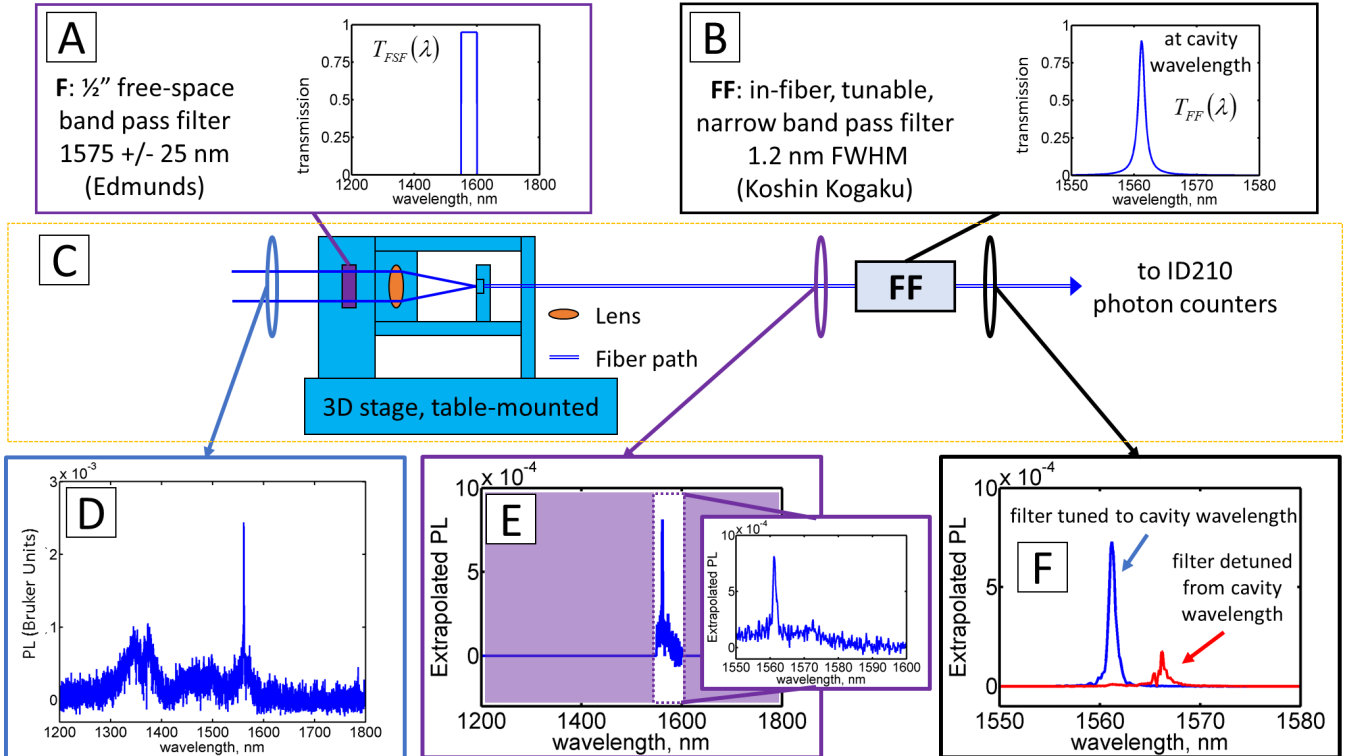


Figure 4.9: Spectral filtering used for coincidence measurements. (A): The band pass free-space filter (FSF) from Edmunds blocks (with OD4) all but the wavelength range 1550 nm to 1600 nm. (B): The tunable narrow band pass fiber filter (FF) from Koshin Kogaku possesses an approximately Lorentzian lineshape with 1.2 nm FWHM and can be tuned to the cavity wavelength. (C): Schematic of the free-space to fiber coupler assembly and in-line fiber filter (FF), with pre- and post- filtering locations, as plotted in (D) through (F), circled. (D): Example measured spectrum (from Figure 4.8B) before spectral filtering. (E): Extrapolated PL after propagating the spectrum through the free space filter and into the fiber, using the measured pre-filter spectrum $S(\lambda)$ and free space filter transmission spectrum $T_{FSF}(\lambda)$, as well as the measured free-space to fiber coupling efficiency. (F): Extrapolated PL, after both the free space and fiber filters, using the filter transmission spectra $T_{FF}(\lambda; \lambda_0)$ and $T_{FSF}(\lambda)$, and exemplified for the tunable filter both tuned to the cavity wavelength and slightly detuned from it.

$1/e$ decay time was ~ 25 ns, comparable to the 30 ns measured for grating-collected PL in the previous subsection. When the fiber filter was tuned to the cavity wavelength, the $1/e$ decay time was ~ 10 ns, much smaller and likely limited at least in part by the detection gate width (4.00 ns FWHM). These lifetimes are consistent with the cavity photon decaying on a sub-nanosecond timescale associated with the cavity Q , and the $1/e$ decay time of signal at the cavity wavelength being a weight sum of this fast (likely detector limited) decay and the slower background PL decay. With the spectral input of the ID210 detectors understood, coincidence events were measured to test for antibunching.

Coincidence results

Settings for photon coincidence measurements were as follows: excitation at a repetition rate available of 80 MHz with an average pump power of 0.4 mW, detector settings of 4.00 ns effective gate width, gates triggered at the 80 MHz sync signal output of the excitation laser, dead time of 0.1 μ s, and internal efficiency of 10% (largest available). Results presented below are for these settings, but other detector and excitation settings were explored. ID210 dark count rates from the two gratings were 2.7 KHz and 3.7 KHz and detection rates were 0.4 KHz and 0.5 KHz in gated detection mode. In each case, the detection rate on each ID210 was maximized by adjusting the internal ID210 detection gate temporal delay. The detection events on each ID210 were sent to the PicoHarp 300 time correlator, which kept track of coincidence events, i.e. detection events from one ID210 detector relative to the other ID210, as a function of time of arrival between the detection events. The time correlator was operated in time-tagged mode, in which a time stamp was recorded for each photon detection event, and the coincidence rate calculated after data collection was complete. The time bins were 0.512 ns in width (setting the timing resolution) and a total of $\sim 65,000$ time bins recorded. The longest integration time was 28000 seconds (8 hours).

Example coincidence plots are presented in Figure 4.10, in which coincidences were binned at each excitation pulse. No evidence of antibunching

of luminescence at the cavity wavelength was observed over a wide range of detector and excitation settings.

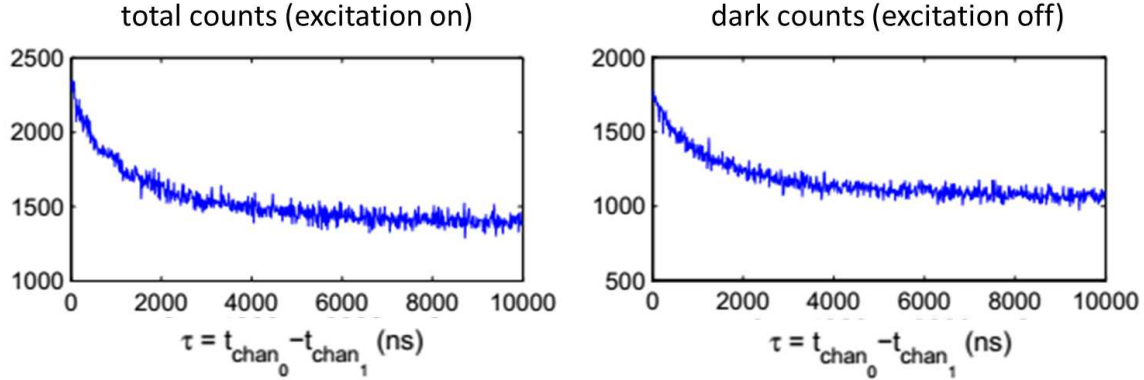


Figure 4.10: Example coincidence plots for total count rate (dark counts plus signal), dark counts only, and the difference of the two. No evidence of antibunching was found for detection and excitation settings considered.

4.3 Discussion

The total (combined) count rate from the single photon detectors under the optimal contrast conditions was 900 counts per second, with $\approx 2/3$ of these attributable to the cavity coupled photons, i.e. 600 counts per second. Even though it was not shown that the photons contributing to this signal were characteristic of a single photon source, it is useful to work backward to estimate the (more relevant) corresponding photon current in the silicon channel waveguide in order to estimate potential performance as an integrated single photon source. We then estimate and compare results to the expected waveguide photon current for a hypothetical single CQD in the PIC cavity, using results of previous chapters.

4.3.1 Extrapolation of PIC-coupled photon rate

A photon emitted into the cavity mode may decay into one of several channels, e.g. directly into free space or into the adjacent photonic crystal wave-

uides. A combination of modeling and characterization of PICs fabricated in the same process at the same foundry, presented in references [189], reports grating to grating peak transmission of 2.6%, and 20% grating coupling efficiencies, from which we can extract the probability a photon passing from waveguide to waveguide to be $0.026/0.2^2 = 0.65$ and the probability of a cavity photon ending up in a waveguide (either of them) to be ~ 0.80 , or 0.4 for a particular waveguide. The probability of a cavity photon to be diffracted out of a specific grating is then $0.4 \times 0.2 = 0.08$, and to be diffracted off-chip 0.16.

Between the grating and the detector are numerous collection optics characterized as follows (refer to Figure 4.2): reflecting objective ($\sim 50\%$), polarizer (95%), mirrors $M_{T1,T2}$ (97% each), mirror $KM_{L,R}$ (97%), and free space to fiber couplers plus fiber filter peak (30%, measured directly). The fiber filter (1.2 nm FWHM, approximately Lorentzian lineshape) passes $\approx 60\%$ of the cavity-coupled PL (1.0 nm FWHM, approximately Lorentzian lineshape). The resulting overall grating to detector efficiency is $\approx 8\%$.

Once at the detector, the probability of detection is tied to the internal quantum efficiency (10% for gated operation) and gate time (4.00 ns) relative to the cavity photon decay time (inversely proportional to the cavity Q). Since the latter is sub-nanosecond, there is no degrading of the efficiency due to the finite gate width.

Overall, the off-chip collection optics and detectors admit a $0.08 \times 0.1 = 0.008$ probability of photon detection. Combining this with the on-chip probability of 0.16, the probability of a cavity photon being detected is ≈ 0.0013 , or ≈ 0.0006 per detector when assuming the cavity photon has equal probability of arriving at either detector.

Using the 600 counts per second total PIC-coupled PL on the detectors, this corresponds to a cavity photon generation rate of ≈ 500 KHz and total waveguide photon generation rate of ≈ 400 KHz, or ≈ 200 KHz per waveguide.

4.3.2 Estimated single CQD results

We now estimate what the theoretical waveguide flux of cavity-coupled photons should be by making use of the the standalone cavity results from Chapters 2 and 3, in which the calculated cavity-CQD scattering rate was ~ 0.8 MHz, the radiative decay rate into other modes was ~ 0.4 MHz, and the extracted trap state lifetime was $\sim 3 \mu\text{s}$.

If we use the same values for a CQD in our PIC cavity and combine it with the observed ~ 60 ns PL decay time (or 16.7 MHz decay rate) for CQDs in the cavity region extracted in Figure 4.6A, the branching ratio of exciton decay into the cavity mode is $(0.8 \text{ MHz})/(16.7 \text{ MHz}) \approx 0.05$. Using also a $\sim 3 \mu\text{s}$ trap state lifetime which on average (for the low radiative efficiency) restricts exciton decay to the ground state and thus exciton generation to a rate of less than $\sim 1/(3 \mu\text{s}) \sim 0.3$ MHz, the corresponding maximum cavity photon generation rate is $\sim 0.05 \times 3 \text{ MHz} \sim 15 \text{ KHz}$. Using the ~ 0.8 probability of a cavity photon entering a waveguide, the estimated (maximum) rate of photons emitted by a single CQD within the PIC cavity is $\sim 10 \text{ KHz}$. If we consider the range of trap state lifetimes extracted in Chapter 3, $\tau_{\text{trap}} \approx 3^{+3}_{-2} \mu\text{s}$, the rate of cavity photons generated spans to ≈ 8 to 50 KHz , and the rate into a specific waveguide is ≈ 3 to 20 KHz .

Note that some model assumptions may bear on these estimates. For example, at least one research group reported photoluminescence from PbX CQDs integrated into a silicon photonic environment larger than could be explained when accounting for depolarization, local photonic density of states, and collection optics [133]. If such an enhancement were to depend on the number of CQDs, e.g. mediated by interdot coupling, then extrapolation of the multiple CQD results to a single CQD would not necessarily hold.

4.3.3 Comparisons and potential use as a single photon source

Comparing the estimated PIC-coupled photon rate in a single waveguide, for a single CQD in the PIC cavity of ≈ 3 to 20 KHz and the photon rate in a single waveguide extrapolated from measured count rates and measured

photon transmission and detection efficiencies of ≈ 200 KHz, it is estimated that there are on the order of at least $200/20 = 10$ (but fewer than $\sim 10^2$) CQDs significantly coupled to the PIC cavity mode. Using an estimated $\sim 500 \text{ nm}^2$ area in which the cavity mode profile is significant on the silicon surface (e.g. see Figure 2.1), this corresponds to a CQD area density of $\sim (10 \text{ to } 100)/(5 \times 100 \text{ nm}^2) \sim 200 \text{ to } 2000$ CQDs per square μm , or average CQD spacing of ~ 20 to 70 nm.

For the coincidence measurement, we seek reduced photon coincidences (a dip) in the curve due to the unavailability of more than one photon emitting from the cavity within the duration of the time bin used. For a single CQD in the PIC cavity, there are two time constants relevant to this availability factor, the net exciton lifetime (~ 60 ns in the cavity region), and the trap lifetime, estimated from the saturation behavior to be $\sim 3 \mu\text{s}$. A detailed model for the expected coincidence behavior for this 4 state system, including the relatively large contribution of background and dark counts, was not developed as part of this dissertation. All that can be concluded from the data in Figure 4.10 at this point is that there is no obvious signature of antibunching on either of these timescales.

Even if a low radiative efficiency CQD with a long trap lifetime could be shown to exhibit antibunching, the present estimated flux of maximum 50 KHz is not ideal. This low rate could potentially be increased with better coupling to the cavity, and a method for minimizing depolarization effects, e.g. as considered in part of Section 3.5. This obviously would require major redesign of the cavity and probably a modified hybrid integration strategy.

Chapter 5

Conclusions

The broad motivation of this dissertation was to develop on-demand single photon sources integrated into silicon-based photonic integrated circuits (PICs), which could be used to advance a variety of quantum information processing experiments and applications. The approach involved the hybrid integration of PbSe CQDs on the surface of L3 photonic crystal microcavities coupled symmetrically to two single TE mode silicon channel waveguides, the ends of which were connected to grating couplers for diffracting waveguide-bound light off chip.

Excitonic emission for incoherently photoexcited PbSe CQDs was successfully captured as photons in the fundamental mode of an L3 cavity as evidenced by (a) their scattering directly into the top half space from the cavity, and (b) their coupling to the single mode waveguides, then off-chip. The power dependence of the cavity-coupled PL signal was thoroughly characterized in both cases, in conjunction with separate studies of the PbSe CQD emission on bare silicon or SOI surfaces. From all of these measurements and modeling efforts, the following conclusions and outlook for future work emerged.

5.1 Conclusions, discussion and significance

If the performance-limiting trap state could be eliminated, the best possible rate of coupling single photons into the single channel waveguide by placing the CQD on the surface of an L3 could be as high as ~ 0.6 MHz (assuming ~ 0.8 probability of cavity to waveguide transfer), limited then by depolarization effects and the intrinsic dipole transition moment. Somehow embedding the CQD at the maximum field position of the L3 cavity fundamental mode would improve this by close to a factor of 9, bringing the emission rate up to ≈ 6 MHz (excluding improvements to depolarization effects).

Several depolarization effects were identified and subtly combined to coincidentally result in a depolarization effect for a CQD in the L3 cavity similar the depolarization effect in solution. These included the presence of the silicon slab, L3 texture, nearby CQDs, and far-field permittivities (e.g. solvent, vacuum, silicon). Depolarization effects still greatly limited potential CQD performance; if, for example, the CQD were embedded in silicon, the CQD emission rate could be increased by a factor of ≈ 11 (beyond the 9-fold improvement due to the mode overlap).

Even if the trap state were eliminated and the CQD were embedded in silicon, the resulting emission rate of $\sim 6 \times 11$ MHz = 66 MHz falls short of best available GHz emission rates of III-V epitaxial CQDs, due to a smaller “intrinsic” dipole moment as discussed in Chapter 3.

Separate studies of the PbSe itself revealed that the radiative efficiency decreases monotonically from in-solvent ($\sim 30\%$), to thick-film ($\sim 20\%$) where the CQDs are presumably in a bath of oleic acid, and on-silicon ($\sim 4\%$ to 10%). Again, proper treatment of depolarization factors was essential for extracting these efficiencies.

Temperature-dependent studies indicate that the quantum yield at least in thick film form, increases by up to 3 to 10 times at cryogenic temperatures, at least for our PbSe CQDs (3 to 5 for CQDs specifically used in this dissertation). Reports from other groups (without quantum yield values quoted), show less temperature dependence and in some cases larger PL at room temperature [93], which suggest possible changes in synthesis that

could improve room temperature performance.

The self-consistency of the methodology (modeling and experiment) and results of all the studies within this dissertation also provide a robust basis for building upon these results in a variety of directions, described in the following section. In sum, the work in this dissertation provides experimental results, general and extensible modeling, and demonstrations that advance understanding of and use of PbX CQDs in SOI PICs in conditions relevant to realization of SOI PIC-integrated, on-demand single photon sources.

5.2 Limitations, strengths, and future work

Viability of PbX CQDs as a single photon emitter in SOI PICs is contingent upon substantial synthesis strategy improvements capable of reducing the non-radiative recombination rate on silicon. If this is shown possible, then using such CQDs with the site-selective binding technique in our lab to ensure only one CQD at cavity antinode, could possibly produce an on-demand SPS compatible with SOI circuits, at roughly a rate of 600 KHz.

If coincidence measurements on such a new sample yielded promising results, this could motivate investigation of alternate cavities (e.g. slot waveguides) to improve CQD-cavity coupling. Similarly, a post-integration, encapsulation process could be used to reduce depolarization effects in such a cavity. Mitigation of depolarization effects could potentially raise the source rate by another order of magnitude and, along with improved CQD-cavity coupling could be combined to improve the emission rate to tens of MHz in conceivable scenarios. These scenarios assume that the ground state manifold of excitons in these new formulations are not overly complex (a wide energy distribution of high oscillator strength transitions), something that experiments would ultimately have to decide.

Alternatively, the spherical PbSe CQDs used in this dissertation could readily be replaced with something similar to a III-V nanowire with QD in-wire [49], the intrinsic dipole moment of which should be superior, and for which epitaxial radial encapsulation might be expected to maximize quantum yield, at the cost of cryogenic operation. “Nanoplatelet” formulations

of PbSe CQDs may also offer improved oscillator strength and radiative efficiency, although it isn't clear that they would be good candidates for single photon emission. The modeling and general processes and characterization techniques developed and described in this dissertation would be directly transferable to that scenario.

In all, the work in this dissertation both significantly advances knowledge of PbX CQD emission, particularly as relevant to their use in on-demand single photon emitters in SOI PICs, and provides tools and readily relatable results to advance these aims further, e.g. through emitter- or SOI photonic-specific improvements as pursued by our laboratory and others.

Bibliography

- [1] IMEC. URL <http://www.imec.be/>. Accessed January 14th, 2016. → pages 115
- [2] WestGrid. URL <http://www.westgrid.ca/>. Accessed January 14th, 2016. → pages xxvii
- [3] ePIXfab. URL <http://www.epixfab.eu/>. Accessed January 14th, 2016. → pages 115
- [4] S. Aaronson and A. Arkhipov. The computational complexity of linear optics. In *Proceedings of the Forty-third Annual ACM Symposium on Theory of Computing*, STOC '11, pages 333–342, New York, NY, USA, 2011. ACM. ISBN 978-1-4503-0691-1.
[doi:10.1145/1993636.1993682](https://doi.org/10.1145/1993636.1993682). → pages 6
- [5] J. Aasi, J. Abadie, B. P. Abbott, R. Abbott, T. D. Abbott, M. R. Abernathy, C. Adams, T. Adams, P. Addesso, R. X. Adhikari, C. Affeldt, O. D. Aguiar, P. Ajith, B. Allen, E. Amador Ceron, D. Amariutei, S. B. Anderson, W. G. Anderson, K. Arai, and M. C. Araya. Enhanced sensitivity of the LIGO gravitational wave detector by using squeezed states of light. *Nature Photonics*, 7(8):613–619, Aug. 2013. ISSN 17494885. [doi:10.1038/nphoton.2013.177](https://doi.org/10.1038/nphoton.2013.177). → pages 6
- [6] K. A. Abel. *Synthesis and Characterization of Colloidal Lead Chalcogenide Quantum Dots and Progress towards Single Photons On-Demand*. PhD thesis, University of Victoria, 2011. → pages 53
- [7] K. A. Abel, H. Qiao, J. F. Young, and F. C. J. M. van Veggel. Four-Fold enhancement of the activation energy for nonradiative decay of excitons in PbSe/CdSe Core/Shell versus PbSe colloidal quantum dots. *The Journal of Physical Chemistry Letters*, 1(15):2334–2338, Aug. 2010. ISSN 1948-7185. [doi:10.1021/jz1007565](https://doi.org/10.1021/jz1007565). → pages 44, 80

- [8] I. Aharonovich, A. D. Greentree, and S. Prawer. Diamond photonics. *Nature Photonics*, 5(7):397–405, July 2011. ISSN 1749-4885. [doi:10.1038/nphoton.2011.54](https://doi.org/10.1038/nphoton.2011.54). → pages 19
- [9] M. K. Akhlaghi, E. Schelew, and J. F. Young. Waveguide integrated superconducting single-photon detectors implemented as near-perfect absorbers of coherent radiation. *Nature Communications*, 6(8233), Sept. 2015. [doi:10.1038/ncomms9233](https://doi.org/10.1038/ncomms9233). → pages xiv, 4, 29, 30
- [10] A. P. Alivisatos. Semiconductor clusters, nanocrystals, and quantum dots. *Science*, 271(5251):933–937, Feb. 1996. [doi:10.1126/science.271.5251.933](https://doi.org/10.1126/science.271.5251.933). → pages 43
- [11] G. Allan and C. Delerue. Confinement effects in PbSe quantum wells and nanocrystals. *Physical Review B*, 70(24):245321, Dec. 2004. ISSN 1098-0121. [doi:10.1103/PhysRevB.70.245321](https://doi.org/10.1103/PhysRevB.70.245321). → pages 43
- [12] J. M. An, A. Franceschetti, and A. Zunger. The excitonic exchange splitting and radiative lifetime in PbSe quantum dots. *Nano Letters*, 7(7):2129, July 2007. ISSN 1530-6984. [doi:10.1021/nl071219f](https://doi.org/10.1021/nl071219f). → pages 74
- [13] J. M. An, M. Califano, A. Franceschetti, and A. Zunger. Excited-state relaxation in PbSe quantum dots. *J. Chem. Phys.*, 128(16):164720, 2008. ISSN 00219606. [doi:10.1063/1.2901022](https://doi.org/10.1063/1.2901022). → pages 83
- [14] A. D. Andreev and A. A. Lipovskii. Effect of anisotropy of band structure on optical gain in spherical quantum dots based on PbS and PbSe. *Semiconductors*, 33(12):1304, Dec. 1999. ISSN 1063-7826. [doi:10.1134/1.1187913](https://doi.org/10.1134/1.1187913). → pages 37
- [15] L. Arizmendi. Photonic applications of lithium niobate crystals. *phys. stat. sol. (a)*, 201(2):253–283, Jan. 2004. ISSN 1521-396X. [doi:10.1002/pssa.200303911](https://doi.org/10.1002/pssa.200303911). → pages 20
- [16] W. K. Bae, J. Joo, L. A. Padilha, J. Won, D. C. Lee, Q. Lin, W.-k. Koh, H. Luo, V. I. Klimov, and J. M. Pietryga. Highly effective surface passivation of PbSe quantum dots through reaction with molecular chlorine. *Journal of the American Chemical Society*, 134(49):20160–20168, Dec. 2012. ISSN 0002-7863. [doi:10.1021/ja309783v](https://doi.org/10.1021/ja309783v). → pages 43, 97

- [17] M. G. Banaee, A. G. Pattantyus-Abraham, M. W. McCutcheon, G. W. Rieger, and J. F. Young. Efficient coupling of photonic crystal microcavity modes to a ridge waveguide. *Applied Physics Letters*, 90(19):193106, May 2007. [doi:10.1063/1.2737369](https://doi.org/10.1063/1.2737369). → pages 27, 34, 51, 115
- [18] H. Bao, B. F. Habenicht, O. V. Prezhdo, and X. Ruan. Temperature dependence of hot-carrier relaxation in PbSe nanocrystals: An ab initio study. *Physical Review B*, 79(23):235306, June 2009. [doi:10.1103/PhysRevB.79.235306](https://doi.org/10.1103/PhysRevB.79.235306). → pages 83
- [19] A. Barenco, D. Deutsch, A. Ekert, and R. Jozsa. Conditional quantum dynamics and logic gates. *Physical Review Letters*, 74:4083–4086, May 1995. [doi:10.1103/PhysRevLett.74.4083](https://doi.org/10.1103/PhysRevLett.74.4083). → pages 7
- [20] S. M. Barnett, B. Huttner, and R. Loudon. Spontaneous emission in absorbing dielectric media. *Physical Review Letters*, 68(25):3698–3701, June 1992. [doi:10.1103/PhysRevLett.68.3698](https://doi.org/10.1103/PhysRevLett.68.3698). → pages 76
- [21] M. G. Bawendi, M. L. Steigerwald, and L. E. Brus. The quantum mechanics of larger semiconductor clusters (“quantum dots”). *Annual Review of Physical Chemistry*, 41:477–496, Oct. 1990. [doi:10.1146/annurev.pc.41.100190.002401](https://doi.org/10.1146/annurev.pc.41.100190.002401). → pages 43
- [22] C. H. Bennet and G. Brassard. Quantum cryptography: Public key distribution and coin tossing. In *IEEE International Conference on Computers, Systems, and Signal Processing, Bangalore*, page 175, 1984. → pages 6
- [23] O. Benson, C. Santori, M. Pelton, and Y. Yamamoto. Regulated and entangled photons from a single quantum dot. *Physical Review Letters*, 84(11):2513–2516, Mar. 2000. [doi:10.1103/PhysRevLett.84.2513](https://doi.org/10.1103/PhysRevLett.84.2513). → pages 33, 34
- [24] W. Bogaerts, D. Taillaert, B. Luyssaert, P. Dumon, J. Van Campenhout, P. Bienstman, D. Van Thourhout, R. Baets, V. Wiaux, and S. Beckx. Basic structures for photonic integrated circuits in silicon-on-insulator. *Optics Express*, 12(8):1583–1591, 2004. [doi:10.1364/OPEX.12.001583](https://doi.org/10.1364/OPEX.12.001583). → pages 19
- [25] C. Bonati, A. Cannizzo, D. Tonti, A. Tortschanoff, F. van Mourik, and M. Chergui. Subpicosecond near-infrared fluorescence upconversion study of relaxation processes in PbSe quantum dots.

Physical Review B, 76(3):033304, July 2007.
[doi:10.1103/PhysRevB.76.033304](https://doi.org/10.1103/PhysRevB.76.033304). → pages 83

- [26] D. Bonneau, E. Engin, K. Ohira, N. Suzuki, H. Yoshida, N. Iizuka, M. Ezaki, C. Natarajan, M. Tanner, R. H. Hadfield, S. Dorenbos, V. Zwiller, J. O'Brien, and M. Thompson. Quantum interference in silicon waveguide circuits. In *Group IV Photonics (GFP), 2011 8th IEEE International Conference on*, pages 1–3, 2011. → pages 23
- [27] D. Bonneau, E. Engin, K. Ohira, N. Suzuki, H. Yoshida, N. Iizuka, M. Ezaki, C. M. Natarajan, M. G. Tanner, R. H. Hadfield, S. N. Dorenbos, V. Zwiller, J. L. O'Brien, and M. G. Thompson. Quantum interference and manipulation of entanglement in silicon wire waveguide quantum circuits. *New Journal of Physics*, 14(4):045003, 2012. [doi:10.1088/1367-2630/14/4/045003](https://doi.org/10.1088/1367-2630/14/4/045003). → pages 20, 23
- [28] A. Boretti. Optical materials: Silicon carbide's quantum aspects. *Nature Photonics*, 8(2):88–90, Feb. 2014. ISSN 1749-4885. [doi:10.1038/nphoton.2013.375](https://doi.org/10.1038/nphoton.2013.375). → pages 20
- [29] P. Borri, W. Langbein, S. Schneider, U. Woggon, R. L. Sellin, D. Ouyang, and D. Bimberg. Rabi oscillations in the excitonic ground-state transition of InGaAs quantum dots. *Physical Review B*, 66(8):081306, Aug. 2002. [doi:10.1103/PhysRevB.66.081306](https://doi.org/10.1103/PhysRevB.66.081306). → pages 79
- [30] R. Bose, D. V. Talapin, X. Yang, R. J. Harniman, P. T. Nguyen, and C. W. Wong. Interaction of infiltrated colloidal PbS nanocrystals with high Q/V silicon photonic bandgap nanocavities for near-infrared enhanced spontaneous emissions. In H. H. Du, editor, *Photonic Crystals and Photonic Crystal Fibers for Sensing Applications*, volume 6005, page 600509. SPIE, Oct. 2005. [doi:10.1117/12.632900](https://doi.org/10.1117/12.632900). → pages 46
- [31] R. Bose, X. Yang, R. Chatterjee, J. Gao, and C. W. Wong. Weak coupling interactions of colloidal lead sulphide nanocrystals with silicon photonic crystal nanocavities near $1.55\text{ }\mu\text{m}$ at room temperature. *Applied Physics Letters*, 90(11):111117, Mar. 2007. [doi:10.1063/1.2714097](https://doi.org/10.1063/1.2714097). → pages 35, 46
- [32] R. Bose, J. F. McMillan, J. Gao, K. M. Rickey, C. J. Chen, D. V. Talapin, C. B. Murray, and C. W. Wong. Temperature-tuning of

near-infrared monodisperse quantum dot solids at $1.5\text{ }\mu\text{m}$ for controllable Förster energy transfer. *Nano Letters*, 8(7):2006–2011, 2008. [doi:10.1021/nl8011243](https://doi.org/10.1021/nl8011243). PMID: 18512994. → pages 68

- [33] R. Bose, J. Gao, J. F. McMillan, A. D. Williams, and C. W. Wong. Cryogenic spectroscopy of ultra-low density colloidal lead chalcogenide quantum dots on chip-scale optical cavities towards single quantum dot near-infrared cavity QED. *Optics Express*, 17(25):22474–22483, Dec. 2009. [doi:10.1364/OE.17.022474](https://doi.org/10.1364/OE.17.022474). → pages 46, 65
- [34] R. Bose, J. F. McMillan, J. Gao, and C. W. Wong. Solution-processed cavity and slow-light quantum electrodynamics in near-infrared silicon photonic crystals. *Applied Physics Letters*, 95(13):131112, Sept. 2009. [doi:10.1063/1.3238555](https://doi.org/10.1063/1.3238555). → pages 46
- [35] D. E. Browne and T. Rudolph. Resource-efficient linear optical quantum computation. *Physical Review Letters*, 95(1):010501, June 2005. [doi:10.1103/PhysRevLett.95.010501](https://doi.org/10.1103/PhysRevLett.95.010501). → pages 13
- [36] S. Buckley, K. Rivoire, and J. Vučković. Engineered quantum dot single-photon sources. *Reports on Progress in Physics*, 75(12):126503, 2012. [doi:10.1088/0034-4885/75/12/126503](https://doi.org/10.1088/0034-4885/75/12/126503). → pages 2, 4, 18
- [37] M. Calic, P. Gallo, M. Felici, K. A. Atlasov, B. Dwir, A. Rudra, G. Biasiol, L. Sorba, G. Tarel, V. Savona, and E. Kapon. Phonon-mediated coupling of InGaAs/GaAs quantum-dot excitons to photonic crystal cavities. *Physical Review Letters*, 106(22):227402, June 2011. [doi:10.1103/PhysRevLett.106.227402](https://doi.org/10.1103/PhysRevLett.106.227402). → pages 80
- [38] G. Calusine, A. Politi, and D. D. Awschalom. Silicon carbide photonic crystal cavities with integrated color centers. *Applied Physics Letters*, 105(1):011123, 2014. [doi:10.1063/1.4890083](https://doi.org/10.1063/1.4890083). → pages 20
- [39] R. A. Campos, B. E. A. Saleh, and M. C. Teich. Quantum-mechanical lossless beam splitter: SU(2) symmetry and photon statistics. *Physical Review A*, 40:1371–1384, Aug 1989. [doi:10.1103/PhysRevA.40.1371](https://doi.org/10.1103/PhysRevA.40.1371). → pages 14
- [40] J. Carolan, C. Harrold, C. Sparrow, E. Martín-López, N. J. Russell, J. W. Silverstone, P. J. Shadbolt, N. Matsuda, M. Oguma, M. Itoh, G. D. Marshall, M. G. Thompson, J. C. F. Matthews, T. Hashimoto,

- J. L. O'Brien, and A. Laing. Universal linear optics. *Science*, 349(6249), July 2015. [doi:10.1126/science.aab3642](https://doi.org/10.1126/science.aab3642). → pages 13, 19
- [41] J. M. Caruge, J. E. Halpert, V. Wood, V. Bulovic, and M. G. Bawendi. Colloidal quantum-dot light-emitting diodes with metal-oxide charge transport layers. *Nature Photonics*, 2(4):247–250, Apr. 2008. ISSN 1749-4885. [doi:10.1038/nphoton.2008.34](https://doi.org/10.1038/nphoton.2008.34). → pages 37
- [42] C. M. Caves. Quantum-mechanical noise in an interferometer. *Physical Review D*, 23(8):1693–1708, Apr. 1981. [doi:10.1103/PhysRevD.23.1693](https://doi.org/10.1103/PhysRevD.23.1693). → pages 6
- [43] H. E. Chappell, B. K. Hughes, M. C. Beard, A. J. Nozik, and J. C. Johnson. Emission quenching in PbSe quantum dot arrays by short-term air exposure. *The Journal of Physical Chemistry Letters*, 2(8):889–893, Apr. 2011. ISSN 1948-7185. [doi:10.1021/jz2001979](https://doi.org/10.1021/jz2001979). → pages xxii, 44, 69, 70, 71, 74, 97, 98, 99, 107
- [44] C. Cheng. A multiquantum-dot-doped fiber amplifier with characteristics of broadband, flat gain, and low noise. *Journal of Lightwave Technology*, 26(11):1404–1410, 2008. URL <http://jlt.osa.org/abstract.cfm?URI=jlt-26-11-1404>. → pages 37
- [45] H. Chew. Radiation and lifetimes of atoms inside dielectric particles. *Physical Review A*, 38(7):3410, Oct. 1988. ISSN 0556-2791. [doi:10.1103/PhysRevA.38.3410](https://doi.org/10.1103/PhysRevA.38.3410). → pages 76
- [46] H. Choi, J.-H. Ko, Y.-H. Kim, and S. Jeong. Steric-hindrance-driven shape transition in PbS quantum dots: Understanding size-dependent stability. *Journal of the American Chemical Society*, 135(14):5278–5281, Apr. 2013. ISSN 0002-7863. [doi:10.1021/ja400948t](https://doi.org/10.1021/ja400948t). → pages 43, 97
- [47] C. J. Chunnillall, I. P. Degiovanni, S. Kück, I. Müller, and A. G. Sinclair. Metrology of single-photon sources and detectors: a review. *Optical Engineering*, 53(8):081910, July 2014. [doi:10.1117/1.OE.53.8.081910](https://doi.org/10.1117/1.OE.53.8.081910). → pages 2
- [48] S. W. Clark, J. M. Harbold, and F. W. Wise. Resonant energy transfer in PbS quantum dots. *The Journal of Physical Chemistry C*, 111(20):7302–7305, May 2007. ISSN 1932-7447. [doi:10.1021/jp0713561](https://doi.org/10.1021/jp0713561). → pages 39

- [49] J. Claudon, J. Bleuse, N. S. Malik, M. Bazin, P. Jaffrennou, N. Gregersen, C. Sauvan, P. Lalanne, and J. Gérard. A highly efficient single-photon source based on a quantum dot in a photonic nanowire. *Nature Photonics*, 4(3):174–177, Jan. 2010. ISSN 1749-4885. [doi:10.1038/nphoton.2009.287](https://doi.org/10.1038/nphoton.2009.287). → pages 140
- [50] J. F. Clauser. Experimental distinction between the quantum and classical field-theoretic predictions for the photoelectric effect. *Physical Review D*, 9:853–860, Feb 1974. [doi:10.1103/PhysRevD.9.853](https://doi.org/10.1103/PhysRevD.9.853). → pages 17
- [51] J. P. Clifford, G. Konstantatos, K. W. Johnston, S. Hoogland, L. Levina, and E. H. Sargent. Fast, sensitive and spectrally tuneable colloidal-quantum-dot photodetectors. *Nat Nano*, 4(1):40–44, Jan. 2009. ISSN 1748-3387. [doi:10.1038/nnano.2008.313](https://doi.org/10.1038/nnano.2008.313). → pages 37
- [52] Collaboration: Authors and editors of the volumes III/17E-17F-41C. *Lead selenide (PbSe) effective masses, Fermi level.*, volume 41C: Non-Tetrahedrally Bonded Elements and Binary Compounds I. SpringerMaterials - The Landolt-Börnstein Database. [doi:10.1007/10681727_899](https://doi.org/10.1007/10681727_899). → pages 39
- [53] M. Collins, C. Xiong, I. Rey, T. Vo, J. He, S. Shahnia, C. Reardon, T. Krauss, M. Steel, A. Clark, and B. Eggleton. Integrated spatial multiplexing of heralded single-photon sources. *Nature Communications*, 4(2582), Oct. 2013. [doi:10.1038/ncomms3582](https://doi.org/10.1038/ncomms3582). → pages 34
- [54] M. Colocci, A. Vinattieri, L. Lippi, F. Bogani, M. Rosa-Clot, S. Taddei, A. Bosacchi, S. Franchi, and P. Frigeri. Controlled tuning of the radiative lifetime in InAs self-assembled quantum dots through vertical ordering. *Applied Physics Letters*, 74(4):564–566, Jan. 1999. [doi:10.1063/1.123146](https://doi.org/10.1063/1.123146). → pages 79
- [55] R. E. Correa, E. A. Dauler, G. Nair, S. H. Pan, D. Rosenberg, A. J. Kerman, R. J. Molnar, X. Hu, F. Marsili, V. Anant, K. K. Berggren, and M. G. Bawendi. Single photon counting from individual nanocrystals in the infrared. *Nano Letters*, 12(6):2953–2958, June 2012. ISSN 1530-6984. [doi:10.1021/nl300642k](https://doi.org/10.1021/nl300642k). → pages 35
- [56] B. O. Dabbousi, J. Rodriguez-Viejo, F. V. Mikulec, J. R. Heine, H. Mattoussi, R. Ober, K. F. Jensen, and M. G. Bawendi.

(CdSe)ZnS core-shell quantum dots: Synthesis and characterization of a size series of highly luminescent nanocrystallites. *J. Phys. Chem. B*, 101(46):9463–9475, Nov. 1997. ISSN 1520-6106.
[doi:10.1021/jp971091y](https://doi.org/10.1021/jp971091y). → pages 43

- [57] Q. Dai, Y. Wang, Y. Zhang, X. Li, R. Li, B. Zou, J. Seo, Y. Wang, M. Liu, and W. W. Yu. Stability study of PbSe semiconductor nanocrystals over concentration, size, atmosphere, and light exposure. *Langmuir*, 25(20):12320–12324, Oct. 2009. ISSN 0743-7463. [doi:10.1021/la9015614](https://doi.org/10.1021/la9015614). → pages 97
- [58] Q. Dai, Y. Zhang, Y. Wang, B. Zou, W. W. Yu, and M. Z. Hu. Ligand effects on synthesis and post-synthetic stability of PbSe nanocrystals. *The Journal of Physical Chemistry C*, 114(39):16160–16167, Oct. 2010. ISSN 1932-7447. [doi:10.1021/jp102660g](https://doi.org/10.1021/jp102660g). → pages 97
- [59] M. Davanço, J. R. Ong, A. B. Shehata, A. Tosi, I. Agha, S. Assefa, F. Xia, W. M. J. Green, S. Mookherjea, and K. Srinivasan. Telecommunications-band heralded single photons from a silicon nanophotonic chip. *Applied Physics Letters*, 100(26):261104, 2012. [doi:10.1063/1.4711253](https://doi.org/10.1063/1.4711253). → pages 20, 34
- [60] D. Deutsch. Quantum theory, the Church-Turing principle and the universal quantum computer. *Proceedings of the Royal Society A*, 400(1818):97–117, July 1985. [doi:10.1103/PhysRevB.90.035312](https://doi.org/10.1103/PhysRevB.90.035312). → pages 6, 7
- [61] I. Djordjevic. *Quantum Information Processing and Quantum Error Correction*. Academic Press, 2012. → pages 10
- [62] D. F. Dorfner, T. Hürlimann, G. Abstreiter, and J. J. Finley. Optical characterization of silicon on insulator photonic crystal nanocavities infiltrated with colloidal PbS quantum dots. *Applied Physics Letters*, 91(23):233111, 2007. [doi:10.1063/1.2822441](https://doi.org/10.1063/1.2822441). → pages 46
- [63] H. Du, C. Chen, R. Krishnan, T. D. Krauss, J. M. Harbold, F. W. Wise, M. G. Thomas, and J. Silcox. Optical properties of colloidal PbSe nanocrystals. *Nano Letters*, 2(11):1321, Nov. 2002. ISSN 1530-6984. [doi:10.1021/nl025785g](https://doi.org/10.1021/nl025785g). → pages 39, 43, 80
- [64] M. D. Eisaman, J. Fan, A. Migdall, and S. V. Polyakov. Invited review article: Single-photon sources and detectors. *Review of*

Scientific Instruments, 82(7):071101, 2011. ISSN 00346748.
[doi:10.1063/1.3610677](https://doi.org/10.1063/1.3610677). → pages 2, 17, 18

- [65] A. K. Ekert. Quantum cryptography based on Bell's theorem. *Physical Review Letters*, 67:661–663, Aug 1991.
[doi:10.1103/PhysRevLett.67.661](https://doi.org/10.1103/PhysRevLett.67.661). → pages 6
- [66] P. G. Eliseev, H. Li, A. Stintz, G. T. Liu, T. C. Newell, K. J. Malloy, and L. F. Lester. Transition dipole moment of InAs/InGaAs quantum dots from experiments on ultralow-threshold laser diodes. *Applied Physics Letters*, 77(2):262–264, 2000. [doi:10.1063/1.126944](https://doi.org/10.1063/1.126944).
→ pages 79
- [67] D. Englund, D. Fattal, E. Waks, G. Solomon, B. Zhang, T. Nakaoka, Y. Arakawa, Y. Yamamoto, and J. Vučković. Controlling the spontaneous emission rate of single quantum dots in a two-dimensional photonic crystal. *Physical Review Letters*, 95:013904, Jul 2005. [doi:10.1103/PhysRevLett.95.013904](https://doi.org/10.1103/PhysRevLett.95.013904). → pages 33, 47, 80
- [68] D. Englund, A. Faraon, B. Zhang, Y. Yamamoto, and J. Vučković. Generation and transfer of single photons on a photonic crystal chip. *Opt. Express*, 15(9):5550–5558, 2007. [doi:10.1364/OE.15.005550](https://doi.org/10.1364/OE.15.005550). → pages 33, 34, 80
- [69] A. Faraon, E. Waks, D. Englund, I. Fushman, and J. Vučković. Efficient photonic crystal cavity-waveguide couplers. *Applied Physics Letters*, 90(7):073102, 2007. [doi:10.1063/1.2472534](https://doi.org/10.1063/1.2472534). → pages 33
- [70] A. Faraon, A. Majumdar, D. Englund, E. Kim, M. Bajcsy, and J. Vučković. Integrated quantum optical networks based on quantum dots and photonic crystals. *New Journal of Physics*, 13(5):055025, 2011. ISSN 1367-2630. [doi:10.1088/1367-2630/13/5/055025](https://doi.org/10.1088/1367-2630/13/5/055025). → pages 19
- [71] R. Feynman. Simulating physics with computers. *International Journal of Theoretical Physics*, 21:467–488, 1982.
[doi:10.1007/BF02650179](https://doi.org/10.1007/BF02650179). → pages 6
- [72] H. Flayac, D. Gerace, and V. Savona. An all-silicon single-photon source by unconventional photon blockade. *Scientific Reports*, 5:11223, June 2015. [doi:10.1038/srep11223](https://doi.org/10.1038/srep11223). → pages 30

- [73] C. A. Foell, E. Schelew, H. Qiao, K. A. Abel, S. Hughes, F. C. J. M. van Veggel, and J. F. Young. Saturation behaviour of colloidal PbSe quantum dot exciton emission coupled into silicon photonic circuits. *Optics Express*, 20(10):10453–10469, May 2012.
[doi:10.1364/OE.20.010453](https://doi.org/10.1364/OE.20.010453). → pages iv, 35, 105
- [74] C. A. Foell, K. A. Abel, F. C. J. M. van Veggel, and J. F. Young. Kinetic analysis of the temperature dependence of PbSe colloidal quantum dot photoluminescence: Effects of synthesis process and oxygen exposure. *Physical Review B*, 89:045139, Jan 2014.
[doi:10.1103/PhysRevB.89.045139](https://doi.org/10.1103/PhysRevB.89.045139). → pages iv, v
- [75] A. Franceschetti, J. Luo, J. An, and A. Zunger. Origin of one-photon and two-photon optical transitions in PbSe nanocrystals. *Physical Review B*, 79(24):241311(R), June 2009. ISSN 1098-0121.
[doi:10.1103/PhysRevB.79.241311](https://doi.org/10.1103/PhysRevB.79.241311). → pages 38
- [76] I. Fushman, D. Englund, and J. Vučković. Coupling of PbS quantum dots to photonic crystal cavities at room temperature. *Applied Physics Letters*, 87(24):241102, Dec. 2005. ISSN 00036951.
[doi:10.1063/1.2138792](https://doi.org/10.1063/1.2138792). → pages 46
- [77] B. D. Geyter and Z. Hens. The absorption coefficient of PbSe/CdSe core/shell colloidal quantum dots. *Applied Physics Letters*, 97(16):161908, 2010. [doi:10.1063/1.3499754](https://doi.org/10.1063/1.3499754). → pages 76
- [78] R. J. Glauber. Coherent and incoherent states of the radiation field. *Physical Review*, 131:2766–2788, Sep 1963.
[doi:10.1103/PhysRev.131.2766](https://doi.org/10.1103/PhysRev.131.2766). → pages 2
- [79] S. V. Goupalov. Selection rules for optical transitions in PbSe nanocrystal quantum dots: Drastic effect of structure inversion asymmetry. *Physical Review B*, 79(23):233305, June 2009. ISSN 1098-0121. [doi:10.1103/PhysRevB.79.233305](https://doi.org/10.1103/PhysRevB.79.233305). → pages 108
- [80] P. Grangier. Experiments with single photons. In T. Damour, O. Darrigol, B. Duplantier, and V. Rivasseau, editors, *Progress in Mathematical Physics*, volume 47, pages 135–149. Birkhäuser Basel, 2006. [doi:10.1007/3-7643-7436-5_5](https://doi.org/10.1007/3-7643-7436-5_5). → pages 17
- [81] F. Grassi, M. Argeri, L. Marchese, and M. Cossi. First principle study of capping energies and electronic states in stoichiometric and nonstoichiometric PbSe nanoclusters. *The Journal of Physical*

Chemistry C, 117(49):26396–26404, Dec. 2013. ISSN 1932-7447.
[doi:10.1021/jp4102465](https://doi.org/10.1021/jp4102465). → pages 43

- [82] A. D. Greentree, B. A. Fairchild, F. M. Hossain, and S. Prawer. Diamond integrated quantum photonics. *Materials Today*, 11(9):22–31, Sept. 2008. ISSN 1369-7021.
[doi:10.1016/S1369-7021\(08\)70176-7](https://doi.org/10.1016/S1369-7021(08)70176-7). → pages 19
- [83] L. K. Grover. Quantum mechanics helps in searching for a needle in a haystack. *Physical Review Letters*, 79:325–328, Jul 1997.
[doi:10.1103/PhysRevLett.79.325](https://doi.org/10.1103/PhysRevLett.79.325). → pages 6
- [84] R. H. Hadfield. Single-photon detectors for optical quantum information applications. *Nature Photonics*, 3(12):696–705, Dec. 2009. ISSN 1749-4885. [doi:10.1038/nphoton.2009.230](https://doi.org/10.1038/nphoton.2009.230). → pages 27
- [85] J. M. Harbold and F. W. Wise. Photoluminescence spectroscopy of PbSe nanocrystals. *Physical Review B*, 76(12):125304, Sept. 2007.
[doi:10.1103/PhysRevB.76.125304](https://doi.org/10.1103/PhysRevB.76.125304). → pages 80
- [86] J. M. Harbold, H. Du, T. D. Krauss, K. Cho, C. B. Murray, and F. W. Wise. Time-resolved intraband relaxation of strongly confined electrons and holes in colloidal PbSe nanocrystals. *Physical Review B*, 72(19):195312, Nov. 2005. [doi:10.1103/PhysRevB.72.195312](https://doi.org/10.1103/PhysRevB.72.195312). → pages 83
- [87] N. C. Harris, Y. Ma, J. Mower, T. Baehr-Jones, D. Englund, M. Hochberg, and C. Galland. Efficient, compact and low loss thermo-optic phase shifter in silicon. *Optics Express*, 22(9):10487–10493, May 2014. [doi:10.1364/OE.22.010487](https://doi.org/10.1364/OE.22.010487). → pages 20, 23
- [88] A. W. Harrow, A. Hassidim, and S. Lloyd. Quantum algorithm for linear systems of equations. *Physical Review Letters*, 103:150502, Oct 2009. [doi:10.1103/PhysRevLett.103.150502](https://doi.org/10.1103/PhysRevLett.103.150502). → pages 6
- [89] B. J. M. Hausmann, B. Shields, Q. Quan, P. Maletinsky, M. McCutcheon, J. T. Choy, T. M. Babinec, A. Kubanek, A. Yacoby, M. D. Lukin, and M. Lončar. Integrated diamond networks for quantum nanophotonics. *Nano Letters*, 12(3):1578–1582, Mar. 2012. ISSN 1530-6984. [doi:10.1021/nl204449n](https://doi.org/10.1021/nl204449n). → pages 19
- [90] J. Heo, T. Zhu, C. Zhang, J. Xu, and P. Bhattacharya. Electroluminescence from silicon-based photonic crystal microcavities

- with PbSe quantum dots. *Optics Letters*, 35(4):547–549, Feb. 2010.
[doi:10.1364/OL.35.000547](https://doi.org/10.1364/OL.35.000547). → pages 46
- [91] U. Hohenester, A. Laucht, M. Kaniber, N. Hauke, A. Neumann, A. Mohtashami, M. Seliger, M. Bichler, and J. J. Finley. Phonon-assisted transitions from quantum dot excitons to cavity photons. *Physical Review B*, 80(20):201311, Nov. 2009.
[doi:10.1103/PhysRevB.80.201311](https://doi.org/10.1103/PhysRevB.80.201311). → pages 80
- [92] C. K. Hong, Z. Y. Ou, and L. Mandel. Measurement of subpicosecond time intervals between two photons by interference. *Physical Review Letters*, 59:2044–2046, Nov 1987.
[doi:10.1103/PhysRevLett.59.2044](https://doi.org/10.1103/PhysRevLett.59.2044). → pages 16
- [93] B. K. Hughes, D. A. Ruddy, J. L. Blackburn, D. K. Smith, M. R. Bergren, A. J. Nozik, J. C. Johnson, and M. C. Beard. Control of PbSe quantum dot surface chemistry and photophysics using an alkylselenide ligand. *ACS Nano*, May 2012. ISSN 1936-0851.
[doi:10.1021/nn301405j](https://doi.org/10.1021/nn301405j). → pages x, xxii, 44, 69, 70, 71, 74, 97, 98, 99, 107, 139
- [94] S. Hughes, P. Yao, F. Milde, A. Knorr, D. Dalacu, K. Mnaymneh, V. Sazonova, P. J. Poole, G. C. Aers, J. Lapointe, R. Cheriton, and R. L. Williams. Influence of electron-acoustic phonon scattering on off-resonant cavity feeding within a strongly coupled quantum-dot cavity system. *Physical Review B*, 83(16):165313, Apr. 2011.
[doi:10.1103/PhysRevB.83.165313](https://doi.org/10.1103/PhysRevB.83.165313). → pages 80
- [95] P. C. Humphreys, B. J. Metcalf, J. B. Spring, M. Moore, X.-M. Jin, M. Barbieri, W. S. Kolthammer, and I. A. Walmsley. Linear optical quantum computing in a single spatial mode. *Physical Review Letters*, 111(15):150501, Oct. 2013.
[doi:10.1103/PhysRevLett.111.150501](https://doi.org/10.1103/PhysRevLett.111.150501). → pages 13
- [96] C. A. Husko, A. S. Clark, M. J. Collins, A. De Rossi, S. Combri'e, G. Lehoucq, I. H. Rey, T. F. Krauss, C. Xiong, and B. J. Eggleton. Multi-photon absorption limits to heralded single photon sources. *Scientific Reports*, 3, Nov. 2013. [doi:10.1038/srep03087](https://doi.org/10.1038/srep03087). → pages 34
- [97] A. H. Ip, S. M. Thon, S. Hoogland, O. Voznyy, D. Zhitomirsky, R. Debnath, L. Levina, L. R. Rollny, G. H. Carey, A. Fischer, K. W. Kemp, I. J. Kramer, Z. Ning, A. J. Labelle, K. W. Chou,

- A. Amassian, and E. H. Sargent. Hybrid passivated colloidal quantum dot solids. *Nature Nanotechnology*, 7(9):577–582, Sept. 2012. ISSN 1748-3387. [doi:10.1038/nnano.2012.127](https://doi.org/10.1038/nnano.2012.127). → pages 43
- [98] A. B. J. Clarke. *The SQUID handbook*. Wiley-VCH, 2004. → pages 6
- [99] H. Jin, F.-M. Liu, P. Xu, J.-L. Xia, M.-L. Zhong, Y. Yuan, J.-W. Zhou, Y.-X. Gong, W. Wang, and S.-N. Zhu. On-chip generation and manipulation of entangled photons based on reconfigurable lithium-niobate waveguide circuits. *Physical Review Letters*, 113(10):103601–, Sept. 2014. [doi:10.1103/PhysRevLett.113.103601](https://doi.org/10.1103/PhysRevLett.113.103601). → pages 20
- [100] S. John. Strong localization of photons in certain disordered dielectric superlattices. *Phys. Rev. Lett.*, 58:2486–2489, Jun 1987. [doi:10.1103/PhysRevLett.58.2486](https://doi.org/10.1103/PhysRevLett.58.2486). → pages 24
- [101] S. Kalliakos, Y. Brody, A. Schwagmann, A. J. Bennett, M. B. Ward, D. J. P. Ellis, J. Skiba-Szymanska, I. Farrer, J. P. Griffiths, G. A. C. Jones, D. A. Ritchie, and A. J. Shields. In-plane emission of indistinguishable photons generated by an integrated quantum emitter. *Applied Physics Letters*, 104(22):221109, 2014. [doi:10.1063/1.4881887](https://doi.org/10.1063/1.4881887). → pages 34
- [102] W. Kern. The evolution of silicon wafer cleaning technology. *Journal of The Electrochemical Society*, 137(6):1887–1892, 1990. [doi:10.1149/1.2086825](https://doi.org/10.1149/1.2086825). → pages 54
- [103] A. Kigel, M. Brumer, G. I. Maikov, A. Sashchiuk, and E. Lifshitz. Thermally activated photoluminescence in lead selenide colloidal quantum dots. *Small*, 5(14):1675, July 2009. ISSN 16136810. [doi:10.1002/smll.200801378](https://doi.org/10.1002/smll.200801378). → pages 44
- [104] G. Kim, H. Park, J. Joo, K.-S. Jang, M.-J. Kwack, S. Kim, I. Gyoo Kim, J. Hyuk Oh, S. Ae Kim, J. Park, and S. Kim. Single-chip photonic transceiver based on bulk-silicon, as a chip-level photonic I/O platform for optical interconnects. *Scientific Reports*, 5 (11329), June 2015. [doi:10.1038/srep11329](https://doi.org/10.1038/srep11329). → pages 20
- [105] G.-H. Kim, Y.-H. Lee, A. Shinya, and M. Notomi. Coupling of small, low-loss hexapole mode with photonic crystal slab waveguide mode. *Optics Express*, 12(26):6624–6631, 2004. [doi:10.1364/OPEX.12.006624](https://doi.org/10.1364/OPEX.12.006624). → pages 33

- [106] S. Kim, B. Fisher, H.-J. Eisler, and M. Bawendi. Type-II quantum dots: CdTe/CdSe (Core/Shell) and CdSe/ZnTe (Core/Shell) heterostructures. *Journal of the American Chemical Society*, 125(38): 11466–11467, Sept. 2003. ISSN 0002-7863. [doi:10.1021/ja0361749](https://doi.org/10.1021/ja0361749). → pages 43
- [107] H. J. Kimble. The quantum internet. *Nature*, 453(7198):1023–1030, June 2008. ISSN 0028-0836. [doi:10.1038/nature07127](https://doi.org/10.1038/nature07127). → pages 11
- [108] H. J. Kimble, M. Dagenais, and L. Mandel. Photon antibunching in resonance fluorescence. *Physical Review Letters*, 39:691–695, Sep 1977. [doi:10.1103/PhysRevLett.39.691](https://doi.org/10.1103/PhysRevLett.39.691). → pages 17
- [109] L. C. Kimerling, D. Ahn, A. B. Apsel, M. Beals, D. Carothers, Y.-K. Chen, T. Conway, D. M. Gill, M. Grove, C.-Y. Hong, M. Lipson, J. Liu, J. Michel, D. Pan, S. S. Patel, A. T. Pomerene, M. Rasras, D. K. Sparacin, K.-Y. Tu, A. E. White, and C. W. Wong. Electronic-photonic integrated circuits on the CMOS platform. In J. A. Kubby and G. T. Reed, editors, *Silicon Photonics*, volume 6125, 2006. [doi:10.1117/12.654455](https://doi.org/10.1117/12.654455). → pages 20
- [110] E. Knill, R. Laflamme, and G. J. Milburn. A scheme for efficient quantum computation with linear optics. *Nature*, 409(6816):46–52, Jan. 2001. ISSN 0028-0836. [doi:10.1038/35051009](https://doi.org/10.1038/35051009). → pages 2, 3, 13
- [111] T. L. Koch and U. Koren. Photonic integrated circuits. *AT&T Technical Journal*, 71(1):63–74, Jan. 1992. ISSN 1538-7305. [doi:10.1002/j.1538-7305.1992.tb00148.x](https://doi.org/10.1002/j.1538-7305.1992.tb00148.x). → pages 3
- [112] A. F. Koenderink, M. Kafesaki, C. M. Soukoulis, and V. Sandoghdar. Spontaneous emission rates of dipoles in photonic crystal membranes. *Journal of the Optical Society of America B*, 23(6): 1196–1206, June 2006. [doi:10.1364/JOSAB.23.001196](https://doi.org/10.1364/JOSAB.23.001196). → pages 85
- [113] W.-k. Koh, A. Y. Koposov, J. T. Stewart, B. N. Pal, I. Robel, J. M. Pietryga, and V. I. Klimov. Heavily doped n-type PbSe and PbS nanocrystals using ground-state charge transfer from cobaltocene. *Scientific Reports*, 3:2004, June 2013. [doi:10.1038/srep02004](https://doi.org/10.1038/srep02004). → pages 97
- [114] P. Kok and B. W. Lovett. *Introduction to Optical Quantum Information Processing*. Cambridge University Press, 2010. → pages 3, 6, 13

- [115] P. Kok, W. J. Munro, K. Nemoto, T. C. Ralph, J. P. Dowling, and G. J. Milburn. Linear optical quantum computing with photonic qubits. *Reviews of Modern Physics*, 79:135–174, Jan 2007.
[doi:10.1103/RevModPhys.79.135](https://doi.org/10.1103/RevModPhys.79.135). → pages 3, 13
- [116] L. Kong, Z. C. Feng, Z. Wu, and W. Lu. Temperature dependent and time-resolved photoluminescence studies of InAs self-assembled quantum dots with InGaAs strain reducing layer structure. *Journal of Applied Physics*, 106(1):013512, 2009. [doi:10.1063/1.3159648](https://doi.org/10.1063/1.3159648). → pages 79
- [117] C. Kopp, S. Bernabe, B. Bakir, J.-M. Fedeli, R. Orobtchouk, F. Schrank, H. Porte, L. Zimmermann, and T. Tekin. Silicon photonic circuits: On-CMOS integration, fiber optical coupling, and packaging. *Selected Topics in Quantum Electronics, IEEE Journal of*, 17(3):498–509, 2011. ISSN 1077-260X. → pages 20
- [118] P. T. Kristensen, C. Van Vlack, and S. Hughes. Generalized effective mode volume for leaky optical cavities. *Optics Letters*, 37(10):1649–1651, 2012. [doi:10.1364/OL.37.001649](https://doi.org/10.1364/OL.37.001649). → pages 86
- [119] A. Kuhn, M. Hennrich, and G. Rempe. Deterministic single-photon source for distributed quantum networking. *Phys. Rev. Lett.*, 89:067901, Jul 2002. [doi:10.1103/PhysRevLett.89.067901](https://doi.org/10.1103/PhysRevLett.89.067901). → pages 17
- [120] P. G. Kwiat, K. Mattle, H. Weinfurter, A. Zeilinger, A. V. Sergienko, and Y. Shih. New high-intensity source of polarization-entangled photon pairs. *Phys. Rev. Lett.*, 75:4337–4341, Dec 1995.
[doi:10.1103/PhysRevLett.75.4337](https://doi.org/10.1103/PhysRevLett.75.4337). → pages 17
- [121] T. D. Ladd, F. Jelezko, R. Laflamme, Y. Nakamura, C. Monroe, and J. L. O’Brien. Quantum computers. *Nature*, 464(7285):45–53, Mar. 2010. ISSN 0028-0836. [doi:10.1038/nature08812](https://doi.org/10.1038/nature08812). → pages 10
- [122] M. L. M. Larry A. Coldren, Scott W. Corzine. *Diode Lasers and Photonic Integrated Circuits*. Wiley, 2nd edition, 2012. → pages 3
- [123] A. Laucht, N. Hauke, J. M. Villas-Bôas, F. Hofbauer, G. Böhm, M. Kaniber, and J. J. Finley. Dephasing of exciton polaritons in photoexcited InGaAs quantum dots in GaAs nanocavities. *Physical Review Letters*, 103:087405, 2009.
[doi:10.1103/PhysRevLett.103.087405](https://doi.org/10.1103/PhysRevLett.103.087405). → pages 80

- [124] A. Laucht, S. Pütz, T. Günthner, N. Hauke, R. Saive, S. Frédérick, M. Bichler, M.-C. Amann, A. W. Holleitner, M. Kaniber, and J. J. Finley. A waveguide-coupled on-chip single-photon source. *Physical Review X*, 2:011014, Mar 2012. [doi:10.1103/PhysRevX.2.011014](https://doi.org/10.1103/PhysRevX.2.011014). → pages 33
- [125] M. Lee, W. J. Chung, S. K. Park, M. su Kim, H. S. Seo, and J. J. Ju. Structural and optical characterizations of multi-layered and multi-stacked PbSe quantum dots. *Nanotechnology*, 16(8):1148–1152, Aug. 2005. ISSN 0957-4484. [doi:10.1088/0957-4484/16/8/028](https://doi.org/10.1088/0957-4484/16/8/028). → pages 46, 47
- [126] G. Leuchs and T. Beth. *Quantum Information Processing*. Wiley, 2005. → pages 10
- [127] C. B. Li, C. J. Huang, B. W. Cheng, Y. H. Zuo, R. W. Mao, L. P. Luo, J. Z. Yu, and Q. M. Wang. Cavity-enhanced photoluminescence of SiGe/Si multiquantum wells grown on silicon-on-insulator substrate. *Journal of Applied Physics*, 95(10):5914–5916, 2004. [doi:10.1063/1.1707203](https://doi.org/10.1063/1.1707203). → pages 34
- [128] C. B. Li, B. W. Cheng, Y. H. Zuo, A. P. Morrison, J. Z. Yu, and Q. M. Wang. Influence of the cavity on the low-temperature photoluminescence of SiGe/Si multiquantum wells grown on a silicon-on-insulator substrate. *Applied Physics Letters*, 88(12):121901, 2006. [doi:10.1063/1.2187433](https://doi.org/10.1063/1.2187433). → pages 34
- [129] S. Lloyd. Universal quantum simulators. *Science*, 273(5278):1073–1078, 1996. [doi:10.1126/science.273.5278.1073](https://doi.org/10.1126/science.273.5278.1073). → pages 6
- [130] P. Lodahl, S. Mahmoodian, and S. Stobbe. Interfacing single photons and single quantum dots with photonic nanostructures. *Reviews of Modern Physics*, 87(2):347–400, May 2015. [doi:10.1103/RevModPhys.87.347](https://doi.org/10.1103/RevModPhys.87.347). → pages 34
- [131] B. Lounis and M. Orrit. Single-photon sources. *Reports on Progress in Physics*, 68(5):1129, 2005. [doi:10.1088/0034-4885/68/5/R04](https://doi.org/10.1088/0034-4885/68/5/R04). → pages 2
- [132] L. Lu, A. Mock, and J. O’Brien. Efficient coupling between a photonic crystal nanocavity and a waveguide with directional end-facet emission. *Journal of Optics*, 14(5):055502, 2012. ISSN 2040-8986. [doi:10.1088/2040-8978/14/5/055502](https://doi.org/10.1088/2040-8978/14/5/055502). → pages 33

- [133] T. S. Luk, S. Xiong, W. W. Chow, X. Miao, G. Subramania, P. J. Resnick, A. J. Fischer, and J. C. Brinker. Anomalous enhanced emission from PbS quantum dots on a photonic-crystal microcavity. *Journal of the Optical Society of America B*, 28(6):1365–1373, June 2011. [doi:10.1364/JOSAB.28.001365](https://doi.org/10.1364/JOSAB.28.001365). → pages 46, 47, 136
- [134] X.-S. Ma. Integrated quantum photonics: On-chip teleportation. *Nat Photon*, 8(10):749–751, Oct. 2014. ISSN 1749-4885. [doi:10.1038/nphoton.2014.223](https://doi.org/10.1038/nphoton.2014.223). → pages 12
- [135] V. S. C. Manga Rao and S. Hughes. Single quantum dot spontaneous emission in a finite-size photonic crystal waveguide: Proposal for an efficient “on chip” single photon gun. *Physical Review Letters*, 99(19):193901, Nov. 2007. [doi:10.1103/PhysRevLett.99.193901](https://doi.org/10.1103/PhysRevLett.99.193901). → pages 33
- [136] Y. I. Manin. Vychislomoe i nevychislomoe [computable and noncomputable]. *Sov. Radio.*, pages 13–15, 1980. → pages 6
- [137] F. Masia, W. Langbein, I. Moreels, Z. Hens, and P. Borri. Exciton dephasing in lead sulfide quantum dots by x -point phonons. *Phys. Rev. B*, 83:201309, May 2011. [doi:10.1103/PhysRevB.83.201309](https://doi.org/10.1103/PhysRevB.83.201309). → pages 42
- [138] J. McMillan, M. Yu, W.-k. Koh, C. Murray, D.-L. Kwong, and C. W. Wong. Purcell-enhanced spontaneous emission of colloidal PbS quantum dots in slow-light silicon photonic crystal waveguides at the near-infrared. In *Conference on Lasers and Electro-Optics/International Quantum Electronics Conference*, pages 1–2, 2009. [doi:10.1364/IQEC.2009.IFA4](https://doi.org/10.1364/IQEC.2009.IFA4). → pages 46
- [139] B. J. Metcalf, N. Thomas-Peter, J. B. Spring, D. Kundys, M. A. Broome, P. C. Humphreys, X.-M. Jin, M. Barbieri, W. Steven Kolthammer, J. C. Gates, B. J. Smith, N. K. Langford, P. G. Smith, and I. A. Walmsley. Multiphoton quantum interference in a multiport integrated photonic device. *Nature Communications*, 4:1356, Jan. 2013. [doi:10.1038/ncomms2349](https://doi.org/10.1038/ncomms2349). → pages 18
- [140] X. Michalet, F. F. Pinaud, L. A. Bentolila, J. M. Tsay, S. Doose, J. J. Li, G. Sundaresan, A. M. Wu, S. S. Gambhir, and S. Weiss. Quantum dots for live cells, *in vivo* imaging, and diagnostics. *Science*, 307(5709):538–544, Jan. 2005. ISSN 1095-9203. [doi:10.1126/science.1104274](https://doi.org/10.1126/science.1104274). → pages 37

- [141] I. Moreels, K. Lambert, D. De Muynck, F. Vanhaecke, D. Poelman, J. C. Martins, G. Allan, and Z. Hens. Composition and size-dependent extinction coefficient of colloidal PbSe quantum dots. *Chem. Mater.*, 19(25):6101–6106, Nov. 2007. ISSN 0897-4756.
[doi:10.1021/cm071410q](https://doi.org/10.1021/cm071410q). → pages 87, 105
- [142] I. Moreels, K. Lambert, D. Smeets, D. D. Muynck, T. Nollet, J. C. Martins, F. Vanhaecke, A. Vantomme, C. Delerue, G. Allan, and Z. Hens. Size-dependent optical properties of colloidal PbS quantum dots. *ACS Nano*, 3(10):3023–3030, Oct. 2009. ISSN 1936-0851.
[doi:10.1021/nn900863a](https://doi.org/10.1021/nn900863a). → pages xvi, 38, 76
- [143] I. Moreels, G. Allan, B. De Geyter, L. Wirtz, C. Delerue, and Z. Hens. Dielectric function of colloidal lead chalcogenide quantum dots obtained by a Kramers-Krönig analysis of the absorbance spectrum. *Physical Review B*, 81(23):235319, June 2010.
[doi:10.1103/PhysRevB.81.235319](https://doi.org/10.1103/PhysRevB.81.235319). → pages 79
- [144] J. Mower and D. Englund. Efficient generation of single and entangled photons on a silicon photonic integrated chip. *Physical Review A*, 84:052326, Nov 2011. [doi:10.1103/PhysRevA.84.052326](https://doi.org/10.1103/PhysRevA.84.052326). → pages 30
- [145] C. B. Murray, S. Sun, W. Gaschler, H. Doyle, T. A. Betley, and C. R. Kagan. Colloidal synthesis of nanocrystals and nanocrystal superlattices. *IBM J. Res. Dev.*, 45:47–56, 2001.
[doi:10.1147/rd.451.0047](https://doi.org/10.1147/rd.451.0047). → pages 35, 36
- [146] F. Najafi, J. Mower, N. C. Harris, F. Bellei, A. Dane, C. Lee, X. Hu, P. Kharel, F. Marsili, S. Assefa, K. K. Berggren, and D. Englund. On-chip detection of non-classical light by scalable integration of single-photon detectors. *Nature Communications*, 6, Jan. 2015.
[doi:10.1038/ncomms6873](https://doi.org/10.1038/ncomms6873). → pages 30
- [147] K. Nemoto and W. J. Munro. Nearly deterministic linear optical controlled-NOT gate. *Phys. Rev. Lett.*, 93:250502, Dec 2004.
[doi:10.1103/PhysRevLett.93.250502](https://doi.org/10.1103/PhysRevLett.93.250502). → pages 12
- [148] L. A. Ngah, O. Alibart, L. Labonté, V. D’Auria, and S. Tanzilli. Ultra-fast heralded single photon source based on telecom technology. *Laser & Photonics Reviews*, 9(2):L1–L5, 2015. ISSN 1863-8899. [doi:10.1002/lpor.201400404](https://doi.org/10.1002/lpor.201400404). → pages 17, 18

- [149] M. A. Nielsen and I. L. Chuang. *Quantum Computation and Quantum Information*. Cambridge University Press, 2000. → pages 10, 12
- [150] G. Nootz, L. A. Padilha, P. D. Olszak, S. Webster, D. J. Hagan, E. W. V. Stryland, L. Levina, V. Sukhovatkin, L. Brzozowski, and E. H. Sargent. Role of symmetry breaking on the optical transitions in lead-salt quantum dots. *Nano Letters*, 10(9):3577–3582, Sept. 2010. ISSN 1530-6984. [doi:10.1021/nl1018673](https://doi.org/10.1021/nl1018673). → pages 38
- [151] L. Novotny and B. Hecht. *Principles of Nano-Optics*. Cambridge, 2006. → pages 76
- [152] K. Nozaki, H. Watanabe, and T. Baba. Photonic crystal nanolaser monolithically integrated with passive waveguide for effective light extraction. *Applied Physics Letters*, 92(2):021108, 2008. [doi:10.1063/1.2831916](https://doi.org/10.1063/1.2831916). → pages 33
- [153] A. J. Nozik. Quantum dot solar cells. *Physica E*, 14:115–120, 2002. → pages 37
- [154] A. J. Nozik, M. C. Beard, J. M. Luther, M. Law, R. J. Ellingson, and J. C. Johnson. Semiconductor quantum dots and quantum dot arrays and applications of multiple exciton generation to third-generation photovoltaic solar cells. *Chem. Rev.*, 110(11): 6873–6890, 2010. [doi:10.1021/cr900289f](https://doi.org/10.1021/cr900289f). → pages 37
- [155] J. O’Brien, B. Patton, M. Sasaki, and J. Vučković. Focus on integrated quantum optics. *New Journal of Physics*, 15(3):035016, 2013. [doi:10.1088/1367-2630/15/3/035016](https://doi.org/10.1088/1367-2630/15/3/035016). → pages 12
- [156] T. Okuno, Y. Masumoto, M. Ikezawa, T. Ogawa, and A. A. Lipovskii. Size-dependent picosecond energy relaxation in PbSe quantum dots. *Applied Physics Letters*, 77(4):504–506, July 2000. [doi:10.1063/1.127025](https://doi.org/10.1063/1.127025). → pages 83
- [157] S. Olivier, C. Smith, H. Benisty, C. Weisbuch, T. Krauss, R. Houdre, and U. Oesterle. Cascaded photonic crystal guides and cavities: spectral studies and their impact on integrated optics design. *Quantum Electronics, IEEE Journal of*, 38(7):816–824, 2002. ISSN 0018-9197. [doi:10.1109/JQE.2002.1017592](https://doi.org/10.1109/JQE.2002.1017592). → pages 33

- [158] A. Omari, P. Geiregat, D. Van Thourhout, and Z. Hens. Light absorption in hybrid silicon-on-insulator/quantum dot waveguides. *Optics Express*, 21(20):23272–23285, 2013.
[doi:10.1364/OE.21.023272](https://doi.org/10.1364/OE.21.023272). → pages 112
- [159] Y. Ooka, T. Tetsumoto, A. Fushimi, W. Yoshiki, and T. Tanabe. CMOS compatible high-Q photonic crystal nanocavity fabricated with photolithography on silicon photonic platform. *Scientific Reports*, 5:11312, June 2015. [doi:10.1038/srep11312](https://doi.org/10.1038/srep11312). → pages 26
- [160] Y. Ota, S. Iwamoto, N. Kumagai, and Y. Arakawa. Impact of electron-phonon interactions on quantum-dot cavity quantum electrodynamics. e-print: arXiv:0908.0788v1, 2009. URL <http://arxiv.org/abs/0908.0788v1>. → pages 80
- [161] M. Paillard, X. Marie, E. Vanelle, T. Amand, V. K. Kalevich, A. R. Kovsh, A. E. Zhukov, and V. M. Ustinov. Time-resolved photoluminescence in self-assembled InAs/GaAs quantum dots under strictly resonant excitation. *Applied Physics Letters*, 76(1):76–78, Jan. 2000. [doi:10.1063/1.125661](https://doi.org/10.1063/1.125661). → pages 79
- [162] Y. Pan, H. Bai, L. Pan, Y. Li, M. C. Tamargo, M. Sohel, and J. R. Lombardi. Size controlled synthesis of monodisperse PbTe quantum dots: using oleylamine as the capping ligand. *Journal of Materials Chemistry*, 22(44):23593–23601, 2012. ISSN 0959-9428.
[doi:10.1039/C2JM15540K](https://doi.org/10.1039/C2JM15540K). → pages 97
- [163] R. B. Patel, A. J. Bennett, I. Farrer, C. A. Nicoll, D. A. Ritchie, and A. J. Shields. Two-photon interference of the emission from electrically tunable remote quantum dots. *Nature Photonics*, 4: 632–635, 2010. [doi:10.1038/nphoton.2010.161](https://doi.org/10.1038/nphoton.2010.161). → pages 19
- [164] A. G. Pattantyus-Abraham, H. Qiao, J. Shan, K. A. Abel, T.-S. Wang, F. C. J. M. van Veggel, and J. F. Young. Site-selective optical coupling of PbSe nanocrystals to Si-based photonic crystal microcavities. *Nano Letters*, 9(8):2849, Aug. 2009. ISSN 1530-6984.
[doi:10.1021/nl900961r](https://doi.org/10.1021/nl900961r). → pages xvii, 35, 46, 47, 51, 55, 56, 57, 58, 64
- [165] W. Pernice, C. Schuck, O. Minaeva, M. Li, G. Goltsman, A. Sergienko, and H. Tang. High-speed and high-efficiency travelling wave single-photon detectors embedded in nanophotonic circuits. *Nature Communications*, 3:1325, Dec. 2012.
[doi:10.1038/ncomms2307](https://doi.org/10.1038/ncomms2307). → pages 30

- [166] C. B. Poitras, M. Lipson, H. Du, M. A. Hahn, and T. D. Krauss. Photoluminescence enhancement of colloidal quantum dots embedded in a monolithic microcavity. *Applied Physics Letters*, 82(23):4032, June 2003. ISSN 00036951. [doi:10.1063/1.1581007](https://doi.org/10.1063/1.1581007). → pages 46
- [167] A. Politi, M. J. Cryan, J. G. Rarity, S. Yu, and J. L. O'Brien. Silica-on-silicon waveguide quantum circuits. *Science*, 320(5876):646–649, 2008. [doi:10.1126/science.1155441](https://doi.org/10.1126/science.1155441). → pages 19
- [168] A. Politi, J. Matthews, M. Thompson, and J. O'Brien. Integrated quantum photonics. *Selected Topics in Quantum Electronics, IEEE Journal of*, 15(6):1673–1684, 2009. ISSN 1077-260X. [doi:10.1109/JSTQE.2009.2026060](https://doi.org/10.1109/JSTQE.2009.2026060). → pages 12
- [169] E. Pomarico, B. Sanguinetti, C. I. Osorio, H. Herrmann, and R. T. Thew. Engineering integrated pure narrow-band photon sources. *New Journal of Physics*, 14(3):033008, 2012. ISSN 1367-2630. [doi:10.1088/1367-2630/14/3/033008](https://doi.org/10.1088/1367-2630/14/3/033008). → pages 18
- [170] R. Prevedel, P. Walther, F. Tiefenbacher, P. Bohi, R. Kaltenbaek, T. Jennewein, and A. Zeilinger. High-speed linear optics quantum computing using active feed-forward. *Nature*, 445(7123):65–69, Jan. 2007. ISSN 0028-0836. [doi:10.1038/nature05346](https://doi.org/10.1038/nature05346). → pages 13
- [171] D. Qi, M. Fischbein, M. Drndić, and S. Šelmić. Efficient polymer-nanocrystal quantum-dot photodetectors. *Applied Physics Letters*, 86(9):093103, 2005. [doi:10.1063/1.1872216](https://doi.org/10.1063/1.1872216). → pages 37
- [172] H. Qiao, K. A. Abel, F. C. J. M. van Veggel, and J. F. Young. Exciton thermalization and state broadening contributions to the photoluminescence of colloidal PbSe quantum dot films from 295 to 4.5 k. *Physical Review B*, 82(16):165435, Oct. 2010. [doi:10.1103/PhysRevB.82.165435](https://doi.org/10.1103/PhysRevB.82.165435). → pages 41, 42, 44, 53, 59, 68, 69, 74, 80, 84, 89, 99, 106, 112
- [173] R. Quintero-Torres, C. A. Foell, J. Pichaandi, F. C. J. M. van Veggel, and J. F. Young. Photoluminescence dynamics in solid formulations of colloidal PbSe quantum dots: Three-dimensional versus two-dimensional films. *Applied Physics Letters*, 101(12):121904, 2012. [doi:10.1063/1.4752737](https://doi.org/10.1063/1.4752737). → pages iv, v, xvii, xviii, 55, 61, 66
- [174] R. Quintero-Torres, F. C. J. M. van Veggel, and J. F. Young. Temperature dependence of Förster thermalization and population

- decay in PbSe nanocrystals. *The Journal of Physical Chemistry C*, 118(2):1377–1385, Jan. 2014. ISSN 1932-7447.
[doi:10.1021/jp4109046](https://doi.org/10.1021/jp4109046). → pages 67, 112
- [175] M. T. Rakher, R. Bose, C. W. Wong, and K. Srinivasan. Spectroscopy of $1.55\text{ }\mu\text{m}$ PbS quantum dots on Si photonic crystal cavities with a fiber taper waveguide. *Applied Physics Letters*, 96(16):161108, 2010. [doi:10.1063/1.3396988](https://doi.org/10.1063/1.3396988). → pages 46, 47, 65
- [176] M. T. Rakher, R. Bose, C. W. Wong, and K. Srinivasan. Fiber-based cryogenic and time-resolved spectroscopy of PbS quantum dots. *Optics Express*, 19(3):1786–1793, Jan. 2011.
[doi:10.1364/OE.19.001786](https://doi.org/10.1364/OE.19.001786). → pages 46
- [177] T. C. Ralph, N. K. Langford, T. B. Bell, and A. G. White. Linear optical controlled-NOT gate in the coincidence basis. *Phys. Rev. A*, 65:062324, Jun 2002. [doi:10.1103/PhysRevA.65.062324](https://doi.org/10.1103/PhysRevA.65.062324). → pages 15
- [178] G. Reithmaier, S. Lichtmannecker, T. Reichert, P. Hasch, K. Müller, M. Bichler, R. Gross, and J. J. Finley. On-chip time resolved detection of quantum dot emission using integrated superconducting single photon detectors. *Scientific Reports*, 3:1901, May 2013.
[doi:10.1038/srep01901](https://doi.org/10.1038/srep01901). → pages 34
- [179] J. P. Reithmaier, G. Sek, A. Löffler, C. Hofmann, S. Kuhn, S. Reitzenstein, L. V. Keldysh, V. D. Kulakovskii, T. L. Reinecke, and A. Forchel. Strong coupling in a single quantum dot-semiconductor microcavity system. *Nature*, 432(7014):197–200, Nov. 2004. ISSN 0028-0836. [doi:10.1038/nature02969](https://doi.org/10.1038/nature02969). → pages 47
- [180] V. Rinnerbauer, H. Egelhaaf, K. Hingerl, P. Zimmer, S. Werner, T. Warming, A. Hoffmann, M. Kovalenko, W. Heiss, G. Hesser, and F. Schaffler. Energy transfer in close-packed PbS nanocrystal films. *Physical Review B*, 77(8), Feb. 2008. ISSN 1098-0121.
[doi:10.1103/PhysRevB.77.085322](https://doi.org/10.1103/PhysRevB.77.085322). → pages 44
- [181] F. Rossi. *Theory of Semiconductor Quantum Devices*. Springer, 2010. → pages 74
- [182] C. Roy and S. Hughes. Phonon-dressed Mollow triplet in the regime of cavity quantum electrodynamics: Excitation-induced dephasing and nonperturbative cavity feeding effects. *Physical Review Letters*,

106(24):247403, June 2011. [doi:10.1103/PhysRevLett.106.247403](https://doi.org/10.1103/PhysRevLett.106.247403). → pages 80

- [183] C. Santori, M. Pelton, G. Solomon, Y. Dale, and Y. Yamamoto. Triggered single photons from a quantum dot. *Physical Review Letters*, 86:1502–1505, Feb 2001. [doi:10.1103/PhysRevLett.86.1502](https://doi.org/10.1103/PhysRevLett.86.1502). → pages 33, 34
- [184] C. Santori, D. Fattal, and Y. Yamamoto. *Single-photon Devices and Applications*. Wiley, Nov. 2010. → pages 2
- [185] E. H. Sargent. Infrared quantum dots. *Advanced Materials*, 17(5): 515–522, Mar. 2005. ISSN 0935-9648. [doi:10.1002/adma.200401552](https://doi.org/10.1002/adma.200401552). → pages 46, 47
- [186] S. Scheel, L. Knöll, D. Welsch, and S. M. Barnett. Quantum local-field corrections and spontaneous decay. *Physical Review A*, 60 (2):1590–1597, Aug. 1999. [doi:10.1103/PhysRevA.60.1590](https://doi.org/10.1103/PhysRevA.60.1590). → pages 76
- [187] M. Scheele, J. H. Engel, V. E. Ferry, D. Hanifi, Y. Liu, and A. P. Alivisatos. Nonmonotonic size dependence in the hole mobility of methoxide-stabilized PbSe quantum dot solids. *ACS Nano*, 7(8): 6774–6781, Aug. 2013. ISSN 1936-0851. [doi:10.1021/nn401657n](https://doi.org/10.1021/nn401657n). → pages 97
- [188] E. Schelew. Characterization of photonic crystal based silicon-on-insulator optical circuits fabricated by a CMOS foundry. Master’s thesis, University of British Columbia, 2011. → pages 27
- [189] E. Schelew, G. Rieger, and J. Young. Characterization of integrated planar photonic crystal circuits fabricated by a CMOS foundry. *Journal of Lightwave Technology*, 31(2):239–248, Jan. 2013. ISSN 0733-8724. [doi:10.1109/JLT.2012.2228466](https://doi.org/10.1109/JLT.2012.2228466). → pages xxiii, 27, 34, 114, 115, 121, 135
- [190] E. Schelew, M. K. Akhlaghi, and J. F. Young. Integrating single photon sources and high-efficiency, low dark count single photon detectors using photonic crystal microcavities in silicon-on-insulator waveguides. In *Nonlinear Optics: Novel Phenomena, Materials and Applications*, 2015. → pages 34

- [191] A. Schwagmann, S. Kalliakos, I. Farrer, J. P. Griffiths, G. A. C. Jones, D. A. Ritchie, and A. J. Shields. On-chip single photon emission from an integrated semiconductor quantum dot into a photonic crystal waveguide. *Applied Physics Letters*, 99(26):261108, Dec. 2011. [doi:10.1063/1.3672214](https://doi.org/10.1063/1.3672214). → pages 47
- [192] A. Schwagmann, S. Kalliakos, D. J. P. Ellis, I. Farrer, J. P. Griffiths, G. A. C. Jones, D. A. Ritchie, and A. J. Shields. In-plane single-photon emission from a L3 cavity coupled to a photonic crystal waveguide. *Optics Express*, 20(27):28614–28624, 2012. [doi:10.1364/OE.20.028614](https://doi.org/10.1364/OE.20.028614). → pages 34
- [193] H. P. Seigneur, M. Weed, M. N. Leuenberger, , and W. V. Schoenfeld. Controlled on-chip single-photon transfer using photonic crystal coupled-cavity waveguides. *Advances in OptoElectronics*, 2011:893086, 2011. [doi:10.1155/2011/893086](https://doi.org/10.1155/2011/893086). → pages 33
- [194] O. E. Semonin, J. C. Johnson, J. M. Luther, A. G. Midgett, A. J. Nozik, and M. C. Beard. Absolute photoluminescence quantum yields of IR-26 dye, PbS, and PbSe quantum dots. *The Journal of Physical Chemistry Letters*, 1(16):2445, 2010. [doi:10.1021/jz100830r](https://doi.org/10.1021/jz100830r). → pages 43
- [195] Y. Shirasaki, G. J. Supran, M. G. Bawendi, and V. Bulovic. Emergence of colloidal quantum-dot light-emitting technologies. *Nat Photon*, 7(1):13–23, Jan. 2013. ISSN 1749-4885. [doi:10.1038/nphoton.2012.328](https://doi.org/10.1038/nphoton.2012.328). → pages 37
- [196] P. Shor. Polynomial-time algorithms for prime factorization and discrete logarithms on a quantum computer. *SIAM Journal on Computing*, 26(5):1484–1509, 1997. [doi:10.1137/S0097539795293172](https://doi.org/10.1137/S0097539795293172). → pages 6
- [197] K. L. Silverman, R. P. Mirin, S. T. Cundiff, and A. G. Norman. Direct measurement of polarization resolved transition dipole moment in InGaAs/GaAs quantum dots. *Applied Physics Letters*, 82 (25):4552–4554, 2003. [doi:10.1063/1.1584514](https://doi.org/10.1063/1.1584514). → pages 79
- [198] J. W. Silverstone, D. Bonneau, K. Ohira, N. Suzuki, H. Yoshida, N. Iizuka, M. Ezaki, C. M. Natarajan, M. G. Tanner, R. H. Hadfield, V. Zwiller, G. D. Marshall, J. G. Rarity, J. L. O'Brien, and M. G. Thompson. On-chip quantum interference between silicon

photon-pair sources. *Nature Photonics*, 8(2):104–108, Feb. 2014.
ISSN 1749-4885. [doi:10.1038/nphoton.2013.339](https://doi.org/10.1038/nphoton.2013.339). → pages 4, 20, 23

- [199] J. W. Silverstone, R. Santagati, D. Bonneau, M. J. Strain, M. Sorel, J. L. O’Brien, and M. G. Thompson. Qubit entanglement between ring-resonator photon-pair sources on a silicon chip. *Nature Communications*, 6, Aug. 2015. [doi:10.1038/ncomms8948](https://doi.org/10.1038/ncomms8948). → pages 4, 23
- [200] C. Sinito, M. J. Fernée, S. V. Goupalov, P. Mulvaney, P. Tamarat, and B. Lounis. Tailoring the exciton fine structure of cadmium selenide nanocrystals with shape anisotropy and magnetic field. *ACS Nano*, 8(11):11651–11656, Nov. 2014. ISSN 1936-0851.
[doi:10.1021/nn5049409](https://doi.org/10.1021/nn5049409). → pages 43
- [201] J. E. Sipe and J. V. Kranendonk. Macroscopic electromagnetic theory of resonant dielectrics. *Phys. Rev. A*, 9:1806–1822, May 1974.
[doi:10.1103/PhysRevA.9.1806](https://doi.org/10.1103/PhysRevA.9.1806). → pages 76
- [202] W. Sohler, H. Hu, R. Ricken, V. Quiring, C. Vannahme, H. Herrmann, D. Büchter, S. Reza, W. Grundkötter, S. Orlov, H. Suche, R. Nouroozi, and Y. Min. Integrated optical devices in lithium niobate. *Opt. Photon. News*, 19(1):24–31, 2008.
[doi:10.1364/OPN.19.1.000024](https://doi.org/10.1364/OPN.19.1.000024). → pages 20
- [203] B.-S. Song, S. Noda, T. Asano, and Y. Akahane. Ultra-high-Q photonic double-heterostructure nanocavity. *Nat Mater*, 4(3):207–210, Mar. 2005. ISSN 1476-1122. [doi:10.1038/nmat1320](https://doi.org/10.1038/nmat1320). → pages 26
- [204] R. Soref. The past, present, and future of silicon photonics. *Selected Topics in Quantum Electronics, IEEE Journal of*, 12(6):1678–1687, 2006. ISSN 1077-260X. [doi:10.1109/JSTQE.2006.883151](https://doi.org/10.1109/JSTQE.2006.883151). → pages 20
- [205] J. P. Sprengers, A. Gaggero, D. Sahin, S. Jahanmirinejad, G. Frucci, F. Mattioli, R. Leoni, J. Beetz, M. Lermer, M. Kamp, S. Höfling, R. Sanjines, and A. Fiore. Waveguide superconducting single-photon detectors for integrated quantum photonic circuits. *Applied Physics Letters*, 99(18):181110, 2011. [doi:10.1063/1.3657518](https://doi.org/10.1063/1.3657518). → pages 30
- [206] J. Steckel, S. Coe-Sullivan, V. Bulović, and M. Bawendi. 1.3 μm to 1.55 μm tunable electroluminescence from PbSe quantum dots embedded within an organic device. *Advanced Materials*, 15(21):

1862–1866, Nov. 2003. ISSN 0935-9648.
[doi:10.1002/adma.200305449](https://doi.org/10.1002/adma.200305449). → pages 46, 47

- [207] J. W. Stouwdam, J. Shan, F. C. J. M. van Veggel, A. G. Pattantyus-Abraham, J. F. Young, and M. Raudsepp. Photostability of colloidal PbSe and PbSe/PbS core/shell nanocrystals in solution and in the solid state. *The Journal of Physical Chemistry C*, 111(3):1086, Dec. 2007. ISSN 1932-7447. [doi:10.1021/jp0648083](https://doi.org/10.1021/jp0648083). → pages 44, 45, 52, 59, 68, 80, 97, 98
- [208] M. Streshinsky, R. Ding, Y. Liu, A. Novack, C. Galland, A. E.-J. Lim, P. Guo-Qiang Lo, T. Baehr-Jones, and M. Hochberg. The road to affordable, large-scale silicon photonics. *Opt. Photon. News*, 24(9):32–39, 2013. [doi:10.1364/OPN.24.9.000032](https://doi.org/10.1364/OPN.24.9.000032). → pages 4, 20, 30
- [209] N. Suzuki, K. Sawai, and S. Adachi. Optical properties of PbSe. *Journal of Applied Physics*, 77(3):1249–1255, Feb. 1995.
[doi:10.1063/1.358926](https://doi.org/10.1063/1.358926). → pages 79
- [210] M. Sykora, A. Y. Koposov, J. A. McGuire, R. K. Schulze, O. Tretiak, J. M. Pietryga, and V. I. Klimov. Effect of air exposure on surface properties, electronic structure, and carrier relaxation in PbSe nanocrystals. *ACS Nano*, 4(4):2021–2034, Apr. 2010. ISSN 1936-0851. [doi:10.1021/nn100131w](https://doi.org/10.1021/nn100131w). → pages 97
- [211] D. V. Talapin and C. B. Murray. PbSe nanocrystal solids for n- and p-channel thin film field-effect transistors. *Science*, 310(5745):86–89, Oct. 2005. [doi:10.1126/science.1116703](https://doi.org/10.1126/science.1116703). → pages 97
- [212] S. Tanzilli, A. Martin, F. Kaiser, M. De Micheli, O. Alibart, and D. Ostrowsky. On the genesis and evolution of integrated quantum optics. *Laser & Photon. Rev.*, 6(1):115–143, Jan. 2012. ISSN 1863-8899. [doi:10.1002/lpor.201100010](https://doi.org/10.1002/lpor.201100010). → pages 12
- [213] L. Turyanska, A. Patanè, M. Henini, B. Hennequin, and N. R. Thomas. Temperature dependence of the photoluminescence emission from thiol-capped PbS quantum dots. *Applied Physics Letters*, 90(10):101913, 2007. ISSN 00036951. [doi:10.1063/1.2711529](https://doi.org/10.1063/1.2711529). → pages 44
- [214] S. M. Ulrich, S. Ates, S. Reitzenstein, A. Löffler, A. Forchel, and P. Michler. Dephasing of triplet-sideband optical emission of a resonantly driven InAs/GaAs quantum dot inside a microcavity.

Physical Review Letters, 106(24):247402, June 2011.
[doi:10.1103/PhysRevLett.106.247402](https://doi.org/10.1103/PhysRevLett.106.247402). → pages 80

- [215] K. J. Vahala. Optical microcavities. *Nature*, 424(6950):839–846, Aug. 2003. ISSN 0028-0836. [doi:10.1038/nature01939](https://doi.org/10.1038/nature01939). → pages 47
- [216] J. Volz, M. Scheucher, C. Junge, and A. Rauschenbeutel. Nonlinear π phase shift for single fibre-guided photons interacting with a single resonator-enhanced atom. *Nat Photon*, 8(12):965–970, Dec. 2014. ISSN 1749-4885. [doi:10.1038/nphoton.2014.253](https://doi.org/10.1038/nphoton.2014.253). → pages 12
- [217] E. Waks and J. Vučković. Coupled mode theory for photonic crystal cavity-waveguide interaction. *Optics Express*, 13(13):5064–5073, 2005. [doi:10.1364/OPEX.13.005064](https://doi.org/10.1364/OPEX.13.005064). → pages 33
- [218] J. Wang, A. Santamato, P. Jiang, D. Bonneau, E. Engin, J. W. Silverstone, M. Lermer, J. Beetz, M. Kamp, S. Höfling, M. G. Tanner, C. M. Natarajan, R. H. Hadfield, S. N. Dorenbos, V. Zwiller, J. L. O’Brien, and M. G. Thompson. Gallium arsenide (GaAs) quantum photonic waveguide circuits. *Optics Communications*, 327: 49–55, Sept. 2014. ISSN 0030-4018. [doi:10.1364/JOSAB.13.001039](https://doi.org/10.1364/JOSAB.13.001039). → pages 19
- [219] N. A. Wasley. *Nano-photonics in III-V Semiconductors for Integrated Quantum Optical Circuits*. Springer International Publishing, 2014. [doi:10.1007/978-3-319-01514-9](https://doi.org/10.1007/978-3-319-01514-9). → pages 34
- [220] B. L. Wehrenberg, C. Wang, and P. Guyot-Sionnest. Interband and intraband optical studies of PbSe colloidal quantum dots. *The Journal of Physical Chemistry B*, 106(41):10634–10640, Oct. 2002. ISSN 1520-6106. [doi:10.1021/jp021187e](https://doi.org/10.1021/jp021187e). → pages 39, 43
- [221] F. W. Wise, J. Harbold, S. Clark, and B.-R. Hyun. Electron relaxation in lead-salt quantum dots. volume 5929, pages 59290S–59290S–9, 2005. [doi:10.1117/12.617285](https://doi.org/10.1117/12.617285). → pages 39
- [222] D. C. Wu, J. K. Kao, M. H. Mao, F. Y. Chang, and H. H. Lin. Determination of interband transition dipole moment of InAs/InGaAs quantum dots from modal absorption spectra. In *OSA Technical Digest Series (CD)*, page JTxA111. Optical Society of America, May 2007. → pages 79

- [223] Z. Wu, Z. Mi, P. Bhattacharya, T. Zhu, and J. Xu. Enhanced spontaneous emission at $1.55\text{ }\mu\text{m}$ from colloidal PbSe quantum dots in a Si photonic crystal microcavity. *Applied Physics Letters*, 90(17):171105, Apr. 2007. ISSN 00036951. [doi:10.1063/1.2731657](https://doi.org/10.1063/1.2731657). → pages 46, 47
- [224] J. S. Xia, K. Nemoto, Y. Ikegami, Y. Shiraki, and N. Usami. Silicon-based light emitters fabricated by embedding Ge self-assembled quantum dots in microdisks. *Applied Physics Letters*, 91(1):011104, 2007. [doi:10.1063/1.2754356](https://doi.org/10.1063/1.2754356). → pages 34
- [225] C. Xiong, X. Zhang, A. Mahendra, J. He, D.-Y. Choi, C. J. Chae, D. Marpaung, A. Leinse, R. G. Heideman, M. Hoekman, C. G. H. Roeloffzen, R. M. Oldenbeuving, P. W. L. van Dijk, C. Taddei, P. H. W. Leong, and B. J. Eggleton. Compact and reconfigurable silicon nitride time-bin entanglement circuit. *Optica*, 2(8):724–727, 2015. [doi:10.1364/OPTICA.2.000724](https://doi.org/10.1364/OPTICA.2.000724). → pages 20
- [226] X. Xu, T. Tsuboi, T. Chiba, N. Usami, T. Maruizumi, and Y. Shiraki. Silicon-based current-injected light emitting diodes with Ge self-assembled quantum dots embedded in photonic crystal nanocavities. *Opt. Express*, 20(13):14714–14721, 2012. [doi:10.1364/OE.20.014714](https://doi.org/10.1364/OE.20.014714). → pages 34
- [227] X. Xu, N. Usami, T. Maruizumi, and Y. Shiraki. Enhancement of light emission from Ge quantum dots by photonic crystal nanocavities at room-temperature. *Journal of Crystal Growth*, 378:636–639, Sept. 2013. ISSN 0022-0248. [doi:10.1016/j.jcrysGro.2012.11.002](https://doi.org/10.1016/j.jcrysGro.2012.11.002). → pages 34
- [228] E. Yablonovitch. Inhibited spontaneous emission in solid-state physics and electronics. *Phys. Rev. Lett.*, 58:2059–2062, May 1987. [doi:10.1103/PhysRevLett.58.2059](https://doi.org/10.1103/PhysRevLett.58.2059). → pages 24
- [229] J. Yang, J. Heo, T. Zhu, J. Xu, J. Topolancik, F. Vollmer, R. Ilic, and P. Bhattacharya. Enhanced photoluminescence from embedded PbSe colloidal quantum dots in silicon-based random photonic crystal microcavities. *Applied Physics Letters*, 92(26):261110, June 2008. [doi:10.1063/1.2954007](https://doi.org/10.1063/1.2954007). → pages 46
- [230] P. Yao and S. Hughes. Controlled cavity QED and single-photon emission using a photonic-crystal waveguide cavity system. *Physical*

Review B, 80:165128, Oct 2009. [doi:10.1103/PhysRevB.80.165128](https://doi.org/10.1103/PhysRevB.80.165128). → pages 34

- [231] P. Yao, V. Manga Rao, and S. Hughes. On-chip single photon sources using planar photonic crystals and single quantum dots. *Laser & Photon. Rev.*, 4(4):499–516, 2010. ISSN 1863-8899. [doi:10.1002/lpor.200810081](https://doi.org/10.1002/lpor.200810081). → pages 34, 80
- [232] W. S. Zaoui, A. Kunze, W. Vogel, M. Berroth, J. Butschke, F. Letzkus, and J. Burghartz. Bridging the gap between optical fibers and silicon photonic integrated circuits. *Optics Express*, 22(2):1277–1286, 2014. [doi:10.1364/OE.22.001277](https://doi.org/10.1364/OE.22.001277). → pages 20
- [233] C. Zeng, Y. Ma, Y. Zhang, D. Li, Z. Huang, Y. Wang, Q. Huang, J. Li, Z. Zhong, J. Yu, Z. Jiang, and J. Xia. Single germanium quantum dot embedded in photonic crystal nanocavity for light emitter on silicon chip. *Optics Express*, 23(17):22250–22261, 2015. [doi:10.1364/OE.23.022250](https://doi.org/10.1364/OE.23.022250). → pages 34, 35
- [234] Y. Zhang, C. Zeng, D. Li, X. Zhao, G. Gao, J. Yu, and J. Xia. Enhanced light emission from Ge quantum dots in photonic crystal ring resonator. *Opt. Express*, 22(10):12248–12254, 2014. [doi:10.1364/OE.22.012248](https://doi.org/10.1364/OE.22.012248). → pages 34
- [235] L. Zhu, S. Samudrala, N. Stelmakh, and M. Vasilyev. Spontaneous decay of CdSe/ZnS core-shell quantum dots at the air-dielectric interface. *Opt. Express*, 20(3):3144–3151, 2012. [doi:10.1364/OE.20.003144](https://doi.org/10.1364/OE.20.003144). → pages 76
- [236] K. Zhuravlev. PbSe vs. CdSe: Thermodynamic properties and pressure dependence of the band gap. *Physica B: Condensed Matter*, 394(1):1–7, May 2007. ISSN 0921-4526. [doi:10.1016/j.physb.2007.01.030](https://doi.org/10.1016/j.physb.2007.01.030). → pages xvi, 40
- [237] H. Zimmermann. *Silicon Optoelectronic Integrated Circuits*. Springer, 2013. [doi:10.1007/978-3-662-09904-9](https://doi.org/10.1007/978-3-662-09904-9). → pages 20

Appendix A

Dip coating procedural details

Procedural notes for QD monolayer preparation (or generally, dipping) with glove box/dipper setup

1. Establish known weight/solvent volume of nanocrystals
 - a. Weigh empty 1 dram vial (usually \sim 6 g)
 - b. Fill with as-received CQD solution (e.g. CQDs in TCE), \sim 4 mL
 - c. Slowly evaporate solvent under N2 flow, \sim 2-3 hours
 - d. Weigh the vial with CQDs
 - e. Determine the CQD weight by subtracting off empty vial weight
 - f. Constitute CQDs with Hexanes to \sim 5.0 mg/mL
 - g. Mark solvent line, label vial, Teflon tape on threads, cap on
 - h. Have CQD solution in glove box prior to BOE/HF treatment
2. Prepare substrates
 - a. Establish two (or more) \sim 5 mm x 10 mm silicon or SOI wafer pieces. Polished on at least one side, device side
 - b. RCA-1 clean them as best as possible (+pre-RCA solvent rinses)

c. Have on-hand, in H₂O, ready for BOE/HF treatment

3. Prepare cryostat

- a. Remove aluminum mount/backing
- b. Prepare in-cryostat sample stage for accepting two samples. Keep samples near bottom of cryostat window
- c. Keep filled with nitrogen gas before placing into glove box
- d. Have N₂ ready to fill cryostat with steady N₂ flow for immediately after cryostat removal from glove box (after samples in cryostat)
- e. Have cryostat on glove box transfer tray during dip-coating

4. Dip-coating

- a. Dip-coating is ready to occur when:
 - i. Sample substrates are ready to be HF-treated
 - ii. Dipping solution (in vial) is on the dipping stage in the glove box, and positioned such that a sample held by the self-clamping tweezers is a few mm above the solution surface
 - iii. Cryostat is on the sample glove box tray, filled with nitrogen
 - iv. Glove box at positive pressure (for faster transfer chamber backfill)
 - v. Rough pumping on valve just before transfer chamber (but not yet on transfer chamber ... just ready to)
 - vi. N₂ line on right of wet bench is ready to hook up to cryostat and flow N₂ through cryostat immediately after
 - vii. Dipping stage is ready to be controlled (launch Step_dir6 on desktop, run file, and test that you can control stage movement up/down using switch/button controller located on top of desktop computer. Motor is powered by PS below monitor: turn on button on left, and press 'out' for power out)
 - viii. Sample stage of cryostat is ready to accept dipped samples, particularly so region of interest is optically accessible near

bottom of cryostat window. [Recommended: fasten sample to stage done under strong nitrogen flow outside glove box]

- ix. Turbo pump is not spinning, is at STP, and ready to quickly attach to cryostat to pump it down
- b. HF-treat the samples and put on sample tray, if appropriate
- c. Put samples + tray + tweezers into glove box transfer chamber
- d. Evacuate glove box transfer chamber with roughing pump
- e. Once evacuated, close valve from pump to transfer chamber
- f. Backfill transfer chamber with N₂ from glove box, making sure to actively fill glove box with more N₂
- g. When transfer chamber and glove box at same pressure, open door between transfer chamber and glove box
- h. Transfer sample to self-clamping tweezers
- i. Dip-coat by raising/lowering dipping stage
- j. Once dip-coated, put samples into cryostat in desired location
- k. Close glove box/transfer chamber door, open lab room/transfer chamber door
- l. Quickly move cryostat to right of wet bench, flow N₂ through it
- m. Fasten samples to sample stage of cryostat (N₂ flow persistent)
- n. When samples in place, detach N₂ flow hardware (keep cryostat sample chamber valve open) and place cryostat on computer table near turbo pump
- o. Pump down sample chamber with turbo pump, making sure vacuum is quickly established. Pump for ~ 30 minutes after pressure reaches 10⁻⁴ mbar.
- p. After pumped down, close sample chamber valve, then black valve on turbo pump, then turn off pump. Make sure each step successful along the way.